

UNIVERSITÀ DEGLI STUDI DI BRESCIA  
DIPARTIMENTO DI MEDICINA MOLECOLARE E TRASLAZIONALE



---

UNIVERSITÀ  
DEGLI STUDI  
DI BRESCIA

**DOTTORATO DI RICERCA IN  
GENETICA MOLECOLARE, BIOTECNOLOGIE E MEDICINA SPERIMENTALE  
XXXIII CICLO**

Settore Scientifico Disciplinare: BIO/13

**Molecular characterization of GAS5, miR-126-3p and TERRA in  
human hepatocellular carcinoma**

**Relatore:**

Prof. ALESSANDRO SALVI

**Tutor:**

Prof.ssa GIUSEPPINA DE PETRO

**Dottorando:**

Dott. MICHELE MANGANELLI

Anno Accademico 2019/2020

*A Te,  
che sei il mio  
titanio,  
alle supernove*

## TABLE OF CONTENTS

<b>ABSTRACT</b> .....	<b>1</b>
<b>1. INTRODUCTION</b> .....	<b>3</b>
1.1 Human hepatocellular carcinoma (HCC) .....	4
1.1.1 Pathogenesis of HCC.....	5
1.1.1.1 Aetiology.....	5
1.1.1.2 Malignant transformation.....	6
1.1.1.3 Histologic classification of HCC .....	6
1.1.2 Molecular Landscape of HCC .....	8
1.1.3 Telomeres and telomerase .....	9
1.1.3.1 Telomeres .....	9
1.1.3.2 Telomerase .....	9
1.1.3.3 Shelterin complex .....	10
1.1.3.4 Telomere maintenance mechanisms .....	11
1.1.3.5 Alternative Lengthening of Telomeres (ALT).....	12
1.1.3.6 Epigenetic regulation of telomeres .....	13
1.1.4 Telomerase reactivation in HCC .....	13
1.1.5 Altered molecular pathways in HCC .....	14
1.1.6 Molecular classes of HCC .....	16
1.1.7 BCLC staging system and therapeutic strategy .....	16
1.1.7.1 BCLC staging system.....	16
1.1.7.2 Sorafenib .....	17
1.1.7.2.1 Sorafenib targets and cellular effects .....	17
1.1.7.2.2 Hand-foot skin reaction - Burgdorf's reaction.....	18
1.1.7.2.3 Resistance to sorafenib .....	19
1.2 Non-Coding RNAs (ncRNA) .....	19
1.2.1 Long non-coding RNAs (lncRNA).....	19
1.2.1.1 LncRNA biogenesis and classification .....	19
1.2.1.2 Molecular functions of lncRNAs .....	21
1.2.1.3 LncRNAs and cancer .....	21
1.2.2 Telomeric-Repeat Containing RNA (TERRA).....	22
1.2.2.1 TERRA biogenesis .....	22
1.2.2.2 TERRA and telomere maintenance.....	22

1.2.2.3 Chromatin regulation.....	23
1.2.2.4 TERRA under stress.....	23
1.2.2.5 TERRA in cancer .....	24
1.2.3 Growth arrest-specific 5 (GAS5).....	24
1.2.3.1 GAS5 biogenesis.....	24
1.2.3.2 GAS5 functions.....	25
1.2.3.3 GAS5 in cancer .....	25
1.2.4 microRNA (miRNA) .....	26
1.2.4.1 miRNAs biogenesis.....	26
1.2.4.2 miRNA funtions and cancer.....	26
1.2.5 miR-126 .....	27
1.2.5.1 miR-126 biogenesis.....	27
1.2.5.2 miR-126 functions.....	27
1.2.5.3 miR-126 in cancer .....	28
1.3 Tumor biopsy .....	28
1.3.1 Biopsy .....	28
1.3.2 Liquid biopsy in HCC.....	29
1.4 Extracellular Vesicles (EVs) .....	30
1.4.1 EVs Biogenesis and functions .....	30
1.4.2 EVs cargo.....	30
<b>2. AIM OF THE WORK .....</b>	<b>33</b>
<b>3. MATERIALS AND METHODS .....</b>	<b>34</b>
3.1 Cell culture and treatment with sorafenib .....	34
3.2 Tissue and blood samples collection.....	34
3.3 RNA isolation.....	36
3.3.1 RNA isolation from cells and tissues.....	36
3.3.2 RNA isolation from cell secretomes and liquid biopsies.....	37
3.4 RT-PCR for cDNA synthesis .....	38
3.4.1 RT-PCR with random primers.....	38
3.4.2 RT-PCR stem-loop .....	39
3.4.3 TERRA First strand cDNA synthesis .....	39
3.4.4 One-Step RT-PCR and PreAmp .....	40
3.5 Quantitative Real-Time PCR (qPCR) .....	41
3.5.1 TaqMan qPCR .....	41

3.5.2 SYBR-GREEN qPCR.....	42
3.6 Transient Transfection.....	43
3.7 MTT-assay.....	44
3.8 Statistical analysis .....	44
<b>4. RESULTS.....</b>	<b>45</b>
4.1 Characterization of GAS5 and miR-126-3p in untreated and sorafenib treated HCC cells....	45
4.2 GAS5 silencing rescues miR-126-3p expression .....	46
4.3 Effect of miR-126-3p overexpression on cell growth.....	47
4.4 TERRA and telomerase intracellular dysregulation.....	49
4.5 Detection of GAS5, miR-126-3p, TERRA, TERC and TERT mRNA in the EVs of HCC cultured cells.....	51
4.6 Expression study of GAS5, miR-126-3p, TERRA, TERC and TERT mRNA in HCC bioptic specimens .....	56
4.7 GAS5, miR-126-3p, TERRA, TERC and TERT are dysregulated in HCC tissues .....	58
4.8 The analysis of plasma of untreated HCC patients reveal a dysregulated amount of the transcripts GAS5, miR-126-3p and TERRA.....	66
4.9 Study of GAS5, miR-126-3p as circulating transcripts in HCC patients treated with sorafenib .....	69
<b>5. DISCUSSION .....</b>	<b>72</b>
<b>6. CONCLUSIONS AND FUTURE PERSPECTIVES.....</b>	<b>78</b>
<b>7. REFERENCES.....</b>	<b>79</b>
<b>8. AKNOWLEDGMENTS .....</b>	<b>94</b>
<b>9. APPENDIX A .....</b>	<b>95</b>

## ABSTRACT

Il carcinoma epatocellulare (HCC) è il più comune tumore primario del fegato. È un tumore maligno eterogeneo, spesso diagnosticato in uno stadio avanzato, con prognosi sfavorevole, nonché la terza causa di morte per cancro a livello mondiale. Per il trattamento dell'HCC in stadio avanzato non-resecabile il sorafenib rappresenterebbe ancora una prima linea di monoterapia sistemica. Il sorafenib aumenta significativamente la sopravvivenza media dei pazienti con HCC, anche se genera diversi effetti collaterali e molti pazienti sviluppano una resistenza secondaria durante il trattamento. Il sorafenib è un inibitore serin-/treonin- e tirosin- kinasico di diversi pathways oncogenici (CRAF, BRAF, eIF4E, VEGFR-2 and -3, PDGFR- $\beta$  FGFR-1, c-kit, FLT-3 and RET), sia nelle cellule tumorali, sia nelle cellule endoteliali o nei periciti. Tra gli effetti indotti dal sorafenib ci sono variazioni nel trascrittoma, proteoma, nel DNA-metiloma, e disregolazione di molecole ad RNA non-codificante (ncRNAs).

I ncRNAs dimensionalmente possono essere classificati in due grandi famiglie: piccoli RNA non-codificanti (small non-coding RNA; sncRNAs), più piccoli di 200 nt, e lunghi RNA non-codificanti (long non-coding RNA; lncRNAs), più lunghi di 200 nt. Tra i sncRNAs, i miRNAs sono la classe più studiata e caratterizzata. I ncRNAs svolgono differenti funzioni sia a livello fisiologico, sia patologico; sono presenti in diversi distretti anatomici e mostrano un pattern di espressione cellulare/tessuto specifico, come osservato in differenti tipi di tumori.

L'Associazione Europea per lo Studio del Fegato (European Association for the Study of the Liver ; EASL) ha evidenziato la necessità e lo sviluppo di nuovi strumenti ad alta sensibilità per predire e monitorare la risposta terapeutica o la resistenza alla terapia sistemica.

Per meglio comprendere i meccanismi che sottendono la patogenesi dell'HCC, in relazione al trattamento con sorafenib, il principale obiettivo di questo lavoro è caratterizzare i lncRNAs GAS5, TERRA ed il miR-126-3p ed i componenti della telomerasi (TERT mRNA e TERC). GAS5 (Growth Arrest Specific 5) è un lncRNA oncosoppressore coinvolto nella proliferazione cellulare, apoptosi e migrazione. Il miR-126-3p è un miRNA oncosoppressore associato ad angiogenesi ed infiammazione. TERRA è un lncRNA oncosoppressore inibitore della telomerasi e coinvolto nell'omeostasi dei telomeri. Sono quindi studiati due aspetti cardini della biologia dei tumori: la proliferazione cellulare incontrollata ed il potenziale replicativo illimitato delle cellule tumorali umane, in particolare nell'HCC.

Utilizzando la tecnologia array per lncRNAs e miRNAs pato-specifici in un modello *in vitro* di HCC, è stato precedentemente dimostrato che GAS5 è upregolato, mentre il miR-126-3p è downregolato, dopo trattamento con sorafenib. GAS5 ed il miR-126-3p mostrano inoltre dei trend di

espressione intracellulare dose-dipendente, tra loro inversi. In seguito a silenziamento di GAS5, il livello di espressione del miR-126-3p aumenta. L'over-espressione del miR-126-3p riduce la proliferazione cellulare, ma non si osserva nessun effetto additivo al trattamento con sorafenib. TERRA inoltre è differenzialmente espresso nelle cellule sensibili, trattate e resistenti al farmaco. Il sorafenib, tuttavia, comprometterebbe, in maniera diretta o indiretta, la secrezione di vescicole extracellulari (EVs) nel microambiente. L'analisi dei livelli extracellulari di GAS5, miR-126-3p e TERRA nel secretoma del modello *in vitro* di HCC evidenzia come il farmaco in cellule sensibili, trattate e resistenti al sorafenib, generi una variazione dei trascritti non-codificanti, sia a livello delle EVs, sia nella componente libera dalle EVs (depleta). Per meglio comprendere la disregolazione di GAS5, miR-126-3p e TERRA, la loro espressione è stata analizzata in biopsie di HCC e corrispondente controparte peritumorale (PT) di pazienti non trattati con sorafenib. GAS5 è differenzialmente espresso nell'HCC, mentre il miR-126-3p è significativamente downregolato nell'HCC rispetto alla componente PT. TERRA è downregolato in maniera significativa ed al contempo TERT mRNA e TERC mostrano un trend di over-espressione nella componente tumorale. I livelli di GAS5, miR-126-3p e TERRA sono stati valutati anche nelle corrispondenti biopsie liquide prima della resezione chirurgica, e confrontati con individui sani. GAS5 ed il miR-126-3p sono rispettivamente meno e più abbondanti negli individui con HCC. Entrambe le molecole mostrano un buon potere diagnostico. Anche i livelli plasmatici di TERRA sono elevati negli individui HCC, permettendo di discriminare pazienti con HCC da individui sani. Nonostante GAS5, TERRA ed il miR-126-3p siano secreti nell'ambiente extracellulare e presenti nel torrente sanguigno, non sono state osservate correlazioni tra i loro livelli plasmatici l'espressione intratissutale. Infine, per meglio comprendere se GAS5 ed il miR-126-3p potessero anche essere considerati indicatori circolanti di risposta o resistenza al trattamento con sorafenib, sono stati monitorati i loro livelli circolanti e le loro variazioni nel plasma di pazienti HCC durante il follow-up con il farmaco. GAS5 mostra un trend di upregolazione, mentre il miR-126-3p un trend di downregolazione, immediatamente dopo la somministrazione del farmaco. Ciò indicherebbe un possibile ruolo dei suddetti ncRNAs in risposta al farmaco.

In conclusione con il presente studio è stato possibile dimostrare per la prima volta delle variazioni nell'espressione di GAS5, TERRA e miR-126-3p in differenti scenari dell'HCC (a livello intracellulare, nel secretoma, in tessuti normali e tumorali e plasma). La valutazione delle variazioni nell'espressione dei ncRNAs permetterebbe di comprendere potenziali nuovi scenari sugli eventi molecolari legati all'HCC ed al trattamento con sorafenib. Permetterebbe inoltre di individuare nuove molecole come possibili biomarcatori di risposta o resistenza alla terapia, di significativa rilevanza clinica.

## 1 INTRODUCTION

“Cancer” is a catch-all term used to denote a set of diseases characterized by autonomous expansion and spread of a somatic clone. Tumor initiation is likely driven by a subset of cells with stem cell features (CSCs). The cancer clone must co-opt multiple cellular pathways that enable it to disregard the normal constraints on cell growth, modify the local microenvironment to favor its own proliferation, invade through tissue barriers, spread to other organs and evade immune surveillance<sup>1</sup>. No single cellular program directs these behaviours. Rather, there is a large pool of potential pathogenic abnormalities from which individual cancers draw their own combinations: the commonalities of macroscopic features across tumors belie a vastly heterogeneous landscape of cellular abnormalities. In somatic cells heritable variation arises from mutations acquired stochastically throughout life, notwithstanding additional contributions come from germline and epigenetic variations. A subset of these mutations alter the cellular phenotype, and a small subset of those variants confer an advantage on clones during the competition to escape the tight physiological controls wired into somatic cells. Continuous efforts are being made to discover eligible biomarkers for early detection, monitoring, prognosis and prediction of treatment response to better improve the outcome of cancer patients. Moreover, in the *era* of personalized medicine, the information obtained from the blood of each patient may be paramount in assessing the disease outcome and treatment<sup>2</sup>.



## 1.1 Human hepatocellular carcinoma (HCC)

Hepatocellular carcinoma (HCC) is the most common primary liver malignancy. It is a heterogeneous malignant tumor, often diagnosed at an advanced stage and therefore with poor prognosis, as well as the third world cancer-related cause of death. Although more than 80% of the estimated new cases of HCC occurred in less developed regions of the world, its incidence is increasing worldwide, including in more developed countries<sup>3</sup> (Fig.1).

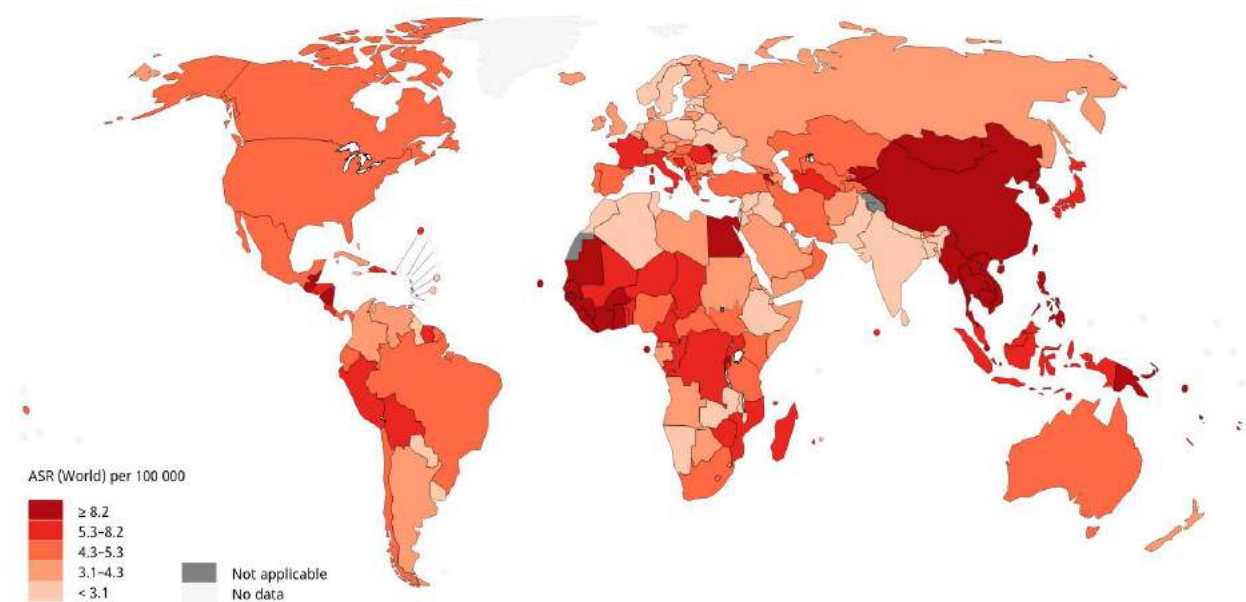


**Fig. 1. Estimated ranked age-standardized incidence rates (ASR) of HCC worldwide.** HCC distribution varies according to geographic location. The disease burden is higher in sub-Saharan Africa and Eastern Asia. Mediterranean countries, such as Italy, have intermediate incidence rates. North and South America have a relatively low incidence. The HCC cases global age distribution is related to dominant viral hepatitis in the underlying population and the age at which it was acquired. In regions of high incidence the most common etiology is HBV transmitted at birth, whereas in regions of moderate-low incidence the most common etiology is HCV acquired later in life. Source: International Agency for Research on Cancer – World Health Organization (WHO); Graphical representation from GloboCan (Global Cancer Observatory), 2018; <https://gco.iarc.fr/>.

## 1.1.1 Pathogenesis of HCC

### 1.1.1.1 Aetiology

Several aetiological factors contribute to the development of HCC in different manner.

**Risk factors.** The risk factors for HCC are well established and comprehend viral infections, as hepatitis B (HBV) and C (HCV) viruses (Fig.1), adeno-associated virus serotype 2 (AAV2), alcohol abuse, non-alcoholic fatty liver disease (NAFLD), non-alcoholic steatohepatitis (NASH), tobacco smoke inhalation and aflatoxin B1 mycotoxin ingestion.

**Mendelian genetic predisposition to HCC.** HCC can develop in patients with Adenomatous polyposis coli (APC) germ-line mutations<sup>4</sup>. HCC predispositions are observed in several rare monogenic metabolic diseases, mainly *via* development of cirrhosis. These include iron (hemochromatosis, HFE1 gene) or copper (Wilson disease, ATP7B gene) overload, tyrosinemia type I (FAH gene), porphyria acute intermittent (HMBS gene) or *cutanea tarda* (UROD gene), and the  $\alpha$ -1-antitripsin deficiency (SERPINA1 gene)<sup>5</sup>. In addition, genetic alterations of glucose metabolism, leading to glycogen storage diseases (particularly type Ia or von Gierke disease, G6PC gene), or to specific maturity onset diabetes of the young type III (MODY3, HNF1A genes) can promote genetic liver adenomatosis occurrence and, in a second step, their rare malignant transformation to HCC without cirrhosis<sup>6-8</sup>.

**Multifactorial genetic predisposition to HCC.** Several single nucleotide polymorphisms (SNPs) were identified to be associated with HCC<sup>9</sup>. Many SNPs alter biologic pathways of carcinogenesis, such as Transmembrane Phosphoinositide 3-Phosphatase And Tensin Homolog 2 (TPTE2)<sup>10</sup> or Dicer-like 1 (DCL1)<sup>11</sup>; immune system regulation MHC Class I Polypeptide-Related Sequence A (MICA)<sup>12</sup>; inflammatory pathway Signal Transducer And Activator of Transcription 4 (STAT4)<sup>13</sup>, tumor necrosis factor (TNF- $\alpha$ ), interleukin (IL-1 $\beta$ ), or transforming growth factor (TGF- $\beta$ )<sup>14</sup>; oxidative stress superoxide dismutase 2 (SOD2) or myeloperoxidase (MPO)<sup>15,16</sup>; iron metabolism with a cooperation between alcohol intake and the hemochromatosis type 1 (HFE1) C282Y mutant variant<sup>17</sup>; DNA repair methylenetetrahydrofolate reductase (MTHFR) or X-Ray Repair Cross Complementing 3 (XRCC3)<sup>18,19</sup>; cell cycle with a major role of Mouse double minute 2 homolog (MDM2)<sup>20</sup> and tumor protein p53 (TP53)<sup>21</sup>; epidermal growth factor (EGF)<sup>22</sup>; detoxification pathways glutathione S-transferase M1 (GTSM1) and Glutathione S-transferase theta-1 (GSTT1)<sup>23</sup>; lipid metabolism patatin-like phospholipase domain-containing protein 3 (PNPLA3)<sup>24</sup>; a polymorphism in DEP Domain Containing 5 (DEPDC5), a gene of unknown function likely implicated in intracellular signal transduction<sup>25</sup>; and in a region containing the UBE4A, KIF1B, PGD genes<sup>26</sup>.

Polymorphisms modulate HCC occurrence at different steps, including predisposition to risk factors, to the severity of the chronic liver disease, highlighting the close relationships among the nature of the exposure, the genetic background, and the mechanism of hepatocyte transformation/proliferation, the evolution to cirrhosis and the malignant transformation and tumor progression<sup>9</sup>.

#### **1.1.1.2 Malignant transformation**

Chronic exposure of the liver to injury causes repeated hepatocyte damage and sets up a vicious cycle of cell death and regeneration, chronic liver inflammation, infiltration by innate and adaptive immune cells and stellate cells, producing a pathological *milieu*, through the development of fibrosis, which eventually results in cirrhosis. Cirrhotic liver exhibits focal areas of abnormal immature hepatocytes, and these dysplastic foci (<1 mm) or dysplastic nodules (≥1 mm; DN) are considered precancerous lesions. The presence of stromal invasion is considered to be the hallmark feature that differentiates early HCC from DNs<sup>27</sup>.

#### **1.1.1.3 Histologic classification of HCC**

HCC is clinically heterogeneous and the histopathologic appearance of HCC also exhibits significant heterogeneity. The range of cellular differentiation extends from very well-differentiated to poorly differentiated tumors. HCCs also exhibit varied morphologic subtypes, including biphenotypic HCCs with combined features of hepatocellular and cholangiocarcinoma, cirrhotomimetic HCC, clear cell HCC, fibrolamellar HCC, granulocyte colony-stimulating factor HCC with major neutrophilic infiltrates, lymphocyte-rich HCC, myxoid HCC, sarcomatoid HCC, scirrhous HCC, and steatohepatic HCC<sup>27-30</sup>.

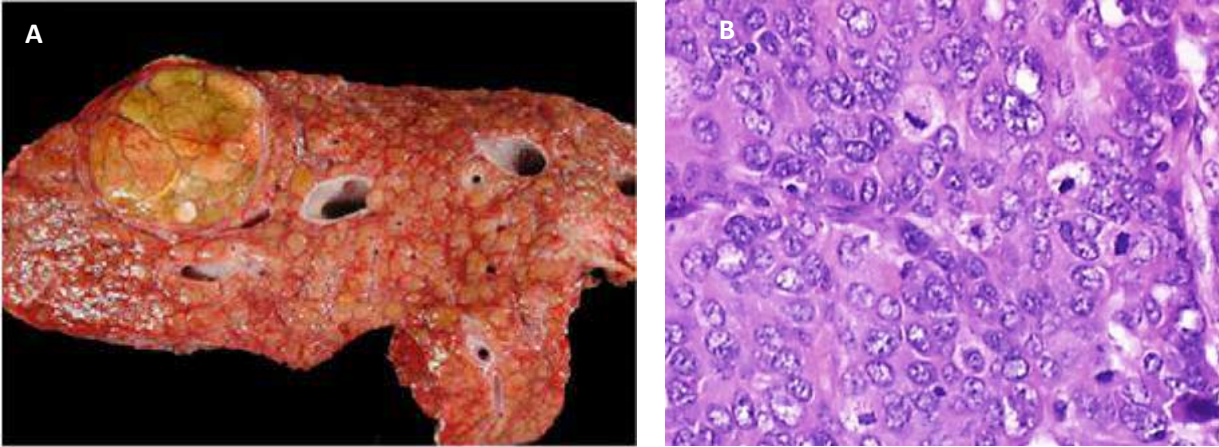


**Fig. 2. Macroscopic and microscopic aspects of HCC.** A) Nodular pattern of HCC developed in a cirrhotic liver. B) Hematoxylin and eosin (H&E) stain in which tumor cells appear large, eosinophilic with prominent nucleoli. Source: Paradies, Recent Results in Cancer Research, 2013<sup>31</sup>.

### 1.1.2 Molecular landscape of HCC

New advances in next-generation –omics platforms (whole genome sequencing, whole-exome sequencing, RNA-sequencing, and genome-wide methylation arrays) have explored and yielded significant insights and explored the HCC molecular landscape (Fig. 3).

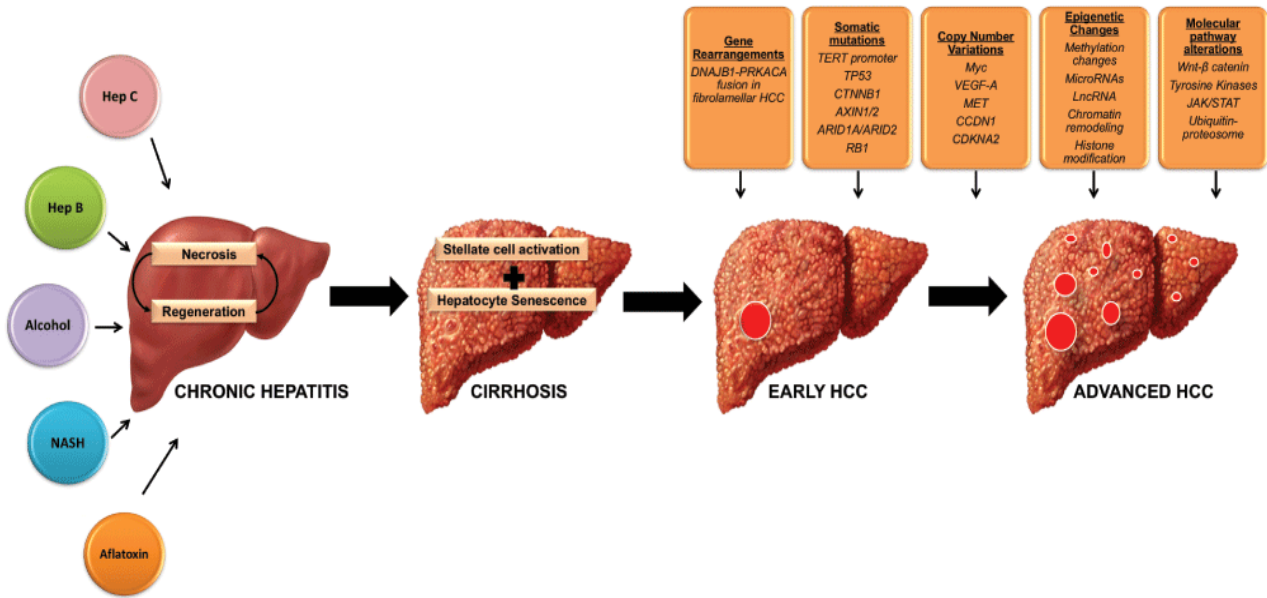


**Fig. 3. Pathogenesis of Hepatocellular Carcinoma.** Chronic exposure of the liver to injury from viral hepatitis, alcohol abuse or NASH causes repeated hepatocyte damage and sets up a vicious cycle of cell death and regeneration which eventually results in cirrhosis. The resultant genomic instability leads to initiation of HCC. Step wise accumulation of multiple genetic events including gene rearrangements, somatic mutations, copy number alterations, epigenetic changes and growth factor pathway alterations eventually lead to tumor progression and metastases. Abbreviations: Hep B, hepatitis B; Hep C, hepatitis C; HCC, hepatocellular carcinoma; NASH, non-alcoholic steatohepatitis. Source: Dhanasekaran *et al.*, F1000Res, 2016<sup>27</sup>.

### 1.1.3 Telomeres and telomerase

#### 1.1.3.1 Telomeres

From the greek τέλος “end”, and μέρος “part”, the term “telomere” defines DNA-protein structures at the end of linear eukaryotic chromosomes<sup>32,33</sup>. The 10–15kb long chromosome terminus consists of a single-stranded protrusion of the G-strand, referred to as the “G-overhang”, that varies between 50-500nt<sup>34</sup>, composed of long stretches of TTAGGG (t-type) repeat arrays with an increasing number of variants toward proximal, subtelomeric regions, the most common being TGAGGG (g-type), TCAGGG (c-type), and TTGGGG (j-type) repeats<sup>35,36</sup>. The G-overhang 3'-end of the telomere invades a region of the telomeric double-stranded DNA (dsDNA) to form a displacement-loop (D-loop) and a looped region of double stranded telomere repeats. Thus, DNA is organized in a large, looped structure called “T-loop”. On the functional level, the T-loop structure masks the DNA terminus from DNA double-stranded breaks (DSBs) repair machinery<sup>37</sup>. For the accurate extension of chromosome ends Nature invented a specialized replication machinery, the “Telomere Terminal Transferase”, or “Telomerase”<sup>38</sup>.

#### 1.1.3.2 Telomerase

The telomerase is constituted by the “telomerase reverse transcriptase” catalytic subunit, encoded by TERT gene, and a “RNA component” encoded by TERC gene (Fig.3 and Fig.4).

Human TERT gene is located on chromosome 5p15.33, spans 40kb in length, and consists of 16 exons and 15 introns. TERT protein (hTERT) is constituted by four structural domains, the telomerase essential N-terminal domain (TEN), the telomerase RNA binding domain (TRBD), the reverse transcriptase domain (RT) and the C-terminal domain (CTE)<sup>39,40</sup>. The TEN domain binds RNA and telomeric DNA contributing to telomerase catalysis<sup>41</sup>. The RT is the central catalytic domain. It consists of seven conserved motifs shared with conventional reverse transcriptases, 1 and 2 and A, B', C, D and E. The 1 and 2 motifs bind incoming nucleotides, while the other five motifs form the catalytic site<sup>39</sup>. A structure called “insertion in finger domains (IFD)”, located between A and B' motifs, is essential for repeat addition processivity<sup>39,42</sup>.

Human TERC gene is located on chromosome 3q26.2 and spans 451nt<sup>43</sup>. TERC (hTR), the integral RNA component within the telomerase catalytic core, contains two conserved and potentially universal structures, the template/pseudoknot domain and the CR4/5 domain (three-

way junction or stem-terminus element). Those two domains comprise the regions required for telomerase activity and are sufficient to provide active telomerase *in vitro*<sup>39</sup>. Further, TERC contains the H/ACA box, a third conserved domain among all known vertebrates. Maturation of TERC involves the binding of dyskerin, NOP10, NHP2 and GAR1 proteins at nascent stage<sup>44</sup>. TERC in the nucleolus assembles with TERT, to form a mature telomerase complex, followed by recognition of Cajal body (CAB) box by telomerase and Cajal body protein 1, WRAP53, that in turn recruits mature telomerase complex to Cajal body<sup>45</sup>. During late S-phase, Cajal body facilitates the recruitment of the telomerase complex to telomeres for the extension of DNA repeats. TERC is ubiquitously expressed in various human cells, while the TERT gene is stringently repressed in most of the human somatic cells after birth. This consequently results in telomerase silencing.

### 1.1.3.3 Shelterin complex

Telomeres, *per se*, are intrinsically unstable and represent fragile sites. Binding of associated proteins that constitute the “Shelterin Complex” ensures stability and assists the accurate extension of chromosome ends<sup>46,47</sup>. Constituents of shelterin complex recruit telomerase, discriminating chromosomal ends from broken ends created by double strand breaks<sup>48</sup>. The shelterin complex comprises six subunits, three DNA-binding and three proteins that act as adaptors and mediate interactions among the constituents<sup>49</sup>. Telomere repeat binding factor 1 and 2 (TRF1 and TRF2) bind to the double-stranded telomere DNA repeats. Protection of telomeres 1 (POT1), through its DNA-binding domain, accumulates at the single-stranded G-rich overhang *via* a ternary complex with TPP1 (abbreviation from TINT1/PTOP/PIP1; proper gene name ACD, adrenocortical dysplasia homolog)<sup>48</sup>. TPP1 connects with TRF interacting nuclear factor 2 (TIN2)<sup>48,50</sup>. TIN2 stabilizes the shelterin complex through simultaneous binding with TRF1, TRF2 and TPP1<sup>51</sup>. Repressor/activator protein 1 (RAP1) also protects telomeres from non-homologous end joining (NHEJ) by forming the T-loop<sup>52</sup>. TRF2 is the main repressor of NHEJ in the G1-phase of the cell cycle. The T-loop conceals the chromosome ends from the DNA damage surveillance and POT1 and TPP1 compete with telomerase for the access to the structure<sup>53,54</sup> (Fig. 4). Unwinding of the T-loop, necessary for telomere elongation, involves a DNA helicase, regulator of telomere elongation helicase 1 (RTEL1)<sup>55,56</sup>. Other critical helicases are involved in resolving the tertiary structures, to allow telomerase to the substrates and they include the RecQ family, Werner syndrome RecQ like helicase (WRN) and Bloom syndrome RecQ like helicase (BLM) members. Those helicases unwinding the G-







RNA template, whereas the 5'-end of the DNA interacts with the template-proximal and template-distal anchor sites. Next, template-directed addition of nucleotides to the 3'-end of the DNA occurs sequentially, until the 5'-end of the template is reached. Telomerase then undergoes translocation and repositions at the 3'-end of the DNA in concert with recognition of the 3'-template boundary<sup>61</sup>. This ability to synthesize DNA depends on the simultaneous translocation of the RNA-DNA duplex away from the active site following each nucleotide addition (type I) and translocation of the 3'-end of the DNA substrate relative to the RNA template (type II)<sup>61,62</sup>. Once telomerase completes its function, DNA  $\alpha$ -primase synthesizes a RNA primer near the 3'-end. DNA polymerase fills in the vacant region. A short region at the 3'-end will remain single-stranded (Fig. 4).

Alexey Olovnikov proposed that the end replication problem causes the progressive telomere shortening and it acts as an internal clock to determine the number of divisions that a cell could experience through its life, thereby controlling the aging of the organism<sup>63</sup>. Replicative senescence limits the replicative potential of primary cells (the so called “Hayflick limit”)<sup>64</sup>.

In the absence of any counterbalancing lengthening mechanism, progressive telomere shortening during cell proliferation eventually results in telomere dysfunction and a DNA damage response (DDR) at chromosome ends. Tumor protein p53 (p53) and retinoblastoma protein (RB) arrest cellular proliferation in the “replicative senescence” or “mortality stage 1 (M1)”<sup>65</sup>. In case of p53 or RB tumor suppressor pathways loss, cell division is still permitted, causing further telomere shortening, resulting in an excess of genomic instability and a massive cell death or “crisis” or “mortality stage 2 (M2)”<sup>66</sup>. Bypass of senescence or crisis and acquisition of unlimited replicative potential is a hallmark of tumorigenesis. 90% of all human cancers achieve an indefinite proliferative potential through the upregulation of telomerase activity<sup>67,68</sup>. Of the remaining 10% of tumors, most counteract telomere attrition using a non-telomerase mechanism referred to as “Alternative Lengthening of Telomeres (ALT)”<sup>69,70</sup>.

#### **1.1.3.5 Alternative Lengthening of Telomeres (ALT)**

ALT mechanism evolves in three steps. In step 1 the single stranded G-overhang at the telomere terminus invades homologous DNA forming an homologous recombination (HR) intermediate structure. In step 2 strand invasion is followed by the template-directed synthesis of telomeric DNA, operated by polymerase  $\delta$  or  $\zeta$ <sup>71,72</sup>. In step 3 the processing of HR

intermediate products occurs before chromosome segregation. The DNA template for new telomeric DNA synthesis by ALT may be a sister chromatid, or telomeres could copy themselves looping out or looping back on themselves. ALT activity has been demonstrated in various cancer types and is strongly correlated with loss of ATP-dependent helicase ATRX or its binding partner, the H3.3 histone chaperone DAXX<sup>73-75</sup>. ATRX-DAXX complex has been demonstrated to bind telomeric repeats and G-quadruplex structures<sup>76</sup>, facilitating replication throughout aberrant secondary structure<sup>77</sup>.

### **1.1.3.6 Epigenetic regulation of telomeres**

Vertebrate telomeric chromatin shows under-acetylation, enrichment in H3K9me3 histone mark mediated by “suppressor of variegation” Suv39h1 and Suv39h2 Histone Methyl Transferases (HMTases)<sup>78,79</sup>. Although telomeres and subtelomeres carry repressive repetitive heterochromatic features, transcriptional activity has been detected at vertebrate telomeres. Recent studies have introduced additional players in telomeric chromatin formation. In particular, DNA methylation sensitive subtelomeric promoters drive towards chromosome ends the expression of “Telomeric repeat-containing RNA (TERRA)” by RNA polymerase II<sup>80,81</sup>.

### **1.1.4 Telomerase reactivation in HCC**

One of the early events in HCC *genesis* is the reactivation of telomerase. This event occurs with different mechanisms. Point mutations in the TERT promoter (G228T and G250T) are present in 54% of liver cancers<sup>82</sup>. HBV insertion in TERT promoter also occurs<sup>83-85</sup>. TERT promoter mutations are rare in lesions of early stages, but the mutational frequency increases rapidly during the transformation of premalignant lesions towards HCC<sup>86,87</sup>. The mechanisms of telomerase reactivation are mutually exclusive and TERT promoter mutations are frequently associated with  $\beta$ -catenin (CTNNB1) mutations, suggesting cooperation between telomerase maintenance and  $\beta$ -catenin pathway in liver tumorigenesis<sup>82,88,89</sup>. 5–10% of HCC have structural variants that activate the TERT gene<sup>88</sup>. Liver cancers had cycles of templated insertions that affect TERT in an hosting chromosome. All these events duplicated the entire TERT gene and linked it to duplications of whole genes, fragments of genes or regulatory elements from elsewhere in the genome, and led to increased expression of TERT<sup>90</sup> (Fig. 3). Other mechanisms of telomerase re-expression remain to be discovered and the role of alternative pathways ALT need to be evaluated.

### 1.1.5 Altered molecular pathways in HCC

Different molecular pathways are altered in HCC genesis (Fig. 3).

**p53 pathway.** The p53 cell cycle pathway is altered in at least half of HCCs, with frequent TP53 mutations, the tumor suppressor gene more frequently mutated in cancer<sup>89,91,92</sup>. The RB pathway that control progression from G1 to S phase of the cell cycle is inactivated in HCC mainly by homozygous deletion of Cyclin Dependent Kinase Inhibitor 2A (CDKN2A)<sup>88</sup> or RB1 mutations<sup>93</sup>.

**WNT/ $\beta$ -catenin pathway.** CTNNB1 mutations are substitutions or in-frame deletions in a hotspot located domain targeted by the APC/AXIN1/GSK-3 $\beta$  inhibitory complex<sup>94,95</sup>.

**PI3K/AKT/mTOR and RAS/RAF/MAPK pathways.** The PI3K/AKT/mTOR and RAS/RAF/MAPK pathways are activated by amplification of the Fibroblast growth factor 19 (FGF19) and Cyclin D1 (CCND1) loci<sup>96,97</sup>. Even activating mutations of PI3-Kinase Catalytic Subunit Alpha (PIK3CA) and inactivating mutations of tuberous sclerosis 1 and 2 (TSC1 and TSC2) lead to activation of the AKT/mTOR signaling in a subset of HCC<sup>88,89</sup>. Homozygous deletion of phosphatase and tensin homolog (PTEN) has been identified in HCCs<sup>98</sup>. Activating mutations of genes belonging to the RAS family are rarely observed in HCC, and inactivating mutations of the RAS inhibitor RSK2 (RP6SKA3), were identified in tumors<sup>91</sup>. RSK2, is located downstream MAPKs and extracellular signal-regulated kinase, and it is a negative control loop of RAS signaling. Inactivation of RSK2 induces a constitutive activation of the RAS pathway<sup>89</sup>.

**VEGF pathway.** Vascular endothelial growth factor (VEGF) ligands VEGF-A, -B, -C, and -D binding induces dimerization and autophosphorylation of VEGFR-1, -2 and -3 receptors. VEGF pathways plays a crucial role in vascular permeability, extra cellular matrix degradation, cellular migration and invasion, tumor grade, outcome, disease recurrence, poor disease-free and overall survival<sup>99</sup>.

**EGFR, IGF, FGF and HGF/c-MET pathway.** The epidermal growth factor receptor (EGFR) is a tyrosine kinase receptor activated by epidermal growth factor (EGF) and transforming growth factor- $\alpha$  (TGF- $\alpha$ ). Upon activation, EGFR forms homo- heterodimers and autophosphorylates different tyrosine residues (Y992, Y1045, Y1068, Y1148 and Y1173) in its intracellular cytoplasmic domain, which in turn leads to initiation of many downstream signal transduction cascades. EGFR pathway regulate cell growth, survival, proliferation, and differentiation.

Insulin growth factors (IGF-1 and IGF-2) ligands binding to IGF-1R triggers rapid receptor autophosphorylation, followed by phosphorylation of intracellular targets, which in turn leads to

PI3K, PKB and the RAS/RAF/MAPK pathway activation. IGF pathway regulates cell proliferation, motility and apoptosis.

FGF substrate 2 (FRS2) can be phosphorylated by FGFR receptors to activate PI3K, RAS/RAF/MAPK and WNT/ $\beta$ -catenin pathways<sup>99</sup>.

Hepatocyte growth factor (HGF) is a multifunction cytokine secreted by mesenchymal cells that can stimulate mitogenesis, cell motility and invasion. HGF is secreted as a single inactive polypeptide and is cleaved by serine proteases into an  $\alpha$ -chain and  $\beta$ -chain. The active form is a heterodimer of the two chains, linked by a disulphide bond. The HGF binds MET tyrosine kinase receptor, predominantly expressed on epithelial cells surface. MET is a heterodimer constituted by an  $\alpha$ -chain and a membrane spanning  $\beta$ -chain with tyrosine kinase activity. MET regulates cell proliferation, migration, survival, branching morphogenesis and angiogenesis and tissue regeneration. HGF binding to MET triggers transphosphorylation of different tyrosine residues (Y1234, 1235, Y1349, Y1356) which in turn activates PI3K, RAS/RAF/MAPK and WNT/ $\beta$ -catenin pathways. c-MET overexpression is linked to a decreased survival<sup>99</sup>.

**JAK-STAT pathway.** Janus kinase (JAK) belongs to a family of non-receptor protein tyrosine kinases comprising of JAK1, JAK2, JAK3, and TYK2 (non-receptor Protein Tyrosine Kinase-2). STATs (STAT1-6) are latent cytoplasmic transcription factors that become activated after recruitment of an activated receptor complex. Binding of various ligands as interferons, interleukins, and growth factors to cell surface receptors, activates associated JAKs, increasing their kinase activity. Activated JAKs then phosphorylate tyrosine residues on the receptor, creating binding sites for Src Homology 2 (SH2) -domain proteins. STATs form hetero- or homodimers and translocate to the nucleus, where they targets the expression of genes involved in immunity, proliferation, differentiation, apoptosis and oncogenesis<sup>99</sup>.

**Oxidative stress pathway.** The oxidative stress pathway is altered by recurrent driver activating mutations of basic leucine zipper nuclear factor erythroid-derived 2-like 2 (NFE2L2 gene that encodes for NRF2 protein) or inactivating Kelch-like ECH-associated protein 1 (KEAP1), preventing proteasome degradation of NRF2 physiologically induced by KEAP1/CUL3 complex ubiquitinylation<sup>91,100</sup>.

**Epigenetic modifiers.** Epigenetic modifiers are recurrently altered in HCC<sup>89</sup>, with inactivating mutations in AT-Rich Interaction Domain 1A and 2 (ARID1A and ARID2)<sup>91;101</sup>, components of the BAF-type SWI/SNF nucleosome remodeling complex. The physiologic role of these complexes is to modify chromatin structure and nucleosome position. Indirectly, they modify transcription fate of the cell. Recurrent somatic mutations in the H3K4 histone methylation writer

family MLL, MLL2, MLL3, and MLL4 genes or HBV insertions in MLL4 are also frequent in HCC<sup>89</sup>.

### **1.1.6 Molecular classes of HCC**

Two main molecular classes, each representing approximately 50% of patients, have been identified in HCC: proliferative and non-proliferative HCC<sup>97,102,103</sup>.

The proliferative class is characterized by activation of RAS, mTOR and IGF signaling and by FGF19 amplification, and associated with HBV-related aetiologies and poor outcomes<sup>97,102,104,105</sup>. Some authors have proposed that there are two subtypes of the proliferative class: the WNT - TGF- $\beta$  group and the progenitor cell group. The progenitor cell group is enriched in progenitor cell markers, such as epithelial cell adhesion molecule, and the overexpression of  $\alpha$ -fetoprotein (AFP  $\geq 400$ ng/ml)<sup>97,102,104-106</sup>.

By contrast, the non-proliferative class is more heterogeneous, but there is still a clear subtype characterized by CTNNB1 mutations that are associated with alcohol-related and HCV-related HCCs<sup>106</sup>. Direct translation of molecular HCC subclasses into clinical management is yet to be achieved.

### **1.1.7 BCLC staging system and therapeutic strategy.**

#### **1.1.7.1 BCLC staging system**

In contrast to the classification system of the majority of neoplasms, classification of HCC is not based on the TNM system, but on the Barcelona Clinic Liver Cancer (BCLC) staging classification, which is endorsed by European and American clinical practice guidelines<sup>107,108</sup> (Fig. 5). BCLC is the only method that takes into account the spread of the tumor, the hepatic function and the presence of symptoms, and thus it has high predictive capacity. This staging system defines five prognostic subclasses and allocates specific treatments for each stage. Five treatments can extend the life expectancy of patients with HCC: surgical resection, liver transplantation, radiofrequency ablation, chemoembolization and sorafenib<sup>107</sup>.

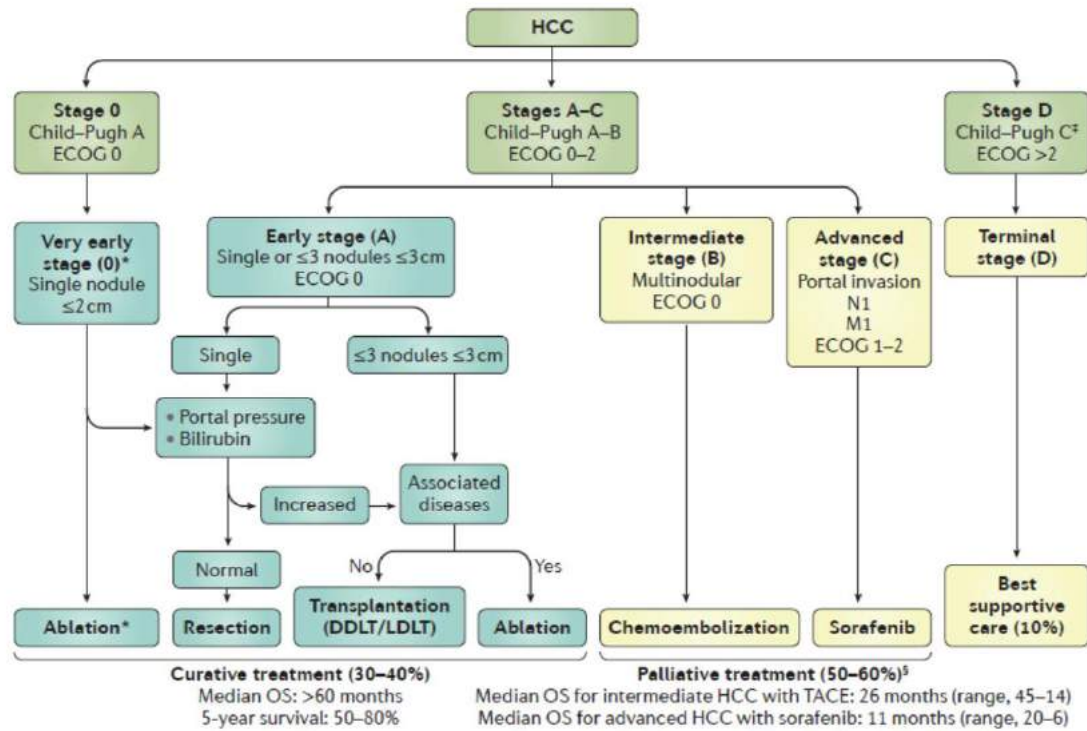


**Fig. 5. BCLC staging system and therapeutic strategy.** The Barcelona Clinic Liver Cancer (BCLC) classification consists of five stages to select the best candidates for the best therapies currently available. Patients with asymptomatic early tumours (stages 0–A) are candidates for radical therapies (resection, transplantation or local ablation). Asymptomatic patients with multinodular hepatocellular carcinoma (HCC; stage B) are suitable for transcatheter arterial chemoembolization (TACE). Patients with advanced symptomatic tumors and/or an invasive tumoral pattern (stage C) are candidates to receive sorafenib. End-stage disease (stage D) includes patients with poor prognoses who should be given the best supportive care possible. DDLT, deceased donor liver transplantation; ECOG, Eastern Cooperative Oncology Group; LDLT, living donor liver transplantation; M1, M1 metastasis; N1, N1 lymph node; OS, overall survival. \*Patients at very early stages (stage 0) can be considered first for ablation in case they have contraindications for liver transplantation. ‡Patients in Child–Pugh class C should be first considered for liver transplantation. §Treatment stage migration (consider the next efficacious treatment in the algorithm when previous therapies fail). Source: LLovet *et al*, *Nat Rev Dis Primer*, 2016<sup>109</sup>.

## 1.1.7.2 Sorafenib

### 1.1.7.2.1 Sorafenib targets and cellular effects

For the treatment of HCC in advanced and/or unresectable stage, the Food and Drug Administration (FDA) and European Medicines Agency (EMA) approved the drug sorafenib. Sorafenib (Nexavar®, BAY 43-9006) [(N-(3-trifluoromethyl-4-chlorophenyl)-N'-(4-(2-methylcarbamoyl pyridine-4-yl) oxyphenyl) urea)] was developed by Bayer and Onyx companies in 1995. It acts as inhibitor of serine/threonine and tyrosine kinases (CRAF, BRAF, eIF4E, VEGFR-2

and -3, PDGFR- $\beta$  FGFR-1, c-kit, FLT-3 and RET) in multiple oncogenic signalling pathways, both in the tumor and endothelial cell or pericytes (Fig. 6)<sup>110</sup>. Among the effects induced by sorafenib and studied by omic-approach there are variations in mRNA transcripts, proteome, DNA methylome as well as dysregulation of ncRNAs<sup>111-114</sup>.

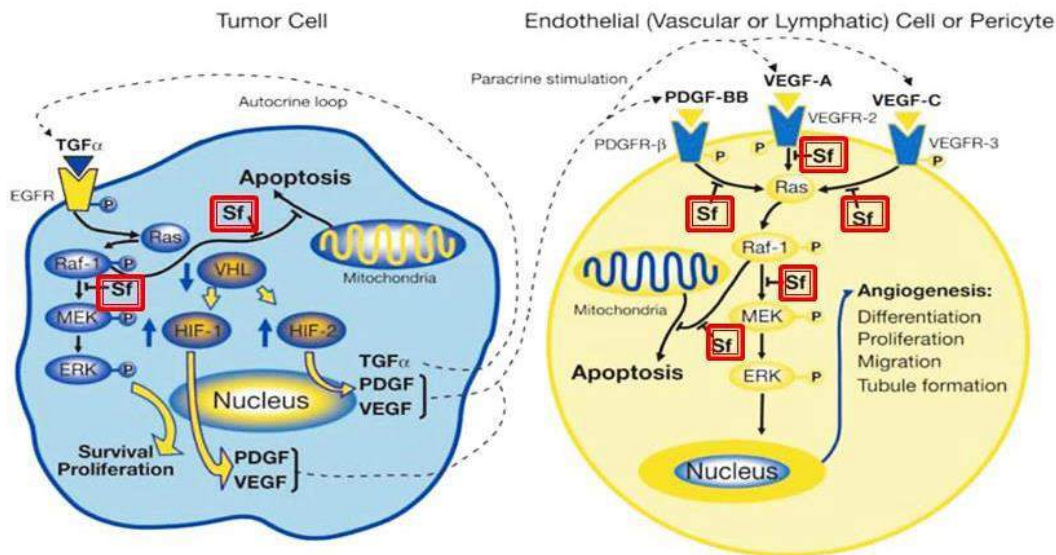


**Fig. 6. Mechanism of action of the multikinase inhibitor sorafenib.** Sorafenib inhibits tumor cell proliferation and angiogenesis *via* targeting numerous serine/threonine and tyrosine kinases in multiple oncogenic signaling pathways. Source: Wilhelm *et al.*, Mol Cancer Therapeutics, 2008<sup>115</sup>.

#### 1.1.7.2.2 Hand-foot skin reaction - Burgdorf's reaction

The recommended dose of sorafenib is 800 mg/die. Median treatment duration is estimated to be 5–6 months. Treatment is associated with manageable adverse effects, such as diarrhea, hand-foot skin reactions (HFSR), fatigue and hypertension. Around 15% of patients are intolerant to sorafenib, and thus treatment needs to be withdrawn, while another 35% of patients require dose reduction. Treatment related liver failure or life-threatening complications are marginal<sup>116</sup>. Grade I, II, III is the most common cutaneous adverse reaction to treatments with multi-targeted tyrosine kinase inhibitors: the histologic changes of HFSR are nonspecific. A vacuolar interface dermatitis with necrotic keratinocytes is most commonly seen, with superficial dermal edema and a perivascular lymphocytic infiltrate<sup>117</sup>. Although the exact mechanism leading to HFSR is unknown, it is thought that the inhibition of both the VEGF and Platelet-derived growth factor receptors (PDGF-R) is necessary.

### **1.1.7.2.3 Resistance to sorafenib**

Sorafenib can significantly extend the median survival time of HCC patients by only 3-5 months and it often may cause drug resistance in many patients. Some patients, due to heterogeneity of HCC, show a primary resistance to sorafenib. The exact mechanism remains unclear. EGFR overexpression and abnormal downstream signaling activation RAS/RAF/MEK/ERK signaling pathway, might contribute to sorafenib resistance. Long-term exposure to sorafenib lead some patients, who initially respond, eventually to give up to the disease, due to a reduced sensitivity of the tumor cells to the drug. Furthermore the occurrence and the maintenance of a second acquired resistance is promoted by PI3K/AKT/mTOR signaling and autophagy, JAK/STAT signaling pathway, Warburg effect and HIF-1 $\alpha$ , EZH2 methyltransferase<sup>118</sup>.

## **1.2 Non-Coding RNAs (ncRNA)**

The human genome encodes for ~20.000 genes, which constitute the 1,5% of the entire genome. The key of our complexity lies in how genes are regulated by the remaining ~99% of the so called “dark matter of the genome”. One of its nuances is represented by non-coding RNAs (ncRNAs)<sup>119</sup>. The development of GWAS (genome-wide association studies), RIP-RNA (RNA immunoprecipitation sequencing), computational prediction from ultra-deep RNA sequencing, and ncRNA chip-based screening techniques, allowed researchers to uncover the widespread expression profile and biological functions of ncRNAs. ncRNAs are divided into two main groups according to their size: long non-coding RNAs (lncRNAs) larger than 200nt, and small non-coding RNAs (sncRNAs) shorter than 200nt<sup>120</sup>. Among the sncRNA, the class of microRNA (miRNAs) is the best studied and characterized class. ncRNAs play different functions in physiological and pathological processes<sup>121</sup>, show a tissue-/cell-specific expression patterns as in tumors<sup>122,123</sup>, reside in different anatomical and biological districts, both associated with AGO proteins, or encapsulated in extracellular vesicles (EVs)<sup>124</sup>.

### **1.2.1 Long non-coding RNAs (lncRNA)**

#### **1.2.1.1 LncRNA biogenesis and classification**

LncRNA is a heterogeneous poorly evolutionary conserved group of RNA, ranging from 200nt to 10Kb in length, found in a plethora of biologic processes across every branch of life. High



throughput transcriptome sequencing has led to the discovery of thousands of lncRNA genes and the number is still growing<sup>125</sup>. The ICGC/TCGA Pan-Cancer Analysis of Whole Genomes (PCAWG) Consortium introduced the Cancer LncRNA Census (CLC), the first compendium of 122 GENCODE lncRNAs with direct causal roles in cancer phenotypes<sup>126</sup>.

LncRNAs are transcribed by RNA Pol II as for protein-coding-genes, with the addition of 5'-capping, H3K4me3 histone modification signatures at the transcriptional start site and H3K36me3 associated with transcriptional elongation and polyadenylation. Some lncRNAs can also be transcribed by RNA Pol III and are non-polyadenylated<sup>125</sup>. LncRNAs show frequent multiple alternative splicing. The majority of lncRNAs possesses a conserved proximal promoter and a secondary RNA structure.

According to the proximity between neighbor transcripts, lncRNAs can be classified into five broad categories<sup>127</sup>: **I) Sense lncRNAs**, transcribed from the sense strand of protein-coding genes, containing exons from protein-coding genes. They may overlap with part of protein-coding genes, or cover the entire sequence of a protein-coding gene. Some sense lncRNAs may function as both RNA and protein-coding gene; **II) Antisense lncRNAs (asRNAs)**, also called Natural Antisense Transcripts (NATs), are transcribed on the opposite strand of protein-coding genes, are frequently overlapped with sense miRNAs at the 5'- or 3'-ends. Antisense transcription across intron regions regulates the local chromatin 3D chromatin organization; **III) Intergenic lncRNAs (lincRNAs)**, are transcriptional units located independently within the genomic interval of two coding genes; **IV) Intronic lncRNAs**, that arise from an intron of a coding gene, without overlapping exons at both ends. They could be either stand-alone unique transcripts or by-products of pre-mRNA processing; **V) Bidirectional lncRNAs**, which initiate in divergent directions from promoter or enhancer regions, giving rise to an enhancer-associated RNAs (eRNAs) and promoter-associated long RNAs (PALRs). These transcripts do not overlap or only partially overlap with the 5'- region of paired protein-coding genes.

LncRNAs vary significantly in size. Those that exceed the length of 10Kb belong to the groups of very long intergenic non-coding RNAs (vlincRNAs) and macroRNAs. vlincRNAs are rarely or not spliced, weakly polyadenylated at 3'-end, localized in close proximity or within protein-coding gene promoters on the same or opposite strand, and function in *cis* as positive regulators of nearby gene transcription. On the other hand, macroRNAs are often antisense to protein-coding genes. Either lncRNA products trigger epigenetic chromatin modifiers or are involved in transcriptional interference mechanisms.

Moreover, intronic and sense lncRNAs could form circular RNAs (circRNAs) due to head-to-tail non-canonical splicing. CircRNAs are predominantly found in the cytosol, where they

function as miRNAs sponges, while some are retained in the nucleus, where they interact with U1 snRNP to promote transcription of their parental genes.

### 1.2.1.2 Molecular functions of lncRNAs

lncRNAs regulate gene expression by transcriptional, post-transcriptional and translational mechanisms. There are four known molecular mechanisms, not mutually exclusive<sup>128</sup>:

- **Signal:** lncRNAs serve as molecular signals, marking space, time, and expression, to regulate transcription in response to various stimuli. Thus, they might be an indicator of transcriptional activity.
- **Decoy:** lncRNAs modulate transcription by sequestering transcription factors, catalytic proteins, subunits of larger chromatin modifying complexes, as well as miRNAs. A canonical example is represented by Growth Arrest Specific 5 (GAS5).
- **Guide:** lncRNAs bind, recruit, localize and direct ribonucleoprotein complexes (RNPs) to specific target genes either in *cis* (near the lncRNA genes) or in *trans* (to distant target genes).
- **Scaffold:** lncRNAs structurally act as platforms for multiple-component-machinery assembly, such as RNPs, histone- or DNA-modifying and nucleosome remodeling complexes, allowing the modulation of several DNA-based processes including transcription, recombination, DNA repair or RNA processing. There is a subclass of lncRNA scaffolds, highly enriched in repetitive sequences, called “architectural lncRNAs (arcRNAs)”, essential for the assembly of particular nuclear substructures.

lncRNAs can also act as riboactivators, enhancing protein activities, or transcriptional co-activators (also called activating ncRNA, ncRNA-a), which possess enhancer-like properties.

Furthermore, lncRNAs can also act as competing endogenous RNAs (ceRNAs), also known as sponge lncRNAs, functioning as mRNA or miRNA sponges to inactivate their pathways<sup>129</sup>. They comprise those lncRNAs and circRNAs that share partial sequence similarity with their targets. Pseudogene-derived lncRNAs are an important source of ceRNAs.

### 1.2.1.3 lncRNAs and cancer

GWAS studies helped to identify different lncRNAs involved in a wide range of human cancers and their dysfunction (up- or down-regulation) is closely associated with tumor development, metabolic processes, progression, metastasis and immune responses<sup>130,131</sup>.

## 1.2.2 Telomeric-Repeat Containing RNA (TERRA)

### 1.2.2.1 TERRA biogenesis

Telomeric-Repeat Containing RNA (TERRA) was discovered in two independent studies by Azzalin<sup>80</sup> and Schoeftner<sup>81</sup> in 2007. TERRA molecules are transcribed from the subtelomeric regions towards chromosome ends by RNA Pol II using the telomeric C-rich strand as template<sup>80,81</sup>. Therefore, TERRA transcripts consist of subtelomeric-derived sequences at their 5'-end and terminate with tandem arrays of G-rich telomeric sequences. TERRA molecules resolve as highly heterogeneous transcripts by Northern blot analyses, ranging from 100nt to 9Kb in mammalian cells<sup>80,81</sup> and it is highly conserved through evolution. TERRA expression is regulated by the chromatin organizing factor CCCTC-binding factor (CTCF) and the cohesin Rad21, which associate with the CpG-TERRA promoters<sup>132-136</sup>. A second class of TERRA promoters were identified in HeLa human cervical carcinoma cells at about 5–10Kb from telomeric tract of 10 distinct chromosome ends<sup>132</sup>. Telomeric repeat-like sequences in internal chromosomal loci, also known as Interstitial Telomeric Sequences (ITSs), are found in a variety of organisms<sup>137</sup>. ITS-transcripts do not always contain the canonical UUAGGG repeat, but also the reverse complement CCCUAA sequence<sup>138</sup>. These findings suggest that TERRA transcribed from ITSs might represent a negligible fraction of the total TERRA population. In human cells, most of TERRA molecules are 7-methylguanosine (m7G) capped at their 5'-end, while only 7% of the total TERRA is polyadenylated at the 3'-end<sup>81,139</sup>. The mechanism of TERRA polyadenylation remains to be elucidated, as a canonical polyadenylation signal is not present at telomeres. TERRA expression in human cells is cell-cycle-dependent, peaking in G1-phase and progressively decreasing during S-phase<sup>140</sup>.

### 1.2.2.2 TERRA and telomere maintenance

In cells with long telomeres TERRA can base-pair with TERC. TERRA can act *in vitro* as TERT allosteric inhibitor. These interactions might be responsible for the TERRA-mediated inhibition of telomerase activity<sup>81</sup>. In cells with short telomeres TERRA may instead coordinate the recruitment of telomerase and encourage subsequent telomere elongation.

TERRA may prevent activation of DNA damage responses at telomeres by promoting the assembly of telomere binding proteins at chromosome ends or telomere capping. TERRA may facilitate DNA replication *in cis* at their telomere of origin, or also *in trans* by relocating to other chromosome ends. Indeed, TERRA transcripts can directly bind both TRF2 and ORC1 (origin replication complex). The formation of this ternary complex may facilitate DNA replication at

telomeres. TERRA transcripts may also indirectly act on DNA damage response pathways by regulating gene expression by regulating heterochromatin formation<sup>141-144</sup>.

In mammalian cells TERRA forms DNA-RNA hybrid structures at telomeres, known as R-loops<sup>145</sup>. Elevated levels of telomeric R-loops are detected in telomerase-negative ALT cancer cells<sup>146</sup>, which express higher levels of TERRA<sup>147</sup>. ALT-positive tumors have also been associated with elevated TERRA levels<sup>74,138</sup>.

### 1.2.2.3 Chromatin regulation

In mammalian cells, TERRA transcripts interact with heterochromatic marks, including H3K9me3 and HP1 (heterochromatin protein 1) proteins<sup>144</sup>, the histone methyltransferase Suv39h1<sup>132</sup> and with chromatin remodeling complexes such as NoRC (nucleolar remodeling complex)<sup>148</sup>, MORF4L2 (a component of the NuA histone acetyltransferase complex), and ARID1A<sup>149</sup>. In addition, TERRA transcripts associate with the histone methyl transferase PRC2 (Polycomb Repressive Complex 2), through a direct interaction with the PRC2 components EZH2 and SUZ12<sup>150</sup>. The G-rich 3'-end of human TERRA forms G-quadruplex structures both *in vitro* and *in vivo*<sup>151-153</sup>. TERRA G-quadruplex structure acts as a binding target for other telomere-binding proteins, such as TLS/FUS (the translocated in liposarcoma/fused in sarcoma protein)<sup>154</sup> and TRF2<sup>144,155</sup>. These interactions can promote H4K20me3 modification at telomeres through the activity of Suv4-20h2 that associates with TLS/FUS<sup>154</sup>. Interaction of TERRA with TRF1 and TRF2 may anchor TERRA transcripts to chromosome ends, sustaining the enzymatic activities of TERRA binding factors at telomeres. Antisense oligonucleotides (ASO) containing locked nucleic acids (LNA) were designed to promote RNase H-mediated degradation of TERRA transcripts. Notably, TERRA depletion resulted in dysregulation of hundreds of genes containing TERRA binding sites<sup>143</sup>.

### 1.2.2.4 TERRA under stress

TERRA expression is induced by stress of different nature<sup>156-160</sup>. Binding of heat shock factor 1 (HSF1) to subtelomeric regions upregulates TERRA expression upon heat shock<sup>156</sup>. TERRA expression is induced by p53 upon treatment of HCT116 cells with the chemotherapeutic agent etoposide or upon culturing them in serum-free medium<sup>157</sup>. Oxidative stress induces TERRA transcription by engaging protein-kinase A (PKA signaling) and cytoskeleton dynamics<sup>158</sup>. TERRA transcripts localize to telomeres in human muscle tissues and its expression is upregulated by the antioxidant transcription factor nuclear respiratory factor 1 (NRF1) during endurance exercise in human myofibers. NRF1 interacts with CpG island in TERRA promoters on multiple subtelomeres

in LB37 non-small cell lung carcinoma and Huh-7 hepatocarcinoma human cell lines. TERRA induction is associated with activation of peroxisome proliferator-activated receptor  $\gamma$  coactivator 1- $\alpha$  (PGC-1 $\alpha$ ), a regulator of energy metabolism upon caloric restriction and endurance exercise, acting as co-activator of transcription factors, including NRF1 by the adenosine 5'-monophosphate (AMP)-activated protein kinase (AMPK)<sup>160</sup>.

### **1.2.2.5 TERRA in cancer**

Little is known regarding TERRA expression in cancer; available data are heterogeneous and obtained with different technologies. TERRA 2q, 10q, 13q, 15q, 16p, 17q, XqYq, expression is elevated in ovarian primary and metastatic tumors, and in stomach, lung and colon cancers compared to matched normal tissue<sup>161</sup>. TERRA 2p and 18p expression gradually decreased in glioblastoma multiforme compared with anaplastic astrocytoma, diffuse astrocytoma, and normal tissue, respectively<sup>162</sup>. 2p and 18p decrease in TERRA expression is significantly related to an increase in different tumor grade of both meningiomas and astrocytomas<sup>163</sup>. TERRA 10q, 15q, XpYp, XqYq expression was higher or similar to those of the adjacent normal tissue in head and neck squamous cell carcinoma<sup>164</sup>. Both 2p and 18p TERRA expression were similar in colon-rectal cancer and paired noncancerous tissues<sup>165</sup>.

### **1.2.3 Growth arrest-specific 5 (GAS5)**

#### **1.2.3.1 GAS5 biogenesis**

GAS5 was discovered in 1998 by screening highly expressed genes in growth-arrested cells. GAS5 is a non-protein coding gene, located at chromosome 1q25.1, comprising 12 exons and 11 introns. It encodes 10 snoRNAs (small nucleolar RNAs) in corresponding introns with a short open reading frame (ORF), rather spliced to yield two mature lncRNAs, ~630nt in length, termed GAS5a and GAS5b, due to the presence of an alternative 5'-splice donor sites in exon 7<sup>166,167</sup>. Saturating cell density or nutrient deprivation might increase GAS5 expression levels and lead to growth arrest at post-transcriptional level<sup>168,169</sup>. The mechanism involves the interplay between non-sense-mediated decay (NMD) and mTOR pathways<sup>170,171</sup>. GAS5 is a 5'-terminal oligopyrimidine RNA. This motif is commonly found in genes that encode proteins to control the translation; in the case of GAS5, it serves to control its transcript levels by mTOR pathway<sup>170,172,173</sup>. When mTOR activity is high, as in actively growing cells, GAS5 transcript is increased due to the presence of the 5'-TOP

sequence. However, due to the short ORF and the presence of multiple termination codons in its sequence, GAS5 transcripts are degraded via NMD, which further resulted in decrease in GAS5 levels. On the contrary, when mTOR pathway is inactivated, as in growth-arrested cells, the translation of GAS5 short ORF is blocked and this in turn prevents NMD pathways, leading to the increased expression of GAS5<sup>169</sup>.

### **1.2.3.2 GAS5 functions**

GAS5 is involved in cell proliferation, apoptosis, migration and invasion, through modulating downstream target genes *via* multiple molecular mechanisms.

GAS5 arrests cells in the G0/G1 phase of the cell cycle<sup>174</sup>. The sequence of GAS5 that interacts with the glucocorticoid receptor (GR) DNA-binding domain resides within exon 12-encoded sequence and comprises an hairpin structure that contains two GRE-like sequences (glucocorticoid response elements), termed GRE-1 and GRE-2, complementary to each other. GAS5 can also interact with other members of the steroid nuclear receptor superfamily members, particularly 3-ketosteroid receptors, such as the mineralocorticoid receptor (MR), the androgen receptor (AR) and progesterone receptor-A (PR), which can bind DNA-activating GREs, but not estrogen receptor  $\alpha$  (ER-  $\alpha$ ) or peroxisome proliferator-activated receptor  $\delta$  (PPAR-  $\delta$ )<sup>175,176</sup>.

GAS5 may also regulate gene expression by binding protein to epigenetically modulate the promoter histone methylation of target gene, serving as ceRNA, regulating protein-coding and non-coding gene expressions at transcriptional or post-transcriptional levels and through kinase signaling regulatory pathways, among others.

### **1.2.3.3 GAS5 in cancer**

GAS5 is downregulated in a variety of malignancies, including non-small cell lung cancer, breast cancer, hepatocellular carcinoma, esophageal carcinoma, gastric cancer, colorectal cancer, pancreatic cancer, cervical cancer, ovarian cancer, renal cell carcinoma, myeloma neoplasms of B-cells. Clinical-pathological characteristics, as histological differentiation, tumor sizes, tumor node metastasis stage, lymph node metastasis, infiltration depth, vascular invasion, overall survival, recurrence-free survival, disease-free survival, and prognosis are highly correlated with GAS5 expression in cancers, indicating GAS5 as a novel diagnostic and prognostic biomarker, as well as therapeutic target in many human cancers<sup>177,178</sup>.

## 1.2.4 microRNA (miRNA)

### 1.2.4.1 miRNAs biogenesis

The first miRNA, *lin-4*, was discovered by Victor Ambros *et al.* in 1993<sup>179</sup>. miRNA genes are interspersed in the genome, with various possible locations: intergenic, as a single gene or in miRNA-clusters, and intragenic in an host gene. The biogenesis of miRNAs is a multistep process. Transcription of miRNAs involves RNA polymerase II or III, producing a long primary stem-loop miRNA, called “pri-miRNA”, capped at the 5'-end and polyadenylated at the 3'-end. Two processing events are required to generate a mature miRNA duplex. In the nucleus the Microprocessor complex, constituted by the RNase III endonuclease DROSHA and DGCR8 (Di George syndrome critical region 8), recognizes dsRNA–ssRNA junction, directs the cleavage and produces an intermediate hairpin ~60-70nt precursor “pre-miRNA” molecule, with a 5'-phosphate and 3'-overhang. The pre-miRNA is translocated from the nucleus to the cytoplasm by Exportin 5-RAN–GTP (XPO5). In the cytosol RNase III endonuclease DICER in complex with the TARBP [Trans-activator RNA (TAR) binding protein] and PACT (interferon-inducible double-stranded RNA-dependent activator) generates the mature miRNA:miRNA duplex. The miRNA-duplex is immediately incorporated into the RISC-complex (RNA-induced-silencing complex), composed of Argonaute (AGO) proteins. Only the 20-25nt single-strand “guide-miRNA” is retained in the RISC (miRISC complex), while the “passenger” strand is discarded and degraded. At the miRISC complex, miRNAs induce translation repression, mRNA degradation, storage and/or secretion (EVs).

“Mirtrons” are pre-miRNA-like hairpins that bypass DROSHA step by splicing and debranching of short-hairpin introns. Mirtron products appear as pre-miRNA mimics from splicing reaction and enter the canonical biogenesis pathway as XPO5 substrates. Moreover, pre-miRNAs can be derived from small nucleolar RNAs (snoRNAs), tRNA precursors and endogenous short hairpin RNAs (siRNAs)<sup>180,181</sup>.

### 1.2.4.2 miRNA functions and cancer

Each miRNA can regulate the expression of hundreds of target mRNAs, while a mRNA can be regulated by multiple miRNAs. The miRNA:mRNA interaction down-regulate or repress gene expression either by hindering the translation machinery or by mediating mRNA degradation. MiRNAs-binding sites commonly lie within the 3'-untranslated region (3'-UTR) “seed region” of the mRNA. miRNA action is not only restricted to processes within the cell, but also extracellularly. These circulating-miRNA are highly stable and resistant to RNase activity, as associated with

carriers, like AGO-proteins, or encapsulated in Extracellular Vesicles (EVs). Thus, miRNAs may also function as signaling molecules, transferring epigenetic information among cells and tissues<sup>182</sup>.

miRNA-guided gene regulation affects cell cycle, proliferation, apoptosis, migration, invasion and metastasis. Thus, miRNAs can act as tumor-suppressor-miR or as oncomiR. Aberrant miRNAs expression patterns in cancer have been documented in several tumor types and they appear to play a fundamental role in onset, progression and metastatization<sup>183</sup>.

## 1.2.5 miR-126

### 1.2.5.1 miR-126 biogenesis

In 2002, Lagos-Quintana *et al.* identified miR-126 in a tissue-specific mouse screen<sup>184,185</sup>. miR-126 and its passenger strand, miR-126\*, are two endothelial cell-specific miRNAs. Both miR-126 and miR126\* are encoded by the epidermal growth factor-like domain 7 (EGFL7) gene<sup>186</sup>. miR-126 usually refers to the 3'-region of the transcript, also termed miR-126-3p, located within the 7th intron of EGFL7 at 9q34.3. On the other hand, miR-126\* refers to the 5'-region of the transcript, also termed miR-123 or miR-126-5p<sup>186,187</sup>. EGFL7 encodes an endothelial cell-derived statin (VE-statin) involved in the regulation of angiogenesis<sup>188</sup>.

### 1.2.5.2 miR-126 functions

Functionally, miR-126 expression is significantly associated with angiogenesis and inflammation. Targeted deletion of miR-126 results in a loss of vascular integrity, which leads to ruptured vessels and impaired endothelial cell migration. miR-126 suppresses sprouty-related EVH1 domain-containing protein 1 (SPRED1) and phosphoinositide-3-kinase regulatory subunit 2 (PI3KR2), both of which inhibit receptor tyrosine kinase-induced signaling via MAPK and PI3K pathways, thereby promoting VEGF signaling and angiogenesis<sup>186,189</sup>.

Although miR-126 expression is usually altered in parallel with the expression of EGFL7 protein, miR-126 can downregulate EGFL7, leading to reduced angiogenesis and cell proliferation *via* a negative feedback loop mechanism<sup>189,190</sup>.

In addition, endogenous miR-126 revealed to inhibit the expression of vascular cell adhesion molecule 1 (VCAM-1) and to prevent leukocyte adhesion and infiltration to further control vascular inflammation<sup>191</sup>.



Furthermore, miR-126 can suppress inflammation and reactive oxygen species production in endothelial cells under hyperglycemic conditions by post-transcriptionally inhibiting the expression of high-mobility group box 1(HMGB1)<sup>192</sup>.

### **1.2.5.3 miR-126 in cancer**

miR-126 acts as a tumor suppressor<sup>187,193</sup> and aberrant expression of miR-126 has been identified in melanoma, osteosarcoma, leukemia and carcinomas of the digestive system, endocrine glands, urogenital system and respiratory system<sup>194,195</sup>. The oncogenic targets of miR-126 associated with HCC include the pro-angiogenic PI3KR2<sup>196</sup> and EGFL7<sup>190,197</sup>, in addition to the pro-metastatic low-density lipoprotein receptor-related protein 6 (LRP6)<sup>196</sup>. Dysregulation of miR-126 is inversely correlated with clinic-pathological parameters of HCC, including tumor size, tumor weight and alpha-fetoprotein (AFP) level, and is involved in tumor angiogenesis, microvascular invasion, tumor metastasis and early recurrence<sup>190,196,198</sup>.

## **1.3 Tumor biopsy**

### **1.3.1 Biopsy**

There is a great interest in biomarker discovery with high sensitivity, high positive predictive value, and high specificity to detect tumor, tumor growth, progression and relapse, and predict and monitoring therapeutic response to improve cancer treatments and patients' survival.

Biopsies have been used by clinicians to diagnose and manage disease for over 1,000 years<sup>199</sup>. Conventional tissue acquisition is invasive, only reflects the genetic profile of the tumor at the time of sampling, shows extensive inter-tumoral and intra-tumoral evolution heterogeneity, conveys risks of complication, has significant costs and limitations. Tumors are dynamic and change their genetic composition, especially after selective pressure of targeted treatment.

Liquid biopsies provide a non-invasive approach to tumor molecular profiling, avoiding to obtain the tumor tissue<sup>200</sup>. Treatment of cancer is shifting from an entity-driven approach to molecular-guided personalized approach<sup>201</sup>. In the *era* of personalized medicine, the information for therapy decisions directly comes from blood, to which patient is the only contributor<sup>2</sup>. The goal of personalized medicine is to select specific treatments for each individual tumor based on its genotype (Fig. 7).

### 1.3.2 Liquid biopsy in HCC

In terms of HCC diagnosis, imaging techniques are currently the gold standard. Dual-phase computerized tomography (CT) scan and magnetic resonance imaging (MRI) show high diagnostic performance in nodules larger than 1-2cm<sup>107</sup>. A panel of immunohistochemistry (IHC) markers, including glypican-3, heat shock protein 70 (HSP70), and glutamine-synthetase has been suggested to increase HCC diagnostic accuracy<sup>202</sup>. The EASL guidelines identified as an unmet need in HCC research the development of new tools for early detection or prediction of response or resistance to systemic therapeutics by liquid biopsy<sup>107</sup>. The current role of liquid biopsy in the management of HCC is still far beyond other solid tumors.

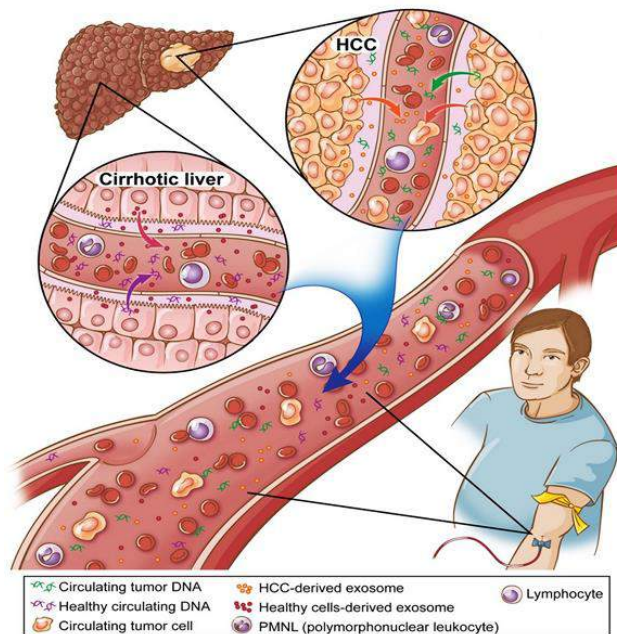


**Fig. 7. Liquid biopsy in HCC.** Unlike circulating tumor cells, circulating cell-free DNA and RNA originate from both tumor and non tumoral tissues. It is feasible to analyze genetic and epigenetic changes. Source: Villanueva *et al.*, *Discovery Medicine*, 2015<sup>203</sup>.

## 1.4 Extracellular Vesicles (EVs)

### 1.4.1 EVs Biogenesis and functions

In the 1980s, Extracellular Vesicles (EVs) were described as vesicles of endosomal origin, secreted from reticulocytes<sup>204</sup>. EVs is an umbrella term used for all lipid bilayer structures released from cells and ranging from 30nm to 2.000nm in size. Currently nomenclature of EVs is based on the size of the vesicles, their floating density, and their cell of origin. The most widely used method of sequential ultracentrifugation yields EV subsets (apoptotic bodies (ABs), micro-vesicles (MVs), and exosomes) based on their sedimentation rate<sup>205,206</sup>. Jan Lötvall *et al.* speculated that EVs might mediate the transfer of mRNA and miRNA from one cell to another<sup>207</sup>. Melo *et al.* showed how cancer cells use “oncosomes” to reprogram adjacent healthy cells, leading to a “field effect” that would facilitate cancer progression<sup>208</sup>.

Exosomes are constitutively generated from late endosomes, which are formed by inward budding multivesicular body membrane (MVBs). Invagination of late endosomal membranes results in the formation of intraluminal vesicles (ILVs) within large MVBs<sup>209</sup>. ADP-ribosylation factor 6 (ARF6)-initiated signaling cascade leads to redistribution of phospholipid-like phosphatidyl-serine, myosin light chain (MLCK) release of MVBs, and shrinking of actin-myosin assemblies<sup>210</sup>. ARF6 is also required for targeting Integrin  $\beta$ -1, MHC-I, and Matrix metalloproteinase-14 (MMP14) to the MVBs<sup>211</sup>. Concomitant with cargo clustering, a set of protein complexes called “endosomal sorting complexes required for transport (ESCRTs)” act on the membrane and its cargo to induce invagination to form ILVs and MVBs<sup>212</sup>. ESCRT-0 clusters ubiquitinates cargos with the help of tumor susceptibility 101 (TSG101), a component ESCRT-I, in association with the Arrestin 1 domain-containing protein 1 (ARRDC1), facilitating its recruitment to MVBs<sup>213</sup>. This is followed by recruitment of ESCRT-II and ESCRT-III that help in budding and in the generation of ILVs that will become exosomes<sup>214</sup>. Albeit simultaneously silencing of key subunits of ESCRT-complexes, ILVs are still formed in MVBs, thus indicating the presence of ESCRT-independent mechanisms<sup>215</sup> (Fig. 8).

### 1.4.2 EVs cargo

EVs are almost ubiquitously present and are commonly found in all body fluids, as well as in the extracellular matrix. EVs cargos (lipids, proteins, nucleic acids, metabolites) reflect their cells of origin, rendering EVs a valuable source of biomarkers. Cargo can be present on the surface, as well as be protected in the lumen of the EVs (Fig. 8).

- **Lipids:** EVs are usually enriched in phosphatidyl-serine, cholesterol, and sphingomyelin<sup>216</sup>.

- **Proteins:** some of the membrane proteins such as tetraspanins, MHC-II, and luminal proteins (TSG101 and ALIX) are used as EV markers. EVs also contain integrins, glycoproteins, and selectins adhesion molecules<sup>217</sup>. Annexins aid EVs intracellular fusion events, through their interactions with phospholipids<sup>218</sup>. RAB protein members assist membrane transport and EV biogenesis<sup>219</sup>. EVs also contain peroxidases, pyruvate dehydrogenase (PDH), enolases, dipeptidylpeptidase-IV (DPP4), aminopeptidase, metalloproteases (MMPs).
- **DNA:** EV-associated extracellular DNA (ex-DNA) has been little studied in terms of its origin, and it is often argued to be produced from dying cells<sup>220</sup>. ABs carry DNA<sup>220,221</sup>, but information on ex-DNA in exosomes and MVs is scarce. EVs from serum and cell culture supernatants have evidenced the presence of ex-DNA<sup>222,223</sup>, of both nuclear and mitochondrial origin<sup>224,225</sup>. The use of EV-associated ex-DNA, independent of its location, could have a huge impact on the biomarker field<sup>224,226</sup>.
- **RNA:** the presence of RNA in ABs was described in 1990, but it was only after 2007 that its functional role began to be explored<sup>207</sup>. The most commonly enriched RNAs in EVs are small RNAs, transfer-RNAs (tRNA), and 18S and 28S rRNAs, ncRNAs, tRNA fragments, piwi-RNA, vault-RNA, and Y RNA<sup>206,227-229</sup>. The selective packaging of RNA in EVs has been reported, and miRNA overexpression studies in cells and analyses of 3'-UTR-specific RNA in EVs have revealed a tendency for RNA loading in EVs<sup>230,231</sup>. The “GGAG motif” in certain miRNAs interacts with heterogeneous nuclear ribonucleoprotein A2/B1 (hnRNPA2B1) to assist their loading in MVBs that contain future exosomes<sup>232</sup>. Certain post-translation modifications such as SUMOylation of ribonucleoproteins, uridylation and adenylation of RNA have been reported to dictate the loading of RNA in EVs and hence the abundance of RNA in EVs<sup>233,234</sup>. AGO2 has been shown to be involved in the loading of miRNA into EVs<sup>235,236</sup>. EV-derived RNA potential boosted the field of exosome research exponentially, especially in biomarker discovery<sup>237,238</sup>.

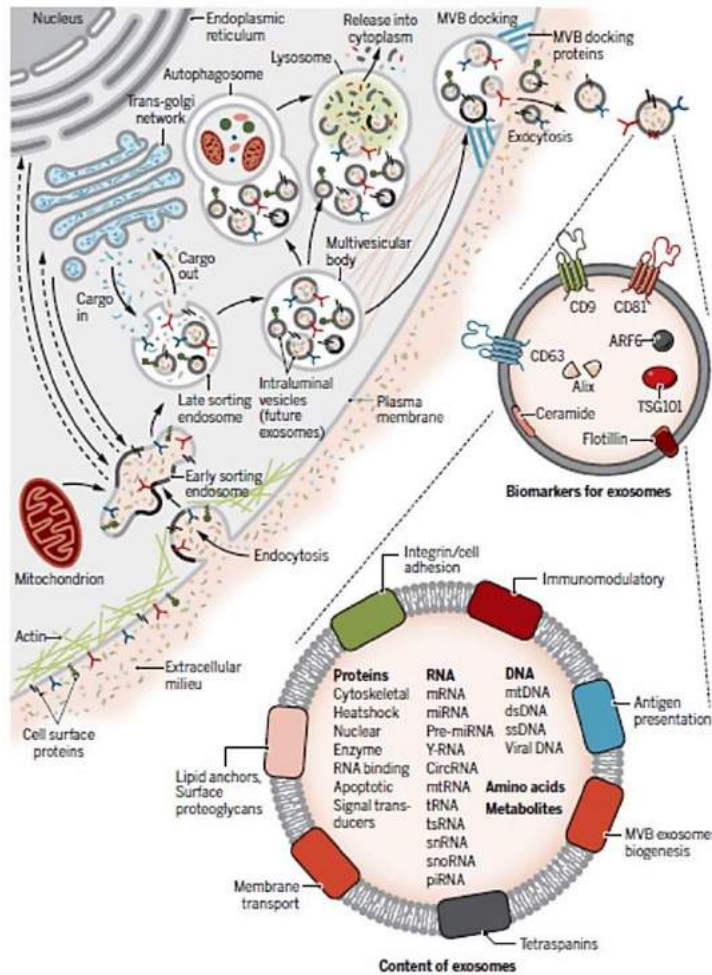


**Fig. 8. Biogenesis and identification of exosomes.** Intraluminal vesicles are formed by endocytosis in response to ligands, pathogens, or other stimuli. These endocytic vesicles mature from early endosomes into late endosomes, which leads to the formation of multivesicular bodies (MVBs). Several proteins are implicated in exosome biogenesis and include Rab GTPases, ESCRT proteins, as well as others that are also used as markers for exosomes (CD9, CD81, CD63, flotillin, TSG101, ceramide, and Alix). Exosome surface proteins include tetraspanins, integrins, immunomodulatory proteins, and more. Exosomes can contain different types of cell surface proteins, intracellular protein, RNA, DNA, amino acids, and metabolites. Source: Kalluri *et al.*, Science, 2020<sup>239</sup>.

## 2 AIM OF THE WORK

New advances in multiomics platforms deepened the insight and explored the HCC molecular landscape and sorafenib benefits. But we are far from grasping the full range of mechanisms that ncRNAs employ to regulate biological processes. The EASL guidelines identified as an unmet need in HCC research the development of new tools with high sensitivity in predicting and monitoring therapeutic response or resistance to systemic therapy, in particular to monotherapy with the multitarget kinase inhibitor sorafenib.

Studies using *in vitro* and animal models of HCC to investigate the mechanism of sorafenib resistance in HCC have explored every aspect of the “hallmark of cancer”, illustrating the multifaceted action of sorafenib. Development of sorafenib resistance in HCC has been linked to aberrant proliferation, evasion of apoptosis, replicative immortality, abnormal angiogenesis, invasion and metastasis potential.

The signatures of aberrant lncRNAs and miRNAs expression in HCC tissues, their extracellular release and stability had led to their exploration as circulating diagnostic and prognostic tool for HCC. Thus, ncRNA-field still represents an active challenging area of research.

Therefore, the main aim of the present work was the study of two pivot hallmarks of cancer development, cell growth and immortality, to further explore novel candidate molecular biomarkers of diagnosis, response or resistance to sorafenib in HCC. In particular lncRNA GAS5 and miR-126-3p are involved in cell cycle regulation and proliferation. On the other hand, lncRNA TERRA, which originates from different *loci* of chromosomes telomeres, would be responsible for the inhibition of telomerase activity and therefore acquisition of unlimited replicative potential.

Starting by the use of RT<sup>2</sup> lncRNA PCR Array Human LncFinder and miScript miRNA PCR Array Human Liver miFinder, we profiled the expression 84 different disease- or pathway-focused lncRNAs and miRNAs in an HCC *in vitro* model, treated and untreated with sorafenib. Among the most dysregulated ncRNAs, we found upregulation of lncRNA GAS5 and downregulation of miR-126-3p. By luciferase-assay we inquired GAS5 ceRNA-function over miR-126-3p<sup>240</sup>. Therefore, the attention was focused on GAS5 and miR-126-3p and their role in HCC *in vitro* model and HCC solid and liquid biopsies.

Also TERRA dysregulation was explored in *in vitro* models and HCC solid and liquid biopsies.

### 3. MATERIALS AND METHODS

#### 3.1 Cell culture and treatment with sorafenib

Human tumor cell lines derived from HCC (HA22T/VGH and SKHep1C3) were used. The HA22T/VGH cell lines was maintained in RPMI-1640 (Life Technologies) with 100 nM Sodium Pyruvate (ThermoFisher Scientific). SKHep1Clone3 (SKHep1C3) cells, selected from human HCC-derived cells (SKHep1: ATCC HTB-52), were maintained in Earle's MEM (Life Technologies). All culture media were supplemented with 10% Fetal Bovine Serum (Euroclone) and 10,000 U/ml penicillin/streptomycin (ThermoFisher). The Fetal Bovine Serum for HA22T/VGH was inactivated at 56°C for 30min. HA22T/VGH and SkHep1C3 sorafenib resistant cells (HA22T/VGH-SR and SkHep1C3-SR) were previously generated previously, treating cells with increasing concentration of sorafenib for about 6 months until the concentration of 10µM sorafenib was reached. Resistant cell lines were continuously supplied with sorafenib at a specific concentration. Cells were cultured at 37°C with 5% CO<sub>2</sub> in 10 cm Ø plates up to almost 90% of confluence.

Sorafenib [N-(3-trifluoromethyl-4-chlorophenyl)-N-(4-(2-methylcarbamoylpyridin-4-yl)oxyphenyl) urea] was synthesized and provided by Bayer Corporation (West Haven, CT, USA). The compound was dissolved in 100% dimethyl sulfoxide (DMSO; Sigma-Aldrich) and diluted with RPMI-1640 or MEM to the required concentration. Sensitive cells were treated with 15µM sorafenib, as it corresponds to the concentration of the drug detectable in plasma of HCC patients during treatment<sup>110</sup>. 0.1% DMSO was added to cultures as a solvent-only negative control in *in vitro* studies.

#### 3.2 Tissue samples and liquid biopsies collection

In this study, 30 HCC subjects underwent surgical resection at ASST Civili Hospital - Surgery Division in Brescia (Italy). All the human HCC tissues (N=25) as well as the corresponding peritumoral (PT) counterparts (resected 1–2 cm from the tumor burden) were subsequently stored in RNA-Later (Invitrogen). Each individual was screened for virology and background pathology. Each biopsy specimen underwent a pathological examination.

Two ml of peripheral blood (N=25) were collected in EDTA-coated blood collection tubes from HCC patients before HCC resection. The peripheral blood of healthy volunteers (N=25) was obtained from the Immunohematology and Transfusion Medicine Service at ASST Civili Hospital in Brescia, Italy. Plasma was obtained from 1 ml of peripheral blood with a first centrifugation step

at 3,000 rpm for 10 min at 4°C followed by a second centrifugation step at 4,000 rpm for 20 min at 4°C.

Ten ml of peripheral blood of 7 subjects (Table 1) treated with sorafenib were collected before the starting of the treatment (T<sub>0</sub>) and at 1 month sequential time points of follow-up treatment from ASST Cremona Hospital – Oncology Division (Italy). Plasma was obtained by centrifugation of peripheral blood at 3,000 rpm for 10 min at 4°C. Each individual was screened for virology and background pathology. All patients received 800mg/day sorafenib (400mg twice/die) as an initial dosage. Dosage reduction took place upon signs of toxicity or adverse effects. Patients continued treatment unless there was clinical progression, unacceptable toxicity, patients refusal or death.

**Table 1.** Characteristics of the 7 HCC patients treated with sorafenib enrolled in the longitudinal study.

	11-LB-01	38-LB-01	55-LB-01	61-LB-01	73-LB-01	92-LB-01	136-LB-01
Sex	M	M	F	M	M	M	F
Age (y)	75	63	50	32	83	72	73
Background disease	Cirrhosis and steatosis	Cirrhosis and viral hepatitis	Cirrhosis and viral hepatitis	Cirrhosis and viral hepatitis	Normal liver	Cirrhosis	Cirrhosis
HBV	-	-	+	+	-	-	-
HCV	-	+	-	-	-	-	-
Grading	2	N/A	N/A	3	N/A	N/A	N/A
AFP (ng/ml)	102.8	76.4	2.4	106,408.7	353.5	104.9	74.1
Local treatments	HCC surgical resection	No	No	No	No	TACE	No
Tumor spread at diagnosis	Liver	Liver and abdominal lymphonodes	Liver	Lungs metastasis	Liver	Liver	Liver, bones and lungs metastasis
N° of blood sample collected (months)	12	4	6	3	3	6	4
PFS (months)	11	7	5	2	3	5	2
OS (months)	42	25	19	5	7	20	ALIVE

The study was approved by the ethical committee of ASST Civili Hospital of Brescia on 2nd October 2012 (NP1230) and ASST Cremona Hospital on 28th December 2015 (NP30769).

Informed consent was obtained from all the subjects enrolled in the study.



### 3.3 RNA isolation

#### 3.3.1 RNA isolation from cells and tissues

Total RNA from cells and tissues was extracted following Chomczynski-Sacchi method<sup>241</sup>. The method is based on the use of a monophasic phenol-guanidinium thiocyanate solution, which dissolves the cell components, preserving nucleic acid integrity.

Cell-culture medium was completely removed and cells were washed with 3 ml of phosphate buffered saline (PBS). PBS was subsequently discarded and cells were disrupted by adding 1ml of TRIzol Lysis Reagent (Qiagen) into the dish. Cells were grinded with a scraper to obtain a cell-lysate, which was subsequently collected into a 1.5 ml microcentrifuge tube.

Total RNA from tissue was obtained by grinding  $\sim 1\text{cm}^3$  of tumor and peritumor tissue in 1ml TRIzol with a TissueRupture (Qiagen) in a 15 ml tube. The tissue lysate was subsequently collected into a 1.5ml microcentrifuge tube.

The following protocol was subsequently used:

- Add 200 $\mu\text{l}$  of chloroform *per* each ml of TRIzol used.
- Shake vigorously for 15 second.
- Add 200 $\mu\text{l}$  of chloroform to the tube containing the homogenate and shake the tube vigorously for 15 seconds.
- Incubate the homogenate for 2 - 3 minutes at room temperature.
- Centrifuge at 12,000 x g for 15 min at 4°C. After centrifugation, the sample separates into 3 phases: an upper, colorless, aqueous phase containing RNA; a white interphase containing proteins; and a lower, red, organic phase containing lipids and DNA.
- Transfer the upper aqueous phase to a new collection tube. Precipitate the RNA adding 500 $\mu\text{l}$  of isopropanol.
- Incubate at room temperature for 10min by inverting up and down several times.
- Centrifuge at 12,000 x g for 10min at 4°C.
- Remove the supernatant and wash the pellet with 1ml of 75% ethanol.
- Centrifuge at 12,000 x g for 5min at 4°C.
- Remove the supernatant and let the pellet dry at room temperature for 15min-20min.
- Hydrate the RNA pellet with a proper amount of RNAase-free/DEPC water.

RNA purity and concentration was assessed and measured by NanoDrop<sup>TM</sup> 1000 Spectrophotometer (ThermoFisher Scientific). In NANODrop, UV absorbance is measured at 230 nm, 260 nm and 280 nm. The A260/A280 ratio of pure RNA should be between 1.8 and 2.0 and the A260/A230 ratio in the range of 2.0–2.2.

RNA integrity was assessed on 0.8% agarose gel stained with ethidium bromide. Intact total RNA presents two sharp clear bands, corresponding to the 28S and 18S rRNA.

### 3.3.2 RNA isolation from cell secretome and liquid biopsies

Total RNA was isolated from cell secretomes and plasma, using miRNeasy Mini Kit (Qiagen), according to the manufacturer's instructions.

HA22T/VGH cells were seeded in a 10 cm Ø plate (4 replicates per each condition) at a density of  $5 \times 10^6$  cells and maintained in complete media until they reached 70% - 80% of confluence. After gentle washes with PBS, cells were incubated with serum-free medium for 24h. Cell lines were supplied with sorafenib at specific concentrations (10µM and 15µM). Collected media were centrifuged at 2,800g x 10min and carefully transferred to new tubes. EVs were isolated and analyzed with qNANO instrument, following Notarangelo *et al.* protocol<sup>242</sup>.

Two ml of blood underwent a first centrifugation step at 3000rpm x 10min and second centrifugation step and 4,000rpm x 20min, at 4°C. 200µl of plasma were used to extract total RNA.

The following protocol was subsequently used:

- Vortex for 1min to mix and ensure that no clumps are visible.
- Add 2.5µl of miScript miRNA mimic spike-in cel-miR-39 (5nM).
- Incubate the homogenate for 5 min at room temperature.
- Add 200µl of chloroform to the tube containing the homogenate and shake the tube vigorously for 15 seconds.
- Incubate the homogenate for 2 - 3 minutes at room temperature.
- Centrifuge for 12,000 x g for 15 min at 4°C. After centrifugation, the sample separates into 3 phases: an upper, colorless, aqueous phase containing RNA; a white interphase containing proteins; and a lower, red, organic phase containing lipids and DNA.
- Transfer the upper aqueous phase to a new collection tube. Add 1.5 volumes of 100% ethanol and mix thoroughly by pipetting up and down several times.
- Pipet up to 700 µl of the sample into an RNeasy Mini spin column in a 2ml collection tube. Close the lid gently and centrifuge at  $\geq 8,000 \times g$  ( $\geq 10,000$  rpm) for 15 seconds at room temperature. Discard the flow-through.
- Repeat the previous step.
- Add 700µl of Buffer RWT to the RNeasy Mini spin column. Close the lid gently and centrifuge for 15 seconds at  $\geq 8,000 \times g$  to wash the column. Discard the flow-through.

- Add 500µl of Buffer RPE onto the RNeasy Mini spin column. Close the lid gently and centrifuge for 15 seconds at  $\geq 8,000 \times g$  to wash the column. Discard the flow-through.
- Add another 500µl of Buffer RPE to the RNeasy Mini spin column. Close the lid gently and centrifuge for 2min at  $\geq 8,000 \times g$  to dry the RNeasy Mini spin column membrane.
- Place the RNeasy Mini spin column into a new 2 ml collection tube, and discard the old collection tube with the flow-through. Centrifuge in a microcentrifuge at full speed for 1 min.

Transfer the RNeasy Mini spin column to a new 1.5ml collection tube. Hydrate RNeasy Mini spin column with 35µl of RNase-free water directly onto the membrane. Close the lid gently and centrifuge for 1min at  $\geq 8,000 \times g$  to elute the RNA. Store the RNA at  $-80^{\circ}\text{C}$ .

RNA purity and concentration was assessed and measured by NanoDrop<sup>TM</sup> 1000 Spectrophotometer.

### **3.4 RT-PCR for cDNA synthesis**

#### **3.4.1 RT-PCR with random primers**

GAS5, TERC, TERT cDNAs from cells and tissues were obtained by Random Primers cDNA synthesis Retrotranscription. The RT mix was prepared as follows:

- 10µl of 5X First Strand Buffer
- 10µl of dNTPs 100mM
- 1µl of 0.1 M DTT (Cleland's reagent)
- 2µl of Random Primers (30ng/µl) (Invitrogen)
- 0.5µl of RNase-OUT Recombinant Ribonuclease Inhibitor (40U/µl) (Invitrogen)
- 1µl of M-MLV RT (200U/µl)
- 1µg of total RNA and Nuclease-free water up to a 50µl total final volume.

The reverse transcription reaction was performed by incubating the samples with T100 Thermal Cycler (Bio-Rad) at  $37^{\circ}\text{C}$  for 1 hour, followed by the inactivation of reaction at  $95^{\circ}\text{C}$  for 5min and on ice for 10min.

Finally, the reaction was diluted 1:5 with Nuclease-free water.

### 3.4.2 RT-PCR stem-loop

miR-126-3p cDNA was synthesized from

- 50ng of total RNA from cells and tissues
- 2,5µl of cell secretomes and plasma total RNA

in 7.5µl final reaction volume using the TaqMan microRNA Reverse Transcription Kit (Applied Biosystems, Foster, CA, USA) and the stem-loop primer for miR-126-3p (Assay ID 002228; Applied Biosystems), RNU48 (reference gene; Assay ID 001006; Applied Biosystems) and cel-miR-39 (spike-in reference gene; Applied Biosystems; ID ID000200), according to the manufacturer's instructions.

The RT mix was prepared as follows:

- 0.075µl of 100mM dNTPs
- 0.5µl of MultiScribe™ Reverse Transcriptase (50U/µl)
- 0.75µl of 10X Reverse Transcription Buffer
- 0.095µl of RNAase Inhibitor (20U/µl)
- 1.5µl of stem-loop specific primer for each target
- 2.08µl of Nuclease-free water
- total RNA and RNAse-free water up to 7.5µl of final volume.

The reverse transcription reaction was performed by incubating the samples with T100 Thermal Cycler (Bio-Rad) at 16°C for 30min, followed by incubation at 42°C for 30min and 85°C for 5min.

### 3.4.3 TERRA First strand cDNA synthesis

TERRA was analyzed following Feretzaki *et al.* protocol<sup>243</sup>, generating a TERRA pool, as follows:

- 1µl of TERRA specific RT primer (diluted 1:50 from 100µM stock solution)
- 1µl of 10mM dNTPs
- 1µg of total RNA from cells or tissues
- H<sub>2</sub>O to a final volume of 12µl

Heat at 65°C for 5min and place in ice at least for 1min. Then prepare the reaction mix in a final volume of 8µl as follows:

- 4µl of Buffer 5X
- 1µl of DTT 0.1M
- 2µl of RNAse-OUT (20U/µl)

- 1µl of SuperScript III (200U/µl)

Assemble the two components to obtain a final reaction mix of 20µl. The reverse transcription reaction was performed with T100 Thermal Cycler (Bio-Rad), by incubating the samples at 55°C for 60min, followed by inactivation at 70°C for 15min.

<b>Table 2. RT Specific Primers</b>	
<b>Primers</b>	<b>Sequence 5'→3'</b>
<b>TERRA</b>	CCCTAACCTAACCTAACCTAACCTAA
<b>β-actin</b>	AGTCCGCCTAGAAGCATTG

### 3.4.4 One-Step RT-PCR and PreAmp

Circulating GAS5 cDNA was synthesized from 2,5µl of cell secretomes and plasma total RNA using the iScript Explore One-Step RT and PreAmp Kit (Bio-Rad), according to the manufacturer's instructions.

The RT mix was prepared as follows:

- 12.5µl of SSoAdvanced PreAmp SuperMix 2X
- 2.5µl of PreAmp Assay pool 200mM
- 0.5µl of iScript Advanced Reverse Transcriptase
- 0.5µl of iScript Reaction Booster
- 2.5µl of total RNA
- 6.5µl of RNase-free water to a final reaction volume of 25µl.

The reverse transcription reaction was performed by:

- Priming at 25°C for 5min
- Reverse Transcription at 45°C for 60min
- RT inactivation at 95°C for 3min
- Pre-Amplification with 14 cycles of temperature variation at 95°C for 15sec and 60°C for 4 min.

Circulating TERRA cDNA was synthesized from 2,5µl of plasma total RNA using the iScript Explore One-Step RT and PreAmp Kit (Bio-Rad) according to the manufacturer's instructions with some modifications.

The RT mix was prepared as follows:

- 12.5µl of SSoAdvanced PreAmp SuperMix 2X
- 2.5µl of PreAmp Assay pool 200mM
- 0.5µl of iScript Advanced Reverse Transcriptase
- 0.5µl of iScript Reaction Booster
- 2.5µl of total RNA
- 6.5µl of RNase-free water to a final reaction volume of 25µl.

The reverse transcription reaction was performed by:

- Denaturing step at 65°C for 5min
- Priming at 25°C for 5min
- Reverse Transcription at 45°C for 60min
- RT inactivation at 95°C for 3min
- Pre-Amplification with 14 cycles of temperature variation at 95°C for 15sec and 60°C for 4 min.

3µl of cDNA was diluted 1:10 for the RT-qPCR.

### **3.5 Quantitative Real-Time PCR (qPCR)**

qRT-PCR amplification was carried out exploiting TaqMan and SYBR-GREEN chemistries. Each reaction was performed in triplicate. Data analysis were performed by 7500 Real-Time PCR System (Applied Biosystems). Gene expression was measured with Livak-Schmittgen ( $2^{-\Delta\Delta C_t}$ ) method<sup>244</sup>.

#### **3.5.1 TaqMan qPCR**

TaqMan RT-qPCR mix for lncRNA and coding-genes was prepared as follows:

- 6.75µl of cDNA obtained from random primers RT-PCR; or cDNA obtained from One-Step RT-PCR and PreAmp was diluted 1:10 and 1.5 µl were used,
- 7.5µl of 2X PrimeTime Gene Expression Master Mix (Applied Biosystems)
- 0.75µl of PrimeTime qPCR Assay 20X: GAS5 (Assay ID: Hs.PT.58.24767969; IDT), RPLP0 (reference gene; Assay ID: Hs.PT.39a.22214824; IDT) and TERC (Assay ID: ID Hs03454202\_s1; ThermoFisher), TERT (Assay ID: Hs00972650\_m1; ThermoFisher) and GAPDH (reference gene; Assay ID: Hs99999905\_m1; ThermoFisher)

- 15µl of qPCR reaction mix was transferred into each well on a MicroAmp optical 96-well Reaction plate (Applied Biosystems)
- carefully, tightly seal the plate with MicroAmp Optical Adhesive Film (Applied Biosystems).
- The plate was centrifuged for 1min at 1000 x g at room temperature to remove bubbles
- Incubate at 50°C for 2min and then 95°C for 10min
- 40 cycles of PCR are performed at 95°C for 15sec and 60°C for 60sec.

TaqMan RT-qPCR mix for miR-126-3p was prepared as follows:

- 1.33µl of reverse transcription product
- 10µl of TaqMan Universal PCR Master Mix 2X (Applied Biosystems)
- 1µl of TaqMan MicroRNA Assay 20X: miR-126-3p (Assay ID 002228; Applied Biosystems), RNU48 (reference gene; Assay ID 001006; Applied Biosystems) and cel-miR-39 (spike-in reference gene; Applied Biosystems; ID ID000200)
- 7.67µl of Nuclease-free water.
- 20µl of qPCR reaction mix was transferred into each well on a MicroAmp optical 96-well Reaction plate (Applied Biosystems)
- carefully, tightly seal the plate with MicroAmp Optical Adhesive Film (Applied Biosystems).
- The plate was centrifuged for 1min at 1000 x g at room temperature to remove bubbles
- Incubate at 95°C for 10min
- 40 cycles of PCR are performed at 95°C for 15sec and 60°C for 60sec.

### **3.5.2 SYBR-GREEN qPCR**

Currently there are no TERRA TaqMan probes available. TERRA SYBR-GREEN RT-qPCR mix was prepared as follows:

- 2µl of diluted 1:2 cDNA
- 0.5µl of primers forwards and reverse 25µM
- 5µl Power SYBR Green PCR Master Mix (Applied Biosystems) and H<sub>2</sub>O to a total volume of 10µl.
- carefully, tightly seal the plate with MicroAmp Optical Adhesive Film (Applied Biosystems).

- The plate was centrifuged for 1 min at 1,000 x g at room temperature to remove bubbles
- Incubate at 95°C for 10min
- 40 cycles of PCR are performed at 95°C for 15sec and 60°C for 60sec. The qRT-PCR was followed by the dissociation stage for melting curve analysis for each primer pair used as follows: 95°C for 25min, 60°C for 1min and 95°C for 15min.

<b>Table 3. Primers qRT-PCR sequences using SYBR-GREEN</b>		
<b>Primers</b>		<b>5'→3'</b>
TERRA 1	hTel 1_2_10_13q_FOR	GAATCCTGCGCACCGAGAT
	hTel 1_2_10_13q_REV	CTGCACTTGAACCCTGCAATAC
TERRA 2	hTel 15q_FOR	CAGCGAGATTCTCCCAAGCTAAG
	hTel 15q_REV	AACCCTAACCACATGAGCAACG
TERRA 3	hTel XpYp_FOR	GCAAAGAGTGAAAGAACGAAGCTT
	hTel XpYp_REV	CCCTCTGAAAGTGGACCAATCA
β-ACTIN	β-actin_FOR	CCTCGCCTTTGCCGATCC
	β-actin_REV	GGATCTTCATGAGGTAGTCAGT

### 3.6 Transient Transfection

The HA22T/VGH cells were seeded in a 24-well plate at a confluence of 60–80%. To evaluate the effect of GAS5 siRNA transfection on miR-126-3p expression upon sorafenib treatment, cells were pre-treated for 24h with 15μM sorafenib and then transfected with 50nM and 100nM siRNA GAS5 and siRNA Negative Control (siRNA GAS5, Cat. #4390771 assay ID n272331; siRNA NC, Cat. #4390843, Life Technologies) using Lipofectamine 2000 Transfection reagent (Thermofisher), according to the manufacturer's protocol. 48h after transfection, cells were lysed in TRIzol reagent (Life Technologies) and total RNA was extracted.



### 3.7 MTT-assay

MTT assay is a colorimetric assay to assess cell viability. MTT [3-(4,5-dimethylthiazol-2-yl)-5-(3-carboxymethoxyphenyl)-2-(4-sulfophenyl)-2H-tetrazolium] is a yellow tetrazolium compound that following NADPH reduction is converted in a purple colored formazan product. The quantity of formazan product, measured by absorbance at 490nm, is directly proportional to the number of living cells.

HA22T/VGH cells were seeded in a 96-well plate (5 replicates for each experimental condition) at a density of  $4 \times 10^3$  cells/well in complete medium. After 24h cells were treated with 15 $\mu$ M sorafenib or 0.1% DMSO. 24h later cells were transfected with 50/100 nM miR-126-3p mimics or 50/100 nM miR-NC (negative control #1 Cat. #4464058) using Lipofectamine 2000 Transfection reagent (ThermoFisher). After 24h and 48h, viability was assessed with the addition of 15  $\mu$ l/well of sterile CellTiter reagent (Promega). The plates were incubated at 37°C for 2 hours in a humidified, 5% CO<sub>2</sub> atmosphere and the absorbance at 490nm was recorded using the microplate reader EnSight (PerkinElmer, Waltham, MA). The effects of miR-126-3p on cell viability in presence or absence of 15 $\mu$ M sorafenib were evaluated by transfecting the cells with miR-126-3p mimics (ThermoFisher, assay ID AM12841).

### 3.8 Statistical analysis

Statistical analysis were carried out using GraphPad Prism 6.0 software. Student's two tailed t-test was used to compare untreated and treated cells. One-way ANOVA followed by Bonferroni's correction was used to compare miR-126-3p ectopic expression after siRNA GAS5. Two tailed Chi-squared ( $\chi^2$ ) and Fisher's Exact test were used to inquire the significance of clinical characteristics. Wilcoxon paired two-tailed t-test was used to compare gene expression between peritumoral and tumoral tissues. Normal distribution and Student's t-test of the mean were used to test the significance of dysregulation from the mean. Diagnostic performance was evaluated using Receiver Operating Characteristic (ROC) curve analysis. To assess the diagnostic values of multi- assays, logistic regression method was applied. The diagnostic performance of individual as well as combinations of classifiers was computed using MedCalc 19.1.7 software.

Data were considered statistically significant when p-value  $\leq 0.05$ .

## RESULTS

### 4.1 Characterization of GAS5 and miR-126-3p in untreated and sorafenib treated HCC cells

By the use of RT<sup>2</sup> lncRNA PCR Array Human LncFinder and miScript miRNA PCR Array Human Liver miFinder, in our laboratory we observed an upregulation of lncRNA GAS5 and a simultaneous downregulation of miR-126-3p in cultured HA22T/VGH cells following sorafenib treatment. In order to validate those results, the expression of GAS5 and miR-126-3p was measured by RT-qPCR in sensitive and resistant HCC cell lines to sorafenib.

GAS5 resulted significantly upregulated following sorafenib treatment both in HA22T/VGH and SkHep1C3 cells compared to the untreated control ones. On the other hand its expression tended to decrease in the sorafenib resistant (SR) HA22T/VGH cells up to the level of untreated cells, but not in the SkHep1C3-SR cells, where it remained significantly high (Fig. 9A and 9B).

For miR-126-3p, as expected, its expression resulted significantly downregulated in treated HCC cells, compared to the untreated ones. Its expression was significantly even more lower in resistant cells, even if with a different extent in the two HCC cell lines (Fig. 9C and 9D).

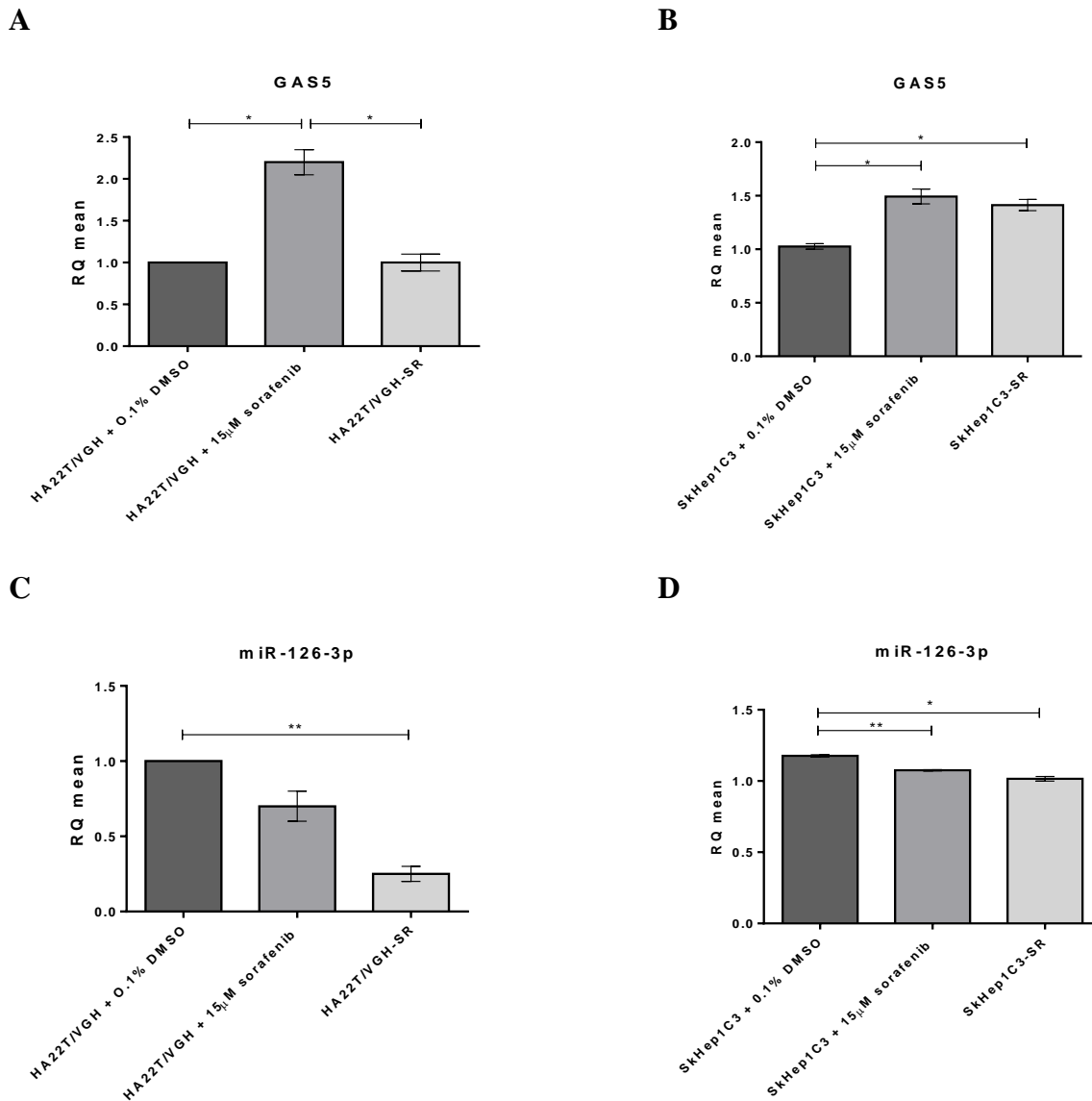


**Fig. 9. Intracellular expression of GAS5 and miR-126-3p.** Intracellular expression levels of GAS5 and miR-126-3p were measured in HA22T/VGH and SkHep1C3 untreated, resistant to sorafenib (SR) and treated with 15 $\mu$ M sorafenib. Histograms are the means of 2 experiments and the bars are  $\pm$  SEM. Unpaired two tailed t-test; \* $p$ <0.05, \*\* $p$ <0.01.

#### 4.2 GAS5 silencing rescues miR-126-3p expression

As GAS5 and miR-126-3p display opposite gene expression following sorafenib treatment, by bioinformatic analysis, a presumed 3'- GAS5 binding site for miR-126-3p was predicted. To verify the ceRNA effect of GAS5 over miR-126-3p, the GAS5 binding site for the miR-126-3p was cloned downstream of the luc2 gene. A decrease in luciferase activity was observed in the presence of miR-126-3p-mimic<sup>240</sup>. To further corroborate those results, a rescue experiment was subsequently performed. siRNA-dependent transient silencing of GAS5 in HA22T/VGH, after

15 $\mu$ M sorafenib treatment for 24h, induced a significant upregulation of miR-126-3p at 48h after transfection (Fig. 10C, 10D).

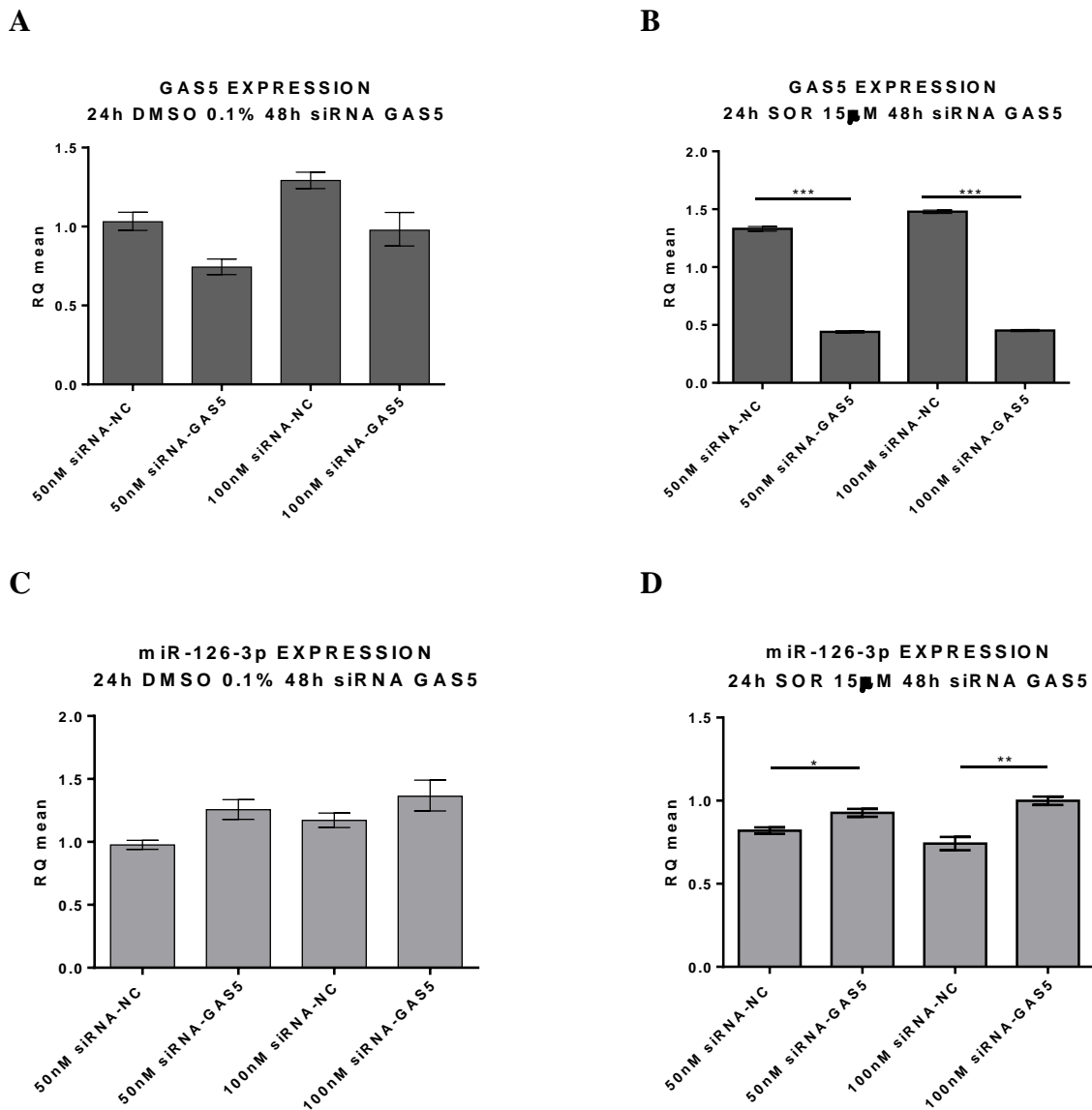


**Fig. 10. Effects of siRNA-GAS5 transient transfection in HA22T/VGH untreated/treated with 15 $\mu$ M sorafenib.** A) Histograms show the GAS5 silencing obtained with 50nM and 100nM siRNA GAS5 in untreated cells. B) Histograms show that GAS5 expression is significantly silenced 48h after transfection in sorafenib treated cells. C) Histograms show the increase of miR-126-3p expression obtained at 50nM and 100nM siRNA GAS5. D) miR-126-3p is significantly upregulated at 48h after GAS5 silencing. Histograms are the means and the bars are  $\pm$  SEM. Unpaired two-tailed t-test; \* $p$ <0.05, \*\* $p$ <0.01, \*\*\* $p$ <0.001.

### 4.3 Effect of miR-126-3p overexpression on cell growth

Since sorafenib limits the viability of HCC cultured cells and led to the opposite expression of GAS5 and miR-126-3p we wanted to assess whether the overexpression of miR-126-3p could influence cell growth. For this purpose HA22T/VGH cells were transfected with miR-126-3p

mimic and, as shown in Fig. 11A and 11B, the ectopic expression of miR-126-3p significantly decreased cell growth after 24h and 48h after transfection, compared to corresponding controls.

Sorafenib also significantly reduced cell viability at 24h and 48h after miR-mimic transfection. However, no additive effects were observed upon the overexpression of miR-126-3p (Fig. 11C and 11D).

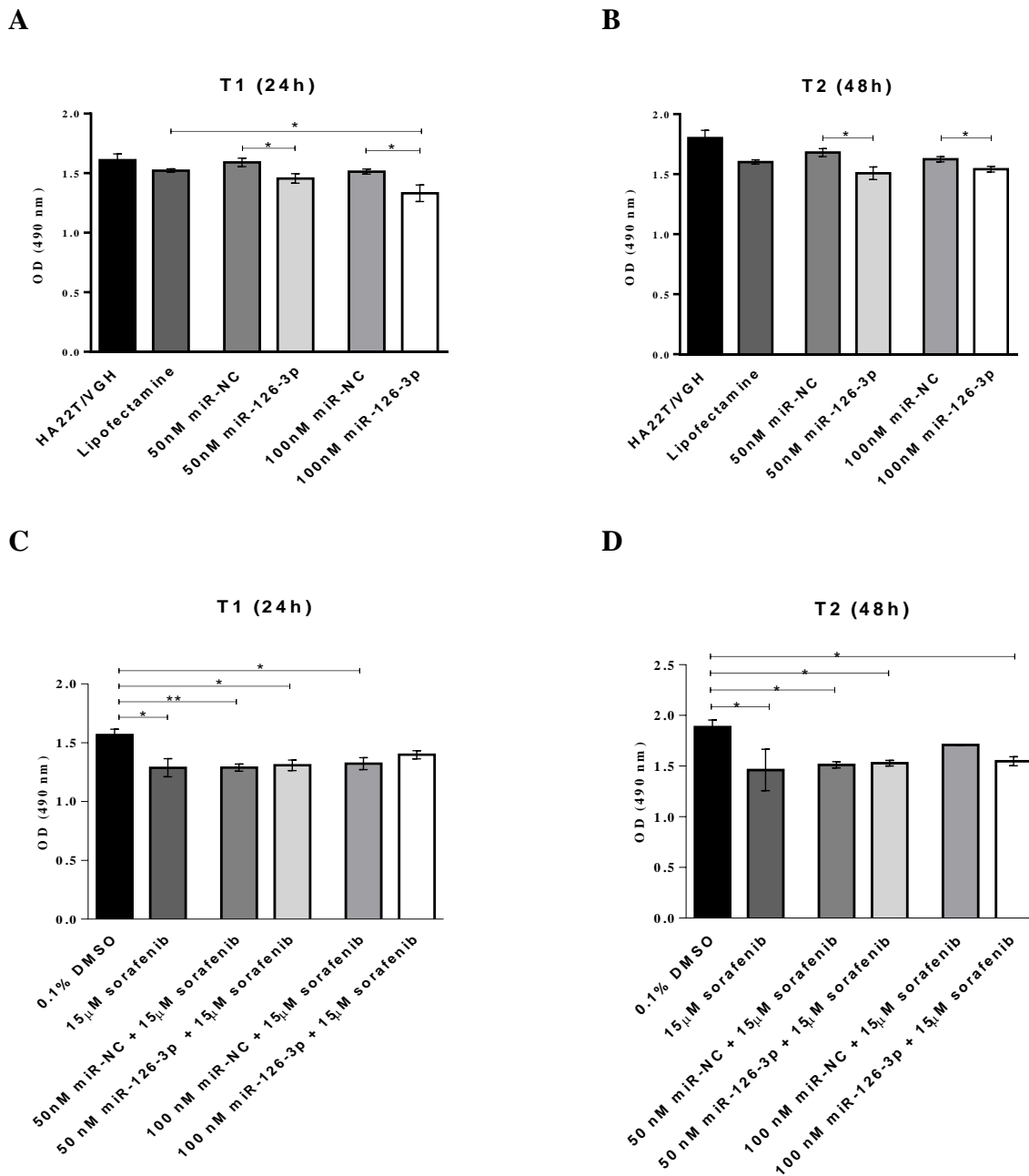


**Fig. 11. Effects of ectopic expression of miR-126-3p mimic on HA22T/VGH cells growth untreated/treated with 15 μM sorafenib.** Histograms are the means and the bars are ± SEM. Results are representative of one of two experiments. One-way ANOVA followed by Bonferroni's correction. \*p<0.05, \*\*p<0.01.

#### 4.4 TERRA and telomerase intracellular dysregulation

In cells with long telomeres TERRA can base-pair with TERC and act as *in vitro* TERT allosteric inhibitor. These interactions might be responsible for the TERRA-mediated inhibition of telomerase activity. In cells with short telomeres TERRA may instead coordinate the recruitment of telomerase and encourage subsequent telomere elongation. TERRA expression was explored in *in vitro* models of HCC in order to understand how telomerase could be affected at the level of TERT mRNA and TERC, and therefore influence cancer cell unlimited replicative potential.

Treatment with sorafenib significantly increased TERRA expression in HA22T/VGH cells compared to the untreated ones. A trend of upregulation was also shared by SkHep1C3, but with a lower grade compared to HA22T/VGH. Both HA22T/VGH-SR and SkHep1C3-SR cells still expressed TERRA at high levels compared to untreated cells (Fig.12A and 12B).

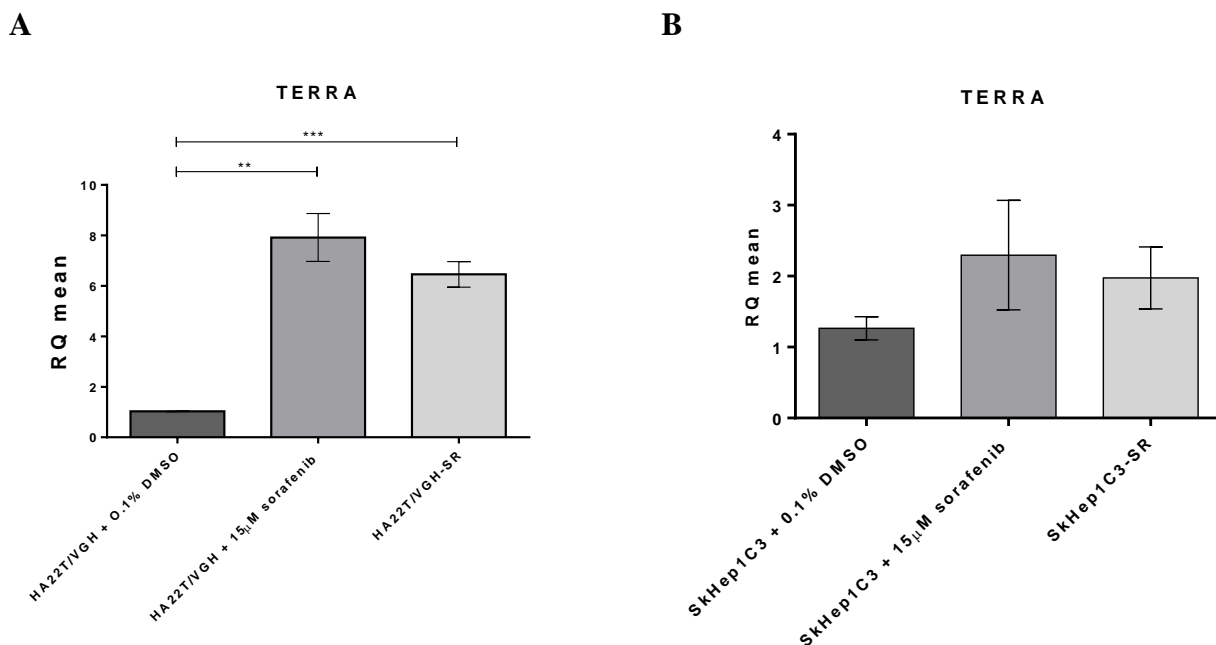


**Fig 12. Intracellular expression of TERRA.** The expression levels of TERRA were measured in HA22T/VGH and SkHep1C3 untreated, resistant to sorafenib (SR) and treated with 15 μM sorafenib. The histograms represent the mean values of 2 experiments, bars are ± SEM. Unpaired two tailed t-test; \*p < 0.05, \*\*p < 0.01, \*\*\*p < 0.001.

TERC and TERT mRNA resulted upregulated following 15 $\mu$ M sorafenib treatment both in HA22T/VGH and SkHep1C3 cells. For sorafenib resistant cells, only TERT mRNA displayed a significant expression variation, in particular a significant expression decrease compared with both untreated and treated cells (Fig 13A and 13B).

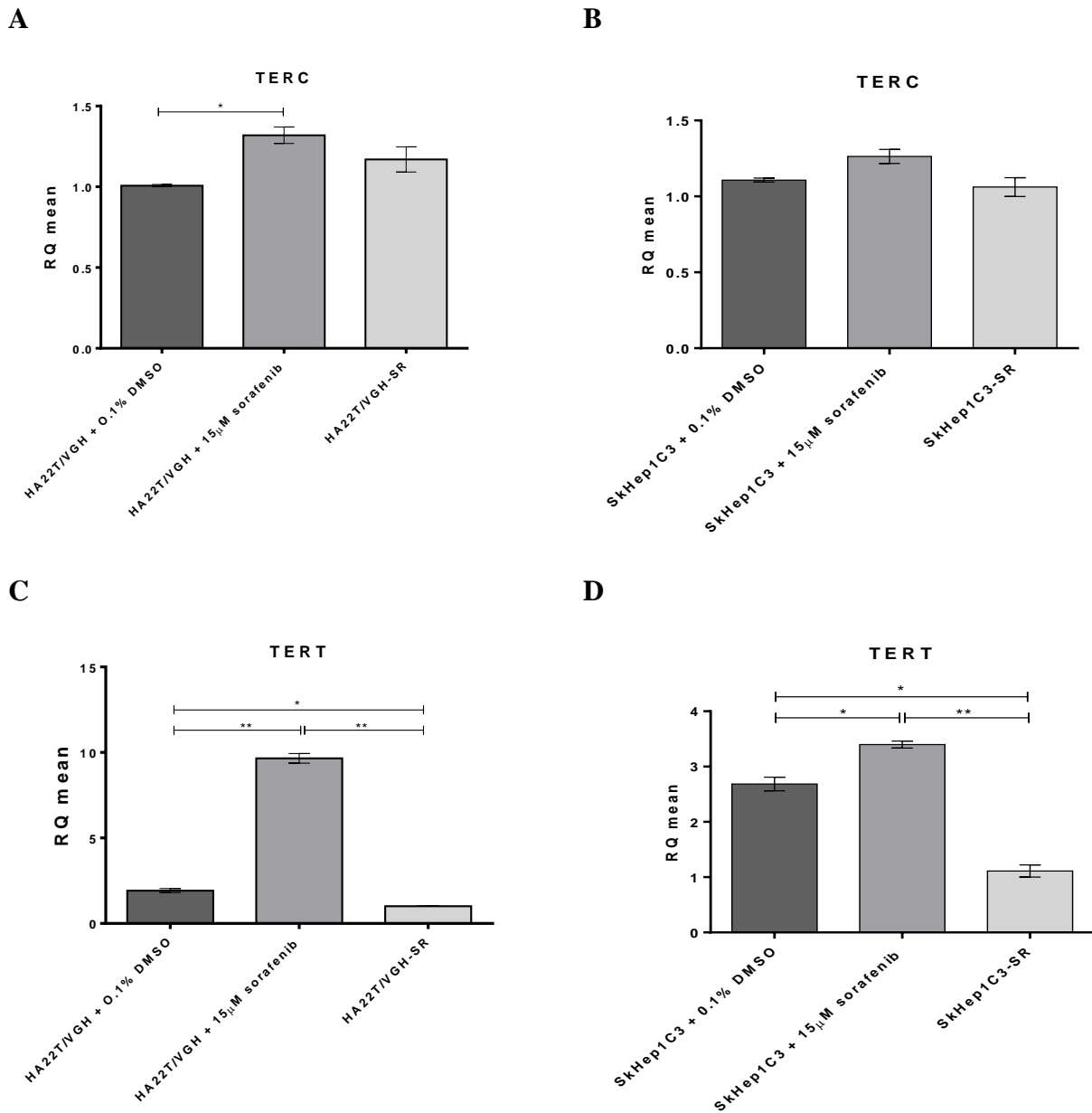


**Fig. 13. Intracellular expression of telomerase.** The expression levels of TERC (A, B) and TERT (C, D) were measured in HA22T/VGH and SkHep1C3 untreated, resistant to sorafenib (SR) and treated with 15 $\mu$ M sorafenib. The histograms represent the mean values of 2 experiments, bars are  $\pm$  SEM. Unpaired two tailed t-test; \*p<0.05, \*\*p<0.01.

#### **4.5 Detection of GAS5, miR-126-3p, TERRA, TERC and TERT mRNA in the EVs of HCC cultured cells**

To better comprehend the variation in the expression of GAS5, miR-126-3p, TERRA, TERT mRNA and TERC in sorafenib treated HCC cells, we decided to study their possible release into the EVs. For this purpose we examined the secretome of HA22T/VGH cells in collaboration with Dr. Vito D'Agostino from University of Trento. EVs were obtained by nickel-based isolation method (NBI) and subsequently analyzed by Q-NANO instrument. NBI exploits a matrix of beads properly functionalized with nickel cations to capture heterogeneous EVs allowing a rapid enrichment of dimensionally heterogeneous (polydisperse) EVs in solution, preserving their integrity and stability. In Q-NANO, a tunable submicron-sized pore separates two fluid chambers, one containing the sample to be analyzed, the other an electrolyte solution. An electric current between the chambers is disrupted when a particle passes through the pore, causing a “blockade” event, the magnitude of which is proportional to the volume of the particle traversing the pore, and the blockade rate directly related to the particle concentration.

HCC cells released different amounts of EVs characterized by several ranges of dimensions. In particular, as shown in Fig. 14 and table 4, HA22T/VGH cells released  $1.63 \cdot 10^8$  EVs/ml. treatment with sorafenib induced an increase of released particles up to  $2.09 \cdot 10^8$  EVs/ml. On the other hand sorafenib-resistant HA22T/VGH cells released  $1.64 \cdot 10^8$  EVs/ml, but with a higher dimension (mean diameter=252nm; mode diameter=202nm).



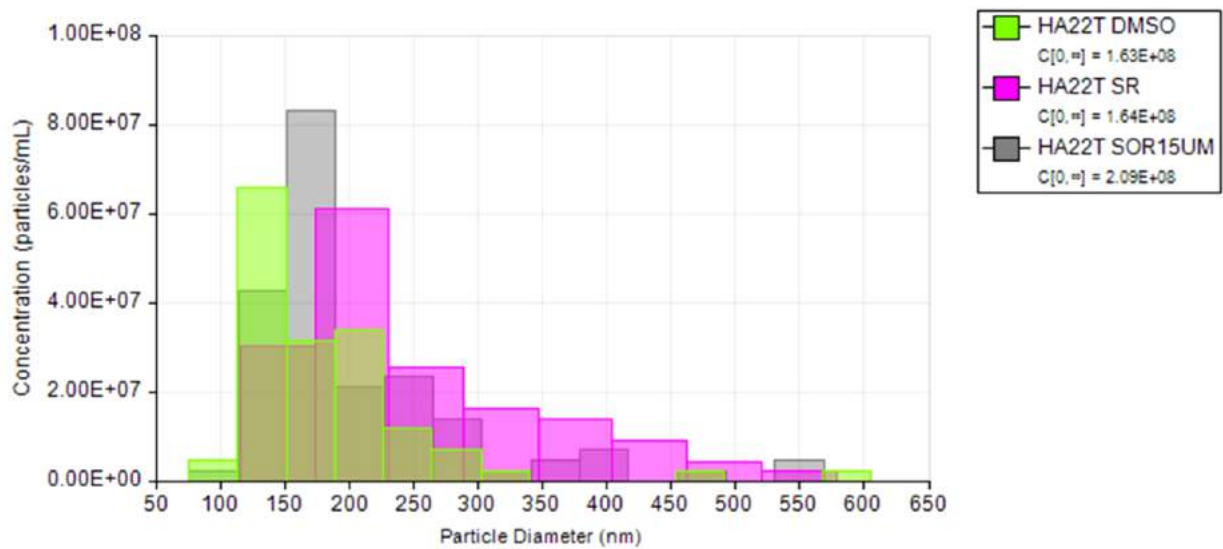


**Table 4.** Q-NANO analysis of HA22T/VGH secretome

Sample Label	Mean Dia (nm)	Mode Dia (nm)	Raw Conc (ml)	Particle Count
HA22T/VGH 0.1% DMSO	185	132	$1.63 * 10^8$	67
HA22T/VGH + 15 $\mu$ M SOR	206	171	<b><math>2.09 * 10^8</math></b>	88
HA22T/VGH-SR	252	<b>202</b>	$1.64 * 10^8$	70

**Fig. 14. Size histogram of EVs particles.** The graph shows the distribution of EVs as a function of their dimension. Dia: diameter; Conc: concentration.

Concerning the extracellular RNA content, HA22T/VGH cells treated and resistant to sorafenib showed a significant increase in GAS5 levels both in the vesicle-free component and in the EVs, compared to the untreated cells (Fig. 15A and 15B). Also an increase in miR-126-3p levels was observed both in the EVs-free component and in the EVs, compared to the untreated cells (Fig. 15C and 15D).

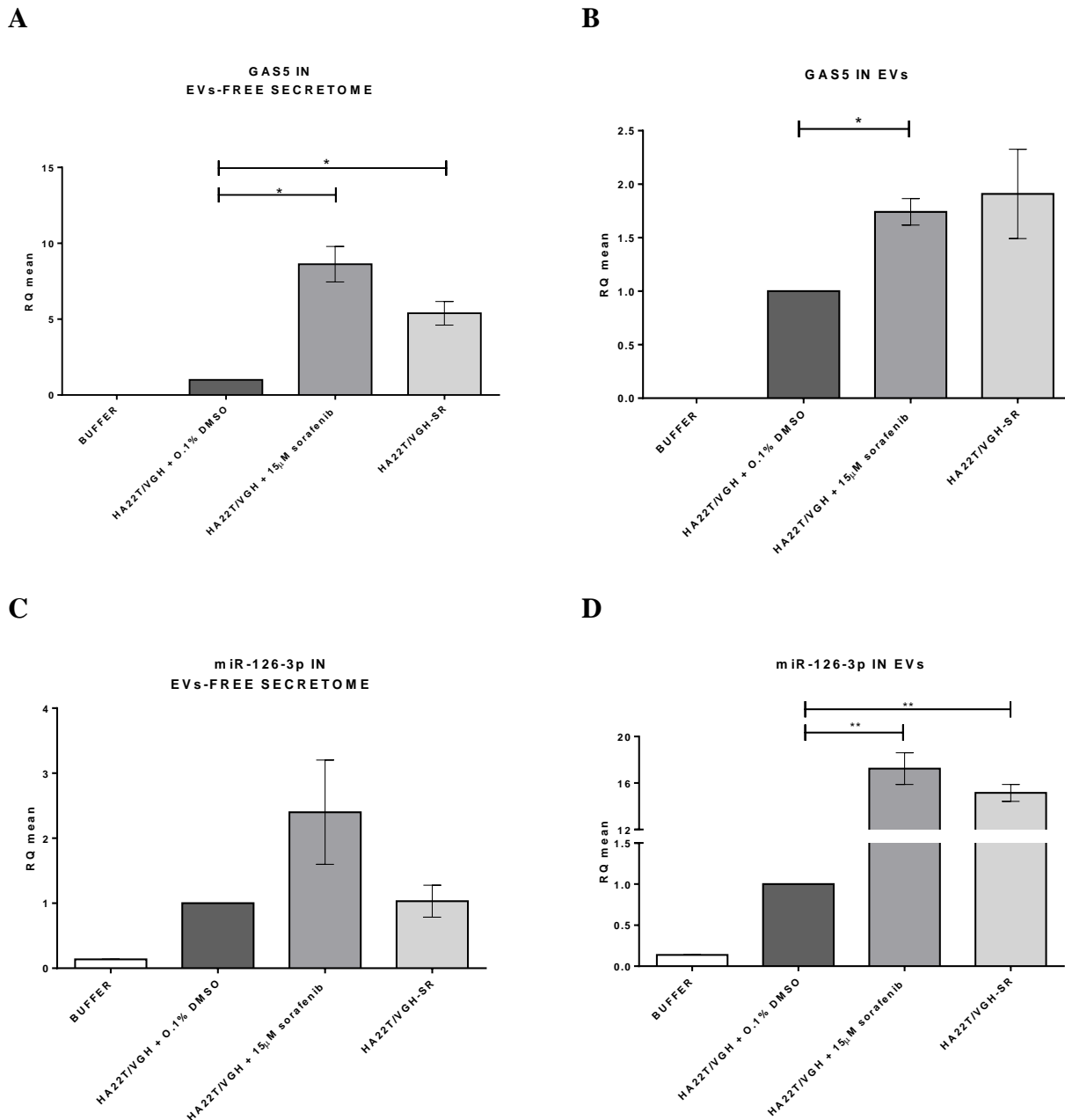


**Fig. 15. Levels of GAS5 and miR-126-3p in HA22T/VGH secretome.** The levels of GAS5 and miR-126-3p were measured in the secretome of HA22T/VGH untreated, resistant to sorafenib (SR) and treated with 15µM sorafenib. Gene expression level was normalized according to the number of particles. The histograms represent the mean values of 2 experiments, bars are  $\pm$  SEM. Unpaired two tailed t-test; \* $p < 0.05$ , \*\* $p < 0.01$ , \*\*\* $p < 0.001$ .

Regarding the extracellular level of TERRA, it has been analyzed for different chromosome locations. Global TERRA level has been obtained as a mean of the different TERRA relative quantifications. HA22T/VGH cells treated with 15 $\mu$ M sorafenib and resistant cells showed a significant decrease in global TERRA amounts both in the EVs-free component (Fig. 16A) and in the EVs (Fig. 16B), compared to the untreated ones.

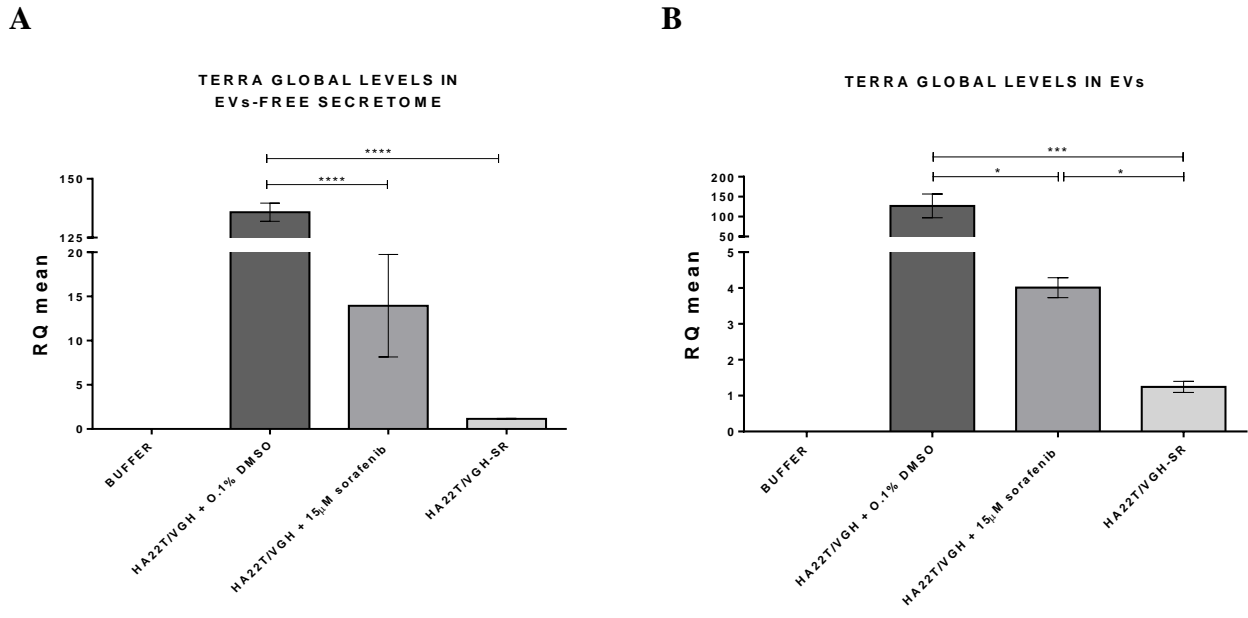


**Fig. 16. Levels of TERRA in HA22T/VGH secretome.** The global level of TERRA was measured in the secretome of HA22T/VGH untreated, resistant to sorafenib (SR) and treated with 15 $\mu$ M sorafenib. Gene expression level was normalized to the number of particles released. Histograms represent the mean values of 2 experiments, bars are  $\pm$  SEM. Unpaired two tailed t-test; \* $p$ <0.05, \*\* $p$ <0.01, \*\*\* $p$ <0.001.

TERC shows a significant dysregulation in the secretome of HA22T/VGH cells with different levels of content. In particular it shows a trend of decrease in the EVs-free component of HA22T/VGH treated cells, while it is significantly decreased in the one of resistant cells. On the contrary TERC level is significantly increased in the EV component of HA22T/VGH treated cells, compared to the EVs of untreated and resistant cells, where the levels are comparable (Fig. 17A and 17B). On the other hand TERT mRNA is not detectable nor in the EVs-free nor EVs components (17C and 17D).

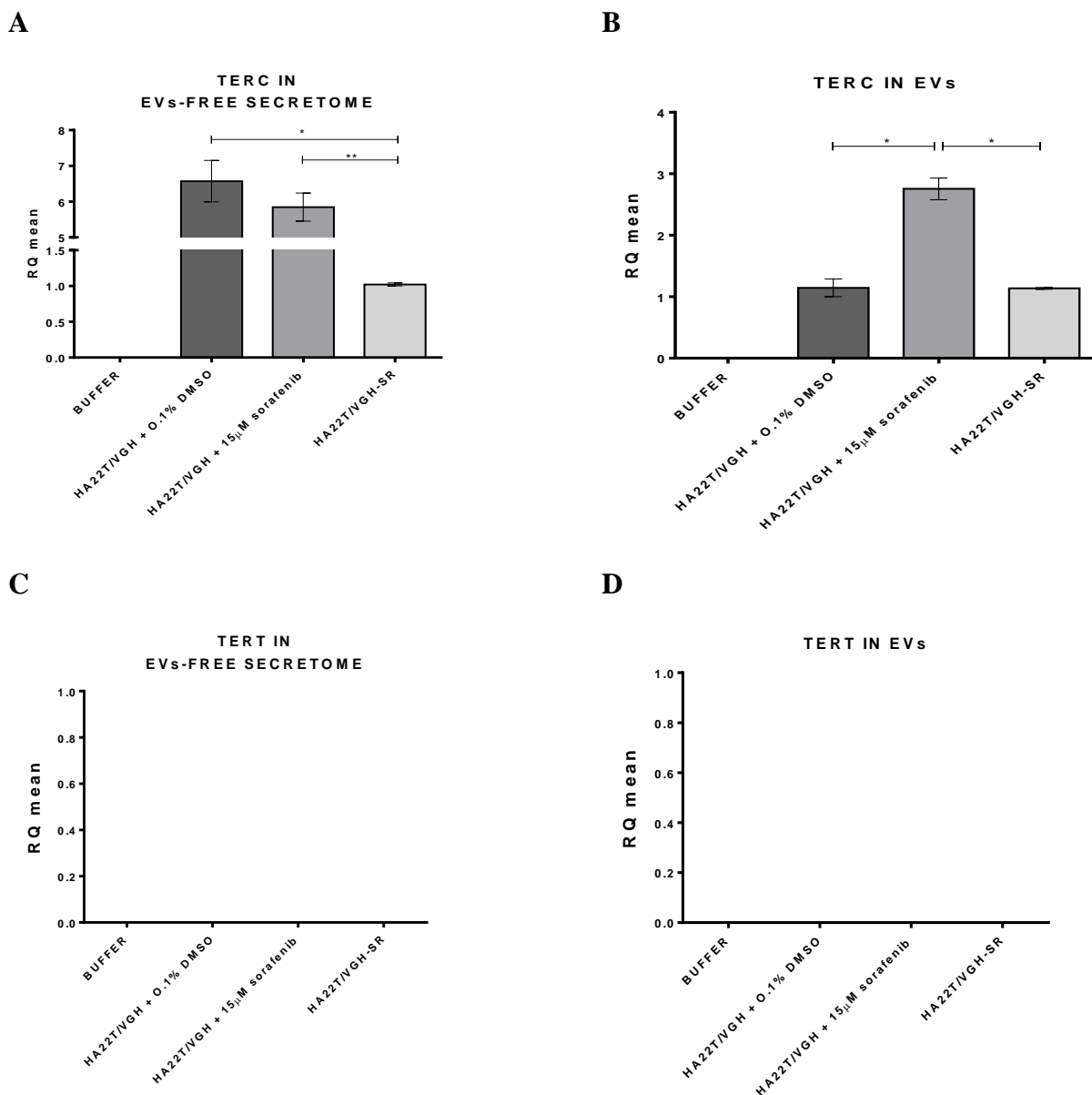


**Fig. 17. Detection of TERT mRNA and TERC in the secretome of HA22T/VGH cells.** The levels of TERC and TERT mRNA were measured in the secretome of HA22T/VGH untreated, resistant to sorafenib (SR) and treated with 15 $\mu$ M sorafenib. Gene expression levels were normalized according to the number of particles. Histograms represent the mean values of 2 experiments, bars are  $\pm$  SEM. Unpaired two tailed t-test; \* $p$ <0.05, \*\* $p$ <0.01.

#### **4.6 Expression study of GAS5, miR-126-3p, TERRA, TERC and TERT mRNA in HCC bioptic specimens**

In the present study we examined tumor and peritumor bioptic specimens of 30 HCC patients. The subjects were 24 men and 6 women with an age ranging from 57 to 82 years. The subjects did not have any apparent distant metastases, and none had been previously treated for HCC before surgical resection of the tumor mass. Patients were analyzed for the presence of the hepatitis B virus (HBV) or hepatitis C virus (HCV). Sixteen patients were positive for HCV, 4 were positive for HBV, and 10 were found to be negative for both HBV and HCV (Table 5).

**Table 5.** Characteristics of the 30 HCC patients enrolled in the study. Baseline characteristics of the study population according to clinical and pathological backgrounds.

PARAMETERS	SUBSET	p-value
<b>TOTAL NUMBER OF PATIENTS ENROLLED</b>	30	
AGE, mean (range)	72,4 (57-82)	
SEX, No (%)		
Male	24 (80%)	
Female	6 (20%)	
<b>CIRRHOSIS, No (%)</b>		
YES	16 (53%)	
NO	12 (41%)	< 0.0001 ****
N/A	2 (6%)	
<b>STEATOSIS, No (%)</b>		
YES	13 (43%)	
NO	15 (50%)	< 0.0001 ****
N/A	2 (8%)	
<b>CHRONIC HEPATITIS, No (%)</b>		
YES	8 (26%)	
NO	20 (66%)	0.0047 **
N/A	2 (8%)	
<b>VON MEYENBURG COMPLEX, No (%)</b>		
YES	1 (4%)	
NO	27 (90%)	1
N/A	2 (6%)	
<b>NORMAL, No (%)</b>		
YES	1 (4%)	
NO	27 (90%)	1
N/A	2 (6%)	
<b>HEPATITIS VIRUS INFECTION, No (%)</b>		
HBV	4 (13%)	0.0047 **
HCV	16 (54%)	< 0.0001 ****
HBV/HCV POSITIVE	0 (0%)	
HBV/HCV NEGATIVE	10 (33%)	< 0.0001 ****
<b>DIMENSION</b>		
< 10 cm	23 (76%)	
> 10 cm	5(16%)	0.0051 **
N/A	2 (6%)	
<b>DIFFERENTIATION GRADE, No (%)</b>		
G1	2 (6%)	
G1-G2	1 (3%)	
G2	16 (53%)	
G2-G3	3 (10%)	
G3	7 (23%)	
G4	0 (0%)	
N/A	1 (3%)	

Values are represented as number of patients (%), except for age, which is presented as mean age. Two tailed Chi-squared ( $\chi^2$ ) and Fisher's Exact test. \*p<0.05, \*\*p<0.01, \*\*\*p<0.001, \*\*\*\* p<0.0001.

#### 4.7 GAS5, miR-126-3p, TERRA, TERC and TERT are dysregulated in HCC tissues

As ncRNAs are dysregulated in *in vitro* experimental conditions both at the intracellular and at the extracellular level, to further understand their dysregulation, the gene expression of the different targets was analyzed in 25 HCC tissues and their corresponding peritumoral (PT) counterparts. Data are presented as Ratio (R). The Ratio, R-value or fold-change, is defined as the HCC vs PT ratio of the relative gene expression level of a specific target in each case. Downregulation was assumed when  $R < 0.7$ , no variation when  $0.7 \leq R \leq 1.3$  and upregulation when  $R > 1.3$ .

To understand whether the pathological background could influence the gene expression of each specific target, each HCC case was stratified according to the background disease.

In order to evaluate whether variation in gene expression could have a potential diagnostic significance, Receiver Operating Characteristic (ROC) curve was generated and analyzed for all the targets to inquire the capability of GAS5, miR-126-3p, TERC, TERT mRNA and TERRA to act as diagnostic tools to successfully distinguish between cancerous and normal tissues.

GAS5 was differently expressed in HCC tissues compared to PT. Considering the R values, two different subpopulations could be distinguished: 14/25 of cases (56%) showed a downregulation or no change in gene expression, whereas 11/25 of cases (44%) showed an upregulation of GAS5 gene expression (Fig. 18A). Overall GAS5 showed a trend of upregulation in HCC tissues compared to PT (Fig. 18B). GAS5 upregulation is mostly influenced by the presence of HCV and liver cirrhosis (Fig. 18C and Table 6). ROC curve analysis evidenced that GAS5 does not show a significant capability in discriminating HCC from peritumoral tissues (Fig. 16D).

miR-126-3p expression (Fig. 19A) resulted significantly downregulated in HCC tissues compared to PT (Fig. 19B). miR-126-3p downregulation is mostly influenced by the presence of HCV, cirrhosis background pathology and G2 tumor grade (Fig. 19C and Table 7). ROC curve analysis highlighted a successful significant diagnostic performance of miR-126-3p in discriminating HCC from normal tissues (Fig. 19D)

There is no evidence of correlation between GAS5 and miR-126-3p expression in the HCC tissues. However, 16/25 cases (64%) showed an inverse trend, with simultaneous high expression of GAS5 and low expression of miR-126-3p.

TERRA expression has been analyzed for different chromosome locations. The global TERRA expression was obtained as a mean of the different TERRA relative quantifications (Fig. 20A). TERRA global expression was significantly downregulated in HCC compared to PT (Fig. 20B). However, two different HCC subpopulations could be distinguished: 19/25 of cases (76%) showed downregulation of TERRA expression, whereas 6/25 cases (24%) showed upregulation of

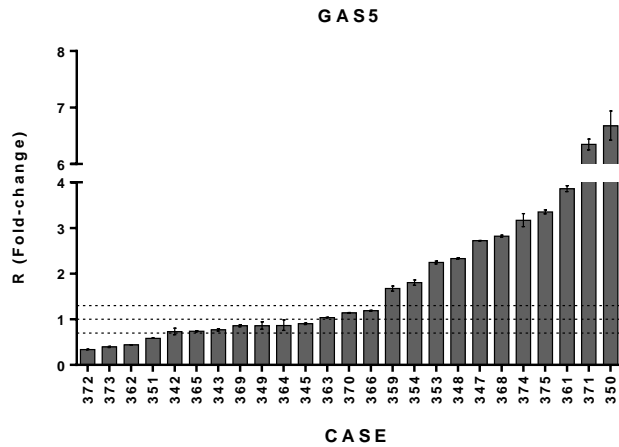
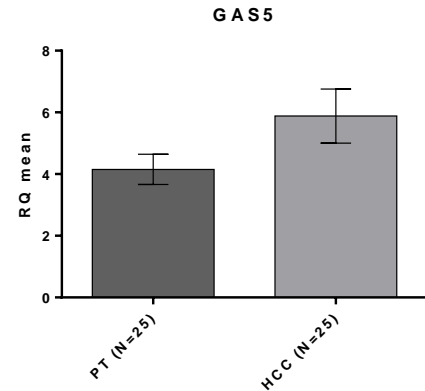
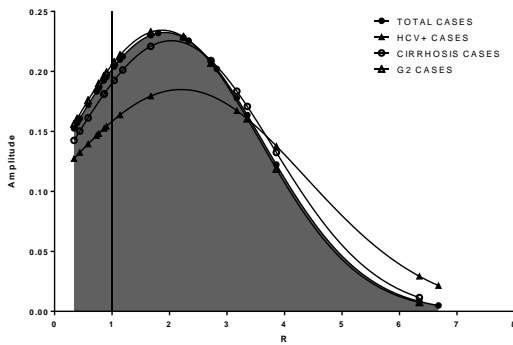
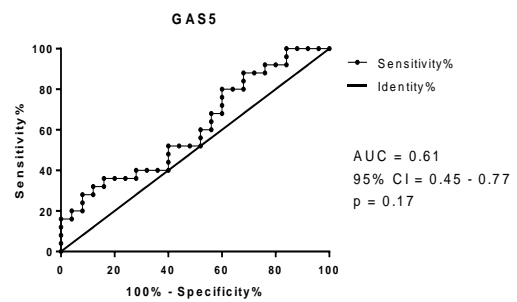
TERRA expression (Fig. 20A). TERRA downregulation appears not to be influenced by the presence of any background disease and ROC curve analysis revealed that TERRA has a significant diagnostic capability in discriminating HCC from peritumoral tissues. Moreover, logistic regression model of classifiers showed that the use of combinational TERRA molecules improves and may represent a significant successful discriminating tool to distinguish HCC from normal tissue (Fig. 21 and Table 9).

TERC expression (Fig. 22A) showed a trend of upregulation in HCC tissues compared to PT (Fig. 22B). TERC upregulation tended to be influenced mostly by the presence of HCV (Fig. 22C). ROC curve analysis did not display a diagnostic performance in distinguishing HCC from normal tissues (Fig. 22D)

TERT mRNA expression (Fig. 23A) was significantly upregulated at different orders of magnitude in HCC tissues compared to the PT ones (Fig. 23B). TERT mRNA upregulation was significantly marked in the cirrhotic pathological *milieu* (Fig. 23C). ROC curve analysis of TERT mRNA expression revealed a successful significant diagnostic ability in discriminating HCC from normal tissues (Fig. 23D).

Finally, taking into account TERRA expression and telomerase components (TERT mRNA and TERC) opposite trend, only 6/25 HCC cases (24%) displayed an inverse trend between TERRA and telomerase component expression. In particular, 15/25 cases (60%) showed a simultaneous low expression of TERRA and high expression of TERT mRNA.



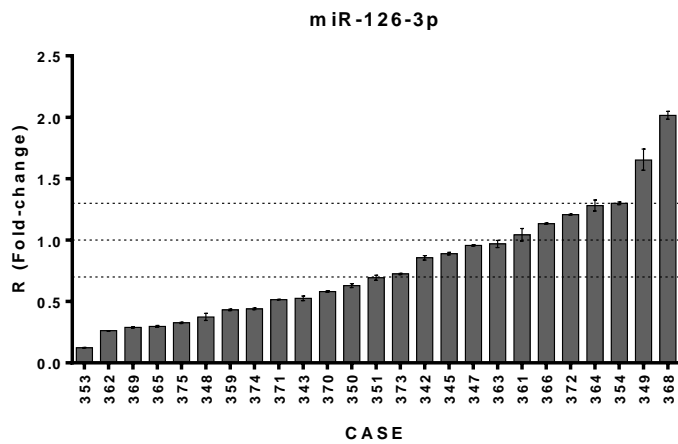
**A****B****C****D**

**Table 6.** Variation of GAS5 expression influenced by clinical-pathological features.

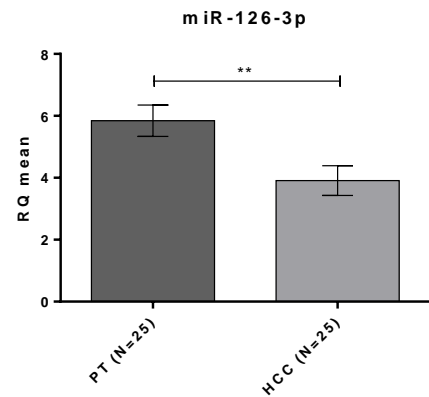
	N	R	SEM	p-value
<b>HCC TOTAL CASES</b>	25	1.91	0.34	0.013 *
<b>HCV+ HCC</b>	14	2.2	0.57	0.057
<b>HCC with CIRRHOSIS</b>	13	2.03	0.49	0.056
<b>G2 HCC</b>	14	1.87	0.45	0.077

**Fig. 18. Tissue expression of GAS5.** A) GAS5 Fold-change. Histograms represent R-values and bars upper and lower limits. Histograms are ordered by increasing R-values. The corresponding case are listed below. Upper and lower dot lines define the range of gene expression variation. B) GAS5 relative quantification mean comparison between PT and HCC. Wilcoxon paired two-tailed t-test. C) Normal distribution of the R-values. The normal distribution of the total cases analyzed underpins the grey area under the curve. The black lines refer to the background disease. Table 6: Student t-test of the mean. D) ROC curve analysis of GAS5 to discriminate HCC from normal tissue. AUC: Area Under the ROC Curve. CI: Confidence Interval. \* $p < 0.05$ .

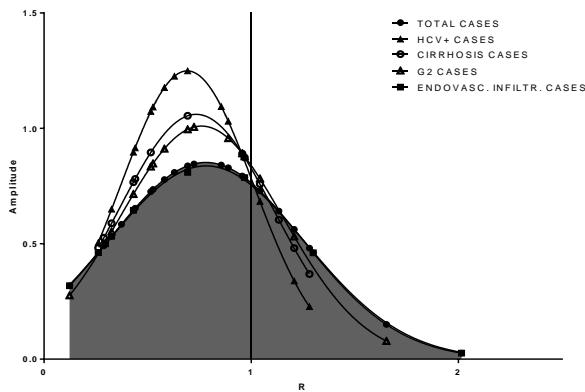
**A**



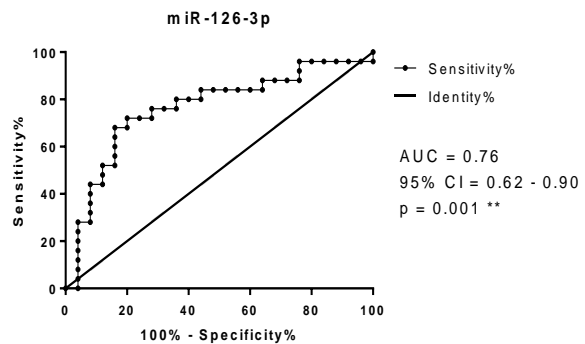
**B**



**C**



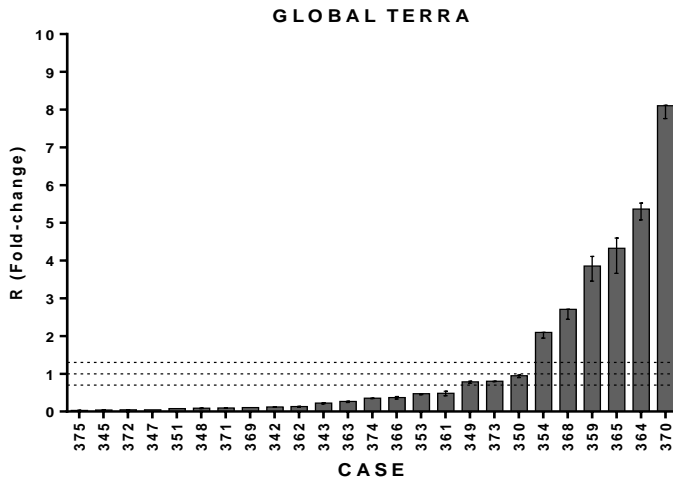
**D**



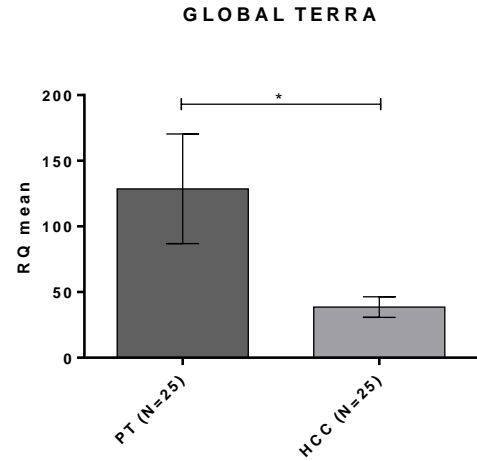
	<b>N</b>	<b>R</b>	<b>SEM</b>	<b>p-value</b>
<b>HCC TOTAL CASES</b>	25	0.78	0.09	0.027 *
<b>HCV+ HCC</b>	14	0.69	0.08	0.003 **
<b>HCC with CIRRHOSIS</b>	13	0.73	0.1	0.025 *
<b>G2 HCC</b>	14	0.76	0.1	0.04 *
<b>HCC with ENDOVASCULAR INFILTRATION</b>	9	0.7	0.2	0.19

**Fig. 19. Tissue expression of miR-126-3p.** A) miR-126-3p Fold-change. Histograms represent R-values and bars upper and lower limits. Histograms are ordered by increasing R-values. The corresponding case are listed below. Upper and lower dot lines define the range of gene expression variation. B) miR-126-3p relative quantification mean comparison between PT and HCC. Wilcoxon paired two-tailed t-test. C) Normal distribution of the R-values. The normal distribution of the total cases analyzed underpins the grey area under the curve. The black lines refer to the background disease. Table 7: Student t-test of the mean. D) ROC curve analysis of miR-126-3p to discriminate HCC from normal tissue. AUC: Area Under the ROC Curve. CI: Confidence Interval. \*p<0.05, \*\*p<0.01.

**A**



**B**



**C**

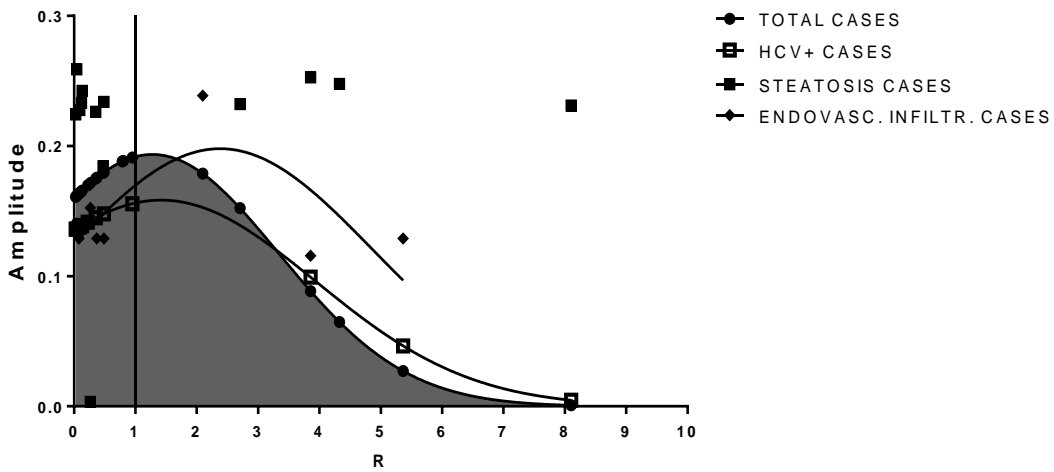


**Table 8.** Variation of TERRA expression influenced by clinical-pathological features.

	N	R	SEM	p-value
<b>HCC TOTAL CASES</b>	25	1.28	0.41	0.5
<b>HCV+ HCC</b>	17	1.43	0.25	0.45
<b>HCC with STEATOSIS</b>	15	0.84	0.36	0.66
<b>HCC with ENDOVASCULAR INFILTRATION</b>	11	1.69	0.44	0.14

**Fig. 20. Tissue expression of TERRA.** A) TERRA Fold-change. Histograms represent R-values and bars upper and lower limits. Histograms are ordered by increasing R-values. The corresponding case are listed below. Upper and lower dot lines define the range of gene expression variation. B) TERRA relative quantification mean comparison between PT and HCC. Wilcoxon paired two-tailed t-test. C) Normal distribution of the R-values. The normal distribution of the total cases analyzed underpins the grey area under the curve. The black lines refer to the background disease. Table 8: Student t-test of the mean. \*p<0.05.

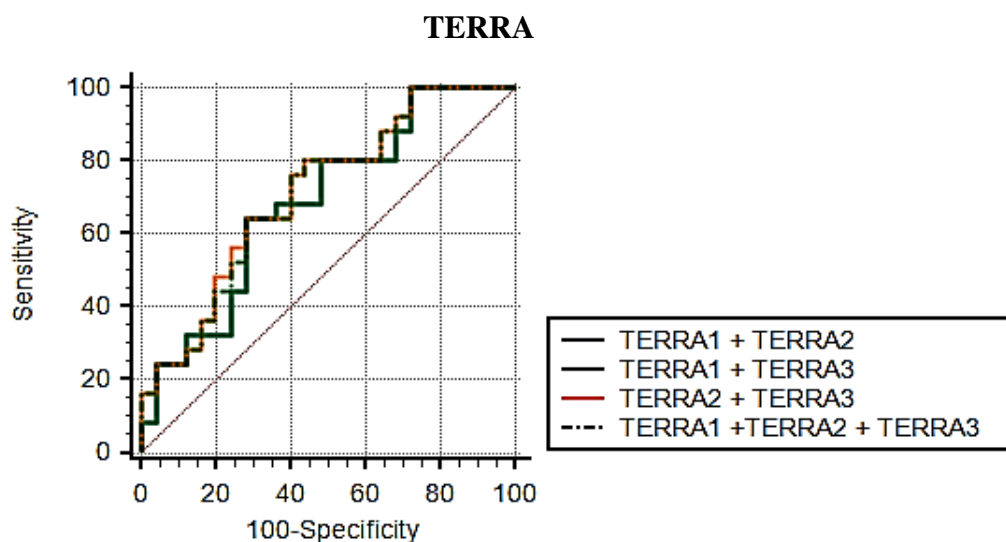
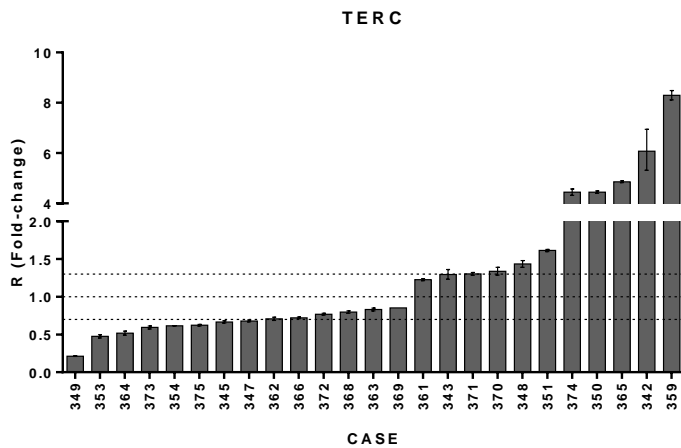


**Table 9.** Diagnostic performance of TERRA in HCC tissues.

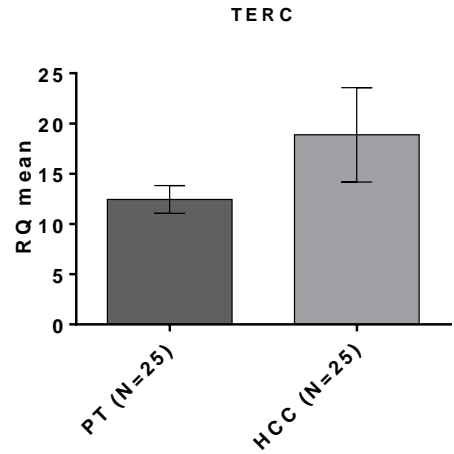
TARGET	Sensitivity	Specificity	AUC	SE	95% CI	p-value
<b>TERRA1</b>	80%	64%	0,706	0,075	0,560 to 0,826	0.0064 **
<b>TERRA2</b>	84%	52%	0,698	0,074	0.551 to 0.819	0.008 **
<b>TERRA3</b>	84%	52%	0,712	0,072	0.567 to 0.831	0.0036 **
<b>TERRA1+TERRA2</b>	52%	80%	0,686	0,075	0.540 to 0.810	0.0166 *
<b>TERRA1+TERRA3</b>	52%	80%	0,71	0,072	0.565 to 0.830	0.0233 *
<b>TERRA2+TERRA3</b>	44%	80%	0,712	0,072	0.567 to 0.831	0.0149 *
<b>TERRA1+TERRA2+TERRA3</b>	44%	80%	0,709	0,073	0.563 to 0.829	0.0382 *

**Fig. 21. ROC curve analysis of TERRA in tissues.** Sensitivity: percent of correctly classified HCC patients. Specificity: percent of correctly classified non-HCC. AUC: Area Under the ROC Curve. CI: Confidence Interval. \* $p < 0.05$ , \*\* $p < 0.01$ .

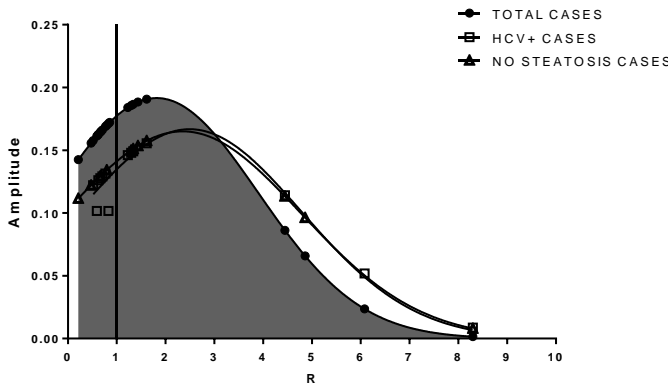
**A**



**B**



**C**



**D**

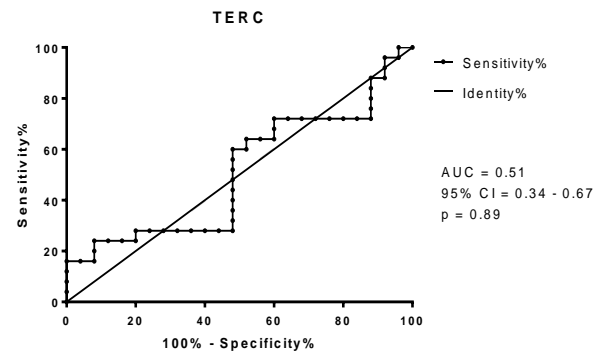
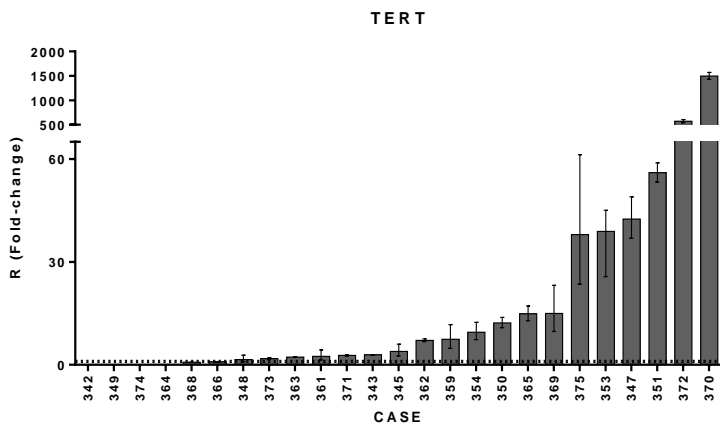


**Table 10.** Variation of TERC expression influenced by clinical-pathological features.

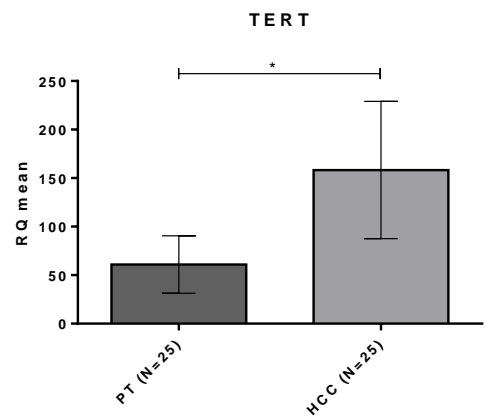
	N	R	SEM	p-value
<b>HCC TOTAL CASES</b>	25	1.81	0.41	0.06
<b>HCV+ HCC</b>	14	2.38	0.65	0.05
<b>HCC without STEATOSIS</b>	12	2.17	0.7	0.07

**Fig. 22. Tissue expression of TERC.** A) TERC Fold-change. Histograms represent R-values and bars upper and lower limits. Histograms are ordered by increasing R-values. The corresponding case are listed below. Upper and lower dot lines define the range of gene expression variation. B) TERC relative quantification mean comparison between PT and HCC. Wilcoxon paired two-tailed t-test. C) Normal distribution of the R-values. The normal distribution of the total cases analyzed underpins the grey area under the curve. The black lines refer to the background disease. Table 10: Student t-test of the mean. D) ROC curve analysis of TERC to discriminate HCC from normal tissue. AUC: Area Under the ROC Curve. CI: Confidence Interval.

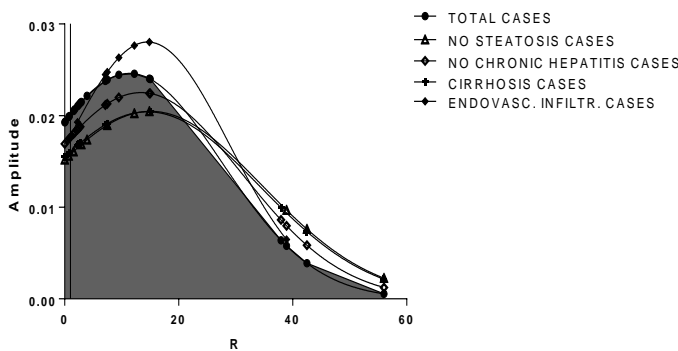
**A**



**B**



**C**



**D**

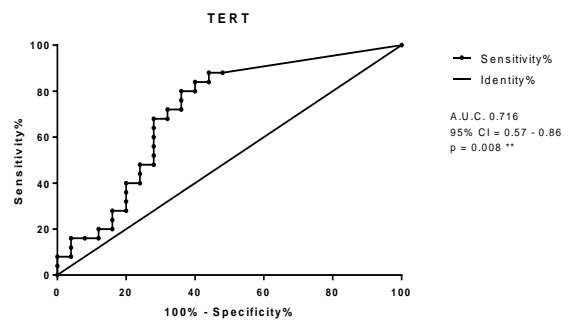


**Table 11.** Variation of TERT mRNA expression influenced by clinical-pathological features.

	<b>N</b>	<b>R</b>	<b>SEM</b>	<b>p-value</b>
<b>HCC TOTAL CASES</b>	23	11.34	3.38	0.005 **
<b>HCC without STEATOSIS</b>	11	15.35	6.35	0.04 *
<b>HCC without CHRONIC HEPATITIS</b>	11	15.35	6.15	0.04 *
<b>HCC with CIRRHOSIS</b>	12	14.54	5.6	0.03 *
<b>HCC with ENDOVASCULAR INFILTRATION</b>	9	14.56	4.74	0.02 *

**Fig. 23. Tissue expression of TERT mRNA.** A) TERT Fold-change. Histograms represent R-values and bars upper and lower limits. Histograms are ordered by increasing R-values. The corresponding case are listed below. Upper and lower dot lines define the range of gene expression variation. B) TERT relative quantification mean comparison between PT and HCC. Wilcoxon paired two-tailed t-test. C) Normal distribution of the R-values. The normal distribution of the total cases analyzed underpins the grey area under the curve. The black lines refer to the background disease. Outliers (cases 370 and 372) were removed. Table 11: Student t-test of the mean. \* $p < 0.05$ , \*\* $p < 0.01$ . D) ROC curve analysis to discriminate HCC from normal tissue. AUC: Area Under the ROC Curve. CI: Confidence Interval.

#### **4.8 The analysis of plasma of untreated HCC patients reveal a dysregulated amount of the transcripts GAS5, miR-126-3p and TERRA**

As damaged liver and tumor microenvironment release intracellular components into circulation and dysregulation of ncRNAs has been observed in *in vitro* and in HCC tissues, circulating levels of GAS5, miR-126-3p and TERRA were also investigated in plasma of untreated HCC patients and healthy individuals.

ROC curve analysis were generated and analyzed for all targets, to inquire the capability of GAS5, miR-126-3p and TERRA to act as tools to successful distinguish HCC from healthy subjects.

Circulating GAS5 levels were significantly lower in plasma of untreated HCC patients compared to healthy individuals (Fig. 24A).

On the other hand circulating miR-126-3p levels were significantly higher in plasma of untreated HCC patients compared to healthy subjects (Fig. 24C).

Finally, circulating TERRA amounts were significantly higher in plasma of untreated HCC patients compared to healthy subjects (Fig. 25A, B and C).

As shown by ROC curve (Fig. 24B, 24D and 25D) analysis, each ncRNA has an excellent diagnostic power. In particular logistic regression model of TERRA classifiers evidenced the significant combinational use of TERRA targets (Fig. 25D and Table 11).

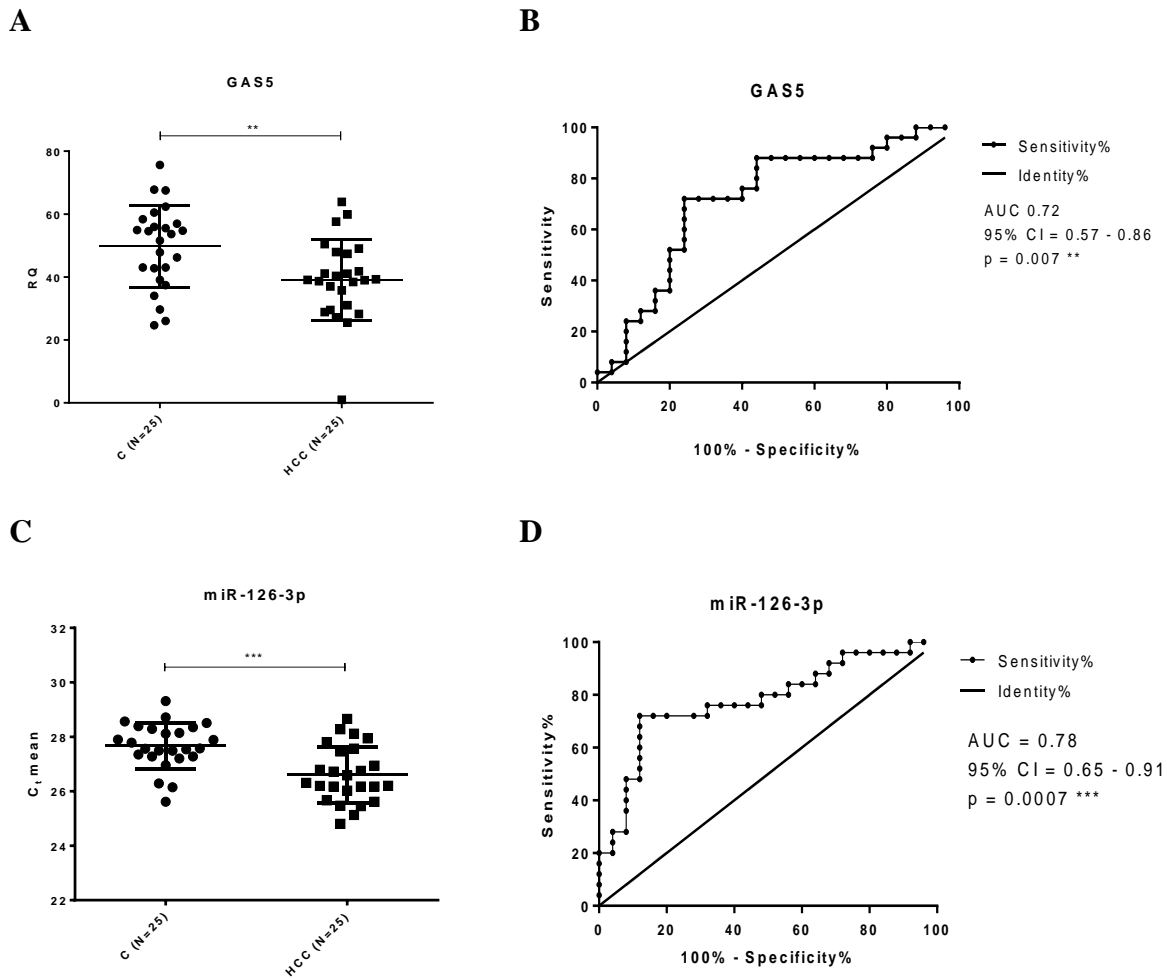


**Fig. 24. Plasma levels of GAS5 and miR-126-3p.** A) GAS5 levels in terms of relative quantification (RQ) in plasma of healthy (C) and HCC individuals. Mann-Whitney U-test. B) ROC curve analysis of GAS5 to discriminate HCC from healthy individuals. C) miR-126-3p levels in terms of  $C_t$  in plasma of healthy (C) and HCC individuals. Unpaired two-tailed t-test. D) ROC curve analysis of miR-126-3p to discriminate HCC from healthy individuals. \* $p < 0.05$ , \*\* $p < 0.01$ , \*\*\* $p < 0.001$ .



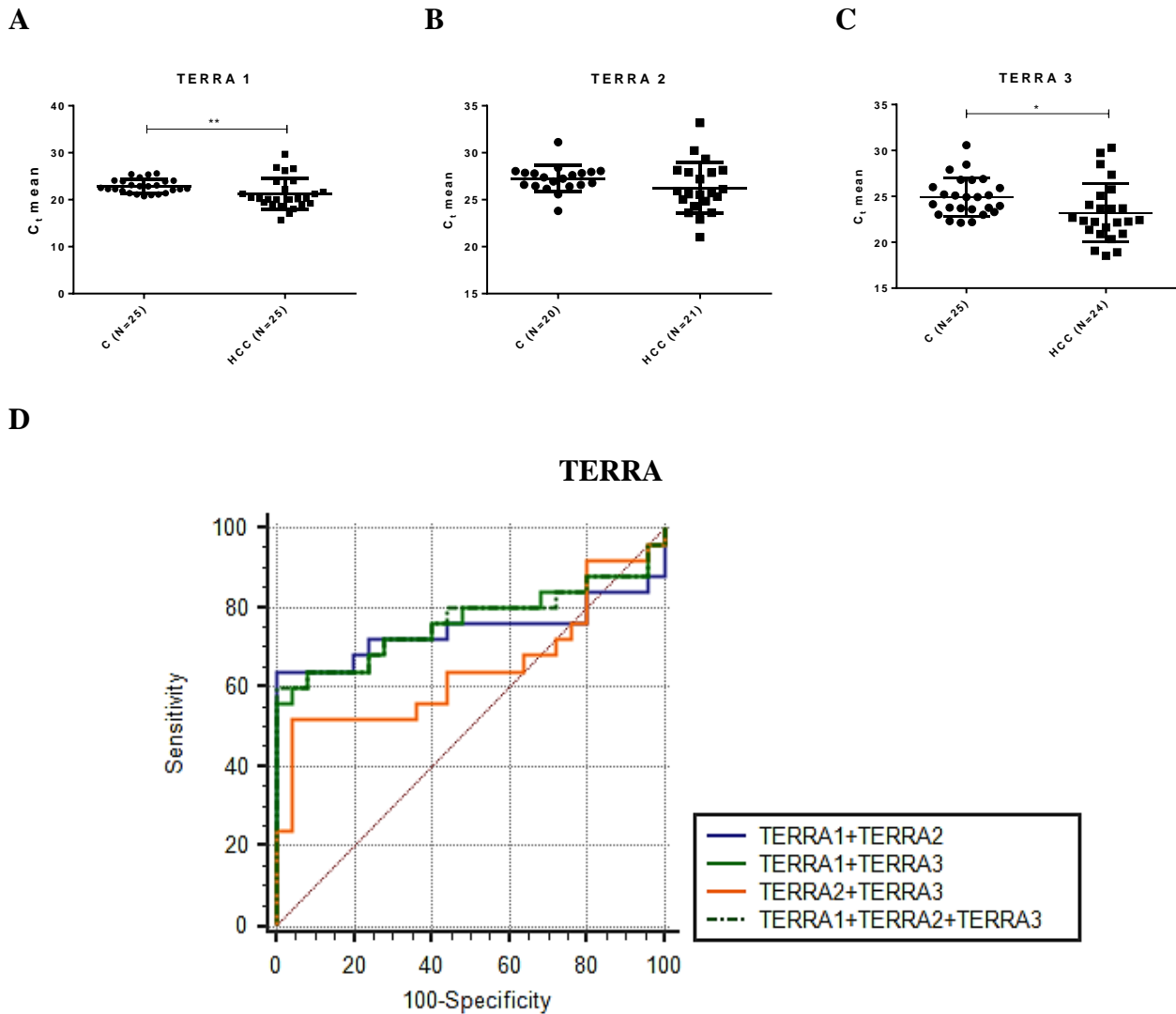


**Table 12.** Diagnostic performance of circulating TERRA in plasma.

TARGET	Sensitivity	Specificity	AUC	SE	95% CI	p-value
TERRA1	60%	100%	0.747	0.079	0.604 to 0.859	0.001 **
TERRA2	52%	92%	0.622	0.084	0.474 to 0.756	0.146
TERRA3	56%	88%	0.686	0.08	0.540 to 0.810	0.02 *
TERRA1+TERRA2	64%	100%	0.742	0.081	0.599 to 0.856	0.002**
TERRA1+TERRA3	64%	92%	0.763	0.074	0.622 to 0,872	0.0004 ***
TERRA2+TERRA3	52%	96%	0.648	0.083	0.500 to 0.778	0.07
TERRA1+TERRA2+TERRA3	60%	100%	0.765	0.074	0.624 to 0.873	0.0004 ***

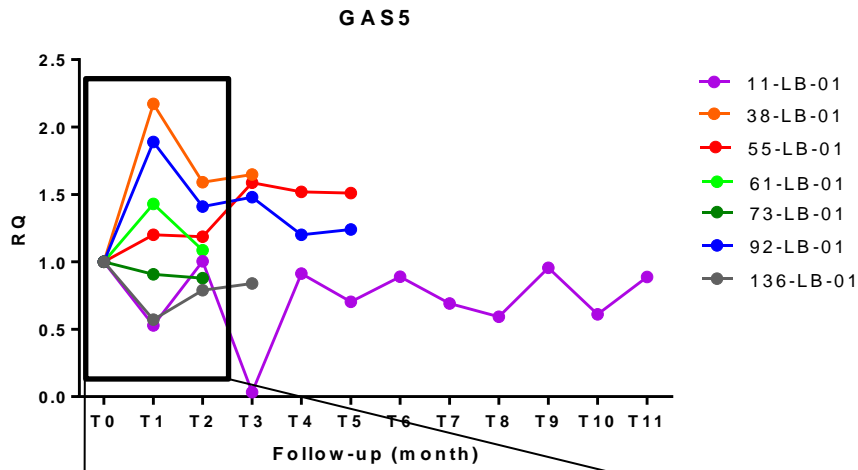
**Fig. 25. Plasma levels of TERRA.** A), B), C) TERRA levels in terms of  $C_t$  in plasma of healthy (C) and HCC individuals. Parametric unpaired two-tailed t-test. D) ROC curve analysis of TERRA to discriminate HCC from healthy individuals. \* $p < 0.05$ , \*\* $p < 0.01$ , \*\*\* $p < 0.001$ .

#### **4.9 Study of GAS5, miR-126-3p as circulating transcripts in HCC patients treated with sorafenib**

Since the treatment with sorafenib may impair intra- and extracellular levels of GAS5 and miR-126-3p in HCC cells, plasma GAS5 and miR-126-3p amounts could also be influenced by sorafenib treatment in HCC patients. Therefore the longitudinal changes of GAS5 and miR-126-3p levels were analyzed in plasma of 7 HCC patients during the follow-up. Plasma were collected before the beginning ( $T_0$ ) and once *per* month during therapy ( $T_n$ ), as described in “Materials and Methods”.

As shown in Fig. 26A and Fig. 27A, dynamic variations of the levels of GAS5 and miR-126-3p were observed during the follow-up of the patients and also at relatively long periods of time (i.e. case 11-LB-01). In particular the attention was focused on the early events of follow-up ( $T_0$ ,  $T_1$ ,  $T_2$ ), as they are shared and available for all patients. As shown in Fig. 26B, four of seven patients (55-LB-01, 61-LB-01, 38-LB-01, 92-LB-01) showed an increase of the level of plasma GAS5 after the first month of treatment with sorafenib ( $T_1$ ) when compared to the basal condition ( $T_0$ ). On the contrary, as reported in Fig. 27B, four of seven patients (11-LB-01, 73-LB-01, 92-LB-01, 136-LB-01) showed a decrease of the amount of miR-126-3p in the plasma after the first month of treatment with sorafenib ( $T_1$ ) when compared to the basal condition ( $T_0$ ).

A



B

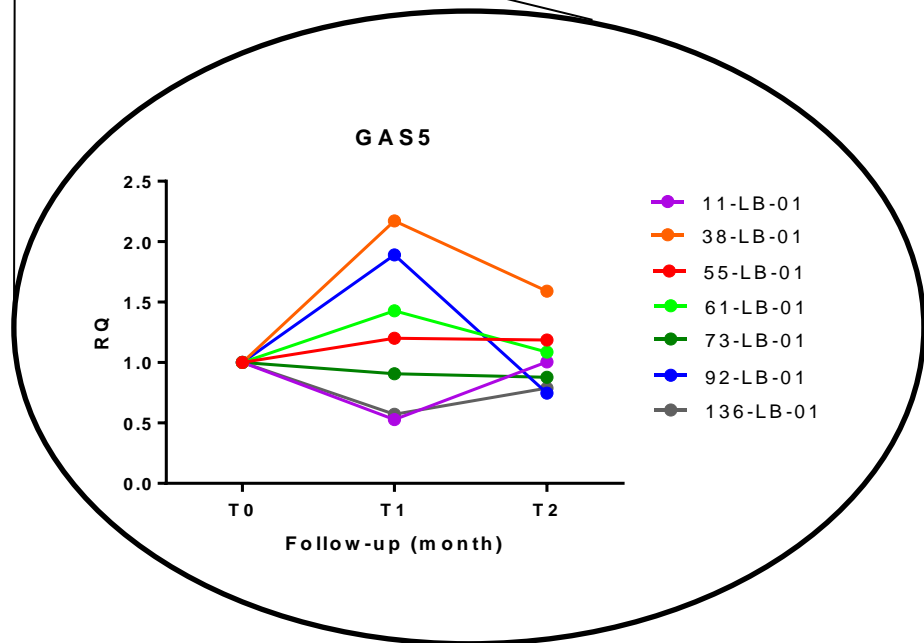
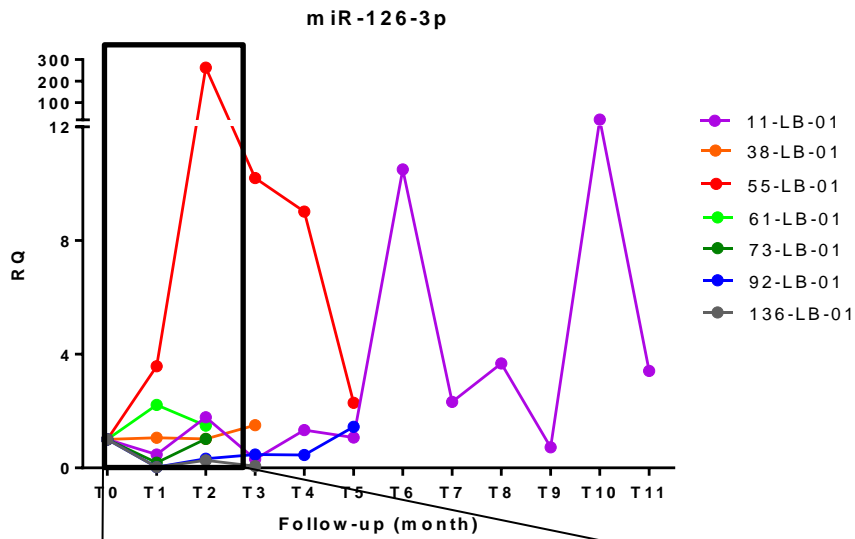


**Fig. 26. Dynamic changes of GAS5 levels in plasma of HCC patients treated with sorafenib.** A) plasma GAS5 levels of the HCC patients at different time-points after sorafenib administration. B) Focus on GAS5 early expression level variations after sorafenib administration. Tn indicates the sequential blood withdrawal point carried out every 1 month. RQ: relative quantification.

A



B

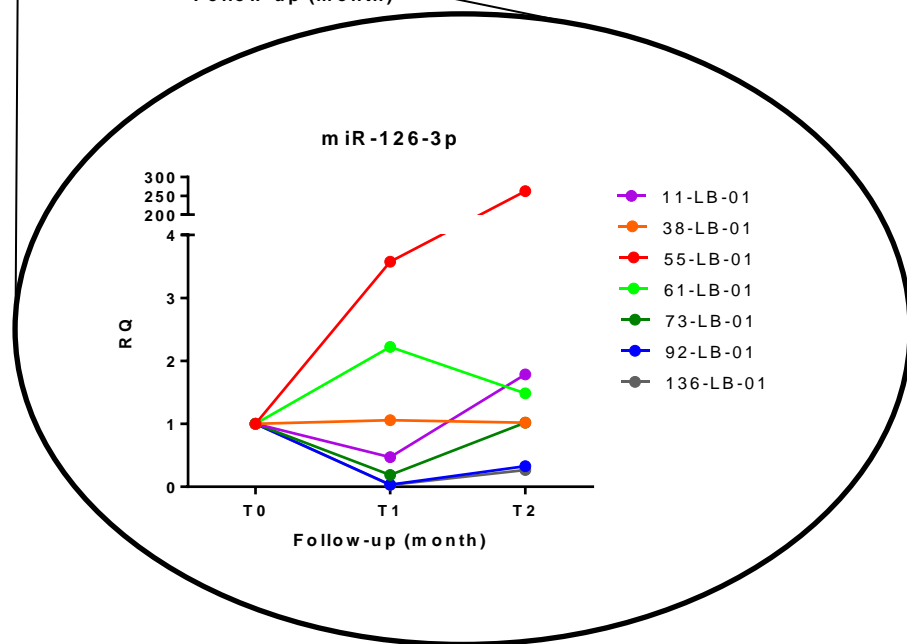


**Fig. 27. Dynamic changes of miR-126-3p levels in plasma of HCC patients treated with sorafenib.** A) plasma miR-126-3p levels of the HCC patients at different time-points after sorafenib administration. B) Focus on miR-126-3p early expression level variations after sorafenib administration. T<sub>n</sub> indicates the sequential blood withdrawal point carried out every 1 month. RQ: relative quantification.

## 5 DISCUSSION

In the past decade, the study of ncRNAs in human cancers has emerged as a new field of research. An increasing number of studies have shown that ncRNAs play an integral role in nearly every aspect of cancer biology. Circulating ncRNAs have been described in different human body fluids, as blood, serum/plasma, urine, and breast milk and are valuable cancer biomarkers for risk assessment, diagnosis, prognosis, and monitoring treatment response. Targeting ncRNAs has the potential to offer novel therapeutic opportunities for cancer treatment.

LncRNAs and miRNAs regulate gene expression at many different levels: at transcriptional, post-transcriptional and post-translational levels. Moreover, there is a cross-regulation between lncRNAs and microRNAs, bulking additional layers of complexity.

In recent years, a large number of studies have found that changes in the expression of ncRNAs have a pivotal role in the development and progression of HCC. In this context it is known that miR-23b-3p negatively co-regulates uPA and MET, and miR-193a-3p negatively regulates uPA in HCC cells. In particular the ectopic expression of miR-23b-3p or miR-193a-3p impaired malignant properties of HCC cells, inhibiting proliferation and increasing apoptosis. Furthermore it has been shown that the expression levels of miR-23b-3p and miR-193a-3p are significantly down-modulated in HCC biptic specimens compared to PT ones, thus contributing to the molecular characterization of HCC diagnosis and prognosis<sup>245,246</sup>.

The multitarget kinase inhibitors sorafenib and lenvatinib proved to significantly extend the median survival time of HCC patients, with lenvatinib non inferior to sorafenib. But, they often causes adverse side-effects and many patients develop a secondary resistance during treatment<sup>247,248</sup>. Recently the atezolizumab with bevacizumab combined immunotherapy resulted in better overall and progression-free survival outcomes than sorafenib in unresectable HCC<sup>249</sup>. However time for immunotherapy drug approval is long, depending on the regulatory agency of each country and on the cost of the treatment; thus sorafenib still represents an effective systemic monotherapy for HCC that can be currently used in several continents and countries. Since 2008, when sorafenib was approved as first line treatment of HCC, many studies have been developed to comprehend the underlying molecular mechanisms and to improve its efficacy; but even today in 2021 a further effort is still needed to identify markers of drug response, sensitivity or drug resistance.

Development of sorafenib resistance in HCC has been linked to aberrant proliferative signaling, evasion of apoptosis, replicative immortality, abnormal angiogenesis, invasion and metastasis potential. Therefore, in my research group we focused the attention on two pivot

hallmarks of cancer development, cell growth and immortality, to further explore novel candidate molecular biomarkers of diagnosis, response or resistance to sorafenib in HCC.

Previously, by RT<sup>2</sup> LncRNA PCR Array Human LncFinder and miScript miRNA PCR Array Human Liver miFinder the expression 84 different disease- or pathway- focused lncRNAs and miRNAs was explored in HA22T/VGH cells, treated and untreated with sorafenib. Among the most dysregulated ncRNAs, lncRNA GAS5 resulted the most upregulated and miR-126-3p was the most downmodulated. GAS5 and miR-126-3p dysregulation was subsequently validated in several HCC, RCC and breast cancer *in vitro* models<sup>240</sup>.

By luciferase reporter assay GAS5 ceRNA-function over miR-126-3p was demonstrated. On the other hand, siRNA-dependent transient silencing of GAS5 in HA22T/VGH after treatment with sorafenib induced a significant upregulation of miR-126-3p.

GAS5 functions as a tumor suppressor; it is downregulated in a variety of malignancies and its dysregulation inversely correlate with clinical-pathological characteristics and outcome<sup>171,172</sup>. Albeit two distinct subpopulations of HCC were observed in this study, GAS5 expression showed a trend of upregulation. These findings seem to be in contrast with current literature reports. However, as Tao *et al.* suggested, GAS5 expression could be correlated with rs145204276 (at 268bp upstream of GAS5 promoter). HCCs with del/del genotype show significantly higher GAS5 expression compared with HCCs with ins/del and ins/ins genotype<sup>250</sup>. Therefore it could merely be speculated that those HCC patients displaying an upregulation of GAS5 expression in the cohort of HCC patients here analyzed may be related to the presence of the above mentioned SNP. However further deep-sequencing analysis are needed to validate this hypothesis.

miR-126 may function as a tumor suppressor; it is downregulated in a variety of malignancies and its dysregulation inversely correlate with clinical-pathological characteristics and outcome<sup>187,193</sup>. miR-126-3p overexpression suppressed HCC cells proliferation, promotes apoptosis and inhibit tumor angiogenesis *in vitro*<sup>197</sup>. In this context, miR-126-3p ectopic expression decreased the growth capacity of HA22T/VGH cells, although miR-126-3p over-expression in sorafenib-treated HA22T/VGH did not further affect the inhibition of proliferation induced by sorafenib. It is challenging to reconcile the observation that miR-126-3p generally has tumor suppression functions with the observation that miR-126-3p expression levels further decreased in sorafenib sensitive ones after treatment and also in drug-resistant cells. It could only be speculated that miR-126-3p marginally contributes to a less aggressive phenotype, in terms of proliferation, of cancer cells after the treatment.

Consequently to better elucidate its dysregulation, miR-126-3p expression was analyzed in HCC and corresponding PT tissues. It resulted significantly downregulated in HCC vs PT, in

agreement with previously reported data in literature. The observation that 64% of HCCs with high GAS5 expression displayed a low miR-126-3p expression, indirectly supports the evidence of GAS5-ceRNA hypothesis towards miR-126-3p.

TERRA appeared to be upregulated in *in vitro* models of HCC, followed sorafenib treatment. This is not surprising as different stresses could induce TERRA transcription and upregulation. TERRA also appeared to be upregulated in HCC resistant cells. TERRA expression varies among cancer cells, based on the mechanism by which cells maintain the length of their telomeres<sup>243,251-253</sup>. TERRA levels have been shown to be consistently lower in cells that overexpress telomerase compared to cells that utilize the homologous recombination-based ALT mechanism<sup>146</sup>, which express higher levels of TERRA<sup>147</sup>. In this context TERRA may promote genomic instability at telomeres and allow ALT in resistant cells, rising a more aggressive phenotype. Additional work is needed to clarify whether TERRA is a cause or consequence of the ALT pathway.

Heterogeneous data are available regarding TERRA expression in different types of cancer tissues, consisting of different TERRA transcripts analyzed with different technologies. TERRA is dysregulated in ovarian primary and metastatic tumors, stomach, lung and colon<sup>161</sup>, glioblastoma multiforme, anaplastic astrocytoma, diffuse astrocytoma<sup>162</sup>, meningiomas and astrocytomas<sup>163</sup>, head and neck squamous cell carcinoma<sup>164</sup> and colorectal cancer (CRC)<sup>165</sup>. Cao *et al.* showed by FISH experiments that TERRA expression was significantly decreased in HCC tissues compared to the corresponding PT<sup>254</sup>. Here TERRA expression was analyzed in 25 HCC and their matching corresponding PT tissues by RT-qPCR. The attention was focused on TERRA molecules transcribed from 1q, 2q, 10q, 13q, 15q, Xp and Yp *loci* of several chromosomes as they best recapitulate global TERRA expression of the cell. Globally TERRA was significantly downregulated in HCC, compared to the PT and its variation in expression did not appeared related to any clinical-pathological characteristics. Only 24% of HCC cases in this study displayed an opposite trend between TERRA and TERT mRNA and TERC. It is known that short telomeres show relatively lower TERRA expression than long telomeres which exhibit higher TERRA expression. At the same time, telomerase activity is known to be at its greatest when telomeres are short and at its lowest activity when telomeres are long. ALT-positive tumors have also been associated with elevated TERRA levels<sup>74,138</sup>. Thus TERRA would act as a negative regulator of telomerase activity in HCC tissues which display long telomeres in favor of the ALT mechanism, while functioning as a positive regulator of telomerase activity in HCC tissues with short telomeres.

The ability of cancer cells to maintain telomeres above a critical length is an essential feature of malignancy. The role of telomerase in mediating unlimited replicative potential in cancer

has long been known<sup>138,255</sup>. Telomerase reactivation in HCC correlates with the upregulation of TERT mRNA and TERC. Observations on telomerase expression presented in this study are largely consistent with previous reports of the presence of telomerase activity in normal and tumor tissues. Even a little amount of TERC is sufficient to telomerase assemble. These data underlined that reactivation of telomerase is required as an earlier step in HCC carcinogenesis in order to bypass replicative senescence in cirrhotic hepatocytes. The increased expression of telomerase makes it an attractive target for intervention. TERT mRNA displayed a potentially sensitive ability to discriminate HCC from peritumoral tissue, thus acting as a good biomarker for screening, early cancer detection, or monitoring residual disease in HCC patients, even after surgical liver resection.

As it is well established, ncRNAs are poured into the extracellular environment both associated with AGO proteins and encapsulated in EVs. qNANO technology and spectroscopic analyses revealed that sensitive cells following sorafenib treatment released an increasing amount of EVs compared to untreated and resistant cells. On the other hand, EVs from HA22T/VGH-SR resistant cells consisted of populations of EVs with a significantly larger diameter compared to the those released from sensitive cells. EVs from sensitive cells treated with sorafenib showed a significant increase in miR-126-3p levels compared to the untreated cells ones. Also a significant increase in GAS5 abundance was observed both in the vesicle-free and in the EVs component compared to the untreated cells. The reason why GAS5 and miR-126-3p are released outside the cells is not yet known. Further investigation are needed to understand their biological role in the extracellular environment. Also TERRA molecules are released into the secretome. A high level of TERRA ncRNA was observed in both fractions, vesicle-free and EVs. Although TERRA is significantly highly released both in EV-free and EVs component of sensitive cells, once treated with sorafenib TERRA levels significantly drops. The reason why TERRA is released outside the cell could be explained by an “alarmin function” as a Damage-associated molecular patterns (DAMPs); when secreted in extracellular vesicles it could induce inflammatory cytokines activation in neighboring cells<sup>256</sup>. Collectively these results would indicate that sorafenib would influence the mechanisms of EVs biogenesis and release and also their RNA content.

*In vitro* results and data from HCC patients prompted to detect ncRNAs also in plasma of HCC patients. Only three previous works reported observations concerning miR-126-3p circulating levels. Gosh *et al.* showed increased miR-126-3p levels in plasma of HBV-positive/HCC patients compared to HBV-positive/non-HCC patients<sup>257</sup> in accordance with the results in the present work. In other two published reports, miR-126-3p circulating levels were measured in serum. Khairy *et al.* found a significant decrease of miR-126-3p in the serum of HCC patients compared to non-HCC group<sup>258</sup>. Ali *et al.* demonstrated that the median serum level of miR-126-3p was significantly



reduced in HCC patients compared to healthy controls<sup>259</sup>. In summary, miR-126-3p has been shown to be upregulated in plasma but downmodulated in serum of HCC patients. This should not be surprising, as differences in miRNAs levels between plasma and serum have been commonly described<sup>260</sup>. In the present work the levels of plasmatic circulating miR-126-3p were higher in HCC patients compared to healthy individuals and it has the potential to be used as a diagnostic discriminator as shown by receiver operating characteristic (ROC) curve analysis.

Very few data are available in literature regarding circulating plasmatic GAS5 in human malignancies. High GAS5 serum levels were associated with good prognosis in patients with glioblastoma<sup>261</sup>, while GAS5 levels were found to be decreased in serum<sup>261</sup> and in plasma<sup>262</sup> of CRC patients compared to healthy subjects. This is the first study in which plasma levels of GAS5 of untreated HCC patients and healthy individuals were compared. Significant lower levels of GAS5 were found in plasma of HCC patients in comparison to healthy individuals and the ROC analysis evidenced the potential ability of circulating GAS5 levels to discriminate HCC patients from healthy subjects.

Circulating TERRA has not been investigated so far. Wang *et al.* showed that TERRA RNA could be detected by RNA-Seq in plasma of healthy or cancer patients. The blood plasma was obtained from 2 healthy subjects and 19 cancer patients, consisting of 10 different cancers that include breast, prostate, colon, duct, kidney, liver, melanoma, ovarian, and stomach<sup>256</sup>. Here, this is the first evidence that extensively highlights TERRA circulating levels in plasma of HCC patients compared to healthy individuals. Significant high levels of TERRA were detected in plasma of HCC patients and the ROC analysis strongly suggest the potential ability of circulating TERRA, alone or in combination, to discriminate HCC patients from healthy individuals.

Despite the fact that ncRNAs expression in HCC cancer cells and tissues is dysregulated and different levels are released in the extracellular environment, there is no correlation between ncRNAs tissues expression and plasma levels. Another apparently contradictory result is the finding of circulating ncRNAs with an opposite regulation in the tumor. As Moshiri *et al.* suggested, the question that arise is whether the profile of circulating ncRNAs could reflect the presence of a cancer, even if they did not originate from tumor cells<sup>260</sup>. Indeed, it is known that systemic patho-physiologic processes can be influenced as well as affect the development of cancer. Thus, it seems likely that tumor-associated systemic processes may also affect the release of ncRNAs from non-tumor cells. Therefore, the release of ncRNAs that do not originate from cancer cells may be indirectly influenced by the presence of a tumor, and types and abundance of circulating ncRNAs may not correlate with cancer-specific tissue ncRNAs.

Finally as sorafenib may induce, directly or indirectly, variations in ncRNAs expression, circulating GAS5 and miR-126-3p were examined in liquid biopsies of HCC patients at longitudinal time points of follow-up treatment. Only Fayda *et al.* described a significant increase of plasma GAS5 levels in head and neck cancer patients, under currently chemotherapy treatments, respectively with partial response/progressive disease *versus* complete response patients<sup>263</sup>. Furthermore, the only available data concerning changes in plasma miR-126-3p in association to therapy comes from uveal melanoma (UM) and metastatic colorectal cancer (mCRC). Triozzi *et al.* described a decrease in miR-126-3p levels in UM patients treated with adjuvant dacarbazine and interferon- $\alpha$ -2b, but no association with outcome was observed<sup>264</sup>. Hansen *et al.* described an increase in miR-126-3p levels in non-responder patients compared to a decrease in responders, exploring the predictive value of plasma miR-126-3p in mCRC during first-line chemotherapy combined with bevacizumab<sup>265</sup>. A distinct variation for each patient was detectable during the whole follow-up, but also a common trend of variation of a specific ncRNA among the different patients treated with sorafenib focusing on the T<sub>1</sub>. The absence of constant levels, but conversely a general fluctuation during the follow-up may suggest the potential sensitiveness to the drug and/or to given clinical conditions of the patients acquired during treatment.

## **6. CONCLUSIONS AND FUTURE PERSPECTIVES**

Over the last decades efforts have been carried out to make sorafenib a more effective drug in the management of different solid tumors as well as to identify novel molecular biomarkers of response or resistance to the treatment. The identification of novel molecules for the characterization of diagnosis, of treatment response or resistance may improve the outcome of HCC patients. However harmonization of procedures are needed before translation to clinical practice to ensure comparable and reliable results.

Therefore, the data presented in the current work derived from the investigation of new aspects of the pathogenetic mechanisms of HCC are an original contribution to the molecular characterization of untreated HCC and of HCC following sorafenib treatment.

Finally, TERRA, GAS5 and miR-126-3p will be validated in future studies, enrolling a larger cohort of HCC patients and animal models of human HCC xenografts treated with sorafenib to validate their role in the response/resistance to sorafenib in HCC.

## 7. REFERENCES

1. Hanahan D, Weinberg RA. Hallmarks of cancer: the next generation. *Cell*. 2011;144(5):646-674.
2. Silvestris N, Ciliberto G, De Paoli P, et al. Liquid dynamic medicine and N-of-1 clinical trials: a change of perspective in oncology research. *J Exp Clin Cancer Res*. 2017;36(1):128.
3. Bray F, Ferlay J, Soerjomataram I, Siegel RL, Torre LA, Jemal A. Global cancer statistics 2018: GLOBOCAN estimates of incidence and mortality worldwide for 36 cancers in 185 countries. *CA Cancer J Clin*. 2018;68(6):394-424.
4. Li M, Gerber DA, Koruda M, O'Neil BH. Hepatocellular carcinoma associated with attenuated familial adenomatous polyposis: a case report and review of the literature. *Clin Colorectal Cancer*. 2012;11(1):77-81.
5. Dragani T. Risk of HCC: Genetic heterogeneity and complex genetics. *Journal of Hepatology*. 2010;52.
6. Willson JS, Godwin TD, Wiggins GA, Guilford PJ, McCall JL. Primary hepatocellular neoplasms in a MODY3 family with a novel HNF1A germline mutation. *J Hepatol*. 2013;59(4):904-907.
7. YANNICK BACQ EJ, CHARLES BALABAUD, EMMANUELLE JEANNOT, BEATRICE SCOTTO, SOPHIE BRANCHEREAU, CHRISTOPHE LAURENT, PASCAL BOURLIER, DANIELE PARIENTE, ANNE DE MURET MONIQUE FABRE, PAULETTE BIOULAC-SAGE and JESSICA ZUCMAN-ROSSI. Familial Liver Adenomatosis Associated With Hepatocyte Nuclear Factor 1-alfa-Inactivation. *GASTROENTEROLOGY* 2003.
8. Calderaro J, Labrune P, Morcrette G, et al. Molecular characterization of hepatocellular adenomas developed in patients with glycogen storage disease type I. *J Hepatol*. 2013;58(2):350-357.
9. Nahon P, Zucman-Rossi J. Single nucleotide polymorphisms and risk of hepatocellular carcinoma in cirrhosis. *J Hepatol*. 2012;57(3):663-674.
10. Clifford RJ, Zhang J, Meerzaman DM, et al. Genetic variations at loci involved in the immune response are risk factors for hepatocellular carcinoma. *Hepatology*. 2010;52(6):2034-2043.
11. Chan KY, Wong CM, Kwan JS, et al. Genome-wide association study of hepatocellular carcinoma in Southern Chinese patients with chronic hepatitis B virus infection. *PLoS One*. 2011;6(12):e28798.
12. Kumar V, Kato N, Urabe Y, et al. Genome-wide association study identifies a susceptibility locus for HCV-induced hepatocellular carcinoma. *Nat Genet*. 2011;43(5):455-458.
13. Jiang DK, Sun J, Cao G, et al. Genetic variants in STAT4 and HLA-DQ genes confer risk of hepatitis B virus-related hepatocellular carcinoma. *Nat Genet*. 2013;45(1):72-75.
14. Tarhuni A, Guyot E, Rufat P, et al. Impact of cytokine gene variants on the prediction and prognosis of hepatocellular carcinoma in patients with cirrhosis. *J Hepatol*. 2014;61(2):342-350.
15. Nahon P, Sutton A, Rufat P, et al. Myeloperoxidase and superoxide dismutase 2 polymorphisms comodule the risk of hepatocellular carcinoma and death in alcoholic cirrhosis. *Hepatology*. 2009;50(5):1484-1493.
16. Nahon P, Sutton A, Rufat P, et al. A variant in myeloperoxidase promoter hastens the emergence of hepatocellular carcinoma in patients with HCV-related cirrhosis. *J Hepatol*. 2012;56(2):426-432.
17. Nahon P, Sutton A, Rufat P, et al. Liver iron, HFE gene mutations, and hepatocellular carcinoma occurrence in patients with cirrhosis. *Gastroenterology*. 2008;134(1):102-110.
18. Long XD, Ma Y, Qu DY, et al. The polymorphism of XRCC3 codon 241 and AFB1-related hepatocellular carcinoma in Guangxi population, China. *Ann Epidemiol*. 2008;18(7):572-578.
19. Yuan JM, Lu SC, Van Den Berg D, et al. Genetic polymorphisms in the methylenetetrahydrofolate reductase and thymidylate synthase genes and risk of hepatocellular carcinoma. *Hepatology*. 2007;46(3):749-758.
20. Dharel N, Kato N, Muroyama R, et al. MDM2 promoter SNP309 is associated with the risk of hepatocellular carcinoma in patients with chronic hepatitis C. *Clin Cancer Res*. 2006;12(16):4867-4871.

21. Yoon YJ, Chang HY, Ahn SH, et al. MDM2 and p53 polymorphisms are associated with the development of hepatocellular carcinoma in patients with chronic hepatitis B virus infection. *Carcinogenesis*. 2008;29(6):1192-1196.
22. Abu Dayyeh BK, Yang M, Fuchs BC, et al. A functional polymorphism in the epidermal growth factor gene is associated with risk for hepatocellular carcinoma. *Gastroenterology*. 2011;141(1):141-149.
23. Wang B, Huang G, Wang D, et al. Null genotypes of GSTM1 and GSTT1 contribute to hepatocellular carcinoma risk: evidence from an updated meta-analysis. *J Hepatol*. 2010;53(3):508-518.
24. Trepo E, Nahon P, Bontempi G, et al. Association between the PNPLA3 (rs738409 C>G) variant and hepatocellular carcinoma: Evidence from a meta-analysis of individual participant data. *Hepatology*. 2014;59(6):2170-2177.
25. Miki D, Ochi H, Hayes CN, et al. Variation in the DEPDC5 locus is associated with progression to hepatocellular carcinoma in chronic hepatitis C virus carriers. *Nat Genet*. 2011;43(8):797-800.
26. Zhang H, Zhai Y, Hu Z, et al. Genome-wide association study identifies 1p36.22 as a new susceptibility locus for hepatocellular carcinoma in chronic hepatitis B virus carriers. *Nat Genet*. 2010;42(9):755-758.
27. Dhanasekaran R, Bandoh S, Roberts LR. Molecular pathogenesis of hepatocellular carcinoma and impact of therapeutic advances. *F1000Res*. 2016;5.
28. Nalesnik MA. Aspects of Hepatocellular Tumor Pathology. In: *Hepatocellular Carcinoma*. 2016:305-329.
29. Collinsworth AL. Histologic Classification of Hepatocellular Carcinoma and Its Clinical Implications. In: *Precision Molecular Pathology of Liver Cancer*. 2018:17-32.
30. Zucman-Rossi J, Villanueva A, Nault JC, Llovet JM. Genetic Landscape and Biomarkers of Hepatocellular Carcinoma. *Gastroenterology*. 2015;149(5):1226-1239 e1224.
31. Paradis V. Histopathology of hepatocellular carcinoma. *Recent Results Cancer Res*. 2013;190:21-32.
32. Luft FC. The end is nigh. *J Mol Med (Berl)*. 2010;88(8):741-743.
33. E.H. Blackburn ESE, J. Lin. Human telomere biology: a contributory and interactive factor in aging, disease risks, and protection. *Science*. 2015;350:1193–1198.
34. McElligott R WR. The terminal DNA structure of mammalian chromosomes. *EMBO J*. 1997;16:705–3714.
35. Robin C.Allshire MDaNDH. Human telomeres contain at least three types of G-rich repeat distributed non-randomly. *Nucleic Acids Research*. 1989;17:4611–4627.
36. Baird DM, Jeffreys, A. J. & Royle, N. J. Mechanisms underlying telomere repeat turnover, revealed by hypervariable variant repeat distribution patterns in the human Xp/Yp telomere. *EMBO J*. 1995;14:5433–5443.
37. Griffith JD CL, Rosenfield S, Stansel RM, Bianchi A, Moss H, T de Lange. Mammalian Telomeres End in a Large Duplex Loop. *Cell*. 1999;97:503–514.
38. Greider CW BE. Identification of a specific telomere terminal transferase activity in tetrahymena extracts. *Cell*. 1985;43:405–413.
39. Podlevsky JD, Chen JJ. It all comes together at the ends: telomerase structure, function, and biogenesis. *Mutat Res*. 2012;730(1-2):3-11.
40. Sandin S, Rhodes D. Telomerase structure. *Curr Opin Struct Biol*. 2014;25:104-110.
41. Jacobs SA, Podell ER, Cech TR. Crystal structure of the essential N-terminal domain of telomerase reverse transcriptase. *Nat Struct Mol Biol*. 2006;13(3):218-225.
42. Lue NF, Lin YC, Mian IS. A conserved telomerase motif within the catalytic domain of telomerase reverse transcriptase is specifically required for repeat addition processivity. *Mol Cell Biol*. 2003;23(23):8440-8449.
43. Zhang Q, Kim NK, Feigon J. Architecture of human telomerase RNA. *Proc Natl Acad Sci U S A*. 2011;108(51):20325-20332.
44. Cech JCSaTR. Human telomerase: biogenesis, trafficking, recruitment, and activation. *Genes Dev*. 2015;29:1095–1105.

45. A.S. Venteicher EBA, Z. Meng, K.E. McCann, R.M. Terns, T.D. Veenstra, M.P. Terns, S.E. Artandi. A Human Telomerase Holoenzyme Protein Required for Cajal Body Localization and Telomere Synthesis. *Science*. 2009;323:644-648.
46. O'Sullivan RJ, Karlseder J. Telomeres: protecting chromosomes against genome instability. *Nat Rev Mol Cell Biol*. 2010;11(3):171-181.
47. Agnel Sfeir TdL. Removal of Shelterin Reveals the Telomere End-Protection Problem. *Science*. 2012;336:593-597.
48. Titia dL. How Telomeres Solve the End-Protection Problem. *Science*. 2009;326:948-952.
49. Martinez P, Blasco MA. Telomeric and extra-telomeric roles for telomerase and the telomere-binding proteins. *Nat Rev Cancer*. 2011;11(3):161-176.
50. Blasco MA. Telomeres and human disease: ageing, cancer and beyond. *Nat Rev Genet*. 2005;6(8):611-622.
51. Xu L, Li S, Stohr BA. The role of telomere biology in cancer. *Annu Rev Pathol*. 2013;8:49-78.
52. Arnoult N, Karlseder J. Complex interactions between the DNA-damage response and mammalian telomeres. *Nat Struct Mol Biol*. 2015;22(11):859-866.
53. Sexton AN, Regalado SG, Lai CS, et al. Genetic and molecular identification of three human TPP1 functions in telomerase action: recruitment, activation, and homeostasis set point regulation. *Genes Dev*. 2014;28(17):1885-1899.
54. Wang F, Podell ER, Zaug AJ, et al. The POT1-TPP1 telomere complex is a telomerase processivity factor. *Nature*. 2007;445(7127):506-510.
55. Uringa EJ, Youds JL, Lisaingo K, Lansdorp PM, Boulton SJ. RTEL1: an essential helicase for telomere maintenance and the regulation of homologous recombination. *Nucleic Acids Res*. 2011;39(5):1647-1655.
56. Sarek G, Vannier JB, Panier S, Petrini JHJ, Boulton SJ. TRF2 recruits RTEL1 to telomeres in S phase to promote t-loop unwinding. *Mol Cell*. 2015;57(4):622-635.
57. Nandakumar J, Cech TR. Finding the end: recruitment of telomerase to telomeres. *Nat Rev Mol Cell Biol*. 2013;14(2):69-82.
58. Moye AL, Porter KC, Cohen SB, et al. Telomeric G-quadruplexes are a substrate and site of localization for human telomerase. *Nat Commun*. 2015;6:7643.
59. Armanios M, Blackburn EH. The telomere syndromes. *Nat Rev Genet*. 2012;13(10):693-704.
60. JD W. Origin of concatemeric T7 DNA. *Nat New Biol*. 1972;239:197-201.
61. Autexier C, Lue NF. The Structure and Function of Telomerase Reverse Transcriptase. *Annual Review of Biochemistry*. 2006;75(1):493-517.
62. Yun Peng ISM, Neal FLue. Analysis of Telomerase Processivity: Mechanistic Similarity to HIV-1 Reverse Transcriptase and Role in Telomere Maintenance. *Molecular Cell*. 2001;7:1201-1211.
63. AM. O. theory of marginotomy. The incomplete copying of template margin in enzymic synthesis of polynucleotides and biological significance of the phenomenon. *J Theor Biol*. 1973;41:181-190.
64. Hayflick L. The limited in vitro lifetime of human diploid cell strains. *Exp Cell Res*. 1965;37:614-636.
65. Stefan Czvitkovich SS, Antoine H.F.M Peters, Evi Deiner, Andrea Wolf, Götz Laible, Susanne Opravil, Hartmut Beug, Thomas Jenuwein. Over-expression of the SUV39H1 histone methyltransferase induces altered proliferation and differentiation in transgenic mice. *Mechanisms of Development*. 2001;107:141-153.
66. Shay JW, Wright WE. Senescence and immortalization: role of telomeres and telomerase. *Carcinogenesis*. 2005;26(5):867-874.
67. Kim NW, Piatyszek MA, Prowse KR, et al. Specific association of human telomerase activity with immortal cells and cancer. *Science*. 1994;266(5193):2011-2015.
68. Kathryn Ann Kolquist LWE, Chistopher M. Counter, Matthew Meyerson, Lee K. Tan, Robert A. Weinberg, Daniel A. Haber & William L. Gerald. Expression of TERT in early premalignant lesions and a subset of cells in normal tissues. *Nat Genet*. 1998;19.
69. Bryan TM EA, Gupta J, Bacchetti S, Reddel RR. Telomere elongation in immortal human cells without detectable telomerase activity. *EMBO J*. 1997;14:4240-4248.

70. Cesare AJ, Reddel RR. Alternative lengthening of telomeres: models, mechanisms and implications. *Nat Rev Genet.* 2010;11(5):319-330.
71. Sharma S, Hicks JK, Chute CL, et al. REV1 and polymerase zeta facilitate homologous recombination repair. *Nucleic Acids Res.* 2012;40(2):682-691.
72. Maloisel L, Fabre F, Gangloff S. DNA polymerase delta is preferentially recruited during homologous recombination to promote heteroduplex DNA extension. *Mol Cell Biol.* 2008;28(4):1373-1382.
73. Heaphy CM, de Wilde RF, Jiao Y, et al. Altered telomeres in tumors with ATRX and DAXX mutations. *Science.* 2011;333(6041):425.
74. Lovejoy CA, Li W, Reisenweber S, et al. Loss of ATRX, genome instability, and an altered DNA damage response are hallmarks of the alternative lengthening of telomeres pathway. *PLoS Genet.* 2012;8(7):e1002772.
75. Lee M, Hills M, Conomos D, et al. Telomere extension by telomerase and ALT generates variant repeats by mechanistically distinct processes. *Nucleic Acids Res.* 2014;42(3):1733-1746.
76. Law MJ, Lower KM, Voon HP, et al. ATR-X syndrome protein targets tandem repeats and influences allele-specific expression in a size-dependent manner. *Cell.* 2010;143(3):367-378.
77. Clynes D, Jelinska C, Xella B, et al. Suppression of the alternative lengthening of telomere pathway by the chromatin remodelling factor ATRX. *Nat Commun.* 2015;6:7538.
78. Garcia-Cao M, O'Sullivan R, Peters AH, Jenuwein T, Blasco MA. Epigenetic regulation of telomere length in mammalian cells by the Suv39h1 and Suv39h2 histone methyltransferases. *Nat Genet.* 2004;36(1):94-99.
79. A H Peters DOC, H Scherthan, K Mechtler, S Sauer, C Schöfer, K Weipoltshammer, M Pagani, M Lachner, A Kohlmaier, S Opravil, M Doyle, M Sibilia, T Jenuwein. Loss of the Suv39h histone methyltransferases impairs mammalian heterochromatin and genome stability. *Cell.* 2001;37:323-337.
80. Azzalin CM, Reichenbach P, Khoriant L, Giulotto E, Lingner J. Telomeric repeat containing RNA and RNA surveillance factors at mammalian chromosome ends. *Science.* 2007;318(5851):798-801.
81. Schoeftner S, Blasco MA. Developmentally regulated transcription of mammalian telomeres by DNA-dependent RNA polymerase II. *Nat Cell Biol.* 2008;10(2):228-236.
82. Nault JC, Zucman-Rossi J. TERT promoter mutations in primary liver tumors. *Clin Res Hepatol Gastroenterol.* 2016;40(1):9-14.
83. Sung WK, Zheng H, Li S, et al. Genome-wide survey of recurrent HBV integration in hepatocellular carcinoma. *Nat Genet.* 2012;44(7):765-769.
84. Paterlini-Brechot P, Saigo K, Murakami Y, et al. Hepatitis B virus-related insertional mutagenesis occurs frequently in human liver cancers and recurrently targets human telomerase gene. *Oncogene.* 2003;22(25):3911-3916.
85. Zapatka M, Borozan I, Brewer DS, et al. The landscape of viral associations in human cancers. *Nat Genet.* 2020;52(3):320-330.
86. Nault JC, Mallet M, Pilati C, et al. High frequency of telomerase reverse-transcriptase promoter somatic mutations in hepatocellular carcinoma and preneoplastic lesions. *Nat Commun.* 2013;4:2218.
87. Hidetoshi Tahara TN, Mikiya Kitamoto, Ryo Nakashio, Jerry W. Shay, Elichi Tahara, Goro Kajiyama, and Toshinori Ide. Telomerase Activity in Human Liver Tissues: Comparison between Chronic Liver Disease and Hepatocellular Carcinomas. *Cancer Research.* 1995;55:2734-2736.
88. Totoki Y, Tatsuno K, Covington KR, et al. Trans-ancestry mutational landscape of hepatocellular carcinoma genomes. *Nat Genet.* 2014;46(12):1267-1273.
89. Schulze K, Imbeaud S, Letouze E, et al. Exome sequencing of hepatocellular carcinomas identifies new mutational signatures and potential therapeutic targets. *Nat Genet.* 2015;47(5):505-511.
90. Li Y, Roberts ND, Wala JA, et al. Patterns of somatic structural variation in human cancer genomes. *Nature.* 2020;578(7793):112-121.
91. Guichard C, Amaddeo G, Imbeaud S, et al. Integrated analysis of somatic mutations and focal copy-number changes identifies key genes and pathways in hepatocellular carcinoma. *Nat Genet.* 2012;44(6):694-698.

92. I. C. Hsu RAM, T. Sun, J. A. Welsh, N. J. Wang & C. C. Harris Mutational hot spot in the p53 gene in human hepatocellular carcinomas. 1991.
93. Ahn SM, Jang SJ, Shim JH, et al. Genomic portrait of resectable hepatocellular carcinomas: implications of RB1 and FGF19 aberrations for patient stratification. *Hepatology*. 2014;60(6):1972-1982.
94. Alix de La Coste BR, Pierre Billuart, Claire-Angélique Renard, Marie-Annick Buendia, Olivier Soubrane, Monique Fabre, Jamel Chelly, Cherif Beldjord, Axel Kahn, and Christine Perret. Somatic mutations of the  $\beta$ -catenin gene are frequent in mouse and human hepatocellular carcinomas. *Proc Natl Acad Sci USA (PNAS)*. 1998.
95. S Satoh YD, Y Furukawa, T Kato, N Miwa, T Nishiwaki, T Kawasoe, H Ishiguro, M Fujita, T Tokino, Y Sasaki, S Imaoka, M Murata, T Shimano, Y Yamaoka, Y Nakamura. AXIN1 Mutations in Hepatocellular Carcinomas, and Growth Suppression in Cancer Cells by Virus-Mediated Transfer of AXIN1. *Nat Genetics*. 2000.
96. Sawey ET, Chanrion M, Cai C, et al. Identification of a therapeutic strategy targeting amplified FGF19 in liver cancer by Oncogenomic screening. *Cancer Cell*. 2011;19(3):347-358.
97. Chiang DY, Villanueva A, Hoshida Y, et al. Focal gains of VEGFA and molecular classification of hepatocellular carcinoma. *Cancer Res*. 2008;68(16):6779-6788.
98. Villanueva A, Chiang DY, Newell P, et al. Pivotal role of mTOR signaling in hepatocellular carcinoma. *Gastroenterology*. 2008;135(6):1972-1983, 1983 e1971-1911.
99. Whittaker S, Marais R, Zhu AX. The role of signaling pathways in the development and treatment of hepatocellular carcinoma. *Oncogene*. 2010;29(36):4989-5005.
100. Sporn MB, Liby KT. NRF2 and cancer: the good, the bad and the importance of context. *Nat Rev Cancer*. 2012;12(8):564-571.
101. Li M, Zhao H, Zhang X, et al. Inactivating mutations of the chromatin remodeling gene ARID2 in hepatocellular carcinoma. *Nat Genet*. 2011;43(9):828-829.
102. Boyault S, Rickman DS, de Reynies A, et al. Transcriptome classification of HCC is related to gene alterations and to new therapeutic targets. *Hepatology*. 2007;45(1):42-52.
103. Lee JS, Heo J, Libbrecht L, et al. A novel prognostic subtype of human hepatocellular carcinoma derived from hepatic progenitor cells. *Nat Med*. 2006;12(4):410-416.
104. Lee JS, Chu IS, Heo J, et al. Classification and prediction of survival in hepatocellular carcinoma by gene expression profiling. *Hepatology*. 2004;40(3):667-676.
105. Hoshida Y, Nijman SM, Kobayashi M, et al. Integrative transcriptome analysis reveals common molecular subclasses of human hepatocellular carcinoma. *Cancer Res*. 2009;69(18):7385-7392.
106. Lachenmayer A, Alsinet C, Savic R, et al. Wnt-pathway activation in two molecular classes of hepatocellular carcinoma and experimental modulation by sorafenib. *Clin Cancer Res*. 2012;18(18):4997-5007.
107. Liver. EAftSot. EASL Clinical Practice Guidelines: Management of hepatocellular carcinoma. *J Hepatol*. 2018;69(1):182-236.
108. Forner A, Reig M, Bruix J. Hepatocellular carcinoma. *The Lancet*. 2018;391(10127):1301-1314.
109. Llovet JM, Zucman-Rossi J, Pikarsky E, et al. Hepatocellular carcinoma. *Nat Rev Dis Primers*. 2016;2:16018.
110. Cervello M, Bachvarov D, Lampiasi N, et al. Molecular mechanisms of sorafenib action in liver cancer cells. *Cell Cycle*. 2012;11(15):2843-2855.
111. Abeni E, Salvi A, Marchina E, Traversa M, Arici B, De Petro G. Sorafenib induces variations of the DNA methylome in HA22T/VGH human hepatocellular carcinoma-derived cells. *Int J Oncol*. 2017;51(1):128-144.
112. Kanthaje S, Makol A, Chakraborti A. Sorafenib response in hepatocellular carcinoma: MicroRNAs as tuning forks. *Hepatol Res*. 2018;48(1):5-14.
113. Keating GM. Sorafenib: A Review in Hepatocellular Carcinoma. *Target Oncol*. 2017;12(2):243-253.
114. Gauthier A, Ho M. Role of sorafenib in the treatment of advanced hepatocellular carcinoma: An update. *Hepatol Res*. 2013;43(2):147-154.



115. Wilhelm SM, Adnane L, Newell P, Villanueva A, Llovet JM, Lynch M. Preclinical overview of sorafenib, a multikinase inhibitor that targets both Raf and VEGF and PDGF receptor tyrosine kinase signaling. *Mol Cancer Ther.* 2008;7(10):3129-3140.
116. Vogel A, Cervantes A, Chau I, et al. Hepatocellular carcinoma: ESMO Clinical Practice Guidelines for diagnosis, treatment and follow-up. *Ann Oncol.* 2018;29(Suppl 4):iv238-iv255.
117. Nagore E, Insa A, Sanmartin O. Antineoplastic therapy-induced palmar plantar erythrodysesthesia ('hand-foot') syndrome. Incidence, recognition and management. *Am J Clin Dermatol.* 2000;1(4):225-234.
118. Zhu YJ, Zheng B, Wang HY, Chen L. New knowledge of the mechanisms of sorafenib resistance in liver cancer. *Acta Pharmacol Sin.* 2017;38(5):614-622.
119. Chi KR. The dark side of the human genome. *Nature.* 2016;538(7624):275-277.
120. Hombach S, Kretz M. Non-coding RNAs: Classification, Biology and Functioning. *Adv Exp Med Biol.* 2016;937:3-17.
121. Tordonato C, Di Fiore PP, Nicassio F. The role of non-coding RNAs in the regulation of stem cells and progenitors in the normal mammary gland and in breast tumors. *Front Genet.* 2015;6:72.
122. Silva A, Bullock M, Calin G. The Clinical Relevance of Long Non-Coding RNAs in Cancer. *Cancers (Basel).* 2015;7(4):2169-2182.
123. Hahne JC, Valeri N. Non-Coding RNAs and Resistance to Anticancer Drugs in Gastrointestinal Tumors. *Front Oncol.* 2018;8:226.
124. Sohel MH. Extracellular/Circulating MicroRNAs: Release Mechanisms, Functions and Challenges. *Achievements in the Life Sciences.* 2016;10:175-186.
125. Quinn JJ, Chang HY. Unique features of long non-coding RNA biogenesis and function. *Nat Rev Genet.* 2016;17(1):47-62.
126. Carlevaro-Fita J, Lanzos A, Feuerbach L, et al. Cancer lncRNA Census reveals evidence for deep functional conservation of long noncoding RNAs in tumorigenesis. *Commun Biol.* 2020;3(1):56.
127. Bar C, Chatterjee S, Thum T. Long Noncoding RNAs in Cardiovascular Pathology, Diagnosis, and Therapy. *Circulation.* 2016;134(19):1484-1499.
128. Wang KC, Chang HY. Molecular mechanisms of long noncoding RNAs. *Mol Cell.* 2011;43(6):904-914.
129. Chiu HS, Somvanshi S, Patel E, et al. Pan-Cancer Analysis of lncRNA Regulation Supports Their Targeting of Cancer Genes in Each Tumor Context. *Cell Rep.* 2018;23(1):297-312 e212.
130. Bolha L, Ravnik-Glavac M, Glavac D. Long Noncoding RNAs as Biomarkers in Cancer. *Dis Markers.* 2017;2017:7243968.
131. Yang Y, Chen L, Gu J, et al. Recurrently deregulated lncRNAs in hepatocellular carcinoma. *Nat Commun.* 2017;8:14421.
132. Porro A, Feuerhahn S, Delafontaine J, Riethman H, Rougemont J, Lingner J. Functional characterization of the TERRA transcriptome at damaged telomeres. *Nat Commun.* 2014;5:5379.
133. Nergadze SG, Farnung BO, Wischnewski H, et al. CpG-island promoters drive transcription of human telomeres. *RNA.* 2009;15(12):2186-2194.
134. Farnung BO, Brun CM, Arora R, Lorenzi LE, Azzalin CM. Telomerase efficiently elongates highly transcribing telomeres in human cancer cells. *PLoS One.* 2012;7(4):e35714.
135. Arnoult N, Van Beneden A, Decottignies A. Telomere length regulates TERRA levels through increased trimethylation of telomeric H3K9 and HP1alpha. *Nat Struct Mol Biol.* 2012;19(9):948-956.
136. Deng Z, Wang Z, Stong N, et al. A role for CTCF and cohesin in subtelomere chromatin organization, TERRA transcription, and telomere end protection. *EMBO J.* 2012;31(21):4165-4178.
137. Julianne Meyne RJB, Holly H, Hobart, T. C. Hsu, Oliver A, Ryder, Oscar G, Ward, John E, Wiley, Doris H, Wurster-Hill, Terry L, Yates & Robert K. Moyzis Distribution of non-telomeric sites of the (TTAGGG)<sub>n</sub> telomeric sequence in vertebrate chromosomes. *Chromosoma.* 1990;99:3-10.
138. Sieverling L, Hong C, Koser SD, et al. Genomic footprints of activated telomere maintenance mechanisms in cancer. *Nat Commun.* 2020;11(1):733.
139. Schoeftner S, Blasco MA. Chromatin regulation and non-coding RNAs at mammalian telomeres. *Semin Cell Dev Biol.* 2010;21(2):186-193.

140. Porro A, Feuerhahn S, Reichenbach P, Lingner J. Molecular dissection of telomeric repeat-containing RNA biogenesis unveils the presence of distinct and multiple regulatory pathways. *Mol Cell Biol.* 2010;30(20):4808-4817.
141. Almeida R, Fernandez-Justel JM, Santa-Maria C, et al. Chromatin conformation regulates the coordination between DNA replication and transcription. *Nat Commun.* 2018;9(1):1590.
142. Beishline K, Vladimirova O, Tutton S, Wang Z, Deng Z, Lieberman PM. CTCF driven TERRA transcription facilitates completion of telomere DNA replication. *Nat Commun.* 2017;8(1):2114.
143. Chu HP, Cifuentes-Rojas C, Kesner B, et al. TERRA RNA Antagonizes ATRX and Protects Telomeres. *Cell.* 2017;170(1):86-101 e116.
144. Deng Z, Norseen J, Wiedmer A, Riethman H, Lieberman PM. TERRA RNA binding to TRF2 facilitates heterochromatin formation and ORC recruitment at telomeres. *Mol Cell.* 2009;35(4):403-413.
145. Yu TY, Kao YW, Lin JJ. Telomeric transcripts stimulate telomere recombination to suppress senescence in cells lacking telomerase. *Proc Natl Acad Sci U S A.* 2014;111(9):3377-3382.
146. Arora R, Lee Y, Wischnewski H, Brun CM, Schwarz T, Azzalin CM. RNaseH1 regulates TERRA-telomeric DNA hybrids and telomere maintenance in ALT tumour cells. *Nat Commun.* 2014;5:5220.
147. Episkopou H, Draskovic I, Van Beneden A, et al. Alternative Lengthening of Telomeres is characterized by reduced compaction of telomeric chromatin. *Nucleic Acids Res.* 2014;42(7):4391-4405.
148. Postepska-Igielska A, Kronic D, Schmitt N, Greulich-Bode KM, Boukamp P, Grummt I. The chromatin remodelling complex NoRC safeguards genome stability by heterochromatin formation at telomeres and centromeres. *EMBO Rep.* 2013;14(8):704-710.
149. Scheibe M, Arnoult N, Kappei D, et al. Quantitative interaction screen of telomeric repeat-containing RNA reveals novel TERRA regulators. *Genome Res.* 2013;23(12):2149-2157.
150. Montero JJ, Lopez-Silanes I, Megias D, M FF, Castells-Garcia A, Blasco MA. TERRA recruitment of polycomb to telomeres is essential for histone trimethylation marks at telomeric heterochromatin. *Nat Commun.* 2018;9(1):1548.
151. Collie GW, Haider SM, Neidle S, Parkinson GN. A crystallographic and modelling study of a human telomeric RNA (TERRA) quadruplex. *Nucleic Acids Res.* 2010;38(16):5569-5580.
152. Randall A, Griffith JD. Structure of long telomeric RNA transcripts: the G-rich RNA forms a compact repeating structure containing G-quartets. *J Biol Chem.* 2009;284(21):13980-13986.
153. Xu Y, Suzuki Y, Ito K, Komiyama M. Telomeric repeat-containing RNA structure in living cells. *Proc Natl Acad Sci U S A.* 2010;107(33):14579-14584.
154. Takahama K, Takada A, Tada S, et al. Regulation of telomere length by G-quadruplex telomere DNA- and TERRA-binding protein TLS/FUS. *Chem Biol.* 2013;20(3):341-350.
155. Biffi G, Tannahill D, Balasubramanian S. An intramolecular G-quadruplex structure is required for binding of telomeric repeat-containing RNA to the telomeric protein TRF2. *J Am Chem Soc.* 2012;134(29):11974-11976.
156. Koskas S, Decottignies A, Dufour S, et al. Heat shock factor 1 promotes TERRA transcription and telomere protection upon heat stress. *Nucleic Acids Res.* 2017;45(11):6321-6333.
157. Oh BK, Choi Y, Bae J, Lee WM, Hoh JK, Choi JS. Increased amounts and stability of telomeric repeat-containing RNA (TERRA) following DNA damage induced by etoposide. *PLoS One.* 2019;14(11):e0225302.
158. Galigniana NM, Charo NL, Uranga R, Cabanillas AM, Piwien-Pilipuk G. Oxidative stress induces transcription of telomeric repeat-containing RNA (TERRA) by engaging PKA signaling and cytoskeleton dynamics. *Biochim Biophys Acta Mol Cell Res.* 2020;1867(4):118643.
159. Wang Z, Deng Z, Tutton S, Lieberman PM. The Telomeric Response to Viral Infection. *Viruses.* 2017;9(8).
160. Aurélie Diman JB, Florian Poulain, Julie Rodriguez, Marin Purnelle, Harikleia Episkopou, Luc Bertrand, Marc Francaux, Louise Deldicque, Anabelle Decottignies. Nuclear Respiratory Factor 1 and Endurance Exercise Promote Human Telomere Transcription. *Sci Adv.* 2016;2.

161. Deng Z, Wang Z, Xiang C, et al. Formation of telomeric repeat-containing RNA (TERRA) foci in highly proliferating mouse cerebellar neuronal progenitors and medulloblastoma. *J Cell Sci.* 2012;125(Pt 18):4383-4394.
162. Sampl S, Pramhas S, Stern C, Preusser M, Marosi C, Holzmann K. Expression of telomeres in astrocytoma WHO grade 2 to 4: TERRA level correlates with telomere length, telomerase activity, and advanced clinical grade. *Transl Oncol.* 2012;5(1):56-65.
163. Sepideh Dashti FK, Rasoul Salehi, Parvin Mahzouni, Leila Koulivand, Majid Kheirollahi. Comparison of TERRA expression in human brain tumors. *Eur J Oncol.* 2015.
164. Vitelli V, Falvo P, S GN, et al. Telomeric Repeat-Containing RNAs (TERRA) Decrease in Squamous Cell Carcinoma of the Head and Neck Is Associated with Worsened Clinical Outcome. *Int J Mol Sci.* 2018;19(1).
165. Bae SU, Park WJ, Jeong WK, Baek SK, Lee HW, Lee JH. Prognostic impact of telomeric repeat-containing RNA expression on long-term oncologic outcomes in colorectal cancer. *Medicine (Baltimore).* 2019;98(14):e14932.
166. C Schneider RMK, L Philipson. Genes Specifically Expressed at Growth Arrest of Mammalian Cells *Cell.* 1998;54:787-793.
167. STEITZ CMSAJA. Classification of gas5 as a Multi-Small-Nucleolar-RNA (snoRNA) Host Gene and a Member of the 5'-Terminal Oligopyrimidine Gene Family Reveals Common Features of snoRNA Host Genes. *MOLECULAR AND CELLULAR BIOLOGY.* 1998;18:6897-6909.
168. E M Coccia CC, A Charlesworth, C Ciccarelli, G B Rossi, L Philipson, V Sorrentino. Regulation and Expression of a Growth Arrest-Specific Gene (gas5) during Growth, Differentiation, and Development. *MOLECULAR AND CELLULAR BIOLOGY.* 1992:3514-3521.
169. John V. FLEMING SMH, D. Nicholas HARRIES and William D. REES. Effects of nutrient deprivation and differentiation on the expression of growth-arrest genes (gas and gadd) in F9 embryonal carcinoma cells. *Biochem J.* 1998;330:573-579.
170. Mourtada-Maarabouni M, Hasan AM, Farzaneh F, Williams GT. Inhibition of human T-cell proliferation by mammalian target of rapamycin (mTOR) antagonists requires noncoding RNA growth-arrest-specific transcript 5 (GAS5). *Mol Pharmacol.* 2010;78(1):19-28.
171. Tani H, Torimura M, Akimitsu N. The RNA degradation pathway regulates the function of GAS5 a non-coding RNA in mammalian cells. *PLoS One.* 2013;8(1):e55684.
172. C M Smith JAS. Classification of gas5 as a multi-small-nucleolar-RNA (snoRNA) Host Gene and a Member of the 5'-terminal Oligopyrimidine Gene Family Reveals Common Features of snoRNA Host Genes. *Mol Cell Biol.* 1998;18:6897-6909.
173. Meyuhas O. Synthesis of the Translational Apparatus Is Regulated at the Translational Level. *Eur J Biochem.* 2000;267:6321-6330.
174. Liu Y, Zhao J, Zhang W, et al. lncRNA GAS5 enhances G1 cell cycle arrest via binding to YBX1 to regulate p21 expression in stomach cancer. *Sci Rep.* 2015;5:10159.
175. Tomoshige Kino DEH, Takamasa Ichijo, Nancy Nader, George P Chrousos. Noncoding RNA gas5 Is a Growth Arrest- And Starvation-Associated Repressor of the Glucocorticoid Receptor. *Sci Signal.* 2010;3.
176. Hudson WH, Ortlund EA. The structure, function and evolution of proteins that bind DNA and RNA. *Nat Rev Mol Cell Biol.* 2014;15(11):749-760.
177. Yu Y, Hann SS. Novel Tumor Suppressor lncRNA Growth Arrest-Specific 5 (GAS5) In Human Cancer. *Onco Targets Ther.* 2019;12:8421-8436.
178. Isin M, Ozgur E, Cetin G, et al. Investigation of circulating lncRNAs in B-cell neoplasms. *Clin Chim Acta.* 2014;431:255-259.
179. Rosalind Lee RF, Victor Ambros, . The C. elegans Heterochronic Gene lin-4 Encodes Small RNAs with Antisense Complementarity to &II-14 *Cell.* 1993;75:843-854, .
180. Beer mann J, Piccoli MT, Viereck J, Thum T. Non-coding RNAs in Development and Disease: Background, Mechanisms, and Therapeutic Approaches. *Physiol Rev.* 2016;96(4):1297-1325.
181. Ha M, Kim VN. Regulation of microRNA biogenesis. *Nat Rev Mol Cell Biol.* 2014;15(8):509-524.

182. Larrea E, Sole C, Manterola L, et al. New Concepts in Cancer Biomarkers: Circulating miRNAs in Liquid Biopsies. *Int J Mol Sci.* 2016;17(5).
183. Romano G, Veneziano D, Acunzo M, Croce CM. Small non-coding RNA and cancer. *Carcinogenesis.* 2017;38(5):485-491.
184. Mariana Lagos-Quintana RR, Abdullah Yalcin, Jutta Meyer, Winfried Lendeckel, and Thomas Tusch. Identification of Tissue-Specific MicroRNAs from Mouse. *Current Biology.* 2002;12:735–739.
185. Landgraf P, Rusu M, Sheridan R, et al. A mammalian microRNA expression atlas based on small RNA library sequencing. *Cell.* 2007;129(7):1401-1414.
186. Wang S, Aurora AB, Johnson BA, et al. The endothelial-specific microRNA miR-126 governs vascular integrity and angiogenesis. *Dev Cell.* 2008;15(2):261-271.
187. Meister J, Schmidt MHH. miR-126 and miR-126\*: new players in cancer. *ScientificWorldJournal.* 2010;10:2090-2100.
188. Leon H Parker MS, Suk-Won Jin, Alane M Gray, Dimitris Beis, Thanh Pham, Gretchen Frantz, Susan Palmieri, Kenneth Hillan, Didier Y R Stainier, Frederic J De Sauvage, Weilan Ye. The endothelial-cell-derived secreted factor Egfl7 regulates vascular tube formation. *Nature.* 2004;428(6984):754-758.
189. Fish JE, Santoro MM, Morton SU, et al. miR-126 regulates angiogenic signaling and vascular integrity. *Dev Cell.* 2008;15(2):272-284.
190. Ming-Hua Hu C-YM, Xiao-Ming Wang, Chen-Dong Ye, Guang-Xian Zhang, Lin Chen, Jin-Guo Wang. MicroRNA-126 inhibits tumor proliferation and angiogenesis of hepatocellular carcinoma by down-regulating EGFL7 expression. *Oncotarget.* 2016;7.
191. Tamia A. Harris MY, Marcella Ferlito, Joshua T. Mendell, and Charles J. Lowenstein. MicroRNA-126 regulates endothelial expression of vascular cell adhesion molecule 1. *Proc Natl Acad Sci USA.* 2008;105.
192. Tang S-t, Wang F, Shao M, Wang Y, Zhu H-q. MicroRNA-126 suppresses inflammation in endothelial cells under hyperglycemic condition by targeting HMGB1. *Vascular Pharmacology.* 2017;88:48-55.
193. Feng R, Chen X, Yu Y, et al. miR-126 functions as a tumour suppressor in human gastric cancer. *Cancer Lett.* 2010;298(1):50-63.
194. Ebrahimi F, Gopalan V, Smith RA, Lam AK. miR-126 in human cancers: clinical roles and current perspectives. *Exp Mol Pathol.* 2014;96(1):98-107.
195. Hu M, Xiong S, Chen Q, Zhu S, Zhou X. Novel role of microRNA-126 in digestive system cancers: From bench to bedside. *Oncol Lett.* 2019;17(1):31-41.
196. Chengli Du ZL, Linping Cao, Chaofeng Ding, Owusu-ansah K Gyabaah, Haiyang Xie, Lin Zhou, Jian Wu and Shusen Zheng. MiR-126-3p suppresses tumor metastasis and angiogenesis of hepatocellular carcinoma by targeting LRP6 and PIK3R2. *Journal of Translational Medicine.* 2014;12.
197. Cheng Gong JF, Guang Li, Han-Han Liu and Zhi-Su Liu. Effects of microRNA-126 on cell proliferation, apoptosis and tumor angiogenesis via the down-regulating ERK signaling pathway by targeting EGFL7 in hepatocellular carcinoma. *Oncotarget.* 2017;8.
198. Xiang LY, Ou HH, Liu XC, et al. Loss of tumor suppressor miR-126 contributes to the development of hepatitis B virus-related hepatocellular carcinoma metastasis through the upregulation of ADAM9. *Tumour Biol.* 2017;39(6):1010428317709128.
199. Diamantis A, Magiorkinis E, Koutselini H. Fine-needle aspiration (FNA) biopsy: historical aspects. *Folia Histochem Cytobiol.* 2009;47(2):191-197.
200. Crowley E, Di Nicolantonio F, Loupakis F, Bardelli A. Liquid biopsy: monitoring cancer-genetics in the blood. *Nat Rev Clin Oncol.* 2013;10(8):472-484.
201. Roychowdhury S, Iyer MK, Robinson DR, et al. Personalized oncology through integrative high-throughput sequencing: a pilot study. *Sci Transl Med.* 2011;3(111):111ra121.
202. Tremosini S, Forner A, Boix L, et al. Prospective validation of an immunohistochemical panel (glypican 3, heat shock protein 70 and glutamine synthetase) in liver biopsies for diagnosis of very early hepatocellular carcinoma. *Gut.* 2012;61(10):1481-1487.
203. Vullanueva IlaA. Liquid Biopsy in Liver Cancer. *Discovery medicine.* 2015.

204. Rose M, Johnstone MA, James R, Hammond S, Linda Orr O, and Claire Turbide. Vesicle Formation during Reticulocyte Maturation. Association of plasma membrane activities with released vesicles (exosomes). *The journal of biological chemistry*. 1987;262(July 5): 9412-9420.
205. Jeppesen DK, Hvam ML, Primdahl-Bengtson B, et al. Comparative analysis of discrete exosome fractions obtained by differential centrifugation. *J Extracell Vesicles*. 2014;3:25011.
206. Crescitelli R, Lasser C, Szabo TG, et al. Distinct RNA profiles in subpopulations of extracellular vesicles: apoptotic bodies, microvesicles and exosomes. *J Extracell Vesicles*. 2013;2.
207. Valadi H, Ekstrom K, Bossios A, Sjostrand M, Lee JJ, Lotvall JO. Exosome-mediated transfer of mRNAs and microRNAs is a novel mechanism of genetic exchange between cells. *Nat Cell Biol*. 2007;9(6):654-659.
208. Melo SA, Sugimoto H, O'Connell JT, et al. Cancer exosomes perform cell-independent microRNA biogenesis and promote tumorigenesis. *Cancer Cell*. 2014;26(5):707-721.
209. Colombo M, Raposo G, Thery C. Biogenesis, secretion, and intercellular interactions of exosomes and other extracellular vesicles. *Annu Rev Cell Dev Biol*. 2014;30:255-289.
210. Akers JC, Gonda D, Kim R, Carter BS, Chen CC. Biogenesis of extracellular vesicles (EV): exosomes, microvesicles, retrovirus-like vesicles, and apoptotic bodies. *J Neurooncol*. 2013;113(1):1-11.
211. Muralidharan-Chari V, Clancy J, Plou C, et al. ARF6-regulated shedding of tumor cell-derived plasma membrane microvesicles. *Curr Biol*. 2009;19(22):1875-1885.
212. James H. ESCRT complexes and the biogenesis of multivesicular bodies. *Curr Opin Cell Biol*. 2008;20(1).
213. Nabhan JF, Hu R, Oh RS, Cohen SN, Lu Q. Formation and release of arrestin domain-containing protein 1-mediated microvesicles (ARMMs) at plasma membrane by recruitment of TSG101 protein. *Proc Natl Acad Sci U S A*. 2012;109(11):4146-4151.
214. Colombo M, Moita C, van Niel G, et al. Analysis of ESCRT functions in exosome biogenesis, composition and secretion highlights the heterogeneity of extracellular vesicles. *J Cell Sci*. 2013;126(Pt 24):5553-5565.
215. Stuffers S, Sem Wegner C, Stenmark H, Brech A. Multivesicular endosome biogenesis in the absence of ESCRTs. *Traffic*. 2009;10(7):925-937.
216. Tore Skotland NPH, Kirsten Sandvig, Alicia Llorente. Exosomal lipid composition and the role of ether lipids and phosphoinositides in exosome biology. *J Lipid Res*. 2019.
217. Hoshino A, Costa-Silva B, Shen TL, et al. Tumour exosome integrins determine organotropic metastasis. *Nature*. 2015;527(7578):329-335.
218. Leoni G, Neumann PA, Kamaly N, et al. Annexin A1-containing extracellular vesicles and polymeric nanoparticles promote epithelial wound repair. *J Clin Invest*. 2015;125(3):1215-1227.
219. Jordens I, Marsman M, Kuijl C, Neefjes J. Rab proteins, connecting transport and vesicle fusion. *Traffic*. 2005;6(12):1070-1077.
220. Lars Holmgren AS, Eva Rajnavo Igyi, Judah Folkman, Georg Klein, Ingemar Ernberg, and Kerstin I. Falk. Horizontal Transfer of DNA by the Uptake of Apoptotic Bodies. *Blood*. 2017.
221. Anna Bergsmedh AS, Marie Henriksson, Anders Bratt, M. Judah Folkman, Anna-Lena Spetz and Lars Holmgren. Horizontal transfer of oncogenes by uptake of apoptotic bodies. *PNAS*. 2001.
222. Cai J, Han Y, Ren H, et al. Extracellular vesicle-mediated transfer of donor genomic DNA to recipient cells is a novel mechanism for genetic influence between cells. *J Mol Cell Biol*. 2013;5(4):227-238.
223. Lazaro-Ibanez E, Sanz-Garcia A, Visakorpi T, et al. Different gDNA content in the subpopulations of prostate cancer extracellular vesicles: apoptotic bodies, microvesicles, and exosomes. *Prostate*. 2014;74(14):1379-1390.
224. Kahlert C, Melo SA, Protopopov A, et al. Identification of double-stranded genomic DNA spanning all chromosomes with mutated KRAS and p53 DNA in the serum exosomes of patients with pancreatic cancer. *J Biol Chem*. 2014;289(7):3869-3875.
225. Guescini M, Genedani S, Stocchi V, Agnati LF. Astrocytes and Glioblastoma cells release exosomes carrying mtDNA. *J Neural Transm (Vienna)*. 2010;117(1):1-4.

226. Yang S, Che SP, Kurywchak P, et al. Detection of mutant KRAS and TP53 DNA in circulating exosomes from healthy individuals and patients with pancreatic cancer. *Cancer Biol Ther.* 2017;18(3):158-165.
227. Lasser C, Shelke GV, Yeri A, et al. Two distinct extracellular RNA signatures released by a single cell type identified by microarray and next-generation sequencing. *RNA Biol.* 2017;14(1):58-72.
228. Xiaoyi Huang TY, Michael Tschannen, Zhifu Sun, Howard Jacob, Meijun Du, Meihua Liang, Rachel L Dittmar, Yong Liu, Mingyu Liang, Manish Kohli, Stephen N Thibodeau, Lisa Boardman, Liang Wang. Characterization of Human Plasma-Derived Exosomal RNAs by Deep Sequencing. *BMC Genomics.* 2013.
229. Xiao D, Ohlendorf J, Chen Y, et al. Identifying mRNA, microRNA and protein profiles of melanoma exosomes. *PLoS One.* 2012;7(10):e46874.
230. Squadrito ML, Baer C, Burdet F, et al. Endogenous RNAs modulate microRNA sorting to exosomes and transfer to acceptor cells. *Cell Rep.* 2014;8(5):1432-1446.
231. Kurochkin AOBaIV. Exosomes secreted by human cells transport largely mRNA fragments that are enriched in the 3'-untranslated regions. *Biology Direct.* 2013.
232. Villarroja-Beltri C, Gutierrez-Vazquez C, Sanchez-Cabo F, et al. Sumoylated hnRNPA2B1 controls the sorting of miRNAs into exosomes through binding to specific motifs. *Nat Commun.* 2013;4:2980.
233. Munro TP, Magee RJ, Kidd GJ, et al. Mutational analysis of a heterogeneous nuclear ribonucleoprotein A2 response element for RNA trafficking. *J Biol Chem.* 1999;274(48):34389-34395.
234. Koppers-Lalic D, Hackenberg M, Bijnsdorp IV, et al. Nontemplated nucleotide additions distinguish the small RNA composition in cells from exosomes. *Cell Rep.* 2014;8(6):1649-1658.
235. Jasenka Guduric-Fuchs AOC, Bailey Camp, Christina L O'Neill, Reinhold J Medina and David A Simpson. Selective extracellular vesicle-mediated export of an overlapping set of microRNAs from multiple cell types. *BMC Genomics.* 2012.
236. Arroyo JD, Chevillet JR, Kroh EM, et al. Argonaute2 complexes carry a population of circulating microRNAs independent of vesicles in human plasma. *Proc Natl Acad Sci U S A.* 2011;108(12):5003-5008.
237. Taylor DD, Gercel-Taylor C. MicroRNA signatures of tumor-derived exosomes as diagnostic biomarkers of ovarian cancer. *Gynecol Oncol.* 2008;110(1):13-21.
238. Skog J, Wurdinger T, van Rijn S, et al. Glioblastoma microvesicles transport RNA and proteins that promote tumour growth and provide diagnostic biomarkers. *Nat Cell Biol.* 2008;10(12):1470-1476.
239. Kalluri R, LeBleu VS. The biology, function, and biomedical applications of exosomes. *Science.* 2020;367(6478).
240. Faranda T, Grossi I, Manganelli M, et al. Differential expression profiling of long non-coding RNA GAS5 and miR-126-3p in human cancer cells in response to sorafenib. *Sci Rep.* 2019;9(1):9118.
241. Chomczynski P, Sacchi N. Single-step method of RNA isolation by acid guanidinium thiocyanate-phenol-chloroform extraction. *Anal Biochem.* 1987;162(1):156-159.
242. Notarangelo M, Zucal C, Modelska A, et al. Ultrasensitive detection of cancer biomarkers by nickel-based isolation of polydisperse extracellular vesicles from blood. *EBioMedicine.* 2019;43:114-126.
243. Feretzaki M, Lingner J. A practical qPCR approach to detect TERRA, the elusive telomeric repeat-containing RNA. *Methods.* 2017;114:39-45.
244. Livak KJ, Schmittgen TD. Analysis of relative gene expression data using real-time quantitative PCR and the 2<sup>-</sup>(Delta Delta C(T)) Method. *Methods.* 2001;25(4):402-408.
245. Salvi A, Sabelli C, Moncini S, et al. MicroRNA-23b mediates urokinase and c-met downmodulation and a decreased migration of human hepatocellular carcinoma cells. *FEBS J.* 2009;276(11):2966-2982.
246. Alessandro Salvi IC, Edoardo Abeni, Bruna Arici, Ilaria Grossi, Claudia Specchia, Nazario Portolani, Sergio Barlati, Giuseppina De Petro. Effects of miR-193a and sorafenib on hepatocellular carcinoma cells. *Molecular Cancer.* 2013;12.
247. Kudo M. Systemic Therapy for Hepatocellular Carcinoma: Latest Advances. *Cancers (Basel).* 2018;10(11).

248. Kudo M, Finn RS, Qin S, et al. Lenvatinib versus sorafenib in first-line treatment of patients with unresectable hepatocellular carcinoma: a randomised phase 3 non-inferiority trial. *The Lancet*. 2018;391(10126):1163-1173.
249. Finn RS, Qin S, Ikeda M, et al. Atezolizumab plus Bevacizumab in Unresectable Hepatocellular Carcinoma. *N Engl J Med*. 2020;382(20):1894-1905.
250. Tao R, Hu S, Wang S, et al. Association between indel polymorphism in the promoter region of lncRNA GAS5 and the risk of hepatocellular carcinoma. *Carcinogenesis*. 2015;36(10):1136-1143.
251. Marianna Feretzaki PRNaJL. Expression and differential regulation of human TERRA at several chromosome ends. *RNA*. 2019;25:1470-1480.
252. Kreilmeier T, Mejri D, Hauck M, Kleiter M, Holzmann K. Telomere Transcripts Target Telomerase in Human Cancer Cells. *Genes (Basel)*. 2016;7(8).
253. Oh BK, Keo P, Bae J, Ko JH, Choi JS. Variable TERRA abundance and stability in cervical cancer cells. *Int J Mol Med*. 2017;39(6):1597-1604.
254. Cao H, Zhai Y, Ji X, et al. Noncoding telomeric repeat-containing RNA inhibits the progression of hepatocellular carcinoma by regulating telomerase-mediated telomere length. *Cancer Sci*. 2020.
255. S.Bacchetti AJWSa. A survey of telomerase activity in human cancer. *European Journal of Cancer*. 1997;33.
256. Wang Z, Deng Z, Dahmane N, et al. Telomeric repeat-containing RNA (TERRA) constitutes a nucleoprotein component of extracellular inflammatory exosomes. *Proc Natl Acad Sci U S A*. 2015;112(46):E6293-6300.
257. Ghosh A, Ghosh A, Datta S, et al. Hepatic miR-126 is a potential plasma biomarker for detection of hepatitis B virus infected hepatocellular carcinoma. *Int J Cancer*. 2016;138(11):2732-2744.
258. Ahmed Khairy IH, Olfat Shaker, Ayman Yosry. Serum miRNA Panel in Egyptian Patients with Chronic Hepatitis C Related Hepatocellular Carcinoma. *Asian Pac J Cancer Prev*. 2016;17.
259. Ali HEA, Abdel Hameed R, Effat H, et al. Circulating microRNAs panel as a diagnostic tool for discrimination of HCV-associated hepatocellular carcinoma. *Clin Res Hepatol Gastroenterol*. 2017;41(4):e51-e62.
260. Farzaneh Moshiri AS, Laura Gramantieri, Angelo Sangiovanni, Paola Guerriero, Giuseppina De Petro, Cristian Bassi, Laura Lupini, Arash Sattari, Douglas Cheung, Dario Veneziano, Giovanni Nigita, Ram C. Shankaraiah, Nazario Portolani, Paolo Carcoforo, Francesca Fornari, Luigi Bolondi, Antonio Frassoldati, Silvia Sabbioni, Massimo Colombo, Carlo M. Croce and Massimo Negrini. Circulating miR-106b-3p, miR-101-3p and miR-1246 as diagnostic biomarkers of hepatocellular carcinoma. *Oncotarget*.9:15350-15364.
261. Shen J, Hodges TR, Song R, et al. Serum HOTAIR and GAS5 levels as predictors of survival in patients with glioblastoma. *Mol Carcinog*. 2018;57(1):137-141.
262. Liu L, Meng T, Yang XH, et al. Prognostic and predictive value of long non-coding RNA GAS5 and mircoRNA-221 in colorectal cancer and their effects on colorectal cancer cell proliferation, migration and invasion. *Cancer Biomark*. 2018;22(2):283-299.
263. Fayda M, Isin M, Tambas M, et al. Do circulating long non-coding RNAs (lncRNAs) (LincRNA-p21, GAS 5, HOTAIR) predict the treatment response in patients with head and neck cancer treated with chemoradiotherapy? *Tumour Biol*. 2016;37(3):3969-3978.
264. Pierre L Triozzi SA, Wayne Aldrich, Arun D Singh, Ronald Grane and Ernest C Borden. The association of blood angioregulatory microRNA levels with circulating endothelial cells and angiogenic proteins in patients receiving dacarbazine and interferon. *Journal of Translational Medicine*. 2012;10.
265. Hansen TF, Carlsen AL, Heegaard NH, Sorensen FB, Jakobsen A. Changes in circulating microRNA-126 during treatment with chemotherapy and bevacizumab predicts treatment response in patients with metastatic colorectal cancer. *Br J Cancer*. 2015;112(4):624-629.

## 8. ACKNOWLEDGMENTS

It is difficult to express in words acknowledgments up to reflect the recognition to the people who accompanied me in this *iter*.

My deep acknowledgment is addressed to Prof. Giuseppina De Petro for giving me the opportunity to be part of her research group, for her availability, for the knowledge transmitted, for the enthusiasm, the constructive cues and hints provided.

I express my sincere gratitude to Prof. Alessandro Salvi, for his fundamental and indispensable advice, for the trust he placed in me to overcome my limits. Many have been the moments spent in scientific discussions and teachings in the field of research and life.

A heartfelt thanks goes to Dr. Ilaria Grossi for her patience, professionalism and for both the beautiful and the difficult shared moments. Mutual encouragement has never been lacking.

An acknowledgment also goes to the academic body and my colleagues of the Division of Biology and Genetics at the University of Brescia, to my friends near and far, and to all those who always "stand" and supported me.

Last but not least, a special thanks goes to my family, for the immense constant love and unconditional support.

*Michele Manganelli*

*January, 2021*



## 9. APPENDIX A

### PUBLICATIONS

1. Michele Manganelli, Ilaria Grossi, Manuela Ferracin, Paola Guerriero, Massimo Negrini, Michele Ghidini, Chiara Senti, Margherita Ratti, Claudio Pizzo, Rodolfo Passalacqua, Sara Molfino, Gianluca Baiocchi, Nazario Portolani, Giuseppina De Petro, Alessandro Salvi. *Longitudinal dynamic variations of circulating levels of miR-23b-3p, miR-126-3p and lncRNA GAS5 in hepatocellular carcinoma patients treated with sorafenib*. To be submitted to Liver International.
2. Simona Serrati, Letizia Porcelli, Stefania Guida, Anna Ferretta, Rosa Maria Iacobazzi, Tiziana Cocco, Immacolata Maida, Gabriella Tamasi, Claudio Rossi, Michele Manganelli, Stefania Tommasi, Amalia Azzariti and Gabriella Guida. *Tomatine Displays Antitumor Potential in In Vitro Models of Metastatic Melanoma*. Int. J. Mol. Sci. 2020, 21, 5243. DOI: doi.org/10.3390/ijms21155243
3. Guida Stefania, Ciardo Silvana, De Pace Barbara, De Carvalho Nathalie, Farnetani Francesca, Pezzini Claudia, Chester Johanna, Shaniko Kaleci, Manganelli Michele, Guida Gabriella, Giovanni Pellacani. *Atrophic and hypertrophic skin photoaging and MC1R*. J Am Acad of Derm JAAD, 23 Apr 2020. DOI: 10.1016/j.jaad.2020.04.075
4. Guida Stefania, Ciardo Silvana, De Pace Barbara, De Carvalho Nathalie, Peccerillo Francesca, Manfredini Marco, Chester Johanna, Manganelli Michele, Guida Gabriella, Giovanni Pellacani. *The influence of MC1R dermal morphological features of photoexposed skin in women revealed by reflectance confocal microscopy and optical coherence tomography*. Experimental Dermatology, September 2019. DOI: 10.1111/exd.14037
5. Teresa Faranda, Ilaria Grossi, Michele Manganelli, Eleonora Marchina, Gianluca Baiocchi, Nazario Portolani, Marialuisa Crosatti, Giuseppina De Petro, Alessandro Salvi. *Differential expression profiling of long non-coding RNA GAS5 and miR-126-3p in human cancer cells in response to sorafenib*. Scientific Reports, June 2019; (9) DOI: 10.1038/s41598-019-45604-2
6. Flavia A. M. Maggiolini, Stuart Cantsilieris, Pietro D'Addabbo, Michele Manganelli, Bradley P. Coe, Beth L. Dumont, Ashley D. Sanders, Andy Wing, Chun Pang, Mitchell Vollger, Orazio Palumbo, Pietro Palumbo, Maria Accadia, Massimo Carella, Evan E. Eichler, Francesca Antonacci. *Genomic inversions and GOLGA core duplicons underlie disease instability at the 15q25 locus*. PLoS Genet, Mar 2019; 15(3): e1008075. DOI: 10.1371/journal.pgen.1008075.

7. Guida Stefania, Foti Caterina, Michele Manganelli, Bartolomeo Nicola, Pellacani Giovanni, Bonamonte Domenico, Filotico Raffaele, Guida Gabriella. *MC1R genotype and psoriasis: is there a link revealing a phenotypic difference? A pilot study*. J Eur Acad Dermatol Venereol, Mar 2018; 32 (3):p119-p120. DOI: 10.1111/jdv.14607.

## ABSTRACTs

1. Michele Manganelli, Simona Serrati, Letizia Porcelli, Stefania Guida, Anna Ferretta, Rosa Maria Iacobazzi, Tiziana Cocco, Immacolata Maida, Gabriella Tamasi, Claudio Rossi, Stefania Tommasi, Amalia Azzariti, Gabriella Guida. *Tomatine exhibits antitumor potential in in vitro models of metastatic melanoma*. 10th World Congress of Melanoma & 17th EADO Congress 2021 (Roma, 15-17 April, 2021).
2. Michele Manganelli, Iliaria Grossi, Jessica Corsi, Katarina Jurikovà, Emilio Cusanelli, Vito D'Agostino, Sarah Molfino, Gianluca Baiocchi, Nazario Portolani, Alessandro Salvi, Giuseppina De Petro. *Emerging role of TElomeric-Repeat containing RNA TERRA in hepatocellular carcinoma*. ESMO Targeted Anticancer therapies Congress 2021 (01-02 March 2021).
3. Alessandro Salvi, Michele Manganelli, Iliaria Grossi, Gianluca Baiocchi, Nazario Portolani, Giuseppina De Petro. *Circulating microRNAs as promising non-invasive molecular biomarkers of HCC*. 53<sup>rd</sup> AISF Annual Meeting (Rome, 27-28 February 2020). Digestive and Liver Disease, February 2020. DOI: 10.1016/j.dld.2019.12.062
4. Iliaria Grossi, Michele Manganelli, Teresa Faranda, Paola Guerriero, Massimo Negrini, Gianluca Baiocchi, Nazario Portolani, Michele Ghidini, Chiara Senti, Rodolfo Passalacqua, Giuseppina De Petro, Alessandro Salvi. *Circulating ncRNAs as promising non-invasive molecular biomarkers of HCC*. EACR-ESMO Joint Conference on Liquid Biopsies (Bergamo, Italy 15-17 May 2019).
5. Michele Manganelli, Teresa Faranda, Iliaria Grossi, Eleonora Marchina, Gianluca Baiocchi, Nazario Portolani, Marialuisa Crosatti, Giuseppina De Petro, Alessandro Salvi. *Long non-coding RNA GAS5 and miR-126-3p as molecular biomarkers of response to sorafenib in human cancer cells*. Regulatory RNA Cell Symposia (Berlin, Germany 12-14 May 2019).
6. Alessandro Salvi, Iliaria Grossi, Teresa Faranda, Michele Manganelli, Gianluca Baiocchi. *Functional role of microRNA-23b-3p and microRNA-193a-3p*. XVIII Italian Association of Biology and Genetics (AIBG) – National Conference (Ferrara, Italy 21-22 September 2018).

7. Flavia A.M. Maggiolini, Stuart Cantsilieris, Pietro D'addabbo, Michele Manganelli, Bradley P. Coe, Beth L. Dumont, Ashley D. Sanders, Andy Wing Chun Pang, Mitchell R. Vollger, Orazio Palumbo, Pietro Palumbo, Maria Accadia, Massimo Carella, Evan E. Eichler, Francesca Antonacci. *Abstracts of the 12<sup>th</sup> European Cytogenomics Conference 2019*. 12<sup>th</sup> European Cytogenomics Conference (Salzburg, Austria, 06-09 July 2019). *Molecular Cytogenetics*, July 2019. DOI: 10.1186/s13039-019-0439-z
8. Anna Ferretta, Stefania Guida, Michele Manganelli, Immacolata Maida, Tiziana Cocco, Anna Gallone, Stefania Tommasi, Amalia Azzariti, Michele Guida, Gabriella Guida. *Stress response pathways driving tumorigenesis in melanoma cell lines*. XXIII Italian Melanoma Intergroup (IMI) - National Conference (Milan, Italy 5-7 November 2017).

## POSTERS

1. Iliaria Grossi, Michele Manganelli, Teresa Faranda, Paola Guerriero, Massimo Negrini, Gianluca Baiocchi, Nazario Portolani, Michele Ghidini, Chiara Senti, Rodolfo Passalacqua, Giuseppina De Petro, Alessandro Salvi. *Circulating ncRNAs as promising non-invasive molecular biomarkers of HCC*. EACR-ESMO Joint Conference on Liquid Biopsies (Bergamo 15-17/05/2019).
2. Michele Manganelli, Teresa Faranda, Iliaria Grossi, Eleonora Marchina, Gianluca Baiocchi, Nazario Portolani, Marialuisa Crosatti, Giuseppina De Petro, Alessandro Salvi. *Long non-coding RNA GAS5 and miR-126-3p as molecular biomarkers of response to sorafenib in human cancer cells*. Regulatory RNA Cell Symposia (Berlin 12-13-14/05/2019).

*Sed obstinata mente*

*perfer, obdura*

***Gaius Valerius Catullus***



Article

# Tomatine Displays Antitumor Potential in In Vitro Models of Metastatic Melanoma

Simona Serrati <sup>1,†</sup>, Letizia Porcelli <sup>1,†</sup>, Stefania Guida <sup>2</sup> , Anna Ferretta <sup>3</sup> ,  
Rosa Maria Iacobazzi <sup>1</sup>, Tiziana Cocco <sup>3</sup> , Immacolata Maida <sup>3</sup>, Gabriella Tamasi <sup>4</sup> ,  
Claudio Rossi <sup>4</sup>, Michele Manganelli <sup>3</sup> , Stefania Tommasi <sup>5</sup>, Amalia Azzariti <sup>1,‡</sup> and  
Gabriella Guida <sup>3,\*</sup>

<sup>1</sup> Experimental Pharmacology Laboratory, IRCCS Istituto Tumori Giovanni Paolo II, 70124 Bari, Italy; s.serrati@oncologico.bari.it (S.S.); l.porcelli@oncologico.bari.it (L.P.); r.m.iacobazzi@oncologico.bari.it (R.M.I.); a.azzariti@oncologico.bari.it (A.A.)

<sup>2</sup> Dermatology Unit, University of Modena and Reggio Emilia, 41121 Modena, Italy; drstefaniaguida@gmail.com

<sup>3</sup> Department of Basic Medical Sciences Neurosciences and Sense Organs, University of Bari, 70124 Bari, Italy; anna.ferretta@uniba.it (A.F.); tizianamaria.cocco@uniba.it (T.C.); immacolata.maida@uniba.it (I.M.); m.manganelli1991@gmail.com (M.M.)

<sup>4</sup> Department of Biotechnology Chemistry and Pharmacology, University of Siena, 53100 Siena, Italy; gabriella.tamasi@unisi.it (G.T.); claudio.rossi@unisi.it (C.R.)

<sup>5</sup> Molecular Diagnostics and Pharmacogenetics Unit, IRCCS Istituto Tumori Giovanni Paolo II, 70124 Bari, Italy; s.tommasi@oncologico.bari.it

\* Correspondence: gabriella.guida@uniba.it; Tel.: +39-080-544-8555

† These Authors contributed equally as first Authors.

‡ These Authors contributed equally as senior Authors.

Received: 20 May 2020; Accepted: 20 July 2020; Published: 23 July 2020



**Abstract:** There is a growing interest in the cytotoxic effects of bioactive glycoalkaloids, such as  $\alpha$ -tomatine on tumor cells. Here, for the first time, we determine the antitumor potential of tomatine, a mixture of  $\alpha$ -tomatine and dehydrotomatine, in metastatic melanoma (MM) cell lines harboring different BRAF and MC1R variants. We performed cytotoxicity experiments and annexin-V/propidium iodide staining to assess the apoptotic/necrotic status of the cells. ER stress and autophagy markers were revealed by Western Blot, whereas antiangiogenic and vascular-disrupting effects were evaluated through a capillary tube formation assay on matrigel and by ELISA kit for VEGF release determination. Cell invasion was determined by a Boyden chamber matrigel assay. Tomatine reduced 50% of cell viability and induced a concentration-dependent increase of apoptotic cells in the range of 0.5–1  $\mu$ M in terms of  $\alpha$ -tomatine. The extent of apoptosis was more than two-fold higher in <sup>V600</sup>BRAF-D184H/D184H MC1R cells than in BRAF wild-type cells and <sup>V600</sup>BRAF-MC1R wild-type cell lines. Additionally, tomatine increased the LC3I/II autophagy marker, p-eIF2 $\alpha$ , and p-Erk1/2 levels in BRAF wild-type cells. Notably, tomatine strongly reduced cell invasion and melanoma-dependent angiogenesis by reducing VEGF release and tumor-stimulating effects on capillary tube formation. Collectively, our findings support tomatine as a potential antitumor agent in MM.

**Keywords:** metastatic melanoma; tomatine; angiogenesis; apoptosis; autophagy

## 1. Introduction

Malignant melanoma is an aggressive type of tumor that mainly occurs on the skin, and it is characterized by poor prognoses for patients with metastatic disease. Despite novel therapeutic approaches, the treatment of metastatic melanoma (MM) still remains challenging. Therefore,

additional efforts should be made to find more effective strategies for such a disease. Many studies on molecular mechanisms underlying metastatic melanoma progression have highlighted the pivotal role of biochemical pathways involved in endoplasmic reticulum (ER) stress, autophagy, and translational reprogramming [1–3]. We previously demonstrated that the activation of such tumorigenic pathways was strictly related to the genetic status of BRAF and melanocortin 1 receptor (MC1R) [1,2,4,5]. In particular, the <sup>V600</sup>BRAF mutation and its relation with the MC1R–cAMP–MITF–PGC-1 $\alpha$  axis switches on a metabolic reprogramming in melanoma, leading to decreased OXPHOS (oxidative phosphorylation) activity and increased HIF-1 $\alpha$  expression. Additionally, ER stress has been associated with variations in tumor angiogenesis [6,7], which is known to play a key role in cancer growth and invasion.

In the last few years, there has been a growing interest in the beneficial effects of plant compounds and also marine-derived fungi and marine red algae [8,9]. In particular, glycoalkaloids extracted from plants have been investigated for their pharmaceutical and toxicological properties [10,11]. Among these glycoalkaloids is tomatine, a 10:1 mixture of  $\alpha$ -tomatine and dehydrotomatine extracted from tomatoes [12,13]. Tomatine inhibits the growth of many types of human cancer cells, such as colon, breast, leukemia, lung, and prostate [14], and it has the ability to enhance apoptosis of androgen-independent human prostate cancer when given in combination with chemotherapy [15,16]. Interestingly, tomatine has proven to activate caspase-independent apoptosis by inducing the translocation of AIF (apoptosis-inducing factor) from mitochondria to the nucleus, in a neuroblastoma cell line, by triggering the p-ERK/eIF2 $\alpha$  branch of the unfolded protein response [17]. Additionally, tomatine has shown antibiotic, anti-inflammatory, antioxidative, cardiovascular, and immune-stimulating effects, although the mechanisms of these actions need further investigation [10,16]. Currently, no data are available regarding the effects of tomatine on metastatic melanoma.

Furthermore, recent reports have recognized naturally occurring plant-derived substances, such as alkaloids, as antitumor agents endowed with antiangiogenic properties [18]. No data are available on the antiangiogenic effect of tomatine. Here, we seek to evaluate the antitumor potential of tomatine through the evaluation of its effects on proliferation, cell invasion, and tumor-angiogenesis in metastatic melanoma cells with different genetic contexts, basal autophagy, and the activation status of the  $\alpha$  subunit of translation initiation factor 2 (p-eIF2 $\alpha$ ).

## 2. Results

### 2.1. Tomatine Composition

To explore the relevance of the response to tomatine in MM models, commercial tomatine was preliminarily characterized by HPLC–ESI–Qq–MS/MS analyses. Tomatine revealed a mixture of the two glycoalkaloids  $\alpha$ -tomatine and dehydrotomatine, corresponding to  $87.1 \pm 1.6\%$  and  $13.0 \pm 0.8\%$ , respectively (Figure S1), according to [13]. The mixture of the two components and their ratio is comparable to that measured in tomatine extracts from tomato fruits and various vegetative plant tissues, for which the cytotoxic effect, evaluated in several types of cancer cells, has been ascribed to  $\alpha$ -tomatine [10]. In our experiments, we utilized tomatine, which is the mixture of  $\alpha$ -tomatine and dehydrotomatine, but since the active compound is  $\alpha$ -tomatine, we reported the drug concentration of this glycoalkaloid, expressed in micromolar ( $\mu$ M).

### 2.2. Tomatine Displayed Antitumor Potential in MM Cell Lines

In order to evaluate the cytotoxicity of tomatine, MM cell lines HBL, hmel-1, and M3 and normal fibroblast cell line N-FB were treated with increasing concentrations (expressed in terms of  $\alpha$ -tomatine), as reported in Section 4. After 24 h of treatment, cell viability was reduced in a dose-dependent manner in all cell lines, allowing the determination of the concentration of  $\alpha$ -tomatine yielding 50% inhibition of cell viability (IC<sub>50</sub>). The IC<sub>50</sub> values were  $0.53 \pm 0.04$ ,  $0.72 \pm 0.06$ , and  $1.03 \pm 0.04$   $\mu$ M for HBL, hmel1 and M3, respectively. Notably, tomatine was 10-fold less toxic in N-FB than MM cell

lines since the  $IC_{50}$  value was  $9.58 \pm 0.6 \mu\text{M}$ . Dose–response plots, summarizing the data from three independent experiments performed in MM cell lines, are reported in panel A of Figure 1, whereas in panel B, the dot plot shows the dose–response curves of all tested cell lines, allowing for a comparison of cytotoxic effects.

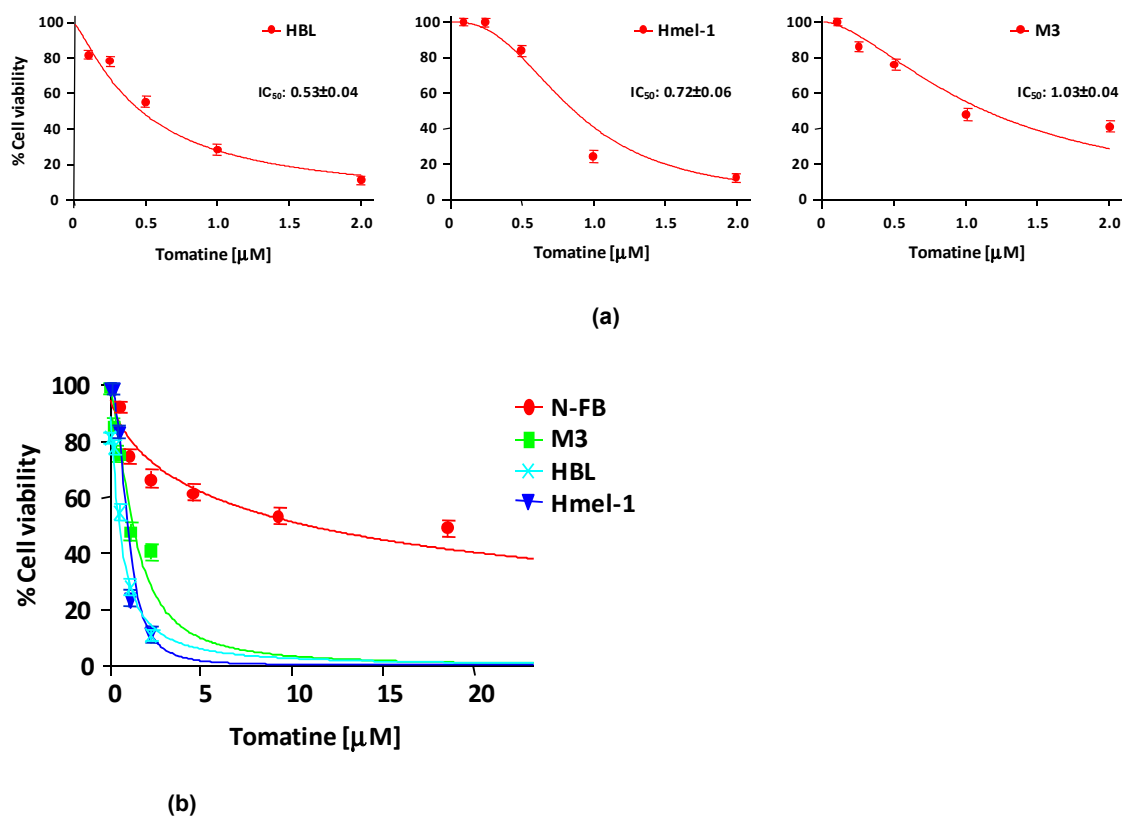


**Figure 1.** Cytotoxicity of tomatine in melanoma cell lines and in N-FB. (a) Cell viability (%)/dose plots of the mean of three different experiments  $\pm$  SD conducted on HBL, hmel-1, and M3 melanoma cancer cells. In each experiment, every drug concentration (expressed in terms of  $\alpha$ -tomatine) was repeated in six identical wells. The inserts in each graph report the  $IC_{50}$  values calculated using Calcsyn software. (b) Dot plot showing the dose–response curves of all tested cell lines, allowing for a comparison of cytotoxic effects.

To further explore the antitumor potential of tomatine, we performed a Boyden chamber matrigel assay to analyze the effect of tomatine on cell invasion. As reported in Figure 2a, melanoma cells showed significant motility in a basal condition; conversely, the addition of tomatine considerably reduced the invasiveness of the cells. As quantified in Figure 2b, tomatine reduced the invasiveness by about 30–35% at the  $\alpha$ -tomatine concentration of  $0.5 \mu\text{M}$  and about 65–80% at  $1 \mu\text{M}$ , suggesting the high inhibitory potential of tomatine on the invasive behavior of such MM cell models.

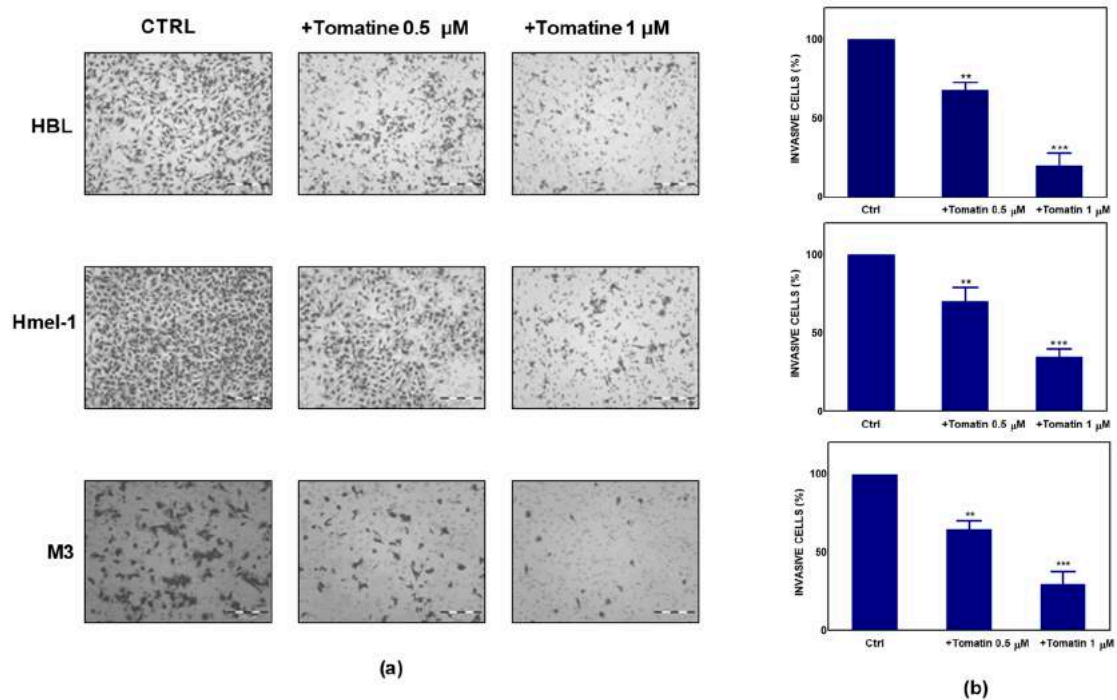


**Figure 2.** Effect of tomatine on melanoma cancer cell invasion. (a) Tomatine-dependent decrease of cancer cells invasion through matrigel-coated porous filters (magnification 50×). (b) Percentage of invasion in melanoma cells treated with tomatine (0.5–1 μM in terms of α-tomatine). Data are shown as mean ± SD of three different experiments performed in triplicate. \*\*  $p < 0.01$  and \*\*\*  $p < 0.001$ , relative to vehicle-treated cells.

### 2.3. Tomatine Induced Cell Death through Apoptosis in Metastatic Melanoma Cells

To verify whether the cytotoxic effect was due to the induction of apoptosis, we performed annexin-V/PI staining of the cells, followed by flow cytometry analysis. For this purpose, we treated the MM cell line with tomatine at three different concentrations of α-tomatine (0.25, 0.5, and 1 μM) for 24 h. The results of the analysis, reported in Figure 3, showed that tomatine induced concentration-dependent apoptosis in all cells. However, in <sup>V600</sup>BRAF M3 carrying a homozygous MC1R polymorphism, the percentage of annexin-V/PI positive cells was two-fold higher than in hmel-1 and HBL, in which tomatine induced comparable levels of apoptosis. Further evaluations, performed after 48 h, confirmed M3 as the most sensitive cell line to the proapoptotic effect of tomatine since the percentage of apoptotic cells increased nearly five-fold at 1 μM α-tomatine versus vehicle-treated cells (data reported in Figure S2).



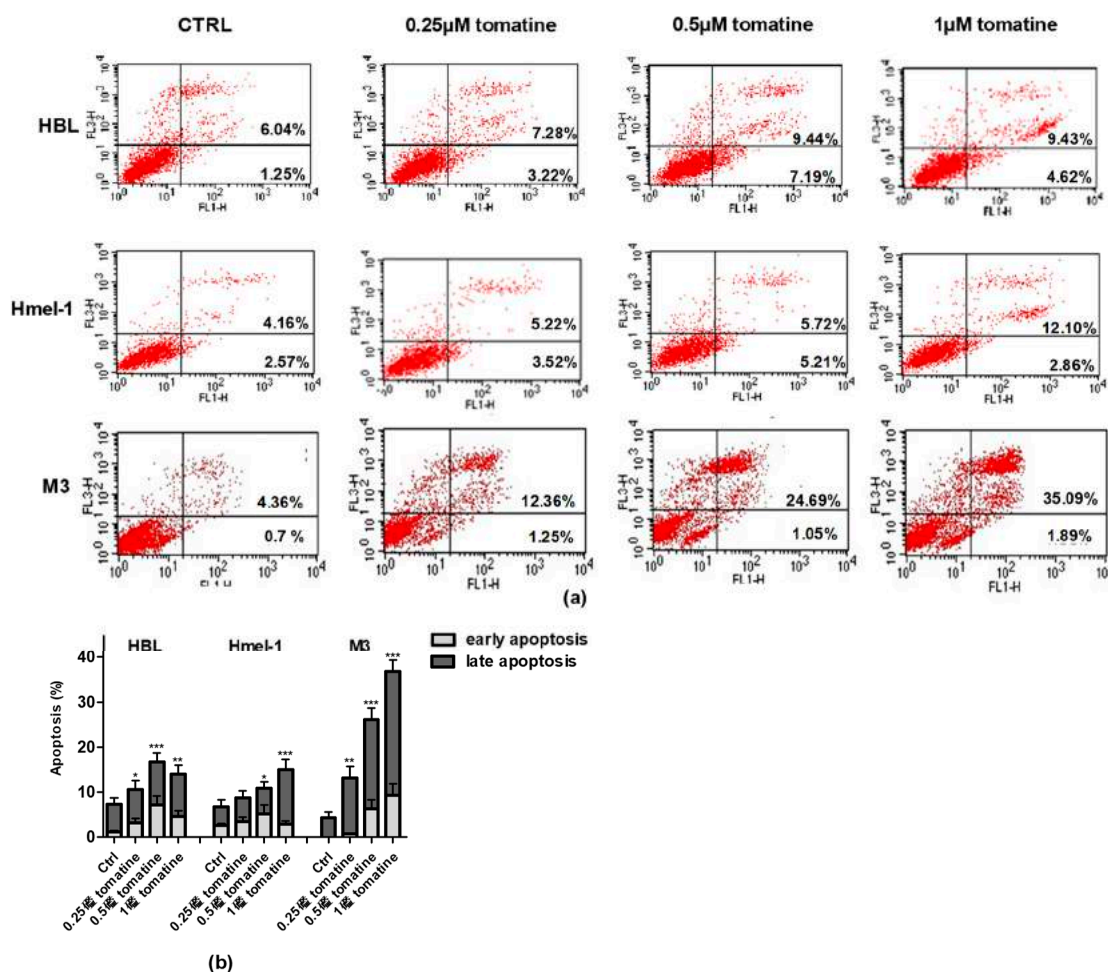


**Figure 3.** Apoptosis induced by tomatine in melanoma cell lines. HBL, hmel-1, and M3 cell lines were treated for 24 h with tomatine at 0.25, 0.5, and 1  $\mu$ M (expressed as  $\alpha$ -tomatine concentrations); afterwards, the cells were stained with annexin-V/PI and analyzed by FACS. (a) Representative analysis of annexin-V/PI stained cells; (b) histograms of the % of annexin-V (early apoptosis) and annexin-V/PI (late apoptosis)-positive cells in vehicle-treated cells and tomatine-treated ones. The results show the mean  $\pm$  SD of three independent experiments. Data are shown as mean  $\pm$  SD of three different experiments performed in triplicate. \*  $p < 0.05$ , \*\*  $p < 0.01$ , and \*\*\*  $p < 0.001$  of apoptosis (early + late), with respect to vehicle-treated cells.

#### 2.4. Tomatine Induced Autophagy in BRAF Wild-Type Cell Line

We previously reported that high levels of autophagy and chronic ER stress were strictly associated with a  $V^{600}$ BRAF genetic context in MM cells [1]. Hence, we investigated the effects of tomatine on the activation/expression levels of p-eIF2 $\alpha$  and LC3 II/I in hmel-1 and M3 cell lines, compared to BRAFwt HBL cells. For this purpose, Western blotting analysis was performed on protein extracts from all cell lines treated with tomatine at 1  $\mu$ M in terms of  $\alpha$ -tomatine versus vehicle-treated ones. We found that tomatine induced a significant increase in p-eIF2 $\alpha$  levels only in HBL cells (Figure 4a). No effect was found in other cell lines. According to these results, we also found an increased LC3II/I ratio in only the BRAFwt cell line (HBL), while no significant variations in both p-eIF2 $\alpha$  and LC3II/I levels were observed in hmel-1 and M3 cell lines (Figure 4b). Furthermore, as also reported in previous research, high levels of autophagy and ERK phosphorylation were strictly associated to a  $V^{600}$ BRAF genetic context [1]. We investigated the effect of tomatine on ERK1/2 activation to understand if the tomatine-dependent increase of autophagy and p-eIF2 $\alpha$  levels could be associated with increased phosphorylation of ERK1/2. Western blot analysis showed a significant increase of p-ERK levels after

treatment with 1  $\mu$ M tomatine in HBL cells, whereas no significant variations were observed in hmel-1 and M3 cell lines (Figure 4c). Collectively, these results suggest that tomatine induced ER stress, autophagy, and apoptosis in the HBL cell line with BRAFwt status.

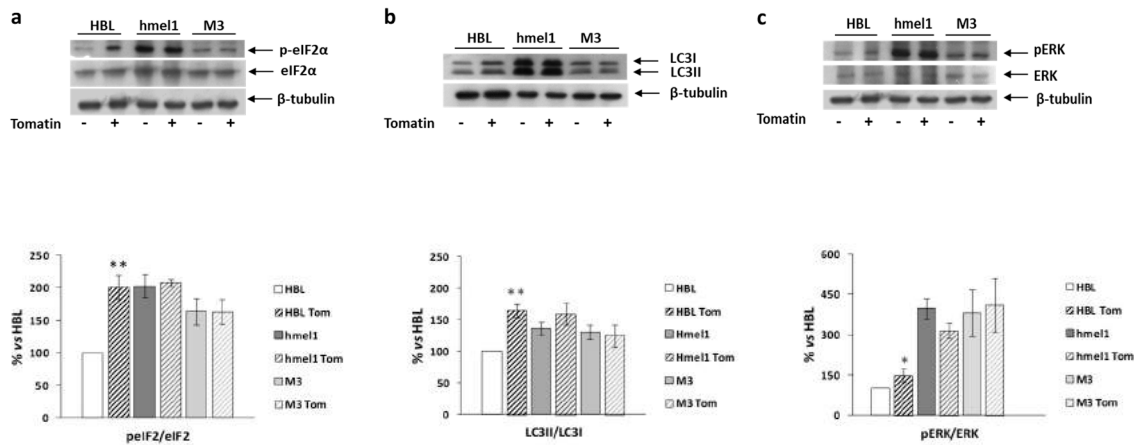


**Figure 4.** The effect of tomatine on the activation/expression levels of p-eIF2 $\alpha$  and LC3 II/I, respectively, and on ERK phosphorylation levels in hmel-1 and M3 cells compared to BRAFwt HBL cells. (a) Representative Western blot of eIF2 $\alpha$  and p-eIF2 $\alpha$  levels, performed on whole cell lysates. Bar graph shows the p-eIF2 $\alpha$ /eIF2 $\alpha$  ratio calculated by densitometric analysis of the protein bands, normalized to tubulin, used as loading control. (b) Representative Western blot of LC3-I and LC3-II levels, performed on whole cell lysates. Bar graph shows the LC3-II/LC3-I ratio calculated by densitometric analysis of the protein bands, normalized to tubulin, used as loading control. (c) Representative Western blot analyses of pERK and ERK levels on whole cell lysates. Bar graph shows the pERK/ERK ratio, calculated by densitometric analysis of the protein bands, normalized to tubulin, used as loading control. Values are the mean  $\pm$  SEM of three independent experiments, expressed as a percentage of the HBL value. Significance was calculated with Student's test; \*  $p < 0.05$ , \*\*  $p < 0.005$  vs. vehicle-treated cells.

### 2.5. Tomatine Displayed Antiangiogenic and Vascular Disrupting Effect

The ability of N-MVECs (microvascular endothelial cells, human dermal microvascular endothelial cells) to move within ECM (extracellular matrix) is the basic requirement in the formation of ordered cords of endothelial cells. The final angiogenic event requires N-MVEC to organize in the interconnection of tubular structures appointed to give origin to blood vessels. We studied capillary tube formation on matrigel. In this assay, N-MVEC produced elongated processes that resulted in the formation of anastomosing cords of cells resembling a capillary plexus [19]. We investigated the effects of tomatine in melanoma-dependent angiogenesis in a vascular-disrupting assay and a neoangiogenesis assay, as described in the Material and Methods section. The addition of tomatine (0.5 and 1  $\mu$ M in terms of  $\alpha$ -tomatine) to the newly formed capillary-like structures, after 3 h incubation with melanoma cell conditioned media (CM), disrupted the network in the presence of HBL and M3 CM, and this effect increased over the following 9 h (data not shown). In contrast, hmel-1-CM seemed to protect the vessels from the vascular disruption activity of tomatine (Figure 5).

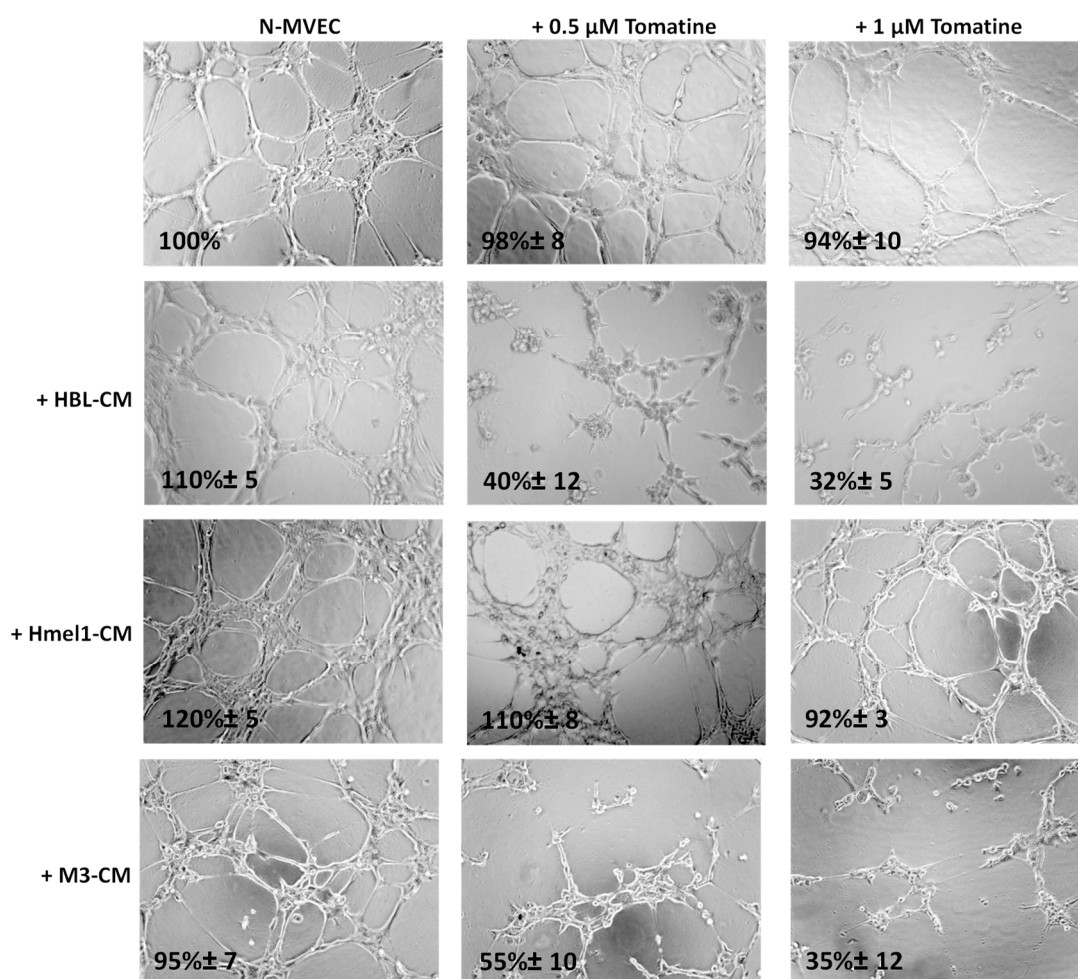


**Figure 5.** Effect of tomatine on melanoma-dependent vascular disruption of N-MVECs (microvascular endothelial cells, human dermal microvascular endothelial cells). Cells ( $12 \times 10^3$ ) were plated on 10–12 mg/mL matrigel-coated tissue culture wells, treated immediately with melanoma cells CM, and after 3 h with tomatine (0.5 and 1  $\mu\text{M}$  in terms of  $\alpha$ -tomatine). The cells were photographed 9 h after plating. Six to nine photographic fields from three plates were scanned for each point, considering as 100% the area occupied by untreated N-MVECs. The results shown are representative of three different experiments.

Since the treatment of N-MVECs with hmel-1-CM stimulated neoangiogenesis and protected endothelial cells from tomatine inhibitory effects, we evaluated the release of VEGF by tumor cells before and after tomatine treatment. The data reported in Figure 6a demonstrated that hmel-1 released the highest amount of VEGF with respect to HBL and M3 cells (1383.41 vs. 326.98 and 73.38 pg/mL). Furthermore, the addition of tomatine to tumor cell lines drastically inhibited the release of the proangiogenic factor from hmel-1 cells with regards to HBL and M3 (837.25 vs. 261.91 and 75.59 pg/mL). Based on these results, a new capillary morphogenesis assay was performed in the presence of hmel-1-CM from cells pretreated with 1  $\mu\text{M}$  in terms of  $\alpha$ -tomatine for 24 h. As shown in Figure 6b, the proangiogenic effect shown in N-MVECs in the presence of hmel-1-CM was drastically reduced with the tomatine-pretreated hmel-1-CM. In order to evaluate whether the effect of tomatine is closely linked to the tumor-derived VEGF, we carried out a capillary morphogenesis assay by adding external VEGF (Figure 6c) to N-MVECs in the experimental conditions previously described. The angiogenetic ability of N-MVECs was partially restored by adding VEGF to pretreated hmel-1-CM, which revealed a correlation between the effects of tomatine treatment and the VEGF released by hmel-1.

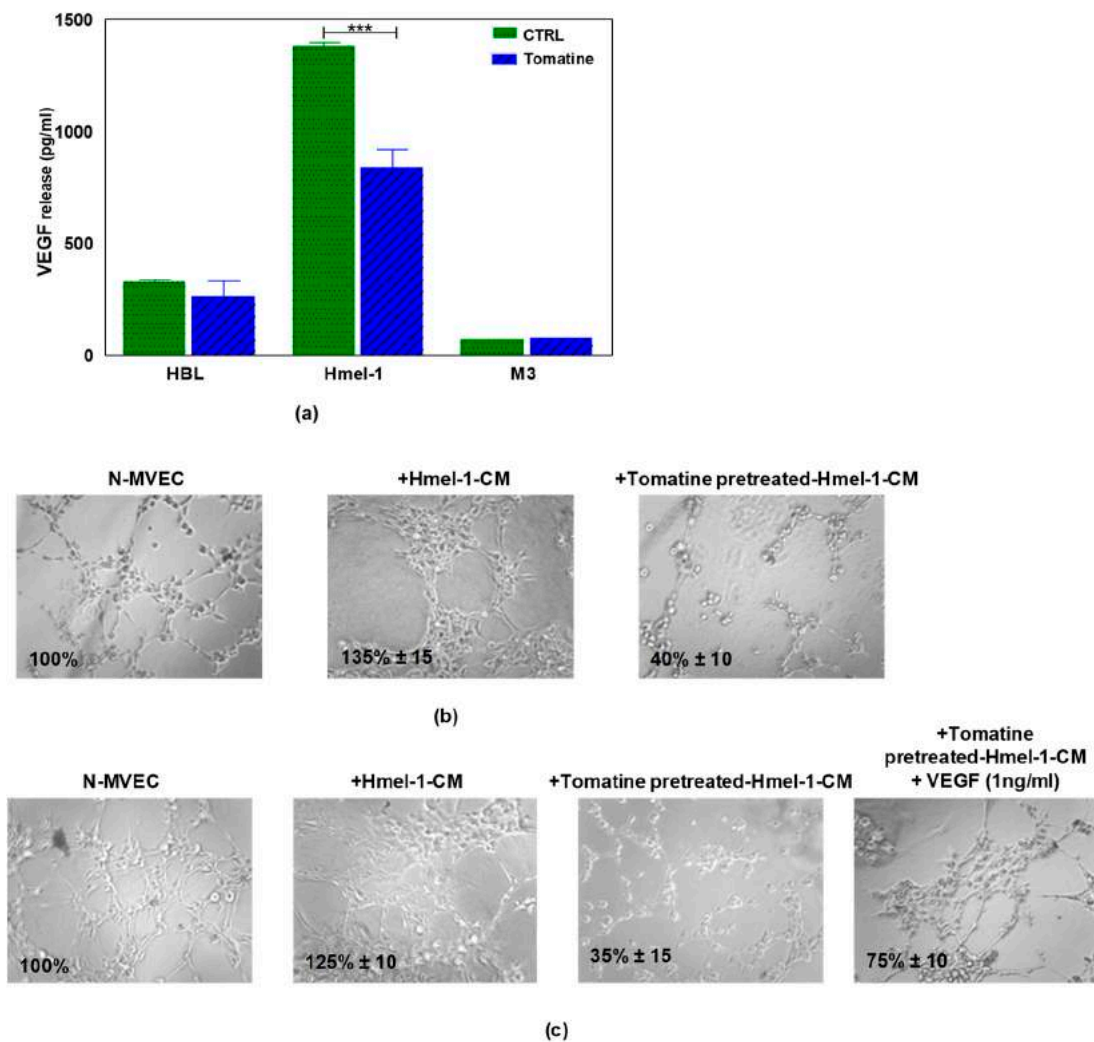


**Figure 6.** Effect of tomatine on VEGF release by metastatic melanoma (MM) cell lines and capillary morphogenesis in N-MVECs. **(a)** The graph displays the VEGF release by HBL, hmel-1, and M3 cells in basal conditions and after tomatine (1  $\mu$ M in terms of  $\alpha$ -tomatine) treatment. Values are means  $\pm$  SD of three independent experiments; significance was calculated with Student's *t*-test; \*\*\*  $p < 0.001$  significantly different from basal control. **(b)** Effect of conditioned medium of hmel-1 and tomatine-pretreated hmel-1-CM, with or without external VEGF. **(c)** On capillary morphogenesis of N-MVECs.

We further evaluated the tomatine effects on tumor neoangiogenesis. Figure 7 shows that after 6 h from plating on matrigel, N-MVECs produced networks of branching cords of cells. The ability to form a stable and tight network can be strengthened by the addition of melanoma cell CM. In particular, a stronger increase of the capillary formation (130%  $\pm$  10%) was observed in the presence of CM from a highly MM hmel-1 cell line; the phenomenon was minor (120%  $\pm$  15%) in HBL-CM and it was almost absent in M3-CM. In the presence of 0.5  $\mu$ M in terms of  $\alpha$ -tomatine, the neoangiogenesis was not affected by hmel-1-CM, while it decreased about 30–40% in the presence of HBL-CM and M3-CM, suggesting less proangiogenic properties of the latter compared to the hmel-1 cell line.



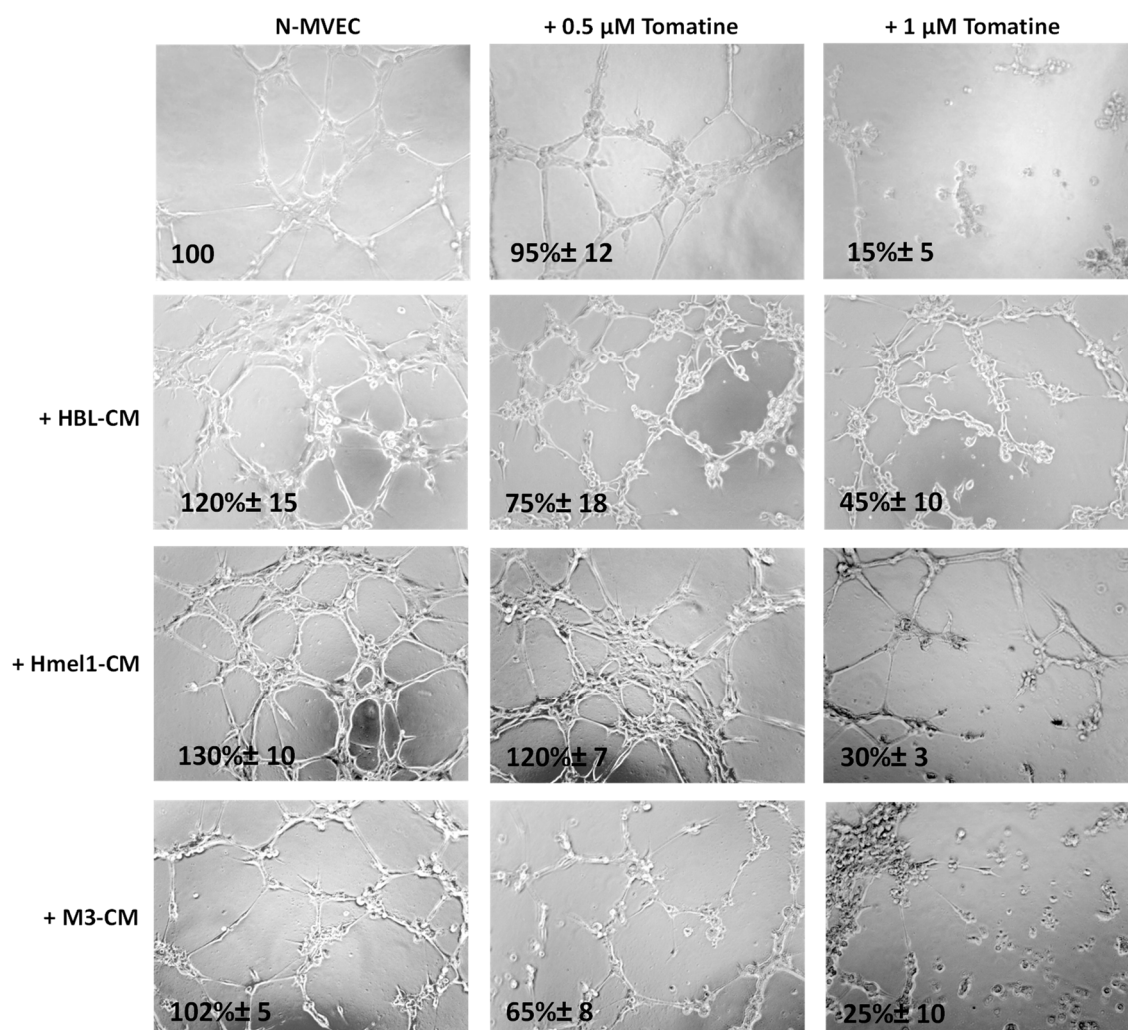


**Figure 7.** Effect of tomatine on melanoma-dependent neoangiogenesis of N-MVECs. Cells were plated on matrigel-coated tissue culture wells and treated with melanoma cell CM in the presence or absence of tomatine (0.5 and 1  $\mu$ M expressed as  $\alpha$ -tomatine concentrations). The cells were photographed 6 h after plating. The results shown are representative of three different experiments.

Interestingly, we observed a substantial reduction of neoangiogenesis when we used 1  $\mu$ M tomatine in all the conditions, demonstrating the notable effect of this compound on neoangiogenesis.

### 3. Discussion

Several studies have indicated that  $\alpha$ -tomatine inhibits the growth of various human cancer cell lines within 1–48 h in a wide range of concentrations [20–25]. Our results show that commercial tomatine inhibited both the cell invasion and cell viability of BRAFwt and <sup>V600</sup>BRAF metastatic melanoma cells within the range of 0.5–1  $\mu$ M (expressed as  $\alpha$ -tomatine concentration) after 24 h treatment and highlight a previously unknown ability of the bioactive compound as an antiangiogenic and vasculature-disrupting agent that is far less toxic to normal fibroblasts. We found that tomatine induced an autophagic phenotype in BRAFwt cells, similar to that displayed in basal conditions by <sup>V600</sup>BRAF cell lines. It is noteworthy that together with the autophagic phenotype, BRAFwt cells (HBL) treated with tomatine showed similar levels of ER stress marker p-eIF2 $\alpha$  to those of hmel1 and M3 at the basal level, together with an increase of p-ERK1/2 level, thus suggesting that these conditions are a prerequisite for cell death induction by tomatine in such cells. ER stress is an adaptive response of cells, occurring when ER fails to cope with the excess of misfolded/unfolded protein loads, and it activates

the unfolded protein response (UPR). The activation of this pathway may drive back the system to the former condition through the activation of autophagy, or alternatively, may result in apoptotic cell death during excessive levels of ER stress [26]. If the ER stress is not tolerable, cells undergo apoptosis, and the UPR promotes the phosphorylation of the  $\alpha$  subunit of translation initiation factor 2 (eIF2 $\alpha$ ), generating a general attenuation of translational processes [27]. Therefore, we can speculate that the activation of the ER stress response led to an autophagic phenotype and a general attenuation of translational processes, with a consequent reduction of cell proliferation and apoptosis induction in the HBL cell line.

Instead, the physiological levels of ER stress and ERK1/2 activation and autophagy were enough to shift the balance towards apoptosis in the other cell lines, and perhaps, the apoptosis expanded in M3 from prolonged ER stress response activation in these cells. Accordingly, Wang et al. [25] reported that  $\alpha$ -tomatine induced ER stress and triggered both caspase-dependent and caspase-independent apoptosis. Additionally, several authors recently reported a correlation between cellular stress response, translational reprogramming, and autophagy and apoptosis induction in the presence of a persistent upstream stress condition [28–30].

Translational control during endoplasmic reticulum stress plays a crucial role in tumor-dependent angiogenic processes. In basal conditions, hypoxia is associated with an increase in HIF-1 $\alpha$  levels and a consequent increase of VEGF expression [31]. However, an upregulation of VEGF is also induced by ER stress [32]. The translation of VEGF [33], as well as of genes implicated in autophagy [34], is regulated by eIF2 $\alpha$  phosphorylation. As a consequence, p-eIF2 $\alpha$  induces an increase in nutrient supply by stimulating angiogenesis and recycling organelles. Accordingly, we found that hmel1 cells, which displayed a high basal level of p-eIF2 $\alpha$  and HIF-1 $\alpha$ , as reported in our previous characterization of such cells [1], released the highest amount of VEGF compared to other cell lines. Therefore, we can speculate that in hmel1, as a result of a basal condition of ER stress, a high physiological level of p-eIF2 $\alpha$  sustained the release of VEGF, which was strongly reduced by tomatine. Hence, the principal effect of tomatine in the hmel1 cell line may be related to the inhibition of VEGF release by cells, as demonstrated by the VEGF-restoring effect on capillary tube formation in the specific assay conducted by adding external VEGF to N-MVECs in the presence of hmel1-pretreated tomatine-derived CM. The CM from other cell lines was less protective against the tomatine antiangiogenic effect, perhaps because these cells released less VEGF than hmel1; other proangiogenic factors may be involved. Aside from the need to confirm our in-vitro results in corresponding in vivo models, collectively, our findings show that tomatine inhibits cell viability as well as the invasive behavior of MM cell lines, and, more importantly, displays valuable antiangiogenic and vascular disrupting effects only in experimental conditions that mimic a proangiogenic tumor microenvironment, perhaps by affecting the ER/p-eIF2 $\alpha$ /VEGF axis of tumor angiogenesis.

## 4. Materials and Methods

### 4.1. Tomatine: HPLC of Chemical Compounds

Tomatine (>75%) was purchased from TCI Chemicals Europe (Zwijndrecht, Belgium). Its actual composition was determined by reverse-phase liquid chromatography, using an HPLC Agilent 1200 Series system (Agilent Technologies, Milano, Italy) coupled with a TSQ Quantum Access mass spectrometer (Thermo Scientific, Milano, Italy), equipped with Electro-Spray ion source (ESI) and triple quadrupole analyzer (QqQ), employing the method previously described by Tamasi et al. [13].

### 4.2. Cell Culture

In the current study, three melanoma cell lines (hmel-1, M3, HBL) were utilized. Hmel-1 and M3 were extracted from skin metastases obtained from human sporadic melanoma biopsy specimens after the informed consent of patients. All cell lines were genotyped for NRAS BRAF and MC1R (Table 1), as described in [1,35,36]. HBL melanoma cells (BRAFWt) were a gift from Prof. G. Ghanem,

Université de Bruxelles, Belgium, which were used as a control for all experiments. In addition, endothelial cells were studied. In detail, N-MVECs (microvascular endothelial cells, human dermal microvascular endothelial cells) were purchased from Lonza (Basel, Switzerland). Cell culture media used for MM cells was high-glucose Dulbecco's modified Eagle's medium (DMEM) supplemented with 10% (*v/v*) fetal bovine serum (FBS), 1% (*v/v*) l-glutamine, and 1% (*v/v*) penicillin/streptomycin at 37 °C in a humidified atmosphere at 5% CO<sub>2</sub>. All materials for cell culturing were purchased from EuroClone, Italy. The EGM2-2 Endothelial Growth Medium-2 BulletKit™ from Lonza, Switzerland, was used for N-MVEC cell culture. N-FB (normal human dermal fibroblasts, Lonza, Switzerland) were grown in an FGM-2 BulletKit (Lonza, Switzerland) supplemented with 2% FBS.

**Table 1.** Genotype of melanoma cell lines analyzed.

Cell Line	Extracted from	MC1R	NRAS	BRAF Exon 15
HBL	metastasis	wt/wt	wt/wt	wt/wt
Hmel-1	metastasis	wt/wt	wt/wt	V600 K/wt
M3	metastasis	D184H/D184H	wt/wt	V600E/V600E

#### 4.3. Cytotoxic Assay

Cells were seeded in 96-well culture plates at a density of 5000 cells/well. After 24 h, the culture medium was replaced with fresh medium (100 µL), with tomatine at increasing concentrations ranging between 0.12 and 2.38 mg/L (corresponding to 0.1–2 µM of α-tomatine; Figure 1). Then, cells were further incubated for 24 h and cell viability was assessed by MTT assay, as previously described [37]. Results were expressed as IC<sub>50</sub> (the half-maximal inhibitory concentration of α-tomatine) or as % cell viability at the tested doses and were reported as dose–response curves using Calcsyn software, which allows IC<sub>50</sub> determination.

#### 4.4. Invasion Assay

A Boyden chamber was used to evaluate invasive ability through matrigel-coated porous filters, as described by [38]. Briefly, 50 mL of cell suspension ( $8 \times 10^3$  cells) was placed in the upper compartment of the chamber, and migration was allowed to occur for 6 h. For assessment of the invasion, tomatine (0.5 and 1 µM in terms of α-tomatine) were dissolved in culture medium and placed in the upper and lower wells. The filter was removed and fixed in methanol. Nonmigrating cells on the upper surface of the filter were removed with a cotton swab, while migrated cells, adhered on the lower filter surface (pore-size 8 µm), were stained with Diff-Quick (Mertz-Dade AG, Dade International, Milan, Italy) and counted using a light microscope (OLYMPUS CKX41) on the whole migration surface per well. Mobilization was measured by the number of cells moving across the filter. Experiments were performed in triplicate. Migration was expressed as the mean ± standard deviation (SD) of the percentage of basal response. Data were indicated with \*  $p < 0.01$ , and \*\*  $p < 0.001$  compared to relative control.

#### 4.5. Apoptosis Assay

The annexin-V–propidium iodide (PI) staining apoptosis test [36] was performed on HBL, hmel-1, and M3 cells after 24 h of incubation, with tomatine in the range of 0.25–1 µM in terms of α-tomatine. The cells were treated according to the instructions provided by the manufacturer. Briefly, after incubation time (24 h) at 37 °C and 5% CO<sub>2</sub>, cells were washed with PBS, suspended in binding buffer and then added with annexin-V FITC and PI for 20 min. The samples were then read by a flow cytometer, FACScan (Becton Dickinson, Milano, Italy).

#### 4.6. Western Blot Analysis

Cells were suspended in hypotonic medium supplemented with an antiproteases cocktail tablet (Roche, Basel, Switzerland) and freeze-thawed three times to obtain total proteins. Western blotting analysis was performed, essentially as described by Ferretta et al. [39]. Total protein content was measured by the Bradford method, and 35 µg was electrophoretically separated on 10% acrylamide gel (Tris-Tricine SDS-PAGE) and transferred to the nitrocellulose membranes of a Trans-Blot® Turbo™ Transfer Pack (#1704158, Bio-Rad, Segrate/Milano, Italy). Blots were blocked for 2 h in blocking buffer (PBS buffer, pH 7.4, with 0.2% Tween 20 and 5% nonfat milk) and incubated with primary antibody. Western blotting analysis of ERK/pERK was as described in Zanna et al. 2013 [35], and phosphorylated peIF2α/eIF2α was performed as described in Maida et al. (2019) [2]. The polyclonal antibodies, anti-eIF2α, and anti-peIF2α Ser51 were purchased from Cell Signaling Technology, Danvers, MA, USA [35]. The lipid-conjugated form of LC3 (LC3 II) localizes to the membranes of autophagosomes, and it can be separated from the nonconjugated form (LC3 I) by immuno-blotting since LC3 II migrates faster than LC3 I due to the extreme hydrophobicity of LC3 II. For LC3 detection, total cell proteins (30 µg) were separated on 12% Tris-Glycine SDS-PAGE and transferred onto nitrocellulose membranes. Western blot analysis was performed using a specific antibody against LC3B (Cell Signaling Technology). The secondary antibody was anti-rabbit HRP and anti-mouse HRP (Millipore, Milano, Italy). Protein was detected by the chemiluminescent detection system (Bio-Rad), and the signal was quantified by densitometric analysis using the Chemidoc imaging system (Bio-Rad). The band intensity was quantitatively determined by densitometric analysis using Image Lab Software 5.2.1 (Bio-Rad Laboratories, Segrate/Milano Italy), and protein level intensity was normalized to tubulin expression. (Figure S3)

#### 4.7. Angiogenesis and Vascular Disruption Assays

The ability of N-MVECs to move within ECM is the basic requirement to form ordered cords of endothelial cells. The final angiogenic event requires N-MVECs to organize in interconnecting tubular structures appointed to give origin to blood vessels. We have studied the capillary tube formation on matrigel. In this assay, N-MVECs produce elongated processes that eventuate in the formation of anastomosing cords of cells resembling a capillary plexus.

Matrigel (50 µL; 10–12 mg/mL) was pipetted into 0.64 cm (diameter) tissue culture wells and polymerized for 30 min to 1 h at 37 °C, as described in [40]. N-MVECs were plated (12 × 10<sup>3</sup>/mL) in EGM-2 (endothelial growth medium, EGM™-2MV BulletKit™ Lonza, Switzerland) and 2% FBS. Capillary morphogenesis was performed in the presence of hmel-1- and M3-conditioned medium and tomatine (0.5–1 µM in terms of α-tomatine). Vascular disruption was evaluated in the same conditions as capillary morphogenesis, adding tomatine after three hours from cell seeding in the presence of the conditioned medium. The effects on morphogenesis and vascular disruption of endothelial cells were recorded after 6 h with an inverted microscope. Results were quantified at 6 h by measuring the percent field occupancy of the capillary projections. Six to nine photographic fields from three plates were scanned for each point.

#### 4.8. Analysis of VEGF Release

Cells were incubated with or without 1 µM tomatine, and cell supernatant from each sample was utilized for the quantification of VEGF release by the Quantikine Human VEGF immunoassay (R&D Systems Minneapolis, MN, USA), as described in [41].

**Supplementary Materials:** The following are available online at <http://www.mdpi.com/1422-0067/21/15/5243/s1>, Figure S1. Multiple Reaction Monitoring (MRM) chromatogram (via positive ion HPLC-ESI-QqQ-MS/MS analysis) of the commercial tomatine showing the presence of α-tomatine and dehydrotomatine. Figure S2: Analysis of Apoptosis after 48 h. Figure S3: Western blot images performed on whole cell lysates and densitometric analysis of protein expression.



**Author Contributions:** Conceptualization, A.A., L.P., and G.G.; methodology, S.S., R.M.I., L.P., A.F., and I.M.; formal analysis, S.S., A.A., L.P., and G.G.; investigation, S.S., L.P., R.M.I., A.F., and I.M.; data curation, A.A., L.P., S.G., A.F., and G.G.; writing—original draft preparation, S.S., A.A., L.P., S.G., and G.G.; writing—review and editing, S.T., T.C., G.T., C.R., and M.M.; supervision, A.A. and G.G.; funding acquisition, A.A. All authors have read and agreed to the published version of the manuscript.

**Funding:** This research was funded by the Italian Ministry of Health, grant Ricerca Corrente 2018–2020 “Meccanismi e strategie per superare la farmaco-resistenza alla terapia target-oriented o all’immunoterapia nel melanoma metastatico”, and grant “Fondi di Ateneo” from the University of Bari, Italy.

**Acknowledgments:** We would like to thank Lewis Parrin for language editing.

**Conflicts of Interest:** The authors declare no conflict of interest.

## References

1. Ferretta, A.; Maida, I.; Guida, S.; Azzariti, A.; Porcelli, L.; Tommasi, S.; Zanna, P.; Cocco, T.; Guida, M.; Guida, G. New insight into the role of metabolic reprogramming in melanoma cells harboring BRAF mutations. *Biochim. Biophys. Acta* **2016**, *1863*, 2710–2718. [[CrossRef](#)] [[PubMed](#)]
2. Maida, I.; Zanna, P.; Guida, S.; Ferretta, A.; Cocco, T.; Palese, L.L.; Londei, P.; Benelli, D.; Azzariti, A.; Tommasi, S.; et al. Translational control mechanisms in cutaneous malignant melanoma: The role of eIF2 $\alpha$ . *J. Transl. Med.* **2019**, *17*, 20. [[CrossRef](#)] [[PubMed](#)]
3. Falletta, P.; Sanchez-Del-Campo, L.; Chauhan, J.; Effern, M.; Kenyon, A.; Kershaw, C.J.; Siddaway, R.; Lisle, R.; Freter, R.; Daniels, M.J.; et al. Translation reprogramming is an evolutionarily conserved driver of phenotypic plasticity and therapeutic resistance in melanoma. *Genes Dev.* **2017**, *31*, 18–33. [[CrossRef](#)] [[PubMed](#)]
4. Guida, S.; Bartolomeo, N.; Zanna, P.T.; Grieco, C.; Maida, I.; De Summa, S.; Tommasi, S.; Guida, M.; Azzariti, A.; Foti, C.; et al. Sporadic melanoma in South-Eastern Italy: The impact of melanocortin 1 receptor (MC1R) polymorphism analysis in low-risk people and report of three novel variants. *Arch. Dermatol. Res.* **2015**, *307*, 495–503. [[CrossRef](#)]
5. Guida, M.; Strippoli, S.; Ferretta, A.; Bartolomeo, N.; Porcelli, L.; Maida, I.; Azzariti, A.; Tommasi, S.; Grieco, C.; Guida, S.; et al. Detrimental effects of melanocortin-1 receptor (MC1R) variants on the clinical outcomes of BRAF V600 metastatic melanoma patients treated with BRAF inhibitors. *Pigment Cell Melanoma Res.* **2016**, *29*, 679–687. [[CrossRef](#)]
6. Binet, F.; Sapiha, P. ER stress and angiogenesis. *Cell Metab.* **2015**, *22*, 560–575. [[CrossRef](#)]
7. Bartoszewski, S.; Collawn, J.F. Unfolded protein response (UPR) integrated signaling networks determine cell fate during hypoxia. *Cell. Mol. Biol. Lett.* **2020**, *25*, 18. [[CrossRef](#)]
8. Pejin, B.; Jovanovic, K.; Mojovic, M.; Savic, A. New and highly potent antitumor natural products from marine-derived fungi: Covering the period from 2003 to 2012. *Curr. Top. Med. Chem.* **2013**, *13*, 2745–2766. [[CrossRef](#)]
9. Pejin, B.; Jovanovic, K.; Savic, A. New antitumour natural products from marine red algae: Covering the period from 2003 to 2012. *Mini-Rev. Med. Chem.* **2015**, *15*, 720–730. [[CrossRef](#)]
10. Friedman, M. Anticarcinogenic, cardioprotective, and other health benefits of tomato compounds lycopene,  $\alpha$ -tomatine, and tomatidine in pure form and in fresh and processed tomatoes. *J. Agric. Food Chem.* **2013**, *61*, 9534–9550. [[CrossRef](#)] [[PubMed](#)]
11. Friedman, M.; Levin, C.E.; Lee, S.-U.; Kim, H.-J.; Lee, I.-S.; Byun, J.-O.; Kozukue, N. Tomatine-containing green tomato extracts inhibit growth of human breast, colon, liver, and stomach cancer cells. *J. Agric. Food Chem.* **2009**, *57*, 5727–5733. [[CrossRef](#)]
12. Friedman, M. Tomato glycoalkaloids: Role in the plant and in the diet. *J. Agric. Food Chem.* **2002**, *50*, 5751–5780. [[CrossRef](#)] [[PubMed](#)]
13. Tamasi, G.; Pardini, A.; Bonechi, C.; Donati, A.; Pessina, F.; Marcolongo, P.; Gamberucci, A.; Leone, G.; Consumi, M.; Magnani, A.; et al. Characterization of nutraceutical components in tomato pulp, skin and locular gel. *Eur. Food Res. Technol.* **2019**, *245*, 907–918. [[CrossRef](#)]
14. Jiang, Q.-W.; Chen, M.-W.; Cheng, K.-J.; Yu, P.-Z.; Wei, X.; Shi, Z. Therapeutic potential of steroidal alkaloids in cancer and other diseases. *Med. Res. Rev.* **2016**, *36*, 119–143. [[CrossRef](#)] [[PubMed](#)]
15. Lee, S.-T.; Wong, P.-F.; Hooper, J.D.; Mustafa, M.R. Alpha-tomatine synergises with paclitaxel to enhance apoptosis of androgen-independent human prostate cancer PC-3 cells in vitro and in vivo. *Phytomedicine Int. J. Phytother. Phytopharm.* **2013**, *20*, 1297–1305. [[CrossRef](#)]

16. Friedman, M. Chemistry and anticarcinogenic mechanisms of glycoalkaloids produced by eggplants, potatoes, and tomatoes. *J. Agric. Food Chem.* **2015**, *63*, 3323–3337. [[CrossRef](#)]
17. Da Silva, D.C.; Andrade, P.B.; Valentão, P.; Pereira, D.M. Neurotoxicity of the steroidal alkaloids tomatine and tomatidine is RIP1 kinase- and caspase-independent and involves the eIF2 $\alpha$  branch of the endoplasmic reticulum. *J. Steroid Biochem. Mol. Biol.* **2017**, *171*, 178–186. [[CrossRef](#)]
18. Liu, C.; Yang, S.; Wang, K.; Bao, X.; Liu, Y.; Zhou, S.; Liu, H.; Qiu, Y.; Wang, T.; Yu, H. Alkaloids from Traditional Chinese Medicine against hepatocellular carcinoma. *Biomed. Pharmacother. Biomed. Pharmacother.* **2019**, *120*, 109543. [[CrossRef](#)] [[PubMed](#)]
19. Giusti, B.; Margheri, F.; Rossi, L.; Lapini, I.; Magi, A.; Serratì, S.; Chillà, A.; Laurenzana, A.; Magnelli, L.; Calorini, L.; et al. Desmoglein-2-integrin Beta-8 interaction regulates actin assembly in endothelial cells: Deregulation in systemic sclerosis. *PLoS ONE* **2013**, *8*, e68117. [[CrossRef](#)]
20. Chao, M.-W.; Chen, C.-H.; Chang, Y.-L.; Teng, C.-M.; Pan, S.-L.  $\alpha$ -Tomatine-mediated anti-cancer activity in vitro and in vivo through cell cycle- and caspase-independent pathways. *PLoS ONE* **2012**, *7*, e44093. [[CrossRef](#)]
21. Lee, K.-R.; Kozukue, N.; Han, J.-S.; Park, J.-H.; Chang, E.-Y.; Baek, E.-J.; Chang, J.-S.; Friedman, M. Glycoalkaloids and metabolites inhibit the growth of human colon (HT29) and liver (HepG2) cancer cells. *J. Agric. Food Chem.* **2004**, *52*, 2832–2839. [[CrossRef](#)] [[PubMed](#)]
22. Shieh, J.-M.; Cheng, T.-H.; Shi, M.-D.; Wu, P.-F.; Chen, Y.; Ko, S.-C.; Shih, Y.-W.  $\alpha$ -Tomatine suppresses invasion and migration of human non-small cell lung cancer NCI-H460 cells through inactivating FAK/PI3K/Akt signaling pathway and reducing binding activity of NF- $\kappa$ B. *Cell Biochem. Biophys.* **2011**, *60*, 297–310. [[CrossRef](#)] [[PubMed](#)]
23. Shih, Y.-W.; Shieh, J.-M.; Wu, P.-F.; Lee, Y.-C.; Chen, Y.-Z.; Chiang, T.-A. Alpha-tomatine inactivates PI3K/Akt and ERK signaling pathways in human lung adenocarcinoma A549 cells: Effect on metastasis. *Food Chem. Toxicol. Int. J. Publ. Br. Ind. Biol. Res. Assoc.* **2009**, *47*, 1985–1995. [[CrossRef](#)] [[PubMed](#)]
24. Lee, S.-T.; Wong, P.-F.; Cheah, S.-C.; Mustafa, M.R. Alpha-tomatine induces apoptosis and inhibits nuclear factor-kappa B activation on human prostatic adenocarcinoma PC-3 cells. *PLoS ONE* **2011**, *6*, e18915. [[CrossRef](#)]
25. Wang, F.-Z.; Dai, X.-L.; Liu, H.-Y. Molecular mechanisms underlying the  $\alpha$ -tomatine-directed apoptosis in human malignant glioblastoma cell lines A172 and U-118 MG. *Exp. Ther. Med.* **2017**, *14*, 6183–6192. [[CrossRef](#)]
26. Márton, M.; Kurucz, A.; Lizák, B.; Margittai, É.; Bánhegyi, G.; Kapuy, O. A systems biological view of life-and-death decision with respect to endoplasmic reticulum stress—The role of pERK pathway. *Int. J. Mol. Sci.* **2017**, *18*, 58. [[CrossRef](#)]
27. Liu, C.Y.; Kaufman, R.J. The unfolded protein response. *J. Cell Sci.* **2003**, *116*, 1861–1862. [[CrossRef](#)]
28. Marciniak, S.J.; Yun, C.Y.; Oyadomari, S.; Novoa, I.; Zhang, Y.; Jungreis, R.; Nagata, K.; Harding, H.P.; Ron, D. CHOP induces death by promoting protein synthesis and oxidation in the stressed endoplasmic reticulum. *Genes Dev.* **2004**, *18*, 3066–3077. [[CrossRef](#)]
29. McCullough, K.D.; Martindale, J.L.; Klotz, L.O.; Aw, T.Y.; Holbrook, N.J. Gadd153 sensitizes cells to endoplasmic reticulum stress by down-regulating Bcl2 and perturbing the cellular redox state. *Mol. Cell. Biol.* **2001**, *21*, 1249–1259. [[CrossRef](#)]
30. García-Jiménez, C.; Goding, C.R. Starvation and pseudo-starvation as drivers of cancer metastasis through translation reprogramming. *Cell Metab.* **2019**, *29*, 254–267. [[CrossRef](#)]
31. Semenza, G.L. Targeting hypoxia-inducible factor 1 to stimulate tissue vascularization. *J. Investig. Med. Off. Publ. Am. Fed. Clin. Res.* **2016**, *64*, 361–363. [[CrossRef](#)] [[PubMed](#)]
32. Pereira, E.R.; Liao, N.; Neale, G.A.; Hendershot, L.M. Transcriptional and post-transcriptional regulation of proangiogenic factors by the unfolded protein response. *PLoS ONE* **2010**, *5*. [[CrossRef](#)] [[PubMed](#)]
33. Stein, I.; Itin, A.; Einat, P.; Skaliter, R.; Grossman, Z.; Keshet, E. Translation of vascular endothelial growth factor mRNA by internal ribosome entry: Implications for translation under hypoxia. *Mol. Cell. Biol.* **1998**, *18*, 3112–3119. [[CrossRef](#)] [[PubMed](#)]
34. Yaman, I.; Fernandez, J.; Liu, H.; Caprara, M.; Komar, A.A.; Koromilas, A.E.; Zhou, L.; Snider, M.D.; Scheuner, D.; Kaufman, R.J.; et al. The zipper model of translational control: A small upstream ORF is the switch that controls structural remodeling of an mRNA leader. *Cell* **2003**, *113*, 519–531. [[CrossRef](#)]

35. Zanna, P.; Maida, I.; Grieco, C.; Guida, S.; Turpin Sevilla, M.C.; De Summa, S.; Tommasi, S.; Vena, G.A.; Filotico, R.; Guida, G. Three novel human sporadic melanoma cell lines: Signaling pathways controlled by MC1R, BRAF and  $\beta$ -catenins. *J. Biol. Regul. Homeost. Agents* **2013**, *27*, 131–141.
36. Zanna, P.; Maida, I.; Turpin Sevilla, M.C.; Susca, F.C.; Filotico, R.; Arciuli, M.; Cassano, N.; Vena, G.A.; Cicero, R.; Guida, G. Molecular characterization of novel melanoma cell lines. *J. Biol. Regul. Homeost. Agents* **2011**, *25*, 239–247.
37. Porcelli, L.; Guida, G.; Quatralo, A.E.; Cocco, T.; Sidella, L.; Maida, I.; Iacobazzi, R.M.; Ferretta, A.; Stolfa, D.A.; Strippoli, S.; et al. Aurora kinase B inhibition reduces the proliferation of metastatic melanoma cells and enhances the response to chemotherapy. *J. Transl. Med.* **2015**, *13*, 26. [[CrossRef](#)]
38. Ciavarella, S.; Laurenzana, A.; De Summa, S.; Pilato, B.; Chillà, A.; Lacalamita, R.; Minoia, C.; Margheri, F.; Iacobazzi, A.; Rana, A.; et al. u-PAR expression in cancer associated fibroblast: New acquisitions in multiple myeloma progression. *BMC Cancer* **2017**, *17*, 215. [[CrossRef](#)]
39. Ferretta, A.; Gaballo, A.; Tanzarella, P.; Piccoli, C.; Capitanio, N.; Nico, B.; Annese, T.; Di Paola, M.; Dell'aquila, C.; De Mari, M.; et al. Effect of resveratrol on mitochondrial function: Implications in parkin-associated familial Parkinson's disease. *Biochim. Biophys. Acta* **2014**, *1842*, 902–915. [[CrossRef](#)]
40. Margheri, F.; Schiavone, N.; Papucci, L.; Magnelli, L.; Serratì, S.; Chillà, A.; Laurenzana, A.; Bianchini, F.; Calorini, L.; Torre, E.; et al. GDF5 regulates TGF $\beta$ -dependent angiogenesis in breast carcinoma MCF-7 cells: In vitro and in vivo control by anti-TGF $\beta$  peptides. *PLoS ONE* **2012**, *7*, e50342. [[CrossRef](#)]
41. Azzariti, A.; Porcelli, L.; Mangia, A.; Saponaro, C.; Quatralo, A.E.; Popescu, O.S.; Strippoli, S.; Simone, G.; Paradiso, A.; Guida, M. Irradiation-induced angiosarcoma and anti-angiogenic therapy: A therapeutic hope? *Exp. Cell Res.* **2014**, *321*, 240–247. [[CrossRef](#)] [[PubMed](#)]



© 2020 by the authors. Licensee MDPI, Basel, Switzerland. This article is an open access article distributed under the terms and conditions of the Creative Commons Attribution (CC BY) license (<http://creativecommons.org/licenses/by/4.0/>).

mutation/copy number analyses will provide more objective evidence; but to date, no clear differentiating genomic characteristics have been identified that can unambiguously separate individual cases. We acknowledge our study is small and we hope that large collaborations, such as the Prospective Cutaneous Lymphoma International Prognostic Index, will help us investigate this interesting subgroup in more detail.

Crystal Gao, MBBS,<sup>a,b</sup> Christopher J. McCormack, FACD,<sup>c,d</sup> Carrie van der Weyden, FRACP, FRCPA,<sup>a</sup> Robert Twigger, RN,<sup>a</sup> Odette Buelens, MANP,<sup>a</sup> Stephen Lade, FRCPA,<sup>e</sup> Christine Khoo, FRCPA,<sup>e</sup> Belinda A. Campbell FRANZCR,<sup>f,g</sup> Michelle Goh, FACD,<sup>c,d</sup> Penny McKelvie, FRCPA,<sup>b</sup> and H. Miles Prince, FRACP, FRCPA<sup>a,b,i</sup>

From the Department of Clinical Haematology, Peter MacCallum Cancer Centre and Royal Melbourne Hospital, Melbourne<sup>a</sup>; the Faculty of Medicine, Nursing, and Health Sciences, Monash University, Clayton<sup>b</sup>; the Department of Surgical Oncology, Peter MacCallum Cancer Centre, Melbourne<sup>c</sup>; the Department of Dermatology, St Vincent's Hospital, Melbourne<sup>d</sup>; the Departments of Pathology<sup>e</sup> and Radiation Oncology,<sup>f</sup> Peter MacCallum Cancer Centre, Melbourne; the Department of Clinical Pathology, University of Melbourne, Parkville<sup>g</sup>; the Department of Pathology, St Vincent's Hospital, Melbourne<sup>b</sup>; and Sir Peter MacCallum Department of Oncology, University of Melbourne, Parkville, Victoria, Australia.<sup>i</sup>

Funding sources: None.

Conflicts of interest: None disclosed.

IRB approval status: Not applicable.

Correspondence and reprint requests to: H. Miles Prince, FRACP, FRCPA, Locked Bag 1, A'Beckett St, Melbourne, VIC 8006, Australia

E-mail: [miles.prince@petermac.org](mailto:miles.prince@petermac.org)

#### REFERENCES

1. Willemze R, Jaffe ES, Burg G, et al. WHO-EORTC classification for cutaneous lymphomas. *Blood*. 2005;105(10):3768-3785.
2. Benner MF, Jansen PM, Vermeer MH, Willemze R. Prognostic factors in transformed mycosis fungoides: a retrospective analysis of 100 cases. *Blood*. 2012;119(7):1643-1649.
3. Kang SK, Chang SE, Choi JH, Sung KJ, Moon KC, Koh JK. Coexistence of CD30-positive anaplastic large cell lymphoma and mycosis fungoides. *Clin Exp Dermatol*. 2002;27(3):212-215.

4. Kadin ME. CD30-rich transformed mycosis fungoides or anaplastic large cell lymphoma? How to get it right. *Br J Dermatol*. 2015;172(6):1478-1479.
5. Fauconneau A, Pham-Ledard A, Cappellen D, et al. Assessment of diagnostic criteria between primary cutaneous anaplastic large-cell lymphoma and CD30-rich transformed mycosis fungoides; a study of 66 cases. *Br J Dermatol*. 2015;172(6):1547-1554.

<https://doi.org/10.1016/j.jaad.2020.04.073>

### Atrophic and hypertrophic skin photoaging and melanocortin-1 receptor (MC1R): the missing link



To the Editor: Photoaging has recently been classified as either atrophic photoaging (AP), characterized by dyspigmentation, erythema, telangiectasia, fine wrinkling, and a tendency to skin cancers, or hypertrophic photoaging (HP), characterized by deep/coarse wrinkles and increased elastosis.<sup>1</sup> However, information regarding the relative genetic backgrounds has not yet been provided.

Recently, we demonstrated different skin photoaging features in individuals with MC1R polymorphisms.<sup>2</sup> The MC1R gene codes for a transmembrane receptor with a high affinity for alpha-melanocyte stimulating hormone. Over 200 MC1R polymorphisms have been described, some showing an impaired pigmentary function. However, other functions, such as antioxidant and DNA repair, have been associated with the same receptor, explaining the association of MC1R polymorphisms not only with the red hair color phenotype (red hair, fair skin, freckles) but also with an increased risk of skin cancers and photoaging.<sup>3,4</sup>

This study aimed to assess the previously unexplored correlation between MC1R status and AP, HP, or control skin photoaging types. The secondary objective was to define the groups with noninvasive imaging.

This analysis was performed with data from a previously published prospective, genetic study of correlations between MC1R and skin photoaging features, revealed by means of a noninvasive imaging technique, standard digital photography with features count (SDP-FC) and reflectance confocal microscopy (RCM) (Supplemental Table I; available via Mendeley at <https://doi.org/10.17632/9nffbwr37j.1>).<sup>2</sup> The study followed the Declaration of Helsinki principles.

Skin photoaging type classification was performed according to erythema and coarse/pronounced wrinkles, as performed by Sachs et al<sup>1</sup>;

**Table I.** Baseline characteristics and statistical analyses of the study population according to clinical and demographic characteristics, MC1R genotype status, standard digital photography and RCM imaging features, grouped according to atrophic or hypertrophic skin photoaging

Characteristics	Total (N = 58)	AP (n = 17)	HP (n = 24)	Control (n = 17)	P value (1-way ANOVA)
Age, y, mean $\pm$ SD (range)	53.1 $\pm$ 3.5 (49-58)	53.3 $\pm$ 3.9 (50-56)	54.2 $\pm$ 3.1 (51-57)	51.5 $\pm$ 3.1 (49-58)	.063
MC1R main polymorphisms,* n (%)	19 (32.8)	15 (62.5) <sup>†‡</sup>	2 (11.8) <sup>†</sup>	2 (11.8) <sup>‡</sup>	.000
Current smokers, n (%)	22 (37.9)	3 (17.6)	11 (45.8)	8 (47.1)	.126
Alcohol consumption >3 times/ week, n (%)	6 (10.3)	3 (17.6)	3 (12.5)	0	.225
Skin color, n (%)					
Fair	2 (3.4)	1 (5.9)	0	1 (5.9)	.724
White	17 (29.3)	5 (29.4)	7 (29.2)	5 (29.4)	
Olive	39 (67.2)	11 (67.2)	17 (64.7)	11 (67.2)	
Eye color, n (%)					
Blue green	18 (31)	5 (29.4)	6 (25)	7 (41.2)	.306
Light brown	19 (32.8)	8 (47.1)	6 (25)	5 (29.4)	
Dark brown	21 (36.2)	4 (23.5)	12 (50)	5 (29.4)	
Hair color, n (%)					
Red/blonde	6 (10.3)	3 (17.6)	1 (4.2)	2 (11.8)	.565
Brown	24 (41.4)	7 (41.2)	12 (50)	5 (29.4)	
Black	28 (48.3)	7 (41.2)	11 (45.8)	10 (58.8)	
Fitzpatrick phototype, n (%)					
I	2 (3.4)	1 (5.9)	0	1 (5.9)	.451
II	33 (56.9)	11 (64.7)	13 (54.2)	9 (52.9)	
III	23 (39.7)	5 (29.4)	11 (45.8)	7 (41.2)	
Average days of sun exposure per annum, mean $\pm$ SD	11.8 $\pm$ 11.1	12.8 $\pm$ 15.5.1	11.9 $\pm$ 10.2	10.5 $\pm$ 7.1	.831
Standard digital photography with features count, mean $\pm$ SD					
ABS scores wrinkles	15.2 $\pm$ 9.8	15.1 $\pm$ 8.6	16.2 $\pm$ 10.9	13.6 $\pm$ 9.6	.709
ABS scores brown spot	43.3 $\pm$ 7.6	49 $\pm$ 8.8 <sup>§  </sup>	40.5 $\pm$ 5.7 <sup>§</sup>	41.6 $\pm$ 5.9 <sup>  </sup>	.001
ABS scores UV spot	28.8 $\pm$ 11.6	33.3 $\pm$ 14.7	28 $\pm$ 8.5	25.5 $\pm$ 11.3	.133
ABS scores red areas	34.9 $\pm$ 6.3	39.5 $\pm$ 4.5 <sup>§  </sup>	32.7 $\pm$ 5.8 <sup>§</sup>	33.3 $\pm$ 6.1 <sup>  </sup>	.001
ABS scores porphyrins	17.3 $\pm$ 10.8	21.2 $\pm$ 11.3	15.9 $\pm$ 9.6	15.3 $\pm$ 11.5	.208
RCM, n (%)					
Mottled pigmentation $\geq$ 50%	5 (8.6)	3 (17.6)	0	2 (11.8)	.109
Irregular honeycombed $\geq$ 50%	4 (6.9)	2 (11.8)	1 (4.2)	1 (5.9)	.64
Sebaceous gland, present	31 (53.4)	7 (41.2)	14 (58.3)	10 (58.8)	.497
Polycyclic papillary contour $\geq$ 50%	6 (10.3)	0	3 (12.5)	3 (17.6)	.225
Thin reticulated collagen $\geq$ 50%	5 (8.6)	1 (5.9)	1 (4.2)	3 (17.6)	.294
Coarse collagen $\geq$ 50%	54 (93.1)	16 (94.1)	23 (95.8)	15 (88.2)	.64
Huddled collagen $\geq$ 50%	4 (6.9)	0	4 (16.7)	0	.047
Curled bright fibers $\geq$ 50%	5 (8.6)	0	4 (16.7)	1 (5.9)	.16
Collagen score					
0	4 (6.9)	1 (5.9) <sup>¶</sup>	1 (4.2) <sup>¶</sup>	2 (11.8)	.035
1-4	46 (79.3)	16 (94.1)	16 (66.7)	14 (82.3)	
5-8	8 (13.8)	0	7 (29.1)	1 (5.9)	

ABS, absolute; ANOVA, Analysis of variance; AP, atrophic photoaging; HP, hypertrophic photoaging; MC1R, melanocortin-1 receptor; RCM, reflectance confocal microscopy; SD, standard deviation; UV, ultraviolet.

\*Include polymorphisms: R151C, R160W, D294H, I155H, V60L, V92M.

<sup>†</sup>Statistically significant with Fisher's exact test for the comparison AP versus HP;  $P < .01$ .

<sup>‡</sup>Statistically significant with Fisher's exact test for the comparison AP versus control;  $P < .01$ .

<sup>§</sup>Statistically significant with Student  $t$  test for the comparison AP versus HP;  $P < .01$ .

<sup>||</sup>Statistically significant with Student  $t$  test for the comparison AP versus control;  $P < .01$ .

<sup>¶</sup>Statistically significant with Fisher's exact test for the comparison AP versus HP;  $P < .05$ .



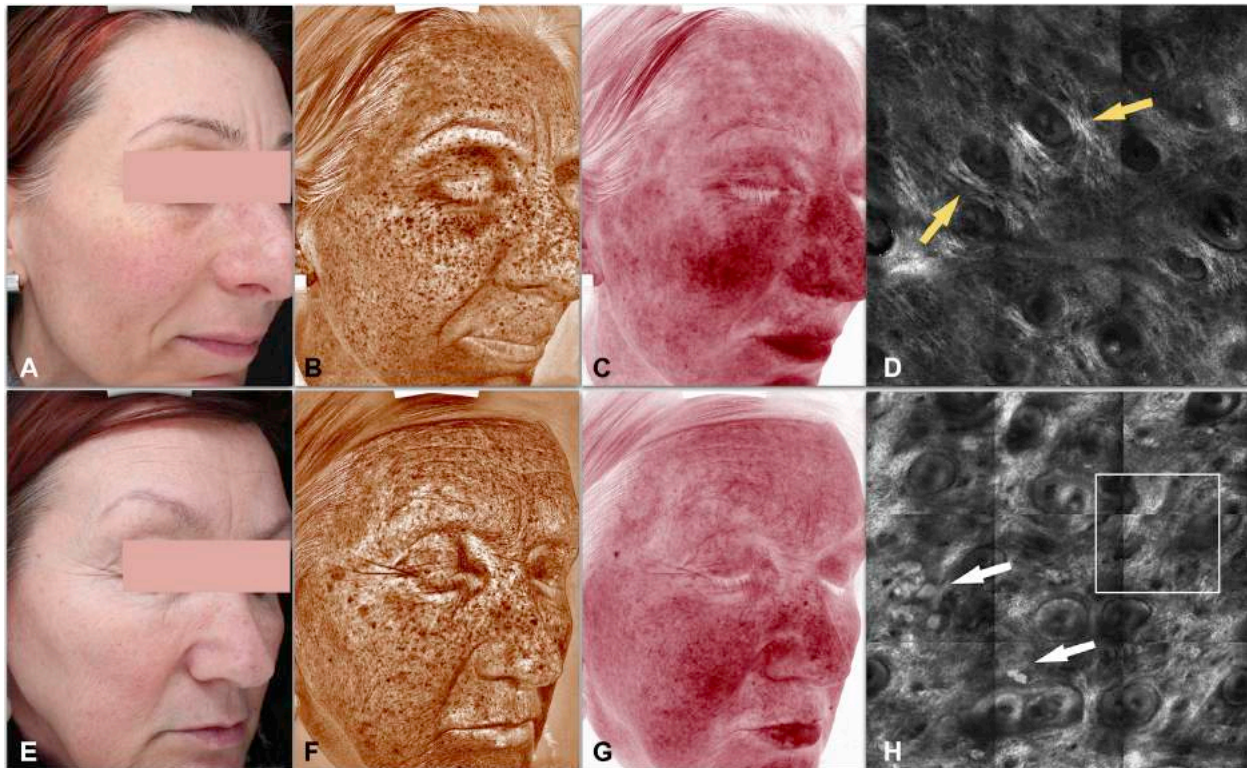


**Fig 1.** Photographs of photoaging. **A**, Standard digital, **(B)** brown spot, **(C)** red area, and **(D)** RCM image showing mainly coarse collagen (yellow arrows) in a 52-year-old woman with atrophic photoaging. **E**, Standard digital, **(F)** brown spot, **(G)** red area, and **(H)** RCM image showing huddle collagen (white arrows) and curled fibers (white square) in a 56-year-old woman classified with hypertrophic photoaging. *RCM*, Reflectance confocal microscopy.

participants without pronounced wrinkles or erythema were categorized as control individuals.

Statistical analyses were performed with SPSS (SPSS Inc, Chicago, IL), version 24.0, using 1-way analysis of variance and chi-square (or Fisher's exact test) or Student *t* test; significant results were put into a logistic regression model. A *P* value of .05 or less was considered significant.

From the sample of 100 middle-aged women (age range: 31-58 years) enrolled in the study, 58 women older than 49 years were selected for this analysis, according to the methodology of Sachs et al<sup>1</sup> (for accurate comparison). **Table I** outlines patient characteristics. The distribution of MC1R polymorphisms, found in 19 women, is presented in Supplemental Table II (available via Mendeley at <https://doi.org/10.17632/9jr452f8y5.1>).

Univariate analysis comparing AP to HP and control groups showed a significant association between skin photoaging types and MC1R status, red areas, brown areas, collagen score, and huddle collagen (**Table I** and **Fig 1**). MC1R polymorphisms and increased red and brown areas were significantly associated with AP, as compared to both HP and control individuals (*P* < .01). Collagen scores were

significantly increased in HP compared with AP participants (*P* < .05) because of increased huddle and curled fibers, or elastosis, in HP participants.<sup>1,5</sup>

Logistic regression analyses showed correlation between AP and MC1R polymorphisms, compared to both control (odds ratio [OR]: 56.2; 95% confidence interval [CI]: 7-453.2; *P* < .01) and HP participants (OR: 234.7; 95% CI: 7.7-7193.8; *P* < .01). In addition, increased red areas were associated with AP compared to HP (OR: 1.38; 95% CI: 1-1.8; *P* = .018).

This study is limited by the small number of female participants only. Despite limitations, these results suggest that the discriminatory variant for skin photoaging type is likely to be the MC1R genotype. Furthermore, this study confirms associations of increased red and brown areas with AP and different collagen morphologies with HP.<sup>1,2</sup>

*Stefania Guida, PhD,<sup>a</sup> Silvana Ciardo, BS,<sup>a</sup> Barbara De Pace, MD,<sup>a</sup> Nathalie De Carvalho, PhD,<sup>a</sup> Francesca Farnetani, MD,<sup>a</sup> Claudia Pezzini, MD,<sup>a</sup> Johanna Chester, BS,<sup>a</sup> Kaleci Shaniko, PhD,<sup>a</sup> Michele Manganelli, PhD,<sup>b</sup> Gabriella Guida, PhD,<sup>b</sup> and Giovanni Pellacani, MD<sup>a</sup>*

From the Dermatology Unit, Surgical, Medical and Dental Department of Morphological Sciences Related to Transplant, Oncological and Regenerative Medicine, University of Modena and Reggio Emilia, Modena, Italy<sup>a</sup>; and Molecular Biology Section, Department of Basic Medical Sciences Neurosciences and Sense Organs, University of Bari, Italy.<sup>b</sup>

Funding sources: None.

Conflicts of interest: None disclosed.

IRB approval status: The study protocol was previously approved by the local Ethics Committee (nr 33/16 prot nr 2560).

Reprints not available from the authors.

Correspondence to: Stefania Guida, PhD, Via del Pozzo 71, 41124 Modena, Italy

E-mail: [drstefaniaguida@gmail.com](mailto:drstefaniaguida@gmail.com)

#### REFERENCES

1. Sachs DL, Varani J, Chubb H, et al. Atrophic and hypertrophic photoaging: clinical, histologic, and molecular features of 2 distinct phenotypes of photoaged skin. *J Am Acad Dermatol*. 2019;81:480-488.
2. Guida S, Ciardo S, De Pace B, et al. The influence of MC1R on dermal morphological features of photo-exposed skin in women revealed by reflectance confocal microscopy and optical coherence tomography. *Exp Dermatol*. 2019;28:1321-1327.
3. Tagliabue E, Gandini S, Bellocco R, et al. MC1R variants as melanoma risk factors independent of at-risk phenotypic characteristics: a pooled analysis from the M-SKIP project. *Cancer Manag Res*. 2018;10:1143-1154.
4. Elfakir A, Ezzedine K, Latreille J, et al. Functional MC1R-gene variants are associated with increased risk for severe photoaging of facial skin. *J Invest Dermatol*. 2010;130:1107-1115.
5. Longo C, Casari A, De Pace B, Simonazzi S, Mazzaglia G, Pellacani G. Proposal for an in vivo histopathologic scoring system for skin aging by means of confocal microscopy. *Skin Res Technol*. 2013;19:e167-e173.

<https://doi.org/10.1016/j.jaad.2020.04.075>

#### Evaluation of online patient education materials concerning skin cancers



*To the Editor:* The Internet has become instrumental in the distribution of health-related information to the general public, and increased access to web-based applications leads to an ever-growing readership. Approximately 80% of adults using the Internet in the United States report that it has influenced their decision-making process on how to approach and treat an illness.<sup>1</sup> Although these resources have great





potential to improve patients' access to important medical information, individuals with low health literacy experience significant disparities, such as decreased use of preventative services, which ultimately results in delayed diagnoses, poor compliance, and higher morbidity and mortality.<sup>2</sup> The American Medical Association and National Institutes of Health recommend that online resources be written between a third and seventh grade reading level.<sup>3</sup> With regard to dermatologic educational materials, there are limited studies on online health literacy.<sup>4</sup> This study approaches the issue from an uncommon perspective by evaluating articles based on key words and studying the usability of websites.

In this article, we provide a comprehensive analysis of 100 online patient education resources pertaining to skin cancer. A Google search was performed on 10 major skin cancer terms (Table I), and the first 10 websites with patient education materials were collected. These 100 articles were then analyzed by using 9 validated readability assessment scales that are widely accepted and used in the medical literature. Although scores varied across the 9 readability assessments, materials related to all search terms were above the recommended level (Table II). The 100 website articles had a mean  $\pm$  standard deviation reading grade level of  $10.63 \pm 2.02$ . Individual article reading levels ranged from a 6.56- to a 16.72-grade level.

With regard to usability, the 3 major skin cancers, basal cell carcinoma, squamous cell carcinoma, and melanoma, were evaluated with the Minervation (Oxford, UK) validation, the LIDA instrument, for health care websites. An analysis of 30 websites showed average scores of 82.4%, 81.9%, and 82.8% for basal cell carcinoma, squamous cell carcinoma, and melanoma, respectively. The majority of websites scored highly with regard to consistency of page layout, support of normal browser navigational tools, and use of the site without third party plug-ins. Areas with a need for improvement pertained to user engagability, website personalization, and use of appropriate nontextual media.

With the continued dispersion of information on the Internet, an emphasis on clear and usable online health information pertaining to common diseases, such as skin cancers, is strongly encouraged. Materials that are not readable serve as barriers to patients, who are often attempting to understand risk factors or treatment options for conditions they have. A system dedicated to health care fields is paramount to the safety and outcomes of our patients. This analysis shows that health websites overall provide helpful and useful information on skin cancers;

# The influence of MC1R on dermal morphological features of photo-exposed skin in women revealed by reflectance confocal microscopy and optical coherence tomography

Stefania Guida<sup>1</sup>  | Silvana Ciardo<sup>1</sup> | Barbara De Pace<sup>1</sup> | Nathalie De Carvalho<sup>1</sup>  |  
 Francesca Peccerillo<sup>1</sup> | Marco Manfredini<sup>1</sup> | Francesca Farnetani<sup>1</sup>  |  
 Johanna Chester<sup>1</sup> | Shaniko Kaleci<sup>1</sup> | Michele Manganelli<sup>2</sup>  | Gabriella Guida<sup>2</sup> |  
 Giovanni Pellacani<sup>1</sup>

<sup>1</sup>Dermatology Unit, Department of Surgical, Medical, Dental and Morphological Science with Interest Transplant, Oncological and Regenerative Medicine, University of Modena and Reggio Emilia, Modena, Italy

<sup>2</sup>Molecular Biology Section, Department of Basic Medical Sciences Neurosciences and Sense Organs, University of Bari, Bari, Italy

## Correspondence

Stefania Guida, Dermatology Unit, Department of Surgical, Medical, Dental and Morphological Science with Interest Transplant, Oncological and Regenerative Medicine, University of Modena and Reggio Emilia, Via del Pozzo 71, 41124 Modena, Italy.

Email: drstefaniaguida@gmail.com

## Abstract

**Background:** The melanocortin 1 receptor (MC1R) gene is one of the major determinants of skin pigmentation. It is a highly polymorphic gene and some of its polymorphisms have been related to specific skin phenotypes, increased risk of skin cancers and skin photoageing. Currently, its contribution to changes in dermal features in photo-exposed skin is unknown.

**Objective:** The main objective of this study is to evaluate the potential correlation between MC1R status and specific healthy photo-exposed skin characteristics.

**Materials and methods:** Skin facial features were estimated by evaluation with standard digital photography with automated features count, reflectance confocal microscopy (RCM) and optical coherence tomography (OCT) in 100 healthy women. Skin of the forearms was used as a control.

**Results:** The study found an association between RHC MC1R polymorphisms and dermal features in photo-exposed areas being represented by increased vessel density and pixel density in OCT ( $P = .025$  and  $P = .001$ , respectively) and increased coarse collagen in RCM ( $P = .034$ ), as compared to non-RHC subjects. To our knowledge this is previously unreported. Additionally, previously reported correlations between light hair colour and pigmented spots with MC1R RHC polymorphisms have been confirmed.

**Conclusions:** Our results suggest the role of RHC MC1R variants in dermal variations of facial skin, as compared to non-RHC variants. To our knowledge this is previously unreported.

## KEYWORDS

dynamic optical coherence tomography, melanocortin 1 receptor, reflectance confocal microscopy, skin photoageing



## 1 | INTRODUCTION

The MC1R gene is highly polymorphic in Caucasian populations, and as many as 200 polymorphisms have been described.<sup>[1]</sup> The MC1R gene codifies for a transmembrane G protein-coupled receptor. The main ligand of this receptor is the  $\alpha$ -melanocyte-stimulating hormone (MSH), a preopiomelanocortin (POMC) derivative. The  $\alpha$ -MSH activates an adenylate cyclase, leading to an increase in intracellular cyclic adenosine monophosphate (cAMP) and a transcriptional activation of the tyrosinase family of genes, thereby regulating melanin biosynthesis, leading from pro-oxidant pheomelanin to the production of photoprotective eumelanin.<sup>[2]</sup>

Several studies have demonstrated an association between MC1R polymorphisms and red hair colour (RHC) phenotype characterized by red hair, fair skin and freckles.<sup>[3–6]</sup> MC1R variants have been classified, according to their penetrance for the RHC phenotype, into strong “R” or RHC alleles, or weak-r forms.<sup>[7,8]</sup> Extensive evidence shows that all the RHC alleles yield hypomorphic proteins, impairing the activation of the cAMP pathway.<sup>[9,10]</sup>

Some MC1R polymorphisms have also been associated with pigmented spots,<sup>[11]</sup> a subjective “inferior youthful appearance”<sup>[12]</sup> and an increased risk of photoageing,<sup>[13]</sup> as compared with wild-type (wt) subjects. Furthermore, melanoma<sup>[14,15]</sup> and non-melanoma skin cancer risk<sup>[16]</sup> have been associated to specific MC1R polymorphisms. Interestingly, MC1R polymorphisms have been related to both sun sensitivity/poor tanning, after ultraviolet (UV) radiation,<sup>[17]</sup> and the decreased ability to repair UV-damaged DNA.<sup>[1]</sup>

Studying histopathologic facial skin variations related to the ageing process has previously been limited by the requirements for facial skin biopsies. Recently, novel non-invasive skin imaging tools, such as reflectance confocal microscopy (RCM) and optical coherence tomography (OCT), have made in vivo skin morphological features assessment possible, widening the scope of application to skin features analyses in other than disease-specific scenarios. RCM enables the dynamic detection of morphologic and functional skin aspects at quasi-histologic resolution<sup>[18]</sup> and has been recently successfully applied to epidermal and dermal changes during skin ageing.<sup>[19]</sup> OCT and dynamic OCT (D-OCT) enable the visualization of vertical and horizontal sections of morphological and microvascular skin features.<sup>[20–22]</sup> However, specific skin features of a photo-exposed area such as the face, as revealed by RCM and OCT/D-OCT, and the correlation with MC1R status have not yet been investigated.

The primary aim of the study was to correlate strong RHC MC1R (RHC group) and non-strong RHC MC1R (non-RHC, including both MC1R weak-r and wt carriers) carriers on patient clinical, comorbidities and skin morphological changes revealed through in vivo skin imaging analyses. Secondary aims included (a) a comparison with non-photo-exposed skin and (b) a subgroup morphological analysis of RHC versus (vs) weak-r carriers vs wt subjects.

## 2 | MATERIALS AND METHODS

### 2.1 | Study design

This prospective, single centre study enrolled women at the Dermatology Unit, University of Modena and Reggio Emilia between June and August 2016. A total of 100 women known to the investigators, between the ages of 30 and 60 years, were invited to participate in the current study. Inclusion criteria specified Caucasian origin, no known dermatological disorders (including personal or family skin cancer history), no history of any other previous cancers or any facial interventions, such as injection of fillers or laser procedures within the previous 6 months, or any type of facial plastic surgery.

The study protocol was approved by the local Ethics Committee (nr 33/16 prot nr 2560) and all participants provided written, informed consent. The study was conducted according to the Declaration of Helsinki Principles. Participants gave their written informed consent.

### 2.2 | Subject data

Subjects were instructed not to apply any facial detergents or cosmetic agents for at least 12 hours prior to the arranged dermatological examination. A standardized questionnaire was delivered to all subjects, including questions referring to personal and clinical information, such as age, sun exposure, smoking and alcohol assumption habits. Clinical examination determined the individual subjects' hair, eye and skin colours.

### 2.3 | Standard digital photography with automated feature evaluation

All subjects were photographed using a digital photography analysis system with automated features evaluation of the face (Canfield Scientific, Inc, New York, NY). This tool enables the estimation of characteristics of the skin that are not visible to the naked eye. The subjects' grading of facial skin texture, erythema and hyperpigmentation were recorded. Standard photography was used to assess rhytides and texture, ultraviolet (UV) light was employed for UV spots and porphyrin examination and cross-polarization light was used for brown spots and red area analyses. For each photograph, areas of skin meeting a threshold level of colour contrast to adjacent skin were defined as spots.<sup>[23]</sup> The software provides an automated evaluation quantifying the per cent area of the face comprising the spots in each of the photographs.

Results were retrieved in terms of absolute (ABS) scores, referred to the intensity of detected instances of the feature being analysed in the total size and area.<sup>[24]</sup>

### 2.4 | Reflectance confocal microscopy

Reflectance confocal microscopy imaging was performed with the confocal VivaScope 1500<sup>®</sup> (MAVIG GmbH, Munich, Germany),

reaching a depth of up to 250  $\mu\text{m}$ , on the right cheek (5 mm below the zygomatic arch), as previously described.<sup>[19]</sup> The inner forearm of each subject was used as control. Four 3 x 3-mm mosaics with a 25- $\mu\text{m}$  step were acquired for each subject, starting from 5 to 10  $\mu\text{m}$  below the stratum corneum, to the first appearance of the honeycomb pattern.

Reflectance confocal microscopy features evaluated in this study included the irregular honeycombed pattern and mottled pigmentation of the epidermis, polycyclic papillary contours and sebaceous glands at the dermo-epidermal junction (DEJ) and thin, coarse or huddle collagen and elastosis at the dermis. These features were described in Supplementary Table S1. RCM images were evaluated by two expert readers, and a third one was involved in case of discordance.

## 2.5 | Optical coherence tomography criteria

Optical coherence tomography images were acquired through the VivoSight OCT<sup>®</sup> (Michelson Diagnostics Ltd., Orpington, UK) at the right cheek (5 mm below the zygomatic arch). The inner forearm of each subject was used as control. OCT employs a swept source tunable diode laser with a peak power of 15 mW at  $\lambda = 1310$  nm for non-invasive real-time skin imaging, up to a 2-mm depth. Vessel measurements were performed on horizontal (parallel to the skin surface) D-OCT images, according to "vessel density," with a 4-point scale (Figure 1) and amount of red pixels, "pixel density," with the ImageJ software<sup>[25]</sup> (Image Processing and Analysis in Java, freeware 2014 version USA) analysis applied to images, all of the same size, at 300  $\mu\text{m}$  depth.<sup>[26]</sup> From the many vertical sections acquired, sections analysed were selected according to the absence of interrupting features (hair shadows, adnexal structures, etc). Features assessed at OCT and D-OCT were outlined in Table S2. OCT and D-OCT images were evaluated by two expert readers, and a third one was involved in case of discordance.

## 2.6 | Melanocortin 1 Receptor genotype and sequence analysis

Melanocortin 1 receptor sequencing was performed from standard blood samples, collected during the dermatological visit. Genomic DNA was extracted from whole frozen blood samples according to the manufacturer's protocol (QIAamp DNA blood kit; QIAGEN). The MC1R gene sequence (FW: 50CCTAAGCTTACTCCTTCCTGCTTCCTGGACA 30; Rv: 50 CTGGAATTCACACTTAAAGCGCGTGACCCG 30) was amplified by polymerase chain reaction (PCR). PCR products were analysed by direct sequencing on both strands using the Eurofins Genomic service (Eurofins Genomics). MC1R variant allele distribution was evaluated and subjects were classified as strong RHC MC1R polymorphisms (RHC group) [R151C, R160W, R142H, D294H, I155H] or non-strong RHC MC1R polymorphisms (non-RHC group); the latter subdivided according to weak-r variants and wt subjects.

## 2.7 | Statistical analysis

Mean and percentage frequency were used to express population characteristics. To test the effect of MC1R status (RHC vs non-RHC)

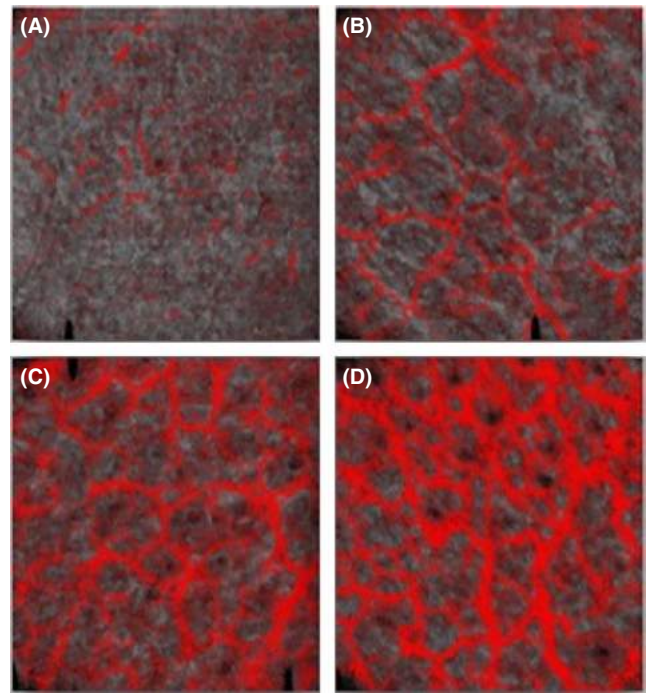


**FIGURE 1** Vessel density scale. Dynamic optical coherence tomography (D-OCT) images in horizontal (parallel to skin surface) section (size 6 x 6 mm; skin depth 300  $\mu\text{m}$ ) showing the 4-point scale used for vessels density assessment. Increasing density is shown: absent (A), low (B), medium (C), high (D)

on clinical comorbid and morphological features, univariate analyses were carried out. For quantitative variables, Student's *t* test was performed and for qualitative variables the Pearson chi-square test or Fisher's test (in case of values  $<5$  in the contingency Table) were performed. Statistically significant variables ( $P \leq .1$ ) in univariate analysis or clinically relevant variables were included in a multivariate logistic model (a stepwise method of variable selection was used to estimate a final model). The relationship between specific skin features and MC1R status was expressed as "Odds Ratio" (OR) with a confidence interval of 95%. Secondary outcomes included the comparison of statistically significant morphological features with non-photo-exposed skin morphological features according to the Pearson chi-square test. The subgroup analysis (weak-r vs wt vs RHC) included statistically significant variables (clinical and morphological features) identified in primary analysis and were assessed according to an ordered logistic regression. All statistical analysis was performed using Stata (version 11.2). Reported significance levels were two-sided, and a threshold of  $P < .05$  was considered statistically significant.

## 3 | RESULTS

### 3.1 | Characteristics of the study population

This study enrolled 100 women invited to participate in the study, of which three subjects were excluded following DNA analysis due to potential bias from two rare MC1R variants (D294Q and D294N).

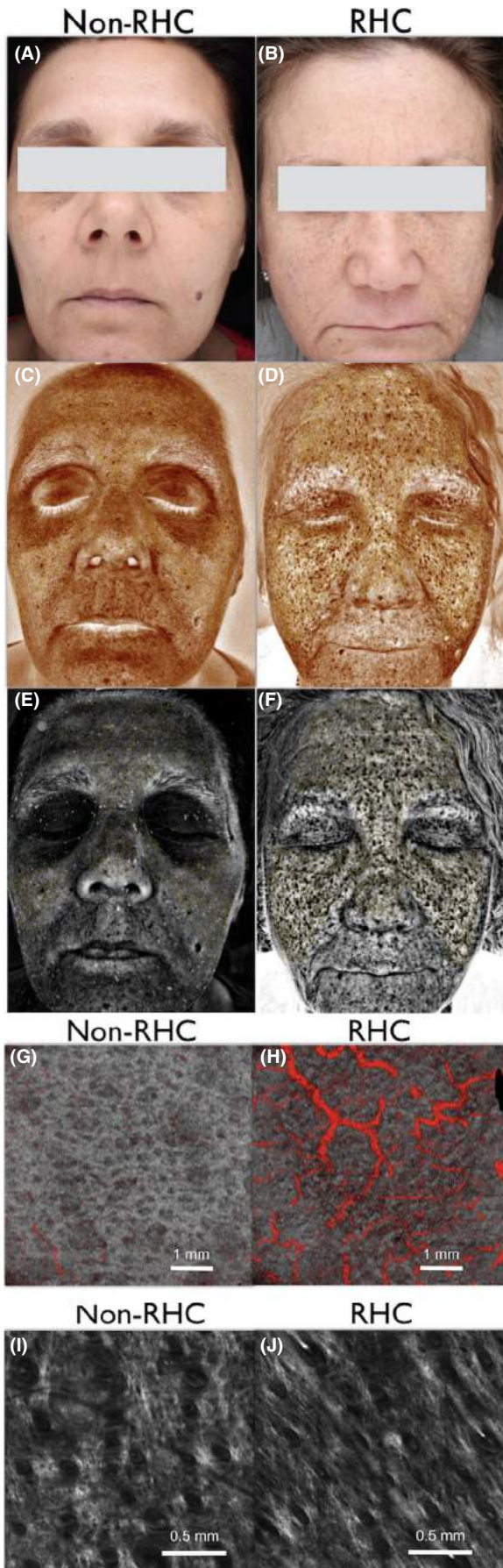


**FIGURE 2** Clinical and non-invasive skin imaging features according to non-RHC vs RHC MC1R status. Pictures of 52-year-old women (A, B) clinical standard photography (C, D) UV light revealing the amount of UV spots (E, F) cross-polarized light revealing brown spots, in a MC1R non-RHC (wt) (A, C, E) and RHC carrier (R160W/V60L) (B, D, F). Dynamic optical coherence tomography (D-OCT) images (size  $6 \times 6$  mm; scale bar 1 mm; skin depth 300  $\mu$ m) showing different density of blood vessels in (G) a MC1R non-RHC and (H) an RHC carrier. Reflectance confocal microscopy images (scale bar 500  $\mu$ m) showing (I) more than 50% of thin reticulated collagen in a MC1R non-RHC carrier and (J) more than 50% of coarse collagen in a MC1R RHC carrier

Therefore, a total of 97 women were included into the dataset for analysis. Subject mean age was  $44.6 \pm 6.7$  (31–58).

Overall, seven non-synonymous MC1R gene polymorphisms were detected in 33 women (34%): all represented by amino-acid substitutions, with no deletions or insertions. A total of 32 subjects were heterozygous MC1R polymorphism carriers (wt/Polymorphism), therefore bearing one non-synonymous MC1R, while one patient carried two MC1R variants: R160W and V60L (red hair subject).

A total of 84 women were non-RHC carriers: 21 carriers of weak-variants and 63 wt. The remaining 13 women were found to carry at least one RHC polymorphism. R151C was the most represented RHC variant, present in five women. (Supplementary Table S3).

## 3.2 | MC1R status and clinical/non-invasive imaging features

### 3.2.1 | Primary outcome

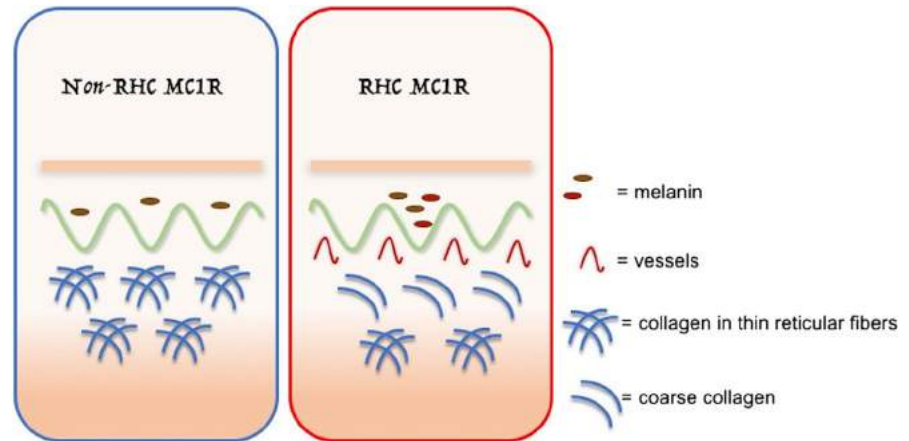
Participants' clinical features according to MC1R status were presented in Supplementary Table S4. RHC and non-RHC groups were not significantly different in terms of comorbidities (including sun exposure) and a significant association between MC1R status and hair colour was confirmed ( $P = .02$ ). Automated digital facial photo features, according to the ABS scores, were presented in Supplementary Table S5. ABS scores were significantly elevated for UV and brown spots ( $P < .01$ ) in the RHC group. Figure 1 (A–F) illustrated UV and brown spots of non-RHC and RHC participants with automated digital facial photographs.

At RCM analysis, morphological features according to non-RHC and RHC were similar. Although not significant, the presence of  $\leq 50\%$  of coarse collagen in RHC participants was over 90% compared to only 69% in non-RHC participants, Supplementary Table S6. Whilst no significant differences were found in dermal and epidermal features in OCT, D-OCT highlighted an increased vessel density ( $P = .038$ ) and pixel density ( $P < .01$ ) in RHC participants, Supplementary Table S7 and Figure 2 (G, H).

Significant and clinically relevant variables were included in a multivariate analysis, highlighting the correlation of UV spots ( $P = .012$ ) and coarse collagen ( $P = .043$ ) according to MC1R status (Figure 2 A–F, I, J, respectively). In detail, there was an 18 times increased risk



**FIGURE 3** Model of photoageing according to non-RHC vs RHC MC1R status in our population. This model shows the presence of pigmented spots, increased vessel density and coarse collagen in RHC MC1R carriers, as compared to non-RHC



for >50% coarse collagen and increased presence of UV spots associated with RHC compared to non-RHC (Supplementary Table S8). Based on these results, a model of photo-exposed skin compartment characteristics, according to MC1R status, has been proposed (Figure 3).

### 3.2.2 | Secondary outcomes

No statistical differences were observed for the analysis in non-photo-exposed skin in RHC vs non-RHC, even for the variables identified as significantly different at primary analysis: the amount of coarse collagen ( $P = .761$ ) and vessels ( $P = .254$ ), data not shown. Further, no differences were found in the subgroup (weak-r vs wt vs RHC) analysis of morphological features (data not shown).

## 4 | DISCUSSION

Previously, the influence of MC1R polymorphisms on dermal morphological changes in photo-exposed skin was undefined.<sup>[13,27]</sup> The current study highlights that photo-exposed skin in RHC polymorphisms carriers, as compared to non-RHC, has more coarse “photoaged” collagen (evidenced in RCM) and more dense vascularity (evidenced in D-OCT).

Cutaneous morphological studies have mostly been applied to malignant lesions, in order to improve diagnostic accuracy and avoid unnecessary excisions.<sup>[28,29]</sup> However, skin changes in other cutaneous processes have been difficult to assess as biopsy, especially for the face, is often difficult to justify due to scarring risk. With the introduction of in vivo assessment tools, the deepest skin layer (dermis) can now be investigated without scarring also in healthy skin.

In the current study, a higher prevalence of coarse collagen in photo-exposed areas associated with RHC vs non-RHC subjects was underlined with RCM analysis. Coarse collagen, which has been previously associated with the skin photoageing process,<sup>[19]</sup> is visualized at RCM as coarse filamentous thick structures with a tendency to be packed. UV irradiation triggers the overproduction of matrix metalloproteinases, such as MMP1, and consequent collagen degradation.

Interestingly, UV exposure is known to increase  $\alpha$ -MSH release, and a role for  $\alpha$ -MSH/MC1R as a regulator pathway of the MMP1 and collagen metabolism has been demonstrated,<sup>[30,31]</sup> thus supporting the potential influence of MC1R status on collagen morphology.

Univariate analysis of D-OCT assessments shows a significant association between vessel density and pixel density in photo-exposed areas for RHC carriers vs non-RHC. It has been proven that the  $\alpha$ MSH/MC1R pathway inhibits angiogenesis through attenuation of the vascular endothelial growth factor (VEGF)/VEGF receptor 2 (R2) signalling pathway.<sup>[32]</sup> Therefore, RHC MC1R polymorphisms may lead to a dysregulation of the anti-angiogenic activity, thus contributing to an increase in vessel density and pixel density.

Clinical assessments in this study confirmed the well-known association of RHC MC1R variants with light hair and pigmented spots. Pigmented spots have been previously associated at semi-automated facial image analysis with multiple MC1R polymorphisms,<sup>[11]</sup> whilst only a non-significant trend has previously been reported for the association between a single MC1R polymorphism and clinical signs of skin photoageing.<sup>[13]</sup> However, there is a significant RHC allele heterozygote carrier effect on skin features, suggesting that variant alleles do not behave in a strictly recessive manner.<sup>[33]</sup> In the current study, the automated facial image analysis revealed a correlation with RHC and an increased prevalence of pigmented spots, with both UV light (UV spot) and cross-polarized light (brown spot). Bustamante et al<sup>[11]</sup> suggested that the increased levels of pro-oxidant pheomelanin associated with RHC may produce an increase in reactive oxygen species, leading to DNA damage. In addition, MC1R is now considered a master regulator, not only for processes involved in pigment production but also for pigment distribution throughout the skin, by means of downstream signalling.<sup>[34–36]</sup> Therefore, the authors suggest that the MC1R status may contribute to the heterogeneous melanin distribution and the appearance of pigmented spots.

Further, in the current study, the correlation between MC1R status, pigmented spots and coarse collagen seem independent of skin colour. This finding has also been reported for pigmented spots<sup>[14]</sup> and skin cancer risk,<sup>[37]</sup> therefore underlying the importance of pigmentary-independent functions of MC1R.<sup>[16]</sup> Accordingly, MC1R expression has been demonstrated in diverse cell types of both the

epidermis, such as melanocytes and keratinocytes, and the dermis, such as fibroblasts and endothelium, but its function has been proven in melanocytes only.<sup>[35,38]</sup>

Melanocortin 1 receptor signalling in melanocytes has been proven to interact with many molecular pathways<sup>[35,39-41]</sup> and carriers of MC1R variants have been shown to have a de-regulated expression of a large number of genes involved in oxidative stress and DNA damage.<sup>[42]</sup> The non-invasive skin imaging in the current study suggests that MC1R status also influences dermal morphology and architectural features, such as vessel density, pixel density and the observation of coarse collagen, which may be explained by those interactions with other, as yet unstudied, pathways.

No significant differences were observed in our subgroup study (weak-r vs wt vs RHC). Some previous authors observed a minor signalling impairment associated with weak-r, or behaviour of weak-r similar to wt<sup>[43,44]</sup> leaving the precise role of the weak-r MC1R variants unknown.

However, Elfakir et al<sup>[13]</sup> previously reported the association of the weak-r V92M variant, and clinically assessed photoageing. Many differences between our study and the study of Elfakir et al<sup>[13]</sup> should be noted. Firstly, the Elfakir study included a much larger population and all subjects carrying weak-r V92M polymorphism, as a single polymorphism or in combination with other variants, were pooled together, without specifying the relative proportion of subjects carrying V92M/wt. In the current study, all patients carrying weak-r V92M polymorphism were V92M/wt only and this may explain our varying results. The included populations were also different in terms of age. Elfakir et al included an older population (range 44-70 vs 30-60 in the current study) with a clinical modality of evaluation only, compared to the addition of morphological assessment in the current study which may have identified early features of photo-exposed skin, not yet observable with clinical assessment only.

The main limitations of our study include the number of subjects enrolled and the representation of RHC compared to non-RHC carriers. However, this proportion is representative of the local population without any known dermatological disorders (especially skin cancer). Further, the population is relatively younger than other comparative studies.

In conclusion, this study confirms the influence previously observed of RHC MC1R polymorphisms on pigmented spots in healthy skin. Non-invasive in vivo skin imaging performed in this study reveals for the first time the role of RHC polymorphisms on morphological and architectural features of the dermis in healthy skin. Future studies should investigate the evolution of these observed morphological and architectural feature changes in the dermal layer in healthy skin and any potential association with skin cancer development.

## ACKNOWLEDGEMENTS

We would like to thank Dr Francesca Faillaci for graphical assistance and Dr Luisa Benassi, Dr Paola Azzoni and Dr Cristina Vaschieri for technical support.

## CONFLICT OF INTERESTS

The authors declare no conflict of interest.

## AUTHOR CONTRIBUTIONS

GS, CS, GP, DCN, PF, MMa, FF, MMi have made substantial contributions to conception and design, or acquisition of data, or analysis and interpretation of data; and GS, CS, BDP, CJ, SK, GG have been involved in drafting the manuscript or revising it critically for important intellectual content. All authors gave final approval of the version to be published and agreed to be accountable for all aspects of the work in ensuring that questions related to the accuracy or integrity of any part of the work are appropriately investigated and resolved.

## ORCID

Stefania Guida  <https://orcid.org/0000-0002-8221-6694>

Nathalie De Carvalho  <https://orcid.org/0000-0002-0823-5731>

Francesca Farnetani  <https://orcid.org/0000-0001-7088-9077>

Michele Manganeli  <https://orcid.org/0000-0002-8219-0252>

## REFERENCES

- [1] JC García-Borrón, Z Abdel-Malek, C Jiménez-Cervantes, *Pigment Cell Melanoma Res.* **2014**, *27*, 699.
- [2] JC García-Borrón, BL Sanchez-Laorden, C Jimenez-Cervantes, *Pigment Cell Res.* **2005**, *18*, 393.
- [3] P Valverde, E Healy, I Jackson, JL Rees, AJ Thody, *Nat. Genet.* **1995**, *11*, 328.
- [4] NF Box, JR Wyeth, LE O'Gorman, NG Martin, RA Sturm, *Hum. Mol. Genet.* **1997**, *6*(11), 1891.
- [5] R Smith, E Healy, S Siddiqui, N Flanagan, PM Steijlen, I Rosdahl, JP Jacques, S Rogers, R Turner, IJ Jackson, MA Birch-Machin, JL Rees, *J. Invest. Dermatol.* **1998**, *111*(1), 119.
- [6] M Bastiaens, J ter Huurne, N Gruis, W Bergman, R Westendorp, BJ Vermeer, JN Bouwes Bavinck, *Hum. Mol. Genet.* **2001**, *10*(16), 1701.
- [7] DL Duffy, NF Box, W Chen, JS Palmer, GW Montgomery, MR James, NK Hayward, NG Martin, RA Sturm, *Hum. Mol. Genet.* **2004**, *13*, 447.
- [8] MD Morgan, E Pairo-Castineira, K Rawlik, O Canela-Xandri, J Rees, D Sims, A Tenesa, IJ Jackson, *Nat. Commun.* **2018**, *9*, 5271.
- [9] PA Frandberg, M Doufexis, S Kapas, V Chhajlani, *Biochem. Biophys. Res. Commun.* **1998**, *245*, 490.
- [10] C Herraiz, C Jimenez-Cervantes, P Zanna, JC García-Borrón, *FEBS Lett.* **2009**, *583*, 3269.
- [11] LC Jacobs, MA Hamer, DA Gunn, J Deelen, JS Lall, D van Heemst, HW Uh, A Hofman, AG Uitterlinden, CEM Griffiths, M Beekman, PE Slagboom, M Kayser, F Liu, T Nijsten, *J. Invest. Dermatol.* **2015**, *135*(1735-42), 11.
- [12] F Liu, MA Hamer, J Deelen, JS Lall, L Jacobs, D van Heemst, PG Murray, A Wollstein, AJ de Craen, HW Uh, C Zeng, A Hofman, AG Uitterlinden, JJ Houwing-Duistermaat, LM Pardo, M Beekman, PE Slagboom, T Nijsten, M Kayser, DA Gunn, *Curr. Biol.* **2016**, *26*(1213-20), 12.
- [13] A Elfakir, K Ezzedine, J Latreille, L Ambroisine, R Jdid, P Galan, S Hercberg, F Gruber, D Malvy, E Tschachler, C Guinot, *J. Invest. Dermatol.* **2010**, *130*(4), 1107.

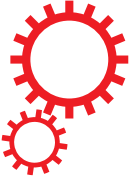
- [14] E Tagliabue, S Gandini, R Bellocco, P Maisonneuve, J Newton-Bishop, D Polsky, D Lazovich, PA Kanetsky, P Ghiorzo, NA Gruis, MT Landi, C Menin, MC Fagnoli, JC García-Borrón, J Han, J Little, F Sera, S Raimondi, *Cancer Manag. Res.* **2018**, 10(1143–54), 14.
- [15] S Guida, N Bartolomeo, PT Zanna, C Grieco, I Maida, S De Summa, S Tommasi, M Guida, A Azzariti, C Foti, R Filotico, G Guida, *Arch. Dermatol. Res.* **2015**, 307(495–503), 15.
- [16] E Tagliabue, S Gandini, JC García-Borrón, P Maisonneuve, J Newton-Bishop, D Polsky, D Lazovich, R Kumar, P Ghiorzo, L Ferrucci, NA Gruis, S Puig, PA Kanetsky, T Motokawa, G Ribas, MT Landi, MC Fagnoli, TH Wong, A Stratigos, P Helsing, G Guida, P Autier, J Han, J Little, F Sera, S Raimondi; M-SKIP Study group, *J. Invest. Dermatol.* **2016**, 136(1914–7), 16.
- [17] E Healy, N Flannagan, A Ray, C Todd, IJ Jackson, JN Matthews, MA Birch-Machin, JL Rees, *Lancet* **2000**, 355(9209), 1072.
- [18] S Guida, C Longo, A Casari, S Ciardo, M Manfredini, C Reggiani, G Pellacani, F Farnetani, G. *Ital. Dermatol. Venereol.* **2015**, 150, 547.
- [19] C Longo, A Casari, F Beretti, AM Cesinaro, G Pellacani, *J. Am. Acad. Dermatol.* **2013**, 68, e73.
- [20] HC Ring, M Mogensen, AA Hussain, N Steadman, C Banzhaf, L Themstrup, GB Jemec, *J. Eur. Acad. Dermatol. Venereol.* **2015**, 29, 890.
- [21] M Ulrich, L Themstrup, N de Carvalho, S Ciardo, J Holmes, R Whitehead, J Welzel, GBE Jemec, G Pellacani, *J. Eur. Acad. Dermatol. Venereol.* **2018**, 32(1), 152.
- [22] L Themstrup, J Welzel, S Ciardo, R Kaestle, M Ulrich, J Holmes, R Whitehead, EC Sattler, N Kindermann, G Pellacani, GB Jemec, *Microvasc. Res.* **2016**, 107, 97.
- [23] H Chajra, G Redziniak, D Auriol, K Schweikert, F Lefevre, *Clin. Cosmet. Investig. Dermatol.* **2015**, 8, 579.
- [24] A Goldsberry, CW Hanke, KE Hanke, *J. Drugs. Dermatol.* **2014**, 13(11), 1312.
- [25] MG Galimberti, S Guida, G Pellacani, PL Bencini, *Dermatol. Ther.* **2018**, 31, e12646.
- [26] N De Carvalho, J Welzel, S Schuh, L Themstrup, M Ulrich, GBE Jemec, J Holmes, S Kaleci, J Chester, L Bigi, S Ciardo, G Pellacani, *Exp. Dermatol.* **2018**, 27(11), 1280.
- [27] JH Rabe, AJ Mamelak, PJ McElgunn, WL Morison, DN Sauder, *J. Am. Acad. Dermatol.* **2006**, 55(1), 19.
- [28] F Farnetani, A Scope, V Coco, S Guida, AM Cesinaro, S Piana, K Peris, G Pellacani, C Longo, *J. Dermatol.* **2016**, 43(12), 1433.
- [29] G Pellacani, P Pepe, A Casari, C Longo, *Br. J. Dermatol.* **2014**, 171(5), 1044.
- [30] M Kiss, M Wlaschek, P Brenneisen, G Michel, C Hommel, TS Lange, D Peus, L Kemeny, A Dobozy, K Scharffetter-Kochanek, T Ruzicka, *Biol. Chem. Hoppe. Seyler.* **1995**, 376, 425.
- [31] M Böhm, M Raghunath, C Sunderkötter, M Schiller, S Ständer, T Brzoska, T Cauvet, HB Schiöth, T Schwarz, TA Luger, *J. Biol. Chem.* **2004**, 279, 6959.
- [32] WT Weng, SC Huang, YL Ma, HH Chan, SW Lin, JC Wu, CY Wu, ZH Wen, EM Wang, CL Wu, MH Tai, *Biochim. Biophys. Acta.* **2014**, 1840(6), 1850.
- [33] RA Sturm, *Melanoma Res.* **2002**, 12, 405.
- [34] JL Rees, *Am. J. Hum. Genet.* **2004**, 75, 739.
- [35] C Herraiz, JC García-Borrón, C Jiménez-Cervantes, C Olivares, *Biochim. Biophys. Acta. Mol. Basis Dis.* **2017**, 1863, 2448.
- [36] CR Goding, H Arnheiter, *Genes. Dev.* **2019**, 33, 983.
- [37] JS Palmer, DL Duffy, NF Box, JF Aitken, LE O’Gorman, AC Green, NK Hayward, NG Martin, RA Sturm, *Am. J. Hum. Genet.* **2000**, 66(1), 176.
- [38] DW Roberts, RA Newton, RA Sturm, *J. Invest. Dermatol.* **2007**, 127, 2472.
- [39] P Zanna, I Maida, C Grieco, S Guida, MC Turpin Sevilla, S De Summa, S Tommasi, GA Vena, R Filotico, G Guida, *J. Biol. Regul. Homeost. Agents.* **2013**, 27(1), 131.
- [40] A Ferretta, I Maida, S Guida, A Azzariti, L Porcelli, S Tommasi, P Zanna, T Cocco, M Guida, G Guida, *Biochim. Biophys. Acta.* **2016**, 1863, 2710.
- [41] M Guida, S Strippoli, A Ferretta, N Bartolomeo, L Porcelli, I Maida, A Azzariti, S Tommasi, C Grieco, S Guida, A Albano, V Lorusso, G Guida, *Pigment Cell Melanoma Res.* **2016**, 29, 679.
- [42] JA Puig-Butille, MJ Escámez, F Garcia-Garcia, G Tell-Marti, À Fabra, L Martínez-Santamaría, C Badenas, P Aguilera, M Pevida, J Dopazo, M del Río, S Puig, *Oncotarget.* **2014**, 5(6), 1439.
- [43] MC Scott, K Wakamatsu, S Ito, AL Kadekaro, N Kobayashi, J Groden, R Kavanagh, T Takakuwa, V Virador, VJ Hearing, ZA Abdel-Malek, *J. Cell Sci.* **2002**, 115, 2349.
- [44] C Dessinioti, C Antoniou, A Katsambas, AJ Stratigos, *Photochem. Photobiol.* **2011**, 87, 978.

## SUPPORTING INFORMATION

Additional supporting information may be found online in the Supporting Information section at the end of the article.


**How to cite this article:** Guida S, Ciardo S, De Pace B, et al. The influence of MC1R on dermal morphological features of photo-exposed skin in women revealed by reflectance confocal microscopy and optical coherence tomography. *Exp Dermatol.* 2019;28:1321–1327. <https://doi.org/10.1111/exd.14037>

# SCIENTIFIC REPORTS



OPEN

## Differential expression profiling of long non-coding RNA GAS5 and miR-126-3p in human cancer cells in response to sorafenib

Teresa Faranda<sup>1</sup>, Ilaria Grossi<sup>1</sup>, Michele Manganelli <sup>1</sup>, Eleonora Marchina<sup>1</sup>, Gianluca Baiocchi<sup>2</sup>, Nazario Portolani<sup>2</sup>, Marialuisa Crosatti<sup>3</sup>, Giuseppina De Petro<sup>1</sup> & Alessandro Salvi<sup>1</sup>

Long non-coding RNAs (lncRNAs) and microRNAs are involved in numerous physio-pathological conditions included cancer. To better understand the molecular mechanism of the oral antitumor multikinase inhibitor sorafenib, we profiled the expression of a panel of lncRNAs and miRNAs by qPCR array in a sorafenib-treated hepatocellular carcinoma (HCC) cell line. Among the most affected ncRNAs, we found that sorafenib mediated the dysregulation of the lncRNAs GAS5, HOTTIP and HOXA-AS2 and the miR-126-3p, in a panel of human cancer cell lines (HCC, renal and breast carcinomas). By luciferase gene reporter assay, we discovered that GAS5 may act as a sponge for miR-126-3p in HCC cells. The expression level of GAS5 and miR-126-3p was verified in human liquid and/or solid biopsies from HCC patients. miR-126-3p expression in HCC tissues was decreased respect to their correspondent peritumoral tissues. The levels of plasmatic circulating miR-126-3p and GAS5 were significantly higher and lower in HCC patients compared to healthy subjects, respectively. This study highlighted the capability of sorafenib to modulate the expression of a wide range of ncRNAs and specifically, GAS5 and miR-126-3p were involved in the response to sorafenib of different cancer cell types.

Non-coding RNAs (ncRNAs) can be divided into 2 classes according to their size: short ncRNAs with less than 200 nt and long ncRNAs (lncRNAs) with more than 200 nt. lncRNAs are a heterogeneous group of RNAs ranging from 200 to 100,000 nt in length with very limited or absent protein-coding capacity. They have been implicated in controlling gene expression, imprinting, and inactivation of X-chromosome, but the effects or mechanisms of action of most lncRNAs remain unknown<sup>1,2</sup>. lncRNAs have been emerging as essential players in the pathogenesis of cancer and their dysregulation has been closely associated with tumor development, progression and metastasis<sup>3,4</sup>.

Among the short ncRNAs, microRNAs (miRNAs) are one of the best studied and characterized classes. Mature miRNAs are about 22 nt long and they mainly control post-transcriptional gene expression by promoting degradation or repressing translation of target mRNAs<sup>5</sup>. In human cancer, the dysregulation of miRNAs expression has been extensively reported<sup>6,7</sup>.

Human hepatocellular carcinoma (HCC) is the most common malignancy of the liver worldwide and ranks as the third cause of cancer-related deaths. HCC develops in cirrhotic liver in 80–90% of patients. HBV, HCV infections and alcohol abuse are the main risk factors of cirrhosis and consequently HCC<sup>8,9</sup>.

Sorafenib is an oral multikinase inhibitor used to treat advanced and unresectable HCCs<sup>10</sup>. It is a small molecule that inhibits several serine/threonine and tyrosine kinases (CRAF, BRAF, VEGFR-2 and -3, PDGFR- $\beta$ , FGFR-1, c-kit, and Fms-like tyrosine kinase 3 (Flt-3)) in multiple oncogenic signaling pathways<sup>11,12</sup>. Although it is an effective anti-tumor treatment, some patients are non-responder, that is resistant to or developing resistance during therapy with sorafenib. For these reasons, efforts have been put into identifying strategies to make sorafenib a more active

<sup>1</sup>Department of Molecular and Translational Medicine, Division of Biology and Genetics, University of Brescia, Brescia, Italy. <sup>2</sup>Department of Clinical and Experimental Sciences, Surgical Clinic, University of Brescia, Brescia, Italy. <sup>3</sup>Department of Respiratory Sciences, University of Leicester, Leicester, UK. Teresa Faranda and Ilaria Grossi contributed equally. Correspondence and requests for materials should be addressed to A.S. (email: [alessandro.salvi@unibs.it](mailto:alessandro.salvi@unibs.it))

drug and to discover biological biomarkers of sensitiveness or resistance<sup>13</sup>. It is known that sorafenib may exert its antitumor activity by a Ras/RAF/MEK/ERK signaling pathway independent-mechanism and that it can target unexpected molecules. In this context, sorafenib may mediate global mRNA expression changes<sup>14</sup>, modulate the miRNome<sup>15</sup> and alter the global DNA methylation profile<sup>16</sup>. It has been demonstrated both *in vitro* and *in vivo* that ectopic modulation of lncRNAs and miRNAs may improve the effectiveness of sorafenib<sup>17,18</sup>.

The main aim of the present work was to study whether the treatment of HCC cells with sorafenib could lead to the dysregulation of the lncRNAs and miRNAs best characterized in physio-pathological conditions. The expression of the most dysregulated ncRNAs identified by qPCR-array was studied in tumor cells derived from renal cell carcinoma (RCC) and breast carcinoma in order to verify more global and wide effects of sorafenib in different cancer types. For RCC, the efficacy and safety of sorafenib has been proved and it is a therapeutic option to treat advanced RCC approved by FDA<sup>19</sup>. In breast cancer clinical trials, the efficacy of sorafenib in combinations with gemcitabine and/or capecitabine in locally advanced or metastatic disease is considered promising<sup>20</sup>. With the discovery of novel molecular biomarkers of response or resistance and new molecular therapeutic targets such as lncRNAs and miRs, it may be possible to identify new experimental strategies to improve the responsiveness of cancer cells to treatment.

## Materials and Methods

**Cell cultures and treatment with sorafenib.** In this study, human tumor cell lines derived from hepatocellular (HA22T/VGH, HUH6, HepG2 and SKHep1C3), breast (MCF-7 and HCC 1937) and renal (ACHN, Caki-1 and CRBM 1990) carcinomas were used. The HA22T/VGH, HUH6, MCF-7 and HCC-1937 cell lines were maintained in RPMI-1640 (Life Technologies) with 100 nM Sodium Pyruvate (ThermoFisher Scientific). HepG2 and SKHep1Clone3 (SKHep1C3), selected from human HCC-derived cells (SKHep1: ATCC HTB-52), were maintained in Earle's MEM (Life Technologies). The renal cancer cell lines ACHN, Caki-1 and CRBM-1990 were kindly provided by Dr Francesca Perut (Istituto Ortopedico Rizzoli, Bologna, Italy) and were maintained in Iscove's Modified Dulbecco's Medium (IMDM; Sigma-Aldrich). All culture media were supplemented with 10% Fetal Bovine Serum (Euroclone) and 10,000 U/ml penicillin/streptomycin (ThermoFisher Scientific). To generate sorafenib resistant cells, HA22T/VGH cells were treated with increasing concentration of sorafenib for about 6 months until the concentration of 10  $\mu$ M sorafenib was reached.

Sorafenib was synthesized and provided by Bayer Corporation (West Haven, CT, USA). This compound was dissolved in 100% dimethyl sulfoxide (DMSO; Sigma-Aldrich) and diluted with RPMI-1640, MEM or IMDM to the required concentration. 0.1% DMSO was added to cultures as a solvent-only negative control in *in vitro* studies.

**Tissues and clinicopathological features of HCC.** All of the human HCC tissues (n = 25) as well as the corresponding peritumoral (PT) non-tumor tissues (resected 1–2 cm from the malignant tumor) and the peripheral blood (n = 25) were obtained from HCC patients (Supplementary Table 1). The peripheral blood of healthy volunteers (n = 25) was obtained from the Immunohematology and Transfusion Medicine Service (Spedali Civili di Brescia, Italy). The study was approved by the ethical committee of Spedali Civili di Brescia on 2<sup>nd</sup> October 2012 (NP1230) and informed consent was obtained from all the subjects enrolled in the study. All methods were performed in accordance with the relevant guidelines and regulations. Each biopsy specimen was confirmed to be either HCC or PT by pathological examination<sup>21</sup>. In this study, 30 HCC subjects underwent surgical resection at Spedali Civili, Surgical Clinic of Brescia (Italy). The subjects consisted of 24 men and 6 women ranging from 57 to 82 years of age. The subjects did not have any apparent distant metastases, and none had been previously treated for HCC. The patients were analyzed for the presence of the hepatitis B virus (HBV) or hepatitis C virus (HCV). Sixteen patients were positive for HCV, 4 were positive for HBV, and 10 were found to be negative for both HBV and HCV.

**lncRNAs and miRNAs profiling.** The total RNA was isolated from cell cultures and from 200  $\mu$ l of plasma using miRNeasy Mini Kit (Qiagen), according to the manufacturer's instructions. The total RNA was isolated from tissue samples using TRIzol reagent (Invitrogen), according to the manufacturer's instructions.

The RT<sup>2</sup> lncRNA PCR Array Human lncFinder (Qiagen) and miScript miRNA PCR Array Human Liver miFinder (Qiagen) were employed to analyze the expression profile of different lncRNAs and miRNAs in HCC cell line (HA22T/VGH) treated or untreated with 15  $\mu$ M sorafenib for 24 hours. In the first experiment we evaluated the expression changes of 84 candidate lncRNAs and 84 miRNAs by using RT<sup>2</sup> lncRNA PCR Array Human lncRNA Finder and Human Liver miFinder miScript miRNA PCR Array (Qiagen) in HA22T/CGH cells treated and untreated with sorafenib according with manufacture's instruction on 7500 Real-Time PCR System. We tested 3 biological replicates and 3 technical replicates for both treated and untreated HA22T/VGH cells. Analysis of the RT-qPCR data was performed using the free web-based PCR Array Data Analysis Software (available at <https://dataanalysis.qiagen.com/pcr/>; Qiagen). The relative expression levels of target lncRNAs/miRNAs were determined by the  $2^{-\Delta\Delta CT}$  method using 5 reference genes included in the array (for lncRNAs: RN7SK, RPLP0, ACTB, B2M, SNORA73A; for miRNAs: SNORD61 SNORD68 SNORD72 SNORD95 SNORD96A RNU6B/RNU6-2). Standard negative controls including "no template" and "no reverse transcriptase" reactions were also included in the arrays. The P-values were calculated by the software using a Student's t-test for each gene in each treatment group compared to the control group.

**Quantitative real-time RT-PCR (qRT-PCR).** *lncRNAs.* cDNA was synthesized from 1  $\mu$ g of total RNA using M-MLV Reverse Transcriptase (Invitrogen) according to the manufacturer's instructions. The qPCR reaction was carried out using PrimeTime Gene Expression Master Mix (Integrated DNA technologies, IDT) and the appropriate PrimeTime qPCR Assay (20 $\times$ ) specific for the lncRNA targeted by the assay (either GAS5, HOXA-AS2 or HOTTIP). For circulating GAS5, 2.5  $\mu$ l of total RNA from plasma was retrotranscribed



and pre-amplified by using iScript Explore One-Step RT and PreAmp kit (BioRad) according to manufacturer's instructions. The cDNA was diluted 1:10 and 1.5  $\mu$ l were used for qPCR analysis together with appropriate PrimeTime qPCR Assay and 2 $\times$  GoTaq Probe qPCR Master Mix (Promega). qPCR reactions were performed in triplicate. The expression levels of GAS5, HOXA-AS2 and HOTTIP were determined using the  $\Delta\Delta$ Ct method using RPLP0 as reference gene to normalize expression of target genes. HCC cases were stratified on the basis of decreasing GAS5 R values ( $R = R_{\text{HCC}}/R_{\text{PT}}$ ). The GAS5 expression levels were considered to be "high" ( $R > 1.3$ ), "unchanged" ( $0.7 < R < 1.3$ ) and "low" ( $R < 0.7$ ).

**miRNAs.** cDNA was synthesized from 50 ng of total RNA (or 3  $\mu$ l purified RNA from plasma for circulating miR-126-3p) using the TaqMan microRNA Reverse Transcription Kit components (ThermoFisher) and the stem-loop primer for miR-126-3p (Applied Biosystems; Assay ID 002228) or RNU-48 (reference gene; Applied Biosystems; Assay ID 001006) and the spike-in cel-miR-39 according to the manufacturer's instructions. qPCR reactions were performed in triplicate. The tissue expression levels of miR-126-3p were determined using the  $\Delta\Delta$ Ct method and RNU-48 as reference gene.

**Cell proliferation assay.** The cells were seeded in a 96-well plate (5 replicates for each experimental condition) at a density of  $2 \times 10^3$  cells/well in complete medium and treated with increasing doses of sorafenib (0, 2.5, 5, 10, 15  $\mu$ M). After 24, 48 and 72 hours, viability was assessed with the addition of 15  $\mu$ l/well of sterile CellTiter reagent (Promega). The plates were incubated at 37 °C for 2 hours in a humidified, 5% CO<sub>2</sub> atmosphere and the absorbance at 490 nm was recorded using the microplate reader EnSight (PerkinElmer, Waltham, MA). The effects of miR-126-3p on cell viability in presence or absence of 15  $\mu$ M sorafenib were evaluated by transfecting the cells with miR-126-3p mimics (ThermoFisher, assay ID AM12841). Briefly, the cells were seeded in a 96-well plate (5 replicates for each experimental condition) at a density of  $4 \times 10^3$  cells/well in complete medium. After 24 h the cells were treated with 15  $\mu$ M sorafenib or 0.1% DMSO. 24 h later the cells were transfected with 50/100 nM miR-126-3p mimics or 50/100 nM miR-NC (negative control #1 cat. n. 4464058) using lipofectamine reagent. After 24 and 48 hours, viability was assessed with the addition of 15  $\mu$ l/well of sterile CellTiter reagent. The plates were incubated at 37 °C for 2 hours in a humidified, 5% CO<sub>2</sub> atmosphere and the absorbance at 490 nm was recorded using the microplate reader EnSight.

**Luciferase gene reporter assay.** The presence of miR-126-3p binding site in the GAS5 sequence was predicted using the bioinformatics tool "IntaRNA" (<http://rna.informatik.uni-freiburg.de/IntaRNA/Input.jsp>)<sup>22</sup>.

The pmirGLO Dual-Luciferase miRNA Target Expression Vector (Promega) was used to experimentally confirm the binding of miRNA by inserting the predicted miRNA target site of GAS5 at the 3' of the firefly luciferase gene (*luc2*). The primers containing the putative binding site of miR-126-3p were custom synthesized (Integrated DNA Technologies) and are the following: Top S2: 5'-AACTGATGGAGTCTCATGGCACAAGAAGATTAT-3'; Bottom S2: 5'-CTAGATAATCTTCTTGTCGCATGAGACTCCATCAGTTT-3'; Top AS2: 5'-AAATAATCTTCTTGTCGCATGAGACTCCATCAGT-3'; Bottom AS2: 5'-CTAGACTGATGGAGTCTCATGGCACAAGAAGATTATTT-3'.

The vector expressing the putative binding site was named pmirGLO GAS2 S2, while the control vector with the corresponding sequence cloned in antisense orientation was named pmirGLO GAS5 AS2. The empty vector was called pmirGLO.

**Transient transfection and dual-luciferase reporter assay.** The HA22T/VGH cells were seeded in a 24-well plate at a confluence of 60–80%. To evaluate the effect on miR-126-3p expression of GAS5 siRNA transfection upon sorafenib treatment, the cells were pre-treated for 24 h with 15  $\mu$ M sorafenib and then transfected with 50 and 100 nM siRNA GAS5 and siRNA Negative Control (siRNA GAS5, cat #4390771 assay ID n272331; siRNA NC, cat #4390843, Life Technologies) using Lipofectamine 2000 transfection reagent (Life Technologies) according to the manufacturer's instruction. 48 hours after transfection, the cells were lysed in TRIzol reagent (Life Technologies) and total RNA was extracted. For dual-luciferase reporter assay, the cells were transfected with 100 nM miR-126-3p mimic (ThermoFisher) at 24 hours after seeding and after further 24 h, they were also transfected with 0.5  $\mu$ g of luciferase reporter constructs using Lipofectamine 2000. Seventy-two hours after seeding, the cells were lysed by adding 100  $\mu$ l of 1 $\times$  passive lysis buffer (PLB) per well (Promega). The activity of Firefly (f-luc) and Renilla (r-luc) luciferases was evaluated by the Dual-Luciferase Reporter (DLR) Assay system (Promega) using the microplate reader EnSight (PerkinElmer).

**Statistical analysis.** Statistical analysis was carried out using GraphPad Prism 7.0 software. Student's t test was used to compare the expression of lncRNAs or miRNAs between the treated group and the untreated group with the sorafenib or to identify variations in cell proliferation. Diagnostic performance of circulating GAS5 and miR-126-3p to distinguish HCC patients from healthy subjects was evaluated using Receiver Operating Characteristic (ROC) curve analysis<sup>23</sup>. All experiments presented were performed at least three times. Data were considered statistically significant when  $P$ -value  $\leq 0.05$ .

## Results

**The treatment of HCC cells with sorafenib led to lncRNAs and miRNAs dysregulation.** To assess whether sorafenib may determine lncRNAs and miRNAs dysregulation, we examined the expression profiles of 84 disease- or pathway- focused lncRNAs and miRNAs in HA22T/VGH cells treated with 15  $\mu$ M sorafenib or with 0.1% DMSO for 24 hours. Overall, 23 lncRNAs and 8 miRNAs resulted significantly dysregulated in sorafenib-treated HA22T/VGH cells compared to cells treated with DMSO. In particular, 3 lncRNAs were up-regulated while 20 were down-regulated (Supplementary Table 2) while regarding miRNAs, 3 were up-regulated and 5 down-modulated (Supplementary Table 3).

**GAS5, HOTTIP and HOXA-AS2 were dysregulated in HCC, renal and breast cancer cells following treatment with sorafenib.** To verify the role of sorafenib in affecting the expression levels of ncRNAs, we selected and focused the attention on 3 lncRNAs and 1 miRNA for subsequent studies. GAS5 was chosen because it was up-regulated by the treatment while HOTTIP and HOXA-AS2 were both down-regulated. miR-126-3p was selected because it was the most down-regulated miRNA. We determined whether such ncRNAs were dysregulated in other HCC cells previously described to be sensitive to sorafenib (SKHep1C3, HuH6 and HepG2)<sup>17</sup> and we expanded testing also to renal (ACHN, Caki-1 and CRBM 1990) and breast (MCF-7 and HCC 1937) cancer cell lines.

Firstly, we evaluated whether the breast and renal cancer cells were sensitive to sorafenib by performing proliferation assay after treatment with increased concentrations of the drug (5, 10, 15  $\mu$ M) for three days. Proliferation was assessed at 24 h, 48 h and 72 h post-drug exposure. Sorafenib significantly inhibited the proliferation of RCC (renal cancer cells) and breast cancer cells in a dose-dependent manner with proliferation decreasing with higher amount of drug used (Fig. 1A–E). However, CRBM 1990 cell line proliferation seemed to be affected to a lower degree at 72 h than the other cell line tested in which exposure to sorafenib had a more prominent effect on proliferation.

Subsequently, we assessed the amount of the selected lncRNAs in the cancer cells used in this study in normal growth condition. GAS5 expression was detected in all the cells analyzed but with some cell lines expressing higher levels than others (Fig. 2A). HOTTIP was expressed at very low levels in HuH6, CRBM 1990 and HCC 1937 cells, while it was not expressed in HepG2, SKHep1C3 and MCF-7 cells (Fig. 2B). HOXA-AS2 was expressed at low levels in all the cell lines but HepG2, HUH6 and MCF7 did not show any expression (Fig. 2C).

In order to assess the trend of GAS5 expression after sorafenib treatment, we measured the GAS5 levels by qPCR in the aforementioned cell lines and treated with 15  $\mu$ M sorafenib for 24 hours. As control, we exposed the cells to 0.1% DMSO for the same amount of time. GAS5 was significantly up-regulated in 7 cell lines out of 9 (HA22T/VGH, HepG2, HUH6, ACHN, Caki-1, MCF-7 and HCC 1937) treated with sorafenib compared to cells treated with DMSO only (Fig. 2D–F). In CRBM 1990 cells, GAS5 was up-regulated when treated with the drug but the difference was not significant. On the contrary, GAS5 was significantly down-modulated in SKHep1C3 cells when exposed to sorafenib. The results obtained in HA22T/VGH cells were in line with the expression profile determined by lncRNA PCR array proving that sorafenib may mediate GAS5 up-regulation in other HCC cells as well as in renal and breast cancer cells. To verify a dose-dependent response between sorafenib treatment and GAS5 upregulation, HA22T/VGH cells were treated with 5, 10 and 15  $\mu$ M sorafenib for 24 h. GAS5 resulted upregulated 2, 2.3 ( $P$ -value < 0.05) and 2.4 ( $P$ -value < 0.01) fold, respectively when compared to 0.1% DMSO treated cells (Supplementary Fig. 1A).

HOTTIP was significantly down-regulated in the 4 cell lines tested (HA22T/VGH, HUH6, ACHN and Caki-1) when they were treated with sorafenib compared to cells treated with 0.1% DMSO (Fig. 2G,H). These data were in agreement with the HOTTIP expression profile obtained by lncRNA PCR array in HA22T/VGH cells and indicated that sorafenib may also mediate HOTTIP down-regulation in another HCC cell line and in two renal cancer cell lines. In addition, HOTTIP showed a trend of down-regulation in the HCC 1937 and CRBM 1990 cell lines, but the expression levels were at the limit of detection (data not shown). As shown in Fig. 2B, the other cell lines (HepG2, SKHep1C3 and MCF-7) did not express HOTTIP.

HOXA-AS2 was significantly down-regulated in 4 cell lines out of 5 (HA22T/VGH, ACHN, CRBM 1990 and HCC 1937) treated with sorafenib compared to DMSO-treated cells (Fig. 2I–K). The data were in accordance with the HOXA-AS2 expression profile obtained by lncRNA PCR array in HA22T/VGH cells and indicated that sorafenib may mediate HOXA-AS2 down-modulation also in renal and breast cancer cells. In Caki-1 cells, HOXA-AS2 seemed to be down-regulated although the difference was not statistically significant. As shown in Fig. 2C, the other cell lines did not express or expressed very low levels of HOXA-AS2 and could not be used for these experiments.

**miR-126-3p was differentially expressed in human cancer cells and it was down-regulated in HCC, renal and breast cancer cells following sorafenib treatment.** It was previously established by qPCR array that miR-126-3p was affected by sorafenib and in particular it was down-regulated in HA22T/VGH cells treated with the drug. Therefore we set out to find if sorafenib affected this miR in other cell lines in a similar way.

Firstly, we measured its expression in normal growth condition with the panel of cells used in this work. As shown in Fig. 3A, miR-126-3p was expressed at various levels in the cells analyzed. Subsequently, we quantified the expression of miR-126-3p after treatment with 15  $\mu$ M sorafenib for 24 hours using the same cell lines (Fig. 3B–D). This miRNA was significantly down-regulated in 8 cell lines out of 9 treated with sorafenib compared to the cells exposed to DMSO. On the contrary, it was significantly up-regulated in Caki-1 cells. Taken together, these data indicate that sorafenib was able to inhibit miR-126-3p expression in several cell lines from different cancer types, paralleling the results obtained in the HA22T/VGH cells. To verify a dose-dependent response between sorafenib treatment and miR-126-3p down-modulation, HA22T/VGH cells were treated with 5, 10 or 15  $\mu$ M sorafenib for 24 h. miR-126-3p resulted 16%, 25% ( $P$ -value < 0.05) and 24% ( $P$ -value < 0.01) down-regulated compared to 0.1% DMSO treated cells (Supplementary Fig. 1B). Furthermore, the GAS5 knockdown induced by 50 nM or 100 nM specific siRNA transfection determined a significant increase of miR-126-3p expression in the same cell line upon sorafenib treatment ( $P$ -value < 0.05 and  $P$ -value < 0.01 versus 50 nM or 100 nM siRNA NC, respectively; Supplementary Fig. 1C,D). These data suggested that the targeting of GAS5 resulted in the up-regulation of miR-126-3p levels upon sorafenib treatment. This finding could suggest that GAS5 may be involved in the regulation of miR-126-3p expression in HA22T/VGH cells treated with sorafenib.

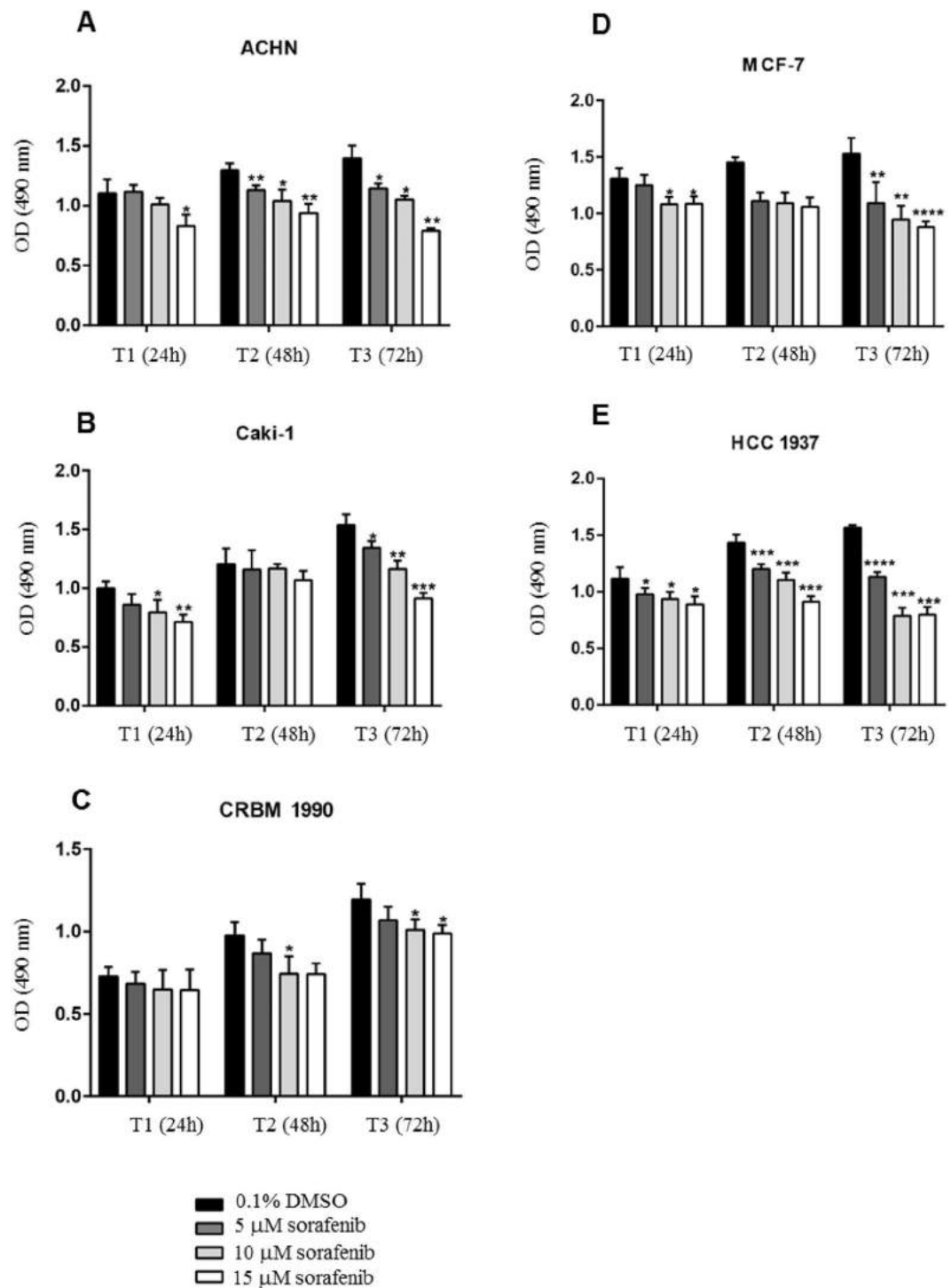


**Figure 1.** Sorafenib treatment inhibited the proliferation of renal and breast cancer cells. These bar charts show the effect of the sorafenib treatment on proliferation of ACHN (A), Caki-1 (B) and CRBM 1990 (C) renal cancer cells and of MCF-7 (D) and HCC 1937 (E) breast cancer cells. The difference between treated and untreated cells was evaluated for significance using unpaired t-test; \* $P$ -value < 0.05, \*\* $P$ -value < 0.01, \*\*\* $P$ -value < 0.001, \*\*\*\* $P$ -value < 0.0001. Bars represent the mean OD readings of samples measured at 490 nm and the lines represent the standard error of the mean (SEM).

**GAS5, HOTTIP, HOXA-AS2, miR-126-3p were dysregulated in sorafenib resistant cells.** In order to verify whether the selected ncRNAs may be dysregulated after the acquisition of resistance to sorafenib, we assessed their expression levels and the cell viability in a sorafenib-resistant cell line derived from HA22T/VGH cells and labelled HA22T/VGH-SR after exposure to the drug. As shown in Fig. 4A, sorafenib clearly elicited distinct

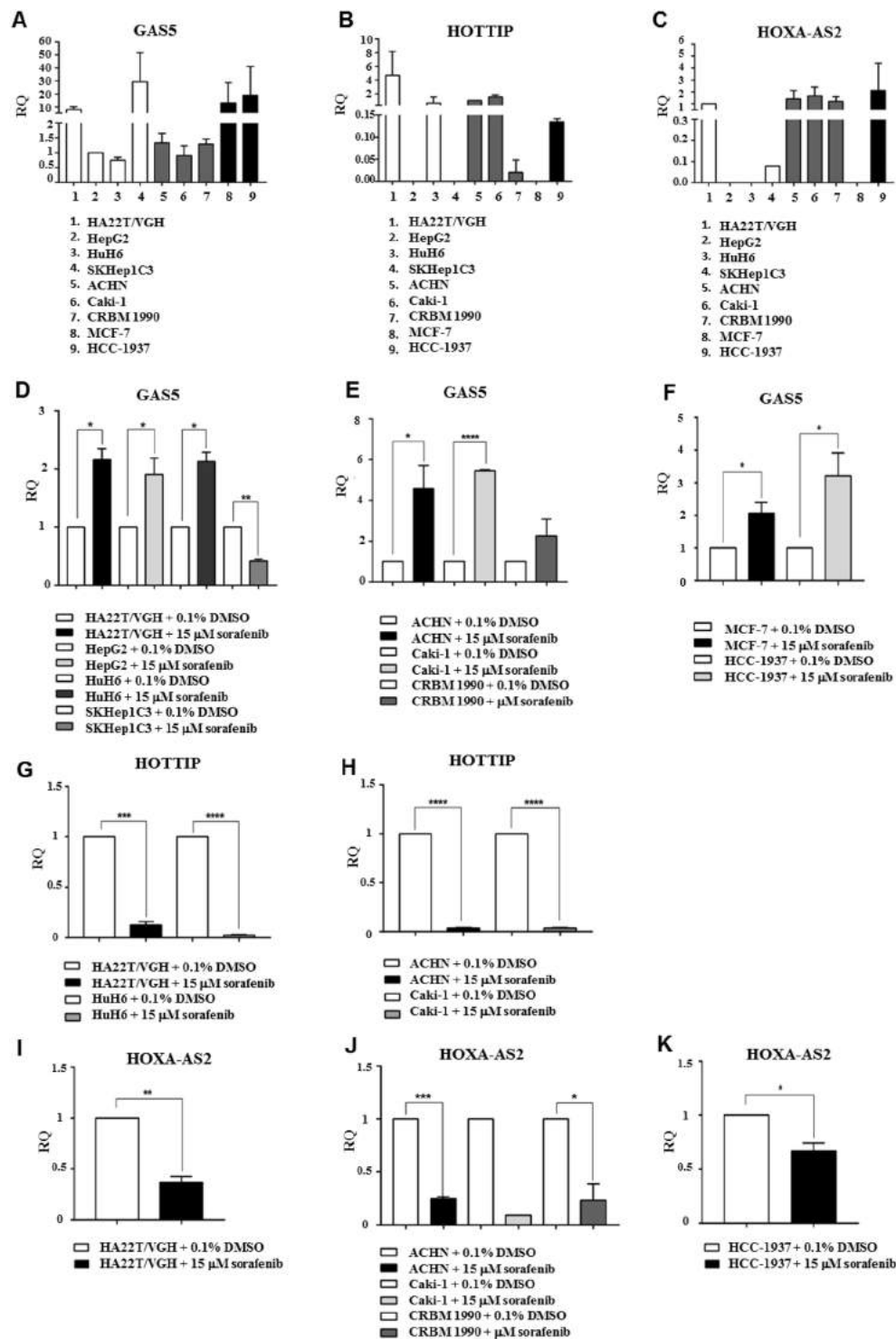


**Figure 2.** GAS5, HOTTIP and HOXA-AS2 were dysregulated in human cancer cells following treatment with sorafenib. The expression levels of GAS5 (A), HOTTIP (B) and HOXA-AS2 (C) in normal growth conditions were measured by qPCR in all of the HCC, renal and breast cancer cells used in this study. Expression of GAS5 (D–F), HOTTIP (G,H) and HOXA-AS2 (I–K) in cancer cells measured by qPCR when cells were exposed to 0.1% DMSO (open bar) or to 15 μM sorafenib (black or grey bars). GAS5 was upregulated in most HCC cell lines but SKHep1C3 (D) and in all but CRBM 1990 renal cells (E) and in all breast (F) cancer cells treated. HOTTIP resulted down-modulated in either HCC (G) or RCC (H) cells treated with 15 μM sorafenib. Similarly, HOXA-AS2 expression levels were down in hepatocellular (I), renal (J) and breast (K) cells exposed to sorafenib when compared with cells exposed to DMSO. Unpaired t-test was used to determine the presence of a statistically significant difference between cells exposed to sorafenib and cells exposed to DMSO only: \**P*-value < 0.05, \*\**P*-value < 0.01, \*\*\**P*-value < 0.001; \*\*\*\**P*-value < 0.0001. The bars represent the mean expression values from 3 experiments and the lines represent the standard error of the mean (SEM).

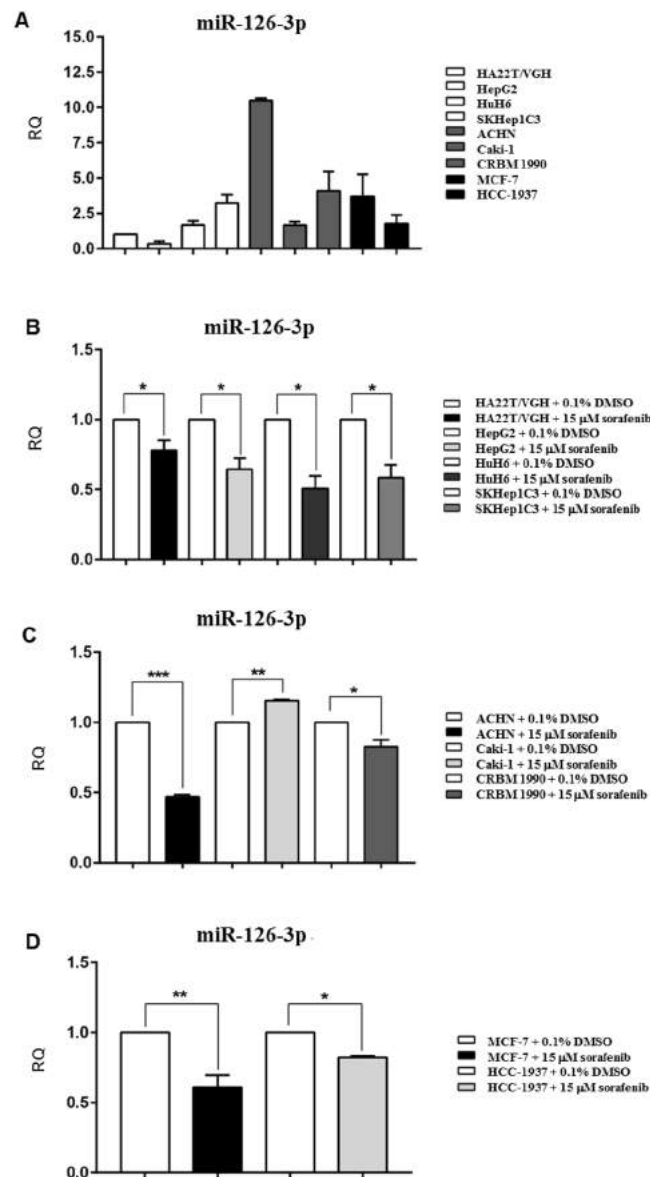


**Figure 3.** miR-126-3p was differentially expressed in HCC, renal and breast cancer cells and it was mostly down-regulated following the treatment with sorafenib. The expression levels of miR-126-3p in normal growth conditions were determined by qPCR in the cell lines used in this study (A). Expression of miR-126-3p in cancer cells was measured by qPCR when cells were exposed to 0.1% DMSO (open bar) or to 15 μM sorafenib (black or grey bars). miR126-3p expression levels were down-regulated in all hepatocellular (B) and breast (D) cells and in most of renal (C) cells exposed to sorafenib when compared with cells exposed to DMSO. The only exception was Caki-1 where it was up-regulated (C). Unpaired t-test was used to determine the presence of a statistically significant difference between cells exposed to sorafenib and cells exposed to DMSO only: \**P*-value < 0.05, \*\**P*-value < 0.01, \*\*\**P*-value < 0.001; \*\*\*\**P*-value < 0.0001. The bars represent the mean expression values from 3 experiments and the lines represent the standard error of the mean (SEM).

effects on cell proliferation with resistant cells maintaining or increasing their viability with incremental concentrations of sorafenib up to 10 μM while sensitive cells started to drop their viability after the concentration of 2.5 μM. This demonstrated that HA22T/VGH-SR cells were resistant to sorafenib treatment until 10 μM dose concentration and showed a 31% proliferation increase (*P*-value ≤ 0.001) in HA22T/VGH-SR cells respect to the sensitive ones.

We compared the expression levels of ncRNAs in resistant cells to the sensitive ones when they were both treated with 15 μM sorafenib for 24 hours and normalized against the expression levels of HA22T/VGH exposed to 0.1% DMSO. GAS5 expression levels were significantly down-regulated in HA22T/VGH-SR compared to HA22T/VGH cells treated with sorafenib (Fig. 4B), while HOXA-AS2 expression was significantly up-regulated. HOTTIP expression levels were downregulated in both sensitive and resistant cells compared to HA22T/VGH cells treated with DMSO although resistant cells showed a slightly higher and significant levels of expression than the sensitive cells when treated with sorafenib (Fig. 4B). These results may suggest that the acquisition of



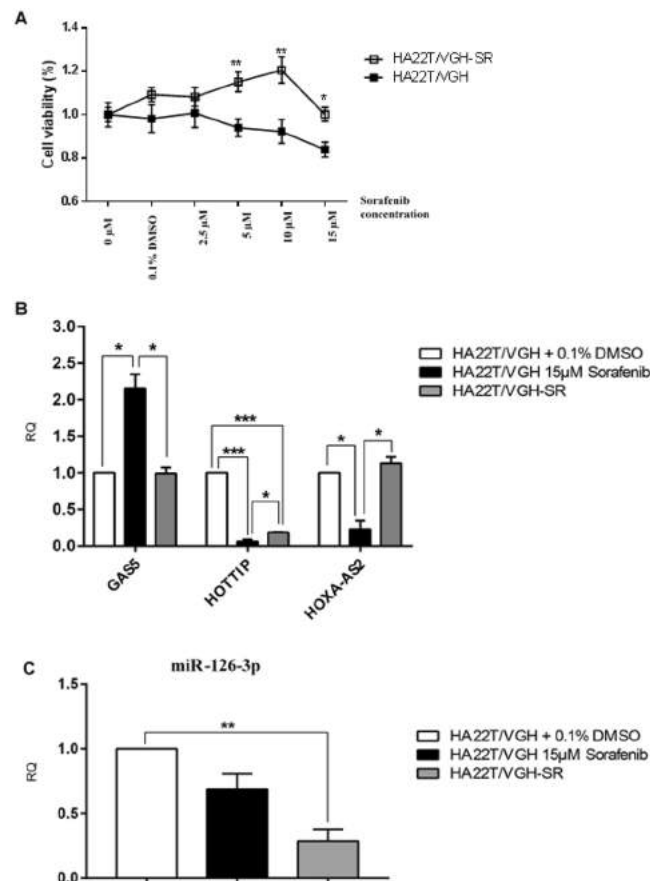


**Figure 4.** GAS5, HOTTIP, HOXA-AS2 and miR-126-3p were dysregulated in sorafenib resistant HCC cells. **(A)** This graph displays the effects of sorafenib treatment on the proliferation of HA22T/VGH resistant cells (HA22T/VGH-SR) compared with the parental sensitive ones. **(B)** Expression of GAS5, HOTTIP, HOXA-AS2 or **(C)** miR-126-3p in HA22T/VGH sensitive cells or HA22T/VGH-SR resistant cells exposed to 15  $\mu$ M sorafenib and in HA22T/VGH cells exposed to 0.1% DMSO. Unpaired t-test was used to determine the presence of a statistically significant difference between either sensitive or resistant cells exposed to sorafenib and sensitive cells exposed to DMSO only: \**P*-value < 0.05, \*\**P*-value < 0.01, \*\*\**P*-value *p* < 0.001; \*\*\*\**P*-value < 0.0001. The bars represent the mean expression values from 3 experiments and the lines represent the standard error of the mean (SEM).

resistance to sorafenib in HA22T/VGH-SR cells may be connected to the restoration of GAS5 and HOXA-AS2 expression to the levels found in the sensitive and untreated cells.

Results with miR-126-3p showed that it was downregulated in HA22T/VGH-SR cells compared to either the cells exposed to DMSO or to HA22T/VGH exposed to sorafenib (Fig. 4C). This may suggest that acquisition of resistance to sorafenib may lead to a further downregulation of this miRNA.

**miR-126-3p directly interacted with GAS5 in HA22T/VGH cells.** Since 7 out of 9 cell lines treated with sorafenib (Figs 2D–F; 3B–D) displayed opposite expression levels between the up-regulated GAS5 and the down-regulated miR-126-3p and the knockdown of GAS5 promoted the increase of miR-126-3p expression in sorafenib treated HA22T/VGH cells (Supplementary Fig. 1C,D), we explored whether GAS5 may act as a ceRNA for miR-126-3p. To do that, we performed bioinformatics analysis using the algorithm IntaRNA (<http://rna.informatik.uni-freiburg.de/IntaRNA/Input.jsp>) that predicted a putative miR-126-3p binding site (BS) within the exon 12 of GAS5 (nt 575–584; ref. n. NR\_002578; Fig. 5A).

To verify a potential direct molecular interaction, a 34-bp long sequence of GAS5 containing the putative miR-126-3p BS was cloned into the pmiRGLO vector (pmiRGLO GAS5 S2). A control construct was obtained by cloning the same fragment in an antisense orientation (pmiRGLO GAS5 AS2). HA22T/VGH cells were then transfected with 100 nM miR-126-3p mimic and with the obtained constructs (pmiRGLO, pmiRGLO GAS5 S2 and pmiRGLO GAS5 AS2). The amounts of luciferase activity detected in HA22T/VGH cells with empty vector with or without miR-126-3p mimic and with antisense construct with miR-126-3p mimic were very similar. However, the pmiRGLO GAS5 S2 construct in presence of miR-126-3p mimic showed a 39% decrease in the luciferase activity compared to the control empty vector without mimic compound (Fig. 5B). The luciferase activity measured here was significantly lower (*P*-value  $\leq$  0.01) compared to the one measured for any other sample.

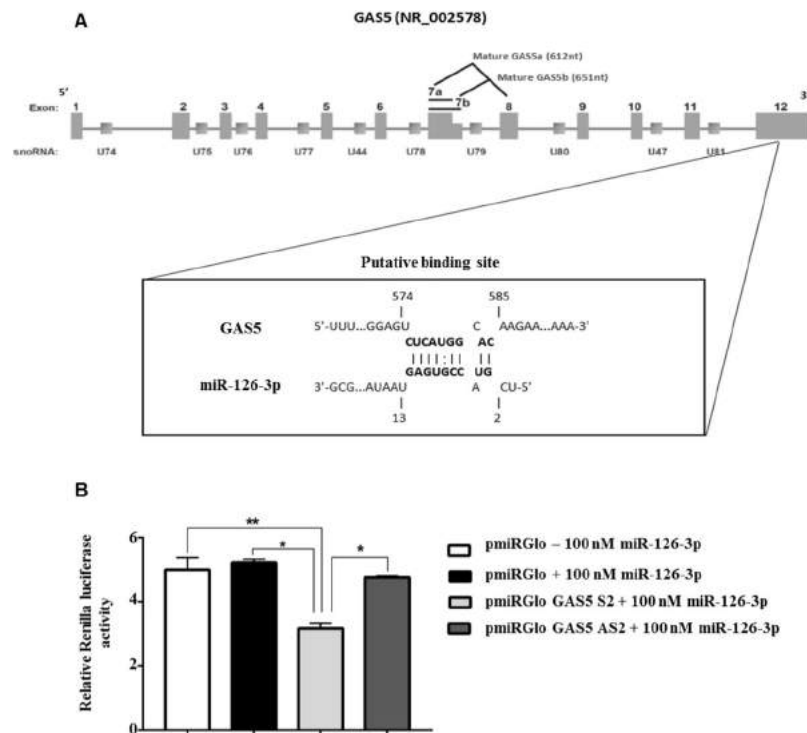


**Figure 5.** miR-126-3p may directly interact with a putative binding site found in GAS5 in HA22T/VGH cells. (A) Bioinformatics analysis showed that GAS5 may harbour a putative binding site for miR-126-3p; the location and the complementarity between miR-126-3p and the putative GAS5 3'-UTR target site are shown in the enlarged inset. (B) Luciferase activity measured in HA22T/VGH cells following ectopic expression of miR-126-3p and co-transfection with pmirGLO, pmirGLO GAS5 S2 or pmirGLO GAS5 AS2. Unpaired t-test was used to determine the presence of a statistically significant difference between the cells transfected with different constructs: \**P*-value < 0.05, \*\**P*-value < 0.01, \*\*\**P*-value *p* < 0.001; \*\*\*\**P*-value < 0.0001. The bars represent the mean luciferase activity values from 3 experiments and the lines represent the standard error of the mean (SEM).

The data showed that the putative BS of the GAS5 was recognized by miR-126-3p and therefore it is possible that GAS5 may act as a sponge for miR-126-3p.

**Effects of miR-126-3p ectopic expression on cell viability in HA22T/VGH treated or not treated with sorafenib.** In order to verify whether miR-126-3p over-expression affected HA22T/VGH cell growth, we transfected the cells with miR-126-3p mimics. miRNA-126-3p ectopic expression significantly inhibited the HA22T/VGH cell viability at 50 and 100 nM concentration compared to the corresponding doses of miR-NC (Fig. 6A) at 24 h and 48 h after transfection.

Since sorafenib mediated the down-modulation of miR-126-3p in tumor cells, we assessed the effects on cell growth of miR-126-3p ectopic expression following sorafenib treatment of HA22T/VGH cells. As expected, a significantly decreased of proliferation ability was observed for cells treated with 15  $\mu$ M sorafenib. However, the concomitant overexpression of miR-126-3p did not affect the proliferation inhibition any further (Fig. 6B). These data would exclude an additive effect using miR-126-3p and sorafenib treatment on HA22T/VGH cell proliferation.

### Expression of miR-126-3p in tissues and plasma of HCC patients and plasmatic detection of GAS5.

Since miR-126-3p was significantly down-modulated after sorafenib treatment in almost all the cells included in the present study, we assessed its expression levels in HCC tissues and plasma from HCC patients to better understand the variation in its expression. miR-126-3p was significantly down-regulated in HCC tissues compared to their matched peritumoral (PT) tissues using qPCR analysis ( $RQ_{\text{HCC}}$  average =  $3.91 \pm 0.48$  vs.  $RQ_{\text{PT}}$  average =  $5.84 \pm 0.51$ ; *P*-value = 0.0074; Fig. 7A). Regarding the expression of GAS5 in the same cohort, we did not find any significant correlation with miR-126-3p expression. However, we observed a high percentage (64%) of cases with simultaneously high GAS5 expression and low miR-126-3p expression (Supplementary Fig. 2). The levels of circulating miR-126-3p were significantly higher in HCC patients compared to controls (Fig. 7B). The plotting was made on the average raw cycle thresholds ( $C_t$ ) since there were no established endogenous miRNAs acting as normalizers for plasma miRs. The average  $C_t$  values of the spike-in cel-miR-39 were the same in the two groups demonstrating good and constant performance of RT and qPCR reactions (Fig. 7C). The ROC curve analysis evidenced the possibility to use the plasmatic miR-126-3p levels to distinguish HCC patients from control subjects (AUC = 0.78; *P*-value = 0.0007; Fig. 7D).

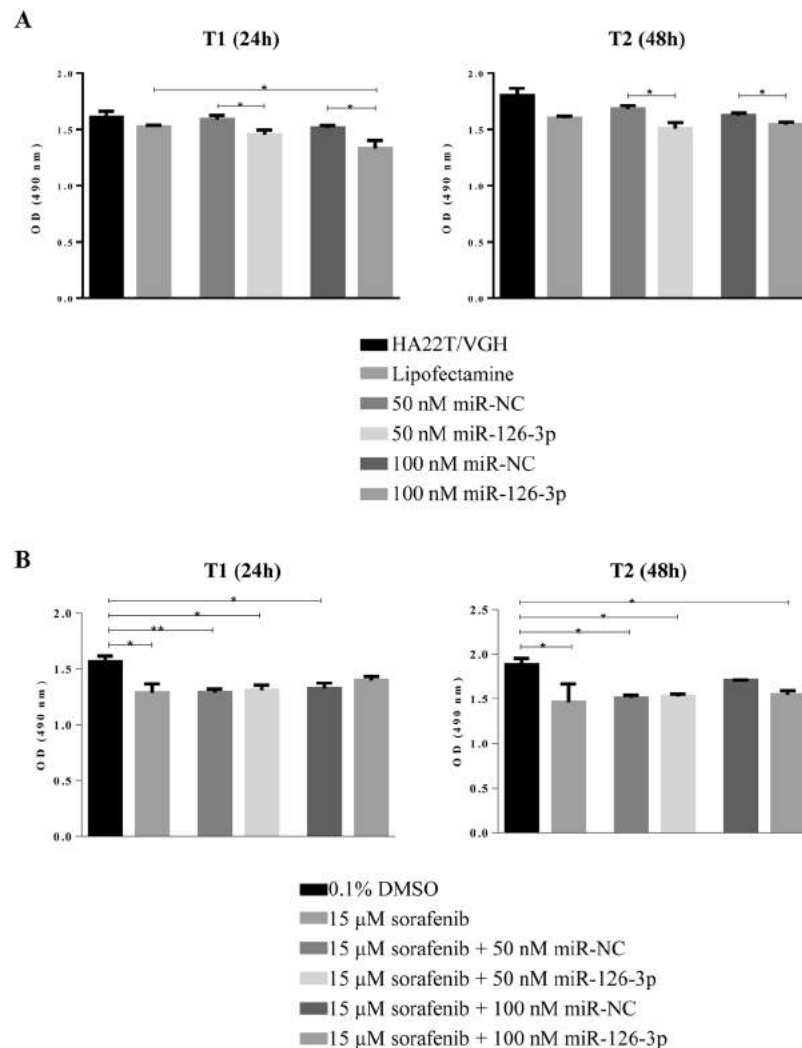


**Figure 6.** Effects of miR-126-3p ectopic expression on HA22T/VGH cells growth untreated/treated with sorafenib. **(A)** MTT assay was performed in HA22T/VGH cells transfected with 50 nM or 100 nM of miR-NC or miR-126-3p. The ectopic expression of miR-126-3p significantly decreased cell growth after 24 hours and 48 hours from transfection compared to corresponding controls. \* $P$ -value < 0.05 versus Lipofectamine or miR-NC in t-Test analysis for unpaired comparison. **(B)** The HA22T/VGH cells were treated with 15 μM sorafenib or vehicle (0.1% DMSO) and transfected with miR-NC or miR-126-3p (50 nM or 100 nM). MTT assay showed that sorafenib significantly reduced cell viability at 24 hours and 48 hours after miRs transfection. No additive effects were observed using the ectopic expression of miR-126-3p. One-way ANOVA followed by Bonferroni test as pair-wise post-hoc test was used to test the significant difference in expression between the different groups: \*\* $P$ -value < 0.01, \* $P$ -value < 0.05. The histograms represent the mean expression values from 5 replicates for each conditions and the lines represent the standard error of the mean (SEM). These graphs are representative of one of two experiments.

In order to assess whether GAS5 was released into the bloodstream, we determined its level in the plasma by qPCR. The expression levels of GAS5 were significantly lower in HCC patients compared to controls (Fig. 7E). The ROC curve analysis evidenced the possibility to use GAS5 to distinguish HCC patients from control subjects (AUC = 0.72;  $P$ -value = 0.007; Fig. 7F).

## Discussion

The main aim of this work was to investigate whether the oral multikinase inhibitor sorafenib could modulate the expression of given ncRNAs in HCC cells. The qPCR array study revealed that a total of 23 lncRNAs (3 up-regulated and 20 down-regulated) and 8 miRNAs (5 down-modulated and 3 upregulated) were significantly dysregulated in sorafenib-treated HCC cells (HA22T/VGH) when they were compared to untreated cells. These findings pointed to the evidence that sorafenib affected mainly the expression levels of the lncRNAs rather than miRNAs included in the array. To our knowledge, this is the first study designed to examine the expression changes of a wide number of lncRNAs after sorafenib treatment of cultured cells. We focused on the expression of GAS5 and HOXA-AS2 since they were the most upregulated and down-modulated genes, respectively and on



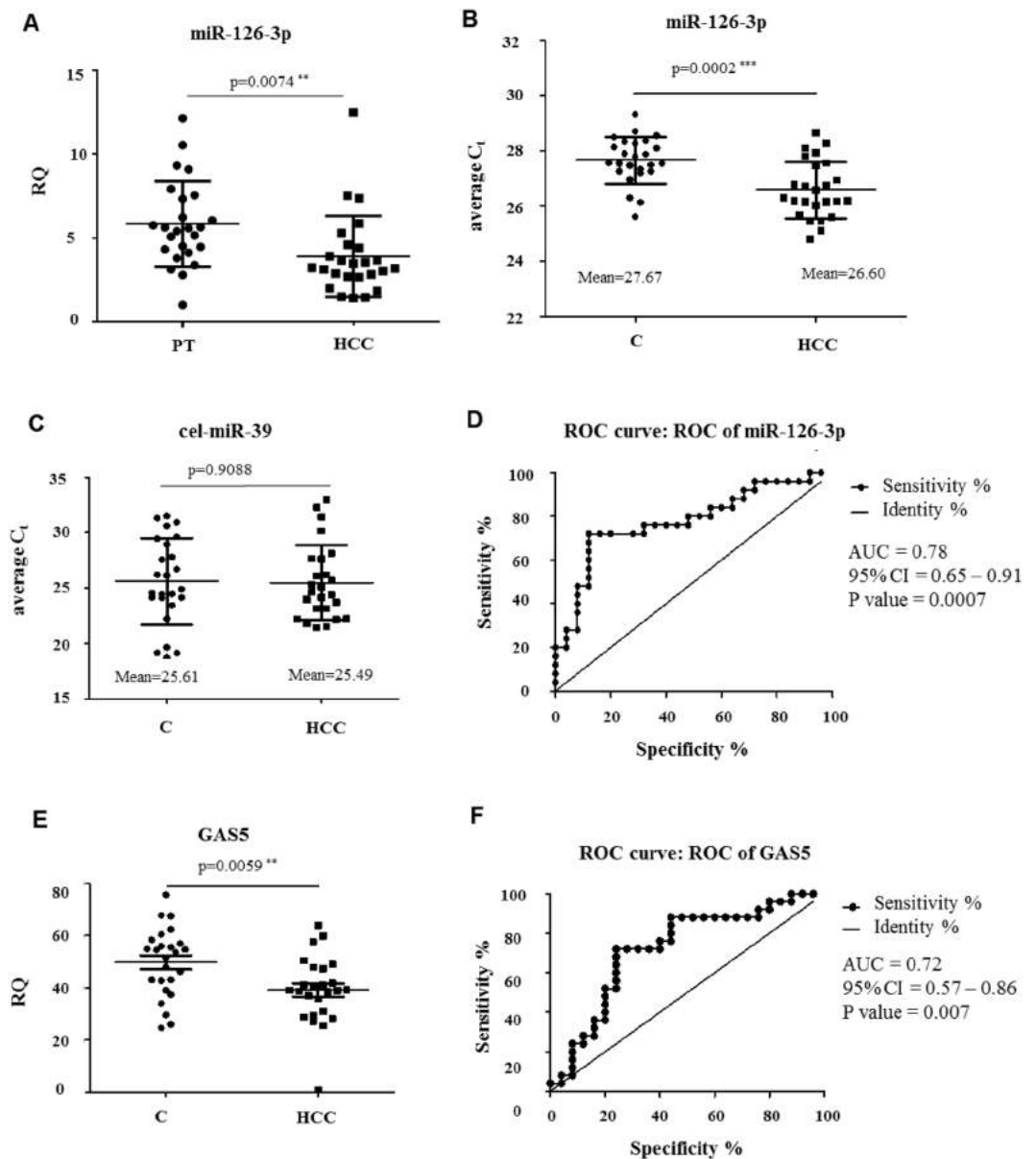


**Figure 7.** miR-126-3p levels in plasma and in tissues and circulating GAS5 in plasma from HCC patients and healthy subjects. (A) miR-126-3p levels were significantly down-modulated in HCC compared to PT (n = 25). Dotplots of the average  $C_t$  of the circulating miR-126-3p (B) and the spike-in cel-miR-39 (C) in healthy subjects and in HCC patients; HCC patients showed higher levels of miR-126-3p in plasma than healthy controls. (D) ROC curve analysis of plasma miR-126-3p. AUC = area under the ROC curve; CI = confidence interval. (E) Dotplot of the circulating GAS5 for healthy subjects or HCC patients; GAS5 levels in HCC patients were significantly lower compared to control subjects. (F) ROC curve analysis of plasma GAS5. AUC = area under the ROC curve; CI = confidence interval. Two-tailed, paired t-test was used to determine the presence of a statistically significant difference between ncRNAs expression in HCC patients against healthy controls or between HCC tumour and peritumoral areas: \*P-value < 0.05, \*\*P-value < 0.01, \*\*\*P-value < 0.001; \*\*\*\*P-value < 0.0001.

the expression of HOTTIP because its down-modulation was at intermediate level. We also chose miR-126-3p because it was the most down-modulated miR.

The expression levels of GAS5 were found to be increased in almost all the cancer cells treated with sorafenib compared to cells exposed to DMSO (except SKHep1C3) proving that sorafenib may up-regulate GAS5 not only in different HCC cell lines but also in renal and breast cancer cells. It is well known that GAS5 acts as tumor-suppressor in several malignancies and it was reported to be significantly lower in clinical renal cell carcinoma (RCC) specimens<sup>24</sup>, breast cancer tissues<sup>25</sup> and HCC tissues<sup>26</sup> when compared to the adjacent normal tissues. Instead, very few data are present in the literature about circulating GAS5 in human malignancies. For example, high GAS5 serum levels were associated with best prognosis in patients with glioblastoma<sup>27</sup> while GAS5

levels were found to be decreased in serum<sup>27</sup> and in plasma<sup>28</sup> of colorectal cancer (CRC) patients compared to control subjects. The plasma levels of GAS5 of HCC patients and control individuals were compared for the first time in the present study. Significant lower levels of GAS5 were found in the plasma of HCC patients in comparison with control subjects and the ROC analysis evidenced the potential ability of circulating GAS5 levels to discriminate HCC patients from control subjects.

Regarding HOTTIP, 4 tumor cell lines (HA22T/VGH, HuH6, ACHN and Caki-1) among the ones tested expressed appreciable levels of this lncRNA and in which HOTTIP was significantly down-regulated following treatment with sorafenib. It is known that HOTTIP can exert oncogenic effects in solid tumors<sup>29</sup> and has been found significantly upregulated in various types of human cancer, including hepatocellular carcinoma, pancreatic, gastric and colorectal cancer. It has also been associated with metastasis, progression and prognosis in several neoplastic diseases<sup>30–32</sup>. Similar considerations can be extended to the lncRNA HOXA-AS2. In fact, the cancer cell lines that exhibited the highest expression levels of this gene in normal growth condition also displayed its down-modulation after sorafenib treatment (HA22T/VGH, ACHN, Caki-1, CRBM 1990 and HCC1937). HOXA-AS2 was previously found to be significantly up-regulated in breast cancer tissues<sup>33</sup> and HCC tissues compared with normal tissues<sup>34</sup> and to promote tumorigenesis of HCC<sup>34</sup>.

The results obtained in the present study indicate that sorafenib mediated the up-regulation of GAS5 and the down-regulation of HOTTIP and HOXA-AS2 in most HCC, renal and breast cancer cells and probably their expression modulation may lead to a less aggressive cancer phenotype of the cells. Subsequent studies will aim to address this issue.

It has been established that some HCC patients are either initially resistant to sorafenib or become resistant to it during its use<sup>35</sup> reducing the efficacy of the treatment. Therefore, efforts have been directed to identify novel predictive molecular biomarkers for primary and/or acquired resistance to sorafenib and to discover novel strategies to improve its effectiveness also by understanding how lncRNAs expression are affected by it. The lncRNAs are known to be involved in chemotherapy and drug resistance or response. Recently, Xue *et al.* have found that HOTAIR is highly upregulated in the tumors of tamoxifen-resistant breast cancer patients compared to their primary counterparts<sup>36</sup>. Liu *et al.* identified that GAS5 was downregulated in sorafenib non-responsive RCCs and that GAS5 overexpression conferred sensitivity to sorafenib in nonresponsive RCC cells<sup>18</sup>. Again, Jean *et al.* found that knockdown of lncRNA TUC338 in HepG2 rendered these cells sensitive to the treatment with sorafenib<sup>37</sup>. In this context, we have found that the sorafenib resistant cells HA22T/VGH-SR (obtained after months of continuous treatment with increasing concentration of sorafenib) expressed levels of GAS5 and HOXA-AS2 comparable to those of sensitive and untreated cells indicating that the cells gradually restored the expression levels of these genes during resistance development. Thus, the quantification of the expression levels of these 2 lncRNAs during the treatment may indicate the onset of drug resistance in HCC cells. It is conceivable that GAS5 and HOXA-AS2 dysregulation occurred not only following sorafenib response, but also after the acquisition of sorafenib-resistance in HA22T/VGH cells.

In the present study, we also reported that sorafenib influenced miR-126-3p expression since it resulted down-modulated following sorafenib treatment in all the cells except Caki-1 cells. miR-126 have been shown to have a significant impact on many human cancer types acting as a tumor suppressor in several tumors. Lower expression of miR-126 in HCC was significantly associated with tumor recurrence and poor survival of patients<sup>38</sup>. miR-126-3p upregulation have been associated with decreased cell proliferation, apoptosis induction, and inhibition of tumor angiogenesis in HCC<sup>39</sup>. In this context, miR-126-3p ectopic expression decreased the growth capacity of HA22T/VGH cells, but the miR-126-3p over-expression in sorafenib-treated HA22T/VGH did not affect further the proliferation inhibition promoted by sorafenib. It is challenging to reconcile the observation that miR-126-3p generally has tumor suppression functions with the observation that miR-126-3p expression levels further decreased in sorafenib sensitive and also in drug-resistant cells after sorafenib treatment. Consequently to better elucidate its role, we measured miR-126-3p levels in HCC tissues from biopsies and we quantified its plasmatic circulating levels. miR-126-3p resulted significantly down-regulated in HCC tissues respect to their peritumoral counterparts (PT), in agreement with other previously reported data<sup>39,40</sup>. The levels of plasmatic circulating miR-126-3p were higher in HCC patients respect to healthy subjects and this has the potential to be used to discriminate HCC patients from healthy people as found by receiver operating characteristic (ROC) curve analysis. To the best of our knowledge, only three previous publications reported data about circulating miR-126 levels. Gosh *et al.* showed increased miR-126-3p expression in plasma of HBV-positive/HCC patients compared to HBV-positive/non-HCC patients<sup>41</sup> in accordance with our results. In other two published reports, the miR-126 circulating levels were measured in serum. Khairy *et al.* found a significant decrease of levels of miR-126 in the serum of HCC patients compared to non-HCC group<sup>42</sup>. Ali *et al.* demonstrated that the median serum level of miR-126-3p was significantly reduced in HCC patients compared to healthy controls<sup>43</sup>. In summary, miR-126-3p has been shown to be upregulated in plasma but down-modulated in serum of HCC patients. This should not be surprising, since the differences in miRs levels between plasma and serum have been commonly described<sup>44</sup>. The question that remain to answer is why miR-126-3p decreased following sorafenib treatment in our cancer *in vitro* models. At the present, we may speculate that miR-126-3p marginally contributes to the less aggressive phenotype of cancer cells observed after drug treatment (*i.e.* in terms of proliferation inhibition). However, the trend of miR-126-3p down-modulation obtained in all the treated cells would suggest that sorafenib may determine the expression variation of this miRNA very likely indirectly. We think that miR-126-3p levels should be further investigated in patients treated or not with sorafenib to verify this hypothesis.

Finally, we found by bioinformatics analysis that GAS5 had a putative binding site for miR-126-3p and demonstrated by luciferase reporter assay a direct interaction between GAS5 and miR-126-3p. It has been previously shown that GAS5 may function as miRNA sponge or competing endogenous RNA (ceRNA) for some miRs included miR-21<sup>45</sup> and miR-222<sup>46</sup> and therefore we hypothesized that GAS5 may act as a sponge for miR-126-3p in HCC cells. In support to this hypothesis, we found that the silencing of GAS5 resulted in miR-126-3p

up-regulation upon sorafenib treatment in the rescue experiment. In addition, 64% of the HCC patients with high GAS5 expression had also miR-126-3p down-modulated.

Circulating ncRNAs have been described in different human body fluids, including serum/plasma and urine and are promising biomarkers for cancer risk assessment, diagnosis, prognosis, and to monitor the treatment response<sup>47–50</sup>. In this context, our results on circulating GAS5 and miR-126-3p would indicate their potential to be used to discriminate HCC patients from healthy subjects. These results may be considered an initial step in the identification of novel non-invasive circulating biomarkers of disease. Future studies will be addressed to verify whether GAS5 and miR-126-3p may be potential early/predictive circulating biomarkers in at high-risk patients (i.e. patients with cirrhosis and/or HBV, HCV chronic hepatitis).

In conclusion, elucidation of the downstream effects of sorafenib treatment may be useful to better understand novel aspects of its mechanism of action that has not been yet completely elucidated and therefore to augment the basic knowledge of intracellular events occurring in cancer cells after sorafenib treatment.

## References

- Quinn, J. J. & Chang, H. Y. Unique features of long non-coding RNA biogenesis and function. *Nature reviews. Genetics* **17**, 47–62, <https://doi.org/10.1038/nrg.2015.10> (2016).
- Jandura, A. & Krause, H. M. The New RNA World: Growing Evidence for Long Noncoding RNA Functionality. *Trends in genetics: TIG* **33**, 665–676, <https://doi.org/10.1016/j.tig.2017.08.002> (2017).
- Bracken, C. P., Scott, H. S. & Goodall, G. J. A network-biology perspective of microRNA function and dysfunction in cancer. *Nature reviews. Genetics* **17**, 719–732, <https://doi.org/10.1038/nrg.2016.134> (2016).
- Huarte, M. The emerging role of lncRNAs in cancer. *Nature medicine* **21**, 1253–1261, <https://doi.org/10.1038/nm.3981> (2015).
- Ha, M. & Kim, V. N. Regulation of microRNA biogenesis. *Nature reviews. Molecular cell biology* **15**, 509–524, <https://doi.org/10.1038/nrm3838> (2014).
- Peng, Y. & Croce, C. M. The role of MicroRNAs in human cancer. *Signal transduction and targeted therapy* **1**, 15004, <https://doi.org/10.1038/sigtrans.2015.4> (2016).
- Grossi, I., Salvi, A., Abeni, E., Marchina, E. & De Petro, G. Biological Function of MicroRNA193a-3p in Health and Disease. *International journal of genomics* **2017**, 5913195, <https://doi.org/10.1155/2017/5913195> (2017).
- Llovet, J. M. *et al.* Hepatocellular carcinoma. *Nature reviews. Disease primers* **2**, 16018, <https://doi.org/10.1038/nrdp.2016.18> (2016).
- Mittal, S. & El-Serag, H. B. Epidemiology of hepatocellular carcinoma: consider the population. *Journal of clinical gastroenterology* **47**(Suppl), S2–6, <https://doi.org/10.1097/MCG.0b013e3182872f29> (2013).
- Raoul, J. L. *et al.* Relationship between baseline hepatic status and outcome, and effect of sorafenib on liver function: SHARP trial subanalyses. *Journal of hepatology* **56**, 1080–1088, <https://doi.org/10.1016/j.jhep.2011.12.009> (2012).
- Aravalli, R. N., Cressman, E. N. & Steer, C. J. Cellular and molecular mechanisms of hepatocellular carcinoma: an update. *Archives of toxicology* **87**, 227–247, <https://doi.org/10.1007/s00204-012-0931-2> (2013).
- Cidon, E. U. Systemic treatment of hepatocellular carcinoma: Past, present and future. *World journal of hepatology* **9**, 797–807, <https://doi.org/10.4254/wjh.v9.i18.797> (2017).
- Zhu, Y. J., Zheng, B., Wang, H. Y. & Chen, L. New knowledge of the mechanisms of sorafenib resistance in liver cancer. *Acta pharmacologica Sinica* **38**, 614–622, <https://doi.org/10.1038/aps.2017.5> (2017).
- Cervello, M. *et al.* Molecular mechanisms of sorafenib action in liver cancer cells. *Cell Cycle* **11**, 2843–2855, <https://doi.org/10.4161/cc.21193> (2012).
- Pehserl, A. M. *et al.* Comprehensive Analysis of miRNome Alterations in Response to Sorafenib Treatment in Colorectal Cancer Cells. *International journal of molecular sciences* **17**, <https://doi.org/10.3390/ijms17122011> (2016).
- Abeni, E. *et al.* Sorafenib induces variations of the DNA methylome in HA22T/VGH human hepatocellular carcinoma-derived cells. *International journal of oncology* **51**, 128–144, <https://doi.org/10.3892/ijo.2017.4019> (2017).
- Salvi, A. *et al.* Effects of miR-193a and sorafenib on hepatocellular carcinoma cells. *Molecular cancer* **12**, 162, <https://doi.org/10.1186/1476-4598-12-162> (2013).
- Liu, L. *et al.* Long non-coding RNA GAS5 sensitizes renal cell carcinoma to sorafenib via miR-21/SOX5 pathway. *Cell Cycle*, <https://doi.org/10.1080/15384101.2018.1475826> (2018).
- Escudier, B. *et al.* Sorafenib for treatment of renal cell carcinoma: Final efficacy and safety results of the phase III treatment approaches in renal cancer global evaluation trial. *Journal of clinical oncology: official journal of the American Society of Clinical Oncology* **27**, 3312–3318, <https://doi.org/10.1200/JCO.2008.19.5511> (2009).
- Zafrafas, M., Papisozomenou, P. & Emmanouilides, C. Sorafenib in breast cancer treatment: A systematic review and overview of clinical trials. *World journal of clinical oncology* **7**, 331–336, <https://doi.org/10.5306/wjco.v7.i4.331> (2016).
- Salvi, A., Abeni, E., Portolani, N., Barlati, S. & De Petro, G. Human hepatocellular carcinoma cell-specific miRNAs reveal the differential expression of miR-24 and miR-27a in cirrhotic/non-cirrhotic HCC. *International journal of oncology* **42**, 391–402, <https://doi.org/10.3892/ijo.2012.1716> (2013).
- Mann, M., Wright, P. R. & Backofen, R. IntaRNA 2.0: enhanced and customizable prediction of RNA-RNA interactions. *Nucleic acids research* **45**, W435–W439, <https://doi.org/10.1093/nar/gkx279> (2017).
- Zweig, M. H. & Campbell, G. Receiver-operating characteristic (ROC) plots: a fundamental evaluation tool in clinical medicine. *Clinical chemistry* **39**, 561–577 (1993).
- Qiao, H. P., Gao, W. S., Huo, J. X., Yang, Z. S. & Long Non-coding, R. N. A. GAS5 Functions as a Tumor Suppressor in Renal Cell Carcinoma. *Asian Pac J Cancer P* **14**, 1077–1082, <https://doi.org/10.7314/APJCP.2013.14.2.1077> (2013).
- Li, W. *et al.* Downregulation of lncRNA GAS5 causes trastuzumab resistance in breast cancer. *Oncotarget* **7**, 27778–27786, <https://doi.org/10.18632/oncotarget.8413> (2016).
- Chang, L. *et al.* Decreased expression of long non-coding RNA GAS5 indicates a poor prognosis and promotes cell proliferation and invasion in hepatocellular carcinoma by regulating vimentin. *Molecular medicine reports* **13**, 1541–1550, <https://doi.org/10.3892/mmr.2015.4716> (2016).
- Shen, J. *et al.* Serum HOTAIR and GAS5 levels as predictors of survival in patients with glioblastoma. *Molecular carcinogenesis* **57**, 137–141, <https://doi.org/10.1002/mc.22739> (2018).
- Liu, L. *et al.* Prognostic and predictive value of long non-coding RNA GAS5 and microRNA-221 in colorectal cancer and their effects on colorectal cancer cell proliferation, migration and invasion. *Cancer biomarkers: section A of Disease markers* **22**, 283–299, <https://doi.org/10.3233/CBM-171011> (2018).
- Lian, Y. *et al.* HOTTIP: a critical oncogenic long non-coding RNA in human cancers. *Molecular bioSystems* **12**, 3247–3253, <https://doi.org/10.1039/c6mb00475j> (2016).
- Li, W., Li, N., Kang, X., Shi, K. & Chen, Q. Prognostic value of the long noncoding RNA HOTTIP in human cancers. *Oncotarget* **8**, 59563–59569, <https://doi.org/10.18632/oncotarget.19166> (2017).
- Tsang, F. H. C. *et al.* Long non-coding RNA HOTTIP is frequently up-regulated in hepatocellular carcinoma and is targeted by tumour suppressive miR-125b. *Liver Int* **35**, 1597–1606, <https://doi.org/10.1111/liv.12746> (2015).

32. Chang, S. *et al.* HOTTIP and HOXA13 are oncogenes associated with gastric cancer progression. *Oncology reports* **35**, 3577–3585, <https://doi.org/10.3892/or.2016.4743> (2016).
33. Fang, Y. *et al.* Long non-coding RNA HOXA-AS2 promotes proliferation and invasion of breast cancer by acting as a miR-520c-3p sponge. *Oncotarget* **8**, 46090–46103, <https://doi.org/10.18632/oncotarget.17552> (2017).
34. Wang, F. *et al.* HOX Antisense lincRNA HOXA-AS2 Promotes Tumorigenesis of Hepatocellular Carcinoma. *Cellular physiology and biochemistry: international journal of experimental cellular physiology, biochemistry, and pharmacology* **40**, 287–296, <https://doi.org/10.1159/000452545> (2016).
35. Nishida, N., Kitano, M., Sakurai, T. & Kudo, M. Molecular Mechanism and Prediction of Sorafenib Chemoresistance in Human Hepatocellular Carcinoma. *Dig Dis* **33**, 771–779, <https://doi.org/10.1159/000439102> (2015).
36. Xue, X. *et al.* LncRNA HOTAIR enhances ER signaling and confers tamoxifen resistance in breast cancer. *Oncogene* **35**, 2746–2755, <https://doi.org/10.1038/nc.2015.340> (2016).
37. Jin, W. D. *et al.* Long non-coding RNA TUC338 is functionally involved in sorafenib-sensitized hepatocarcinoma cells by targeting RASAL1. *Oncology reports* **37**, 273–280, <https://doi.org/10.3892/or.2016.5248> (2017).
38. Chen, H. Y. *et al.* Decreased expression of miR-126 correlates with metastatic recurrence of hepatocellular carcinoma. *Clinical & experimental metastasis* **30**, 651–658, <https://doi.org/10.1007/s10585-013-9569-6> (2013).
39. Gong, C., Fang, J., Li, G., Liu, H. H. & Liu, Z. S. Effects of microRNA-126 on cell proliferation, apoptosis and tumor angiogenesis via the down-regulating ERK signaling pathway by targeting EGFL7 in hepatocellular carcinoma. *Oncotarget* **8**, 52527–52542, <https://doi.org/10.18632/oncotarget.17283> (2017).
40. Hu, M. H. *et al.* MicroRNA-126 inhibits tumor proliferation and angiogenesis of hepatocellular carcinoma by down-regulating EGFL7 expression. *Oncotarget* **7**, 66922–66934, <https://doi.org/10.18632/oncotarget.11877> (2016).
41. Ghosh, A. *et al.* Hepatic miR-126 is a potential plasma biomarker for detection of hepatitis B virus infected hepatocellular carcinoma. *International journal of cancer* **138**, 2732–2744, <https://doi.org/10.1002/ijc.29999> (2016).
42. Khairy, A., Hamza, I., Shaker, O. & Yosry, A. Serum miRNA Panel in Egyptian Patients with Chronic Hepatitis C Related Hepatocellular Carcinoma. *Asian Pacific journal of cancer prevention: APJCP* **17**, 2699–2703 (2016).
43. Ali, H. E. A. *et al.* Circulating microRNAs panel as a diagnostic tool for discrimination of HCV-associated hepatocellular carcinoma. *Clin Res Hepatol Gas* **41**, E51–E62, <https://doi.org/10.1016/j.clinre.2017.06.004> (2017).
44. Moshiri, F. *et al.* Circulating miR-106b-3p, miR-101-3p and miR-1246 as diagnostic biomarkers of hepatocellular carcinoma. *Oncotarget* **9**, 15350–15364, <https://doi.org/10.18632/oncotarget.24601> (2018).
45. Hu, L. *et al.* Long noncoding RNA GAS5 suppresses the migration and invasion of hepatocellular carcinoma cells via miR-21. *Tumour biology: the journal of the International Society for Oncodevelopmental Biology and Medicine* **37**, 2691–2702, <https://doi.org/10.1007/s13277-015-4111-x> (2016).
46. Yu, F. J. *et al.* Long Non-coding RNA Growth Arrest-specific Transcript 5 (GAS5) Inhibits Liver Fibrogenesis through a Mechanism of Competing Endogenous RNA. *J Biol Chem* **290**, 28286–28298, <https://doi.org/10.1074/jbc.M115.683813> (2015).
47. Qi, P., Zhou, X. Y. & Du, X. Circulating long non-coding RNAs in cancer: current status and future perspectives. *Molecular cancer* **15**, <https://doi.org/10.1186/s12943-016-0524-4> (2016).
48. Mitchell, P. S. *et al.* Circulating microRNAs as stable blood-based markers for cancer detection. *P Natl Acad Sci USA* **105**, 10513–10518, <https://doi.org/10.1073/pnas.0804549105> (2008).
49. Grossi, I., Salvi, A., Baiocchi, G., Portolani, N. & De Petro, G. Functional role of microRNA-23b-3p in cancer biology. *Microna*, <https://doi.org/10.2174/2211536607666180629155025> (2018).
50. Salvi, A. *et al.* Analysis of a nanoparticle-enriched fraction of plasma reveals miRNA candidates for Down syndrome pathogenesis. *International journal of molecular medicine* **43**, 2303–2318, <https://doi.org/10.3892/ijmm.2019.4158> (2019).

## Acknowledgements

We thank Dr M. Crosatti (University of Leicester; UK) for the linguistic revision of the manuscript. This work was supported by funding from the Lega Italiana Lotta ai Tumori (LILT), the Italian Ministry of University and Research (FFRB grant), the University of Brescia (local grants), and the Fondazione EULO Brescia. The funding bodies played no role in the design of the study and collection, analysis, and interpretation of data and in writing the manuscript. I.G. was supported by a Postdoctoral fellowship from -Ricerchiamo Onlus-, Brescia, Italy.

## Author Contributions

A.S. and G.D.P. designed the study. T.F., I.G., M.M., A.S. performed the experiments. A.S. wrote and submitted the manuscript. M.C., E.M. and G.D.P. critically revised the manuscript. G.B. and N.P. provided the clinical samples and critically revised the manuscript.

## Additional Information

**Supplementary information** accompanies this paper at <https://doi.org/10.1038/s41598-019-45604-2>.

**Competing Interests:** The authors declare no competing interests.

**Publisher's note:** Springer Nature remains neutral with regard to jurisdictional claims in published maps and institutional affiliations.



**Open Access** This article is licensed under a Creative Commons Attribution 4.0 International License, which permits use, sharing, adaptation, distribution and reproduction in any medium or format, as long as you give appropriate credit to the original author(s) and the source, provide a link to the Creative Commons license, and indicate if changes were made. The images or other third party material in this article are included in the article's Creative Commons license, unless indicated otherwise in a credit line to the material. If material is not included in the article's Creative Commons license and your intended use is not permitted by statutory regulation or exceeds the permitted use, you will need to obtain permission directly from the copyright holder. To view a copy of this license, visit <http://creativecommons.org/licenses/by/4.0/>.

© The Author(s) 2019



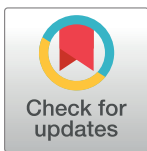
RESEARCH ARTICLE

# Genomic inversions and *GOLGA* core duplicons underlie disease instability at the 15q25 locus

Flavia A. M. Maggiolini<sup>1</sup>, Stuart Cantsilieris<sup>2</sup>, Pietro D'Addabbo<sup>1</sup>, Michele Manganelli<sup>1</sup>, Bradley P. Coe<sup>2</sup>, Beth L. Dumont<sup>3</sup>, Ashley D. Sanders<sup>4</sup>, Andy Wing Chun Pang<sup>5</sup>, Mitchell R. Vollger<sup>2</sup>, Orazio Palumbo<sup>6</sup>, Pietro Palumbo<sup>6</sup>, Maria Accadia<sup>7</sup>, Massimo Carella<sup>6</sup>, Evan E. Eichler<sup>2,8</sup>, Francesca Antonacci<sup>1\*</sup>

**1** Dipartimento di Biologia, Università degli Studi di Bari "Aldo Moro", Bari, Italy, **2** Department of Genome Sciences, University of Washington School of Medicine, Seattle, WA, United States of America, **3** The Jackson Laboratory, Bar Harbor, ME, United States of America, **4** European Molecular Biology Laboratory (EMBL), Genome Biology Unit, Meyerhofstraße 1, Heidelberg, Germany, **5** Bionano Genomics, San Diego, CA, United States of America, **6** Medical Genetics Unit, IRCCS Casa Sollievo della Sofferenza, San Giovanni Rotondo (FG), Italy, **7** Medical Genetics Service, Hospital "Cardinale G. Panico", Via San Pio X n°4, Tricase, LE, Italy, **8** Howard Hughes Medical Institute, University of Washington, Seattle, WA, United States of America

\* francesca.antonacci@uniba.it



**OPEN ACCESS**

**Citation:** Maggiolini FAM, Cantsilieris S, D'Addabbo P, Manganelli M, Coe BP, Dumont BL, et al. (2019) Genomic inversions and *GOLGA* core duplicons underlie disease instability at the 15q25 locus. *PLoS Genet* 15(3): e1008075. <https://doi.org/10.1371/journal.pgen.1008075>

**Editor:** Beth A. Sullivan, Duke University, UNITED STATES

**Received:** October 10, 2018

**Accepted:** March 7, 2019

**Published:** March 27, 2019

**Copyright:** © 2019 Maggiolini et al. This is an open access article distributed under the terms of the [Creative Commons Attribution License](https://creativecommons.org/licenses/by/4.0/), which permits unrestricted use, distribution, and reproduction in any medium, provided the original author and source are credited.

**Data Availability Statement:** Sequencing data from Illumina HiSeq X Ten can be found at the Sequence Read Archive (SRA) under BioProject ID PRJNA493749, as BAM file (GRCh38/hg38). PacBio SMRT sequences of CH17 clones can be found under BioProject ID PRJNA514724. Complete sequences of primate BAC clones ([S3 Table](#)) can be found as NC\_036894.1, NC\_036918.1, AC275844.1, AC212984.3, AC210775.3 and AC211297.2.

## Abstract

Human chromosome 15q25 is involved in several disease-associated structural rearrangements, including microdeletions and chromosomal markers with inverted duplications. Using comparative fluorescence *in situ* hybridization, strand-sequencing, single-molecule, real-time sequencing and Bionano optical mapping analyses, we investigated the organization of the 15q25 region in human and nonhuman primates. We found that two independent inversions occurred in this region after the fission event that gave rise to phylogenetic chromosomes XIV and XV in humans and great apes. One of these inversions is still polymorphic in the human population today and may confer differential susceptibility to 15q25 microdeletions and inverted duplications. The inversion breakpoints map within segmental duplications containing core duplicons of the *GOLGA* gene family and correspond to the site of an ancestral centromere, which became inactivated about 25 million years ago. The inactivation of this centromere likely released segmental duplications from recombination repression typical of centromeric regions. We hypothesize that this increased the frequency of ectopic recombination creating a hotspot of hominid inversions where dispersed *GOLGA* core elements now predispose this region to recurrent genomic rearrangements associated with disease.

## Author summary

Human chromosome 15 derived from a fission event that occurred in the ancestor of great apes. Following inactivation of the ancestral centromere at 15q25 a dispersal of segmental duplications took place, providing templates for ectopic recombination and

**Funding:** SC was supported by a National Health and Medical Research Council (NHMRC) CJ Martin Biomedical Fellowship (#1073726). This work was supported by the “Fondi di Ateneo (CUP H92F17000190005), University of Bari” grant to FA. This work was supported, in part, by US National Institutes of Health grant HG002385 to EEE. The funders had no role in study design, data collection and analysis, decision to publish, or preparation of the manuscript.

**Competing interests:** I have read the journal's policy and the authors of this manuscript have the following competing interests: EEE is on the scientific advisory board (SAB) of DNAnexus, Inc.

predisposing the region to genomic instability. Different disease-associated microdeletions and chromosomal markers have been described with breakpoints mapping within these segmental duplications. To gain insight into the instability at 15q25, we sought to analyze this region in human and nonhuman primates using multiple genomics techniques and demonstrated the presence of two independent inversion events that occurred during great apes evolution. One of these inversions is still polymorphic in humans and may cause, in conjunction with a *GOLGA* core duplicon—a ~14 kbp chromosome 15 repeat, susceptibility to non-allelic homologous recombination leading to pathogenic recurrent rearrangements. Our results support the existence of a strong relationship between inversions and core duplicons and reinforce the hypothesis that *GOLGA* repeats play a fundamental role both in disease and evolution.

## Introduction

Human chromosome 15 was generated by the chromosome fission of an ancestral submetacentric chromosome in the ancestor of great apes. Macaque chromosome 7 represents the ancestral state, as more distantly related organisms have the same configuration [1]. The ancestral centromere at 15q25 inactivated and lost any centromeric satellites, whereas a large cluster of segmental duplications persisted [2]. Following inactivation of the ancestral centromere, the constraint against recombination in this area was likely weakened [3–5], providing an environment permissive to non-allelic rearrangements that promoted the dispersal of the segmental duplications.

The 15q25 locus approximately corresponds to the position of the ancestral centromere [2] and is an unstable region of the human genome enriched in segmental duplications containing the *GOLGA* core duplicon, a ~14 kbp chromosome 15 repeat [6]. Cores represent ancestral duplications where additional duplication blocks have been formed around, and correspond to the expansion of gene families, some of which show signatures of positive selection [7]. *GOLGA* belongs to the golgin subfamily of coiled-coil proteins associated with the Golgi apparatus. These genes appear to have roles in membrane traffic and Golgi structure, but their precise function is in most cases unclear. *GOLGA* encodes a primate-specific gene family that expanded over the last 20 million years [8, 9]. Human chromosome 15 contains nearly 40 copies of the *GOLGA* core element [6], dispersed to multiple locations across the long arm of chromosome 15. *GOLGA* is one of 14 core duplicons associated with the burst of interspersed segmental duplications in the human–great ape ancestral lineage [10, 11] and the most enriched sequence associated with segmental blocks promoting evolutionary rearrangements in primates [12–14] and disease instability, including Prader-Willi/Angelman syndromes, 15q13 microdeletions and 15q24 microdeletions [13, 15–18].

The 15q25 region represents a high-risk locus for pediatric neurologic disease with variable outcomes [2, 19–29]. Different microdeletions and chromosomal markers with inverted duplications of chromosome 15 all have breakpoints mapping within a 3.3 Mbp region containing three blocks of segmental duplications of 350 kbp, 560 kbp and 115 kbp in size. The middle block contains a gap in the last release of the human reference genome (GRCh38/hg38) suggesting the possible presence of different structural haplotypes in this locus. We characterized the organization of this region in human and nonhuman primate genomes by conducting a detailed analysis by fluorescence *in situ* hybridization (FISH), single-cell strand-sequencing (Strand-seq), high-quality finished sequencing using PacBio single-molecule, real-time

(SMRT) sequencing technology, and optical mapping (Bionano) in order to understand the extent of human genetic variation, its origin, and impact on disease.

## Results

### Characterization of chromosome 15q25 inversion variants

Three duplication blocks, containing *GOLGA* repeats, map at the 15q25 region (S1 Table), with the middle one (block B) containing a gap in the reference genome (Fig 1A), suggesting that alternative structural configurations might exist within the human population. To gain insight into the instability associated to disease and evolutionary rearrangements at 15q25 we sought to characterize the organization of this region in more detail in human and nonhuman primate genomes. Using FISH experiments in interphase nuclei, we tested 22 HapMap individuals from different populations for the presence of two putative inversions: the proximal

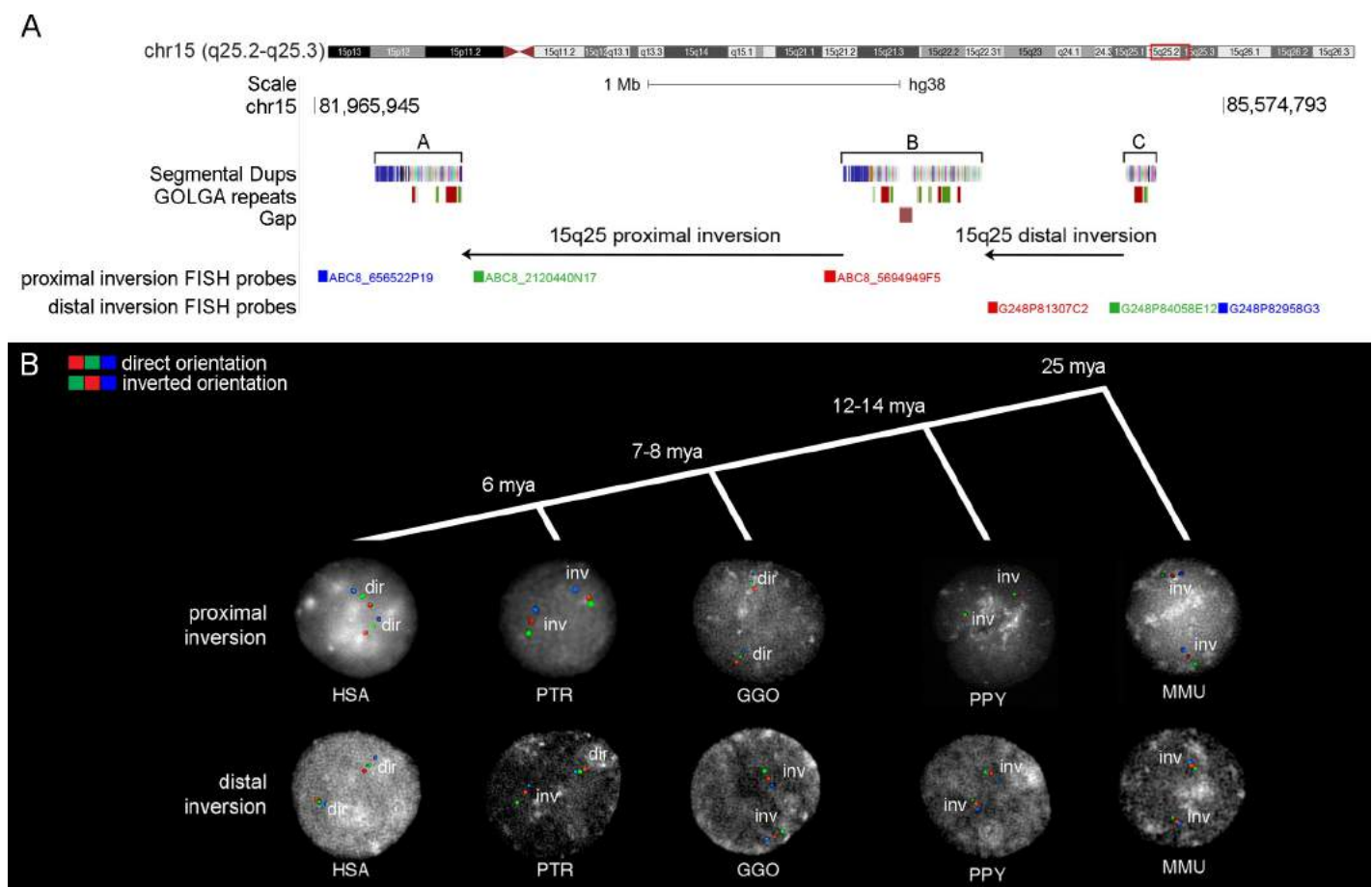


**Fig 1. Experimental validation of genomic inversions at 15q25.** (A) UCSC Genome Browser view of the 15q25 region. Segmental duplication blocks A, B and C are shown with colored boxes. *GOLGA* repeat locations from *blat* analyses of *GOLGA2P10* and *GOLGA6L5P* are depicted with green and red boxes mapping on the plus or minus strand, respectively. Proximal and distal tested inversions are shown with black arrows and fosmid clones used for FISH experiments on interphase nuclei are indicated with colored blocks followed by the fosmid names. Segmental duplication colors show the ancestral origins of duplications based on comparison with mammalian groups assigned by DupMasker [76]. (B) FISH results on interphase nuclei for proximal and distal inversions in each analyzed species. The color order indicates probes relative orientation, with red-green-blue signals showing haplotypes in direct orientation and green-red-blue signals showing inverted haplotypes. FISH analyses of the proximal inversion show that macaque, orangutan, and chimpanzee are all inverted when compared to the human reference genome orientation, while all gorillas are in direct orientation. The distal inversion is polymorphic within the chimpanzee population, while all the other species are inverted in the homozygous state when compared to human. Timing of species divergences is also shown at the top (mya = million years ago). HSA = *Homo sapiens*; PTR = *Pan troglodytes*; GGO = *Gorilla gorilla*; PPY = *Pongo pygmaeus*; MMU = *Macaca mulatta*.

<https://doi.org/10.1371/journal.pgen.1008075.g001>

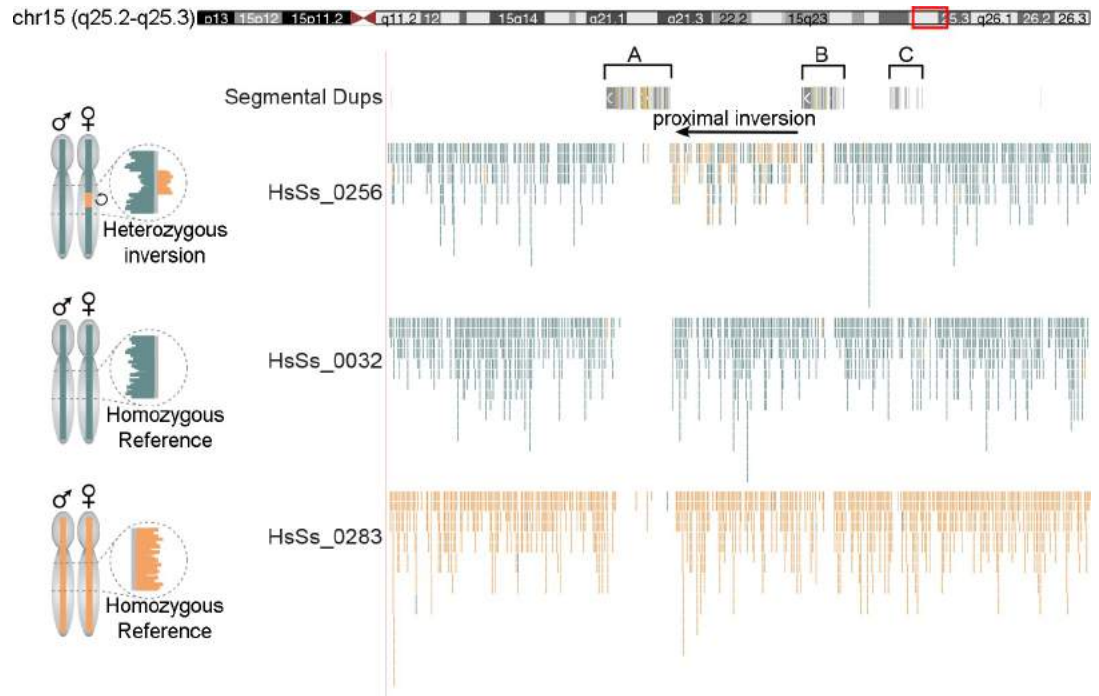


**Fig 2. Strand-seq of the proximal inversion at 15q25.** On the left, ideograms of expected Strand-seq results for each possible inversion genotype are shown. On the right, a UCSC Genome Browser view (coordinates lifted to GRCh37/hg19) of Strand-seq data, BED-formatted and uploaded as custom tracks, of the three libraries is shown. For each cell, aligned reads are indicated as individual lines in Crick (teal) or Watson (orange) state. In the library on the top (HsSs\_0256) mixed Watson and Crick reads at the proximal inversion (black arrow) indicate the heterozygosity of the region while in the others a direct orientation of the region is shown.

<https://doi.org/10.1371/journal.pgen.1008075.g002>

inversion of 1.5 Mbp between duplication blocks A and B (chr15:82534139–84045983) and the distal inversion of 600 kbp between duplication blocks B and C (chr15:84596420–85169772). All individuals tested for both distal and proximal inversions were in direct orientation (Fig 1B; S2 Table).

In order to gain more information regarding the presence and frequency of the 15q25 inversions, we investigated published Strand-seq data from 47 libraries from a pool of 353 separate cord blood and bone marrow donors [30]. In Strand-seq libraries, inversions cause a segmental change in strand orientation at the inverted locus, which allows inversions to be directly visualized and genotyped in single-cell data [30]. One out of 22 informative libraries was heterozygous for the proximal inversion, while all the others were in direct orientation. All 22 libraries were in direct orientation for the distal region (Fig 2). In total, we tested 88 chromosomes (44 chromosomes by FISH analyses and 44 chromosomes by Strand-seq) and showed that only one out of the 88 chromosomes was in inverted orientation for the proximal region (inversion allele frequency of 1.14%) (Table 1).

### Closing the gap in the human reference assembly

In order to close the gap in the reference genome we generated a map of contiguous clones from the CH17 BAC library from a hydatidiform mole-derived (haploid) human cell line (CHM1hTERT) [31]. Using BAC-end sequence pair mapping, we constructed a contiguous set of four BAC clones (S3 Table) and then performed SMRT sequencing. We generated a 657 kbp sequence contig spanning the B block of segmental duplications and closed the gap in this



**Table 1. Summary of inversion frequencies in human and nonhuman primates.** Inversion frequencies for the proximal and distal region based on FISH, Strand-seq and optical mapping analyses are shown. The number of individuals tested for each species is shown in parenthesis.

Species	15q25 proximal inversion frequency	15q25 distal inversion frequency
Human (n = 44)	1.14%	0%
Chimpanzee (n = 9)	100%	39%
Gorilla (n = 5)	0%	100%
Orangutan (n = 5)	100%	100%
Macaque (n = 1)	100%	100%

<https://doi.org/10.1371/journal.pgen.1008075.t001>

region. Miropcats analysis of the CH17 contig versus the human hg38 reference showed that the hydattidiform mole is in direct orientation for the proximal inversion and highlighted the presence of 64 kbp redundant sequence, containing *GOLGA* repeats, that was represented twice within the reference (S1 Fig).

### Evolutionary analyses

In order to investigate the ancestral configuration of the 15q25 region, we compared the orientation of the proximal and distal regions in human with other nonhuman primate species. We tested for the presence of the proximal inversion between duplication blocks A and B by FISH analysis of cell lines from eight chimpanzees (*Pan troglodytes*), four gorillas (*Gorilla gorilla*), four orangutans (*Pongo pygmaeus*), and one macaque (*Macaca mulatta*) (Fig 1B; S2 Table). Moreover, we analyzed Bionano optical mapping data of DNA from one chimpanzee (*Pan troglodytes*), one gorilla (*Gorilla gorilla*) and one orangutan (*Pongo abelii*) (Fig 3; S2 Table). Chimpanzee, orangutan and macaque were found to be inverted when compared to the human reference genome orientation suggesting that this represents the likely ancestral state, while all gorillas were in direct orientation, similar to humans. We conclude that the proximal inversion likely occurred in the human–African great ape ancestor and the chimpanzee configuration may represent incomplete lineage sorting of the ancestral state or the inversion may have occurred at multiple times during great ape evolution as a result of recurrent mutation events involving the duplicated sequences.

Next, we tested for the presence of the distal inversion between duplication blocks B and C by FISH analysis of eight chimpanzees (*Pan troglodytes*), four gorillas (*Gorilla gorilla*), four orangutans (*Pongo pygmaeus*), and one macaque (*Macaca mulatta*). We found this inversion to be widely polymorphic within the chimpanzee population, while all other nonhuman species were inverted in the homozygous state (Fig 1B; S2 Table). Bionano optical mapping data of DNA from one gorilla (*Gorilla gorilla*) and one orangutan (*Pongo abelii*) show that these individuals are inverted in the homozygous state while chimpanzee (*Pan troglodytes*) is in direct orientation for both haplotypes (Fig 3; S2 Table). These data suggest that the inversion occurred in the human–chimpanzee ancestor and is still polymorphic in chimpanzee with a 39% allele frequency (Table 1).

### Duplication analysis

Given the central role of the duplications in both microdeletions and the evolution of inversions [13, 32–38], we compared the duplication architecture among primate species. Using BAC-end sequence pair mapping, we selected three clones from the CH276 orangutan BAC library and one clone from the CH251 chimpanzee library, which spanned the 600 kbp distal inversion breakpoint between blocks B and C, and then sequenced them using PacBio SMRT sequencing (S3 Table; S2 Fig). In orangutan we generated a ~400 kbp sequence contig and

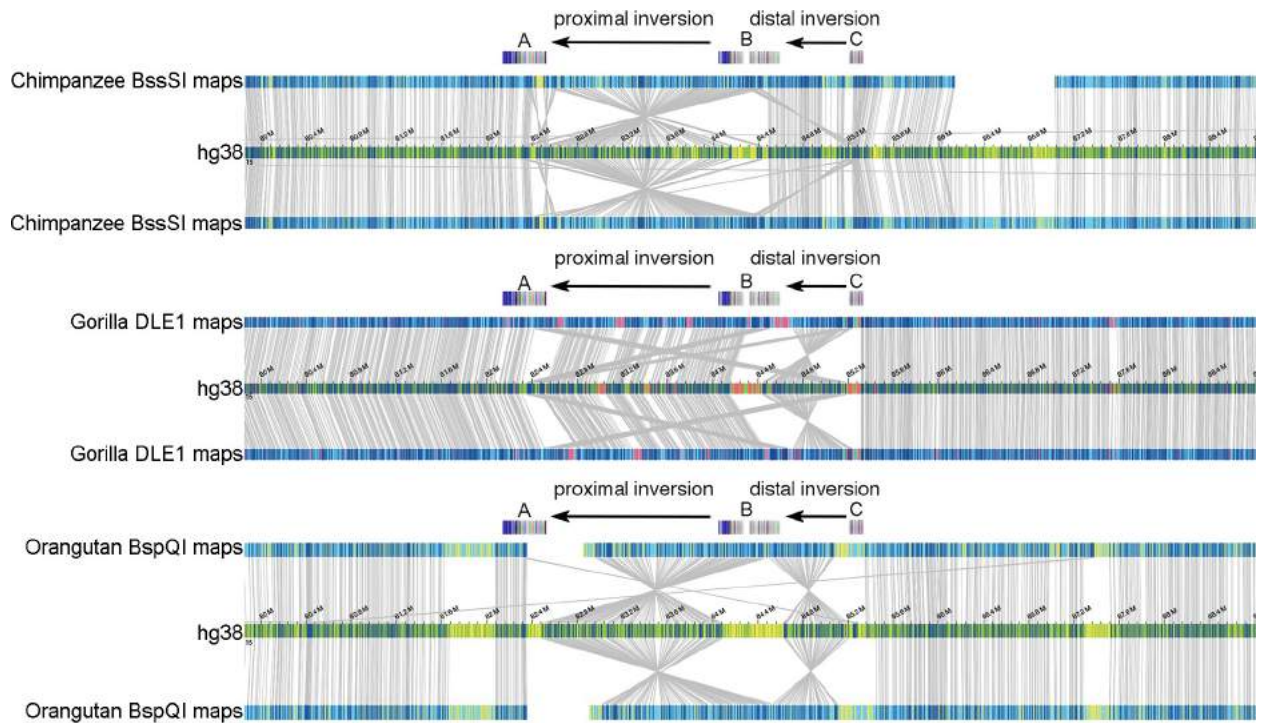


**Fig 3. Bionano analysis of the 15q25 region.** Bionano optical mapping data of three great ape genomes at the 15q25 locus. The two black arrows in each plot denote the two loci where inversions are observed between the apes and human. Segmental duplication blocks A, B and C are also shown with colored boxes. In each display, the top and bottom maps represent the two alleles of the *de novo* assembled genomes for each species with respect to the human reference assembly (hg38 track). The individual labels represent the positions of the label motifs of the enzyme used. The top panel shows the alignments of the assembled Nt.BssSI genome maps of a chimpanzee sample. The blue labels are the aligned labels, whereas the yellow ones are unaligned labels. The middle panel shows gorilla maps generated by DLE-1 enzyme, and the blue and red labels represent aligned and unaligned labels, respectively. Finally, the bottom panel illustrates how an orangutan genome—constructed using Nb.BspQI—is aligned to human, with blue representing aligned labels and yellow the unaligned ones.

<https://doi.org/10.1371/journal.pgen.1008075.g003>

compared this with the human reference assembly. In addition, to confirm the presence of the inversion between duplication blocks B and C, we identified that the inversion would create an ancestral B/C block-hybrid. Sequence analysis demonstrates that this block is missing one copy of the *GOLGA* core duplicon identified in the human B block and two copies in the human C block (S2A Fig). We queried GenBank and identified two additional clones (250 kbp sequence contig) from CH250 macaque BAC library spanning this ancestral B/C block. Comparison of the B/C block-hybrid between orangutan and macaque shows that they both have two copies of *GOLGA* repeats in this region and, therefore, are missing a total of three copies with respect to the human orthologous regions (S2B Fig). The ancestral orientation of the duplication block is itself inverted in the macaque relative to orangutan (S2B Fig), suggesting a restructuring of the duplication architecture of the region during primate evolution. Finally, Miroppeats analyses of a CH251 clone from a chimpanzee (Clint) in homozygous direct orientation for the distal inversion between B/C blocks shows that human and chimpanzee are collinear and both have two copies of *GOLGA* repeats for this region (S2C Fig).

### ***GOLGA* copy number analysis in human and nonhuman primates**

To further investigate the copy number of the *GOLGA* core duplicons in humans and primates, we performed a BLAT analysis using *GOLGA2P10* and *GOLGA6L5P* exon sequences. We generated a map of *GOLGA* repeats in the 15q25 human region, which allowed us to

identify 24 repeats in the latest human reference genome assembly (S1 Table; S3 Fig). We performed the same analysis on primate reference genomes (Clint\_PTRv2/panTro6, gorGor4.1/gorGor4, Susie\_PABv2/ponAbe3 and BCM Mmul\_8.0.1/rheMac8) and found 11 repeats in chimpanzee and gorilla and 13 in orangutan and macaque (S1 Table). However, the exact number of copies could not be determined due to the presence of gaps in the assembly region (3 gaps in chimpanzee, 67 in gorilla, 1 in orangutan and 20 in macaque). To determine the extent to which gaps affected the observed difference in copy number we performed a parallel analysis using four assemblies all built using the same PacBio sequencing technology and FALCON assembly method (chimpanzee Clint\_PTRv2/panTro6, gorilla Susie3, orangutan Susie\_PABv2/ponAbe3, and human PacBioCHM1\_r2). Using whole genome alignments of these four assemblies to GRCh38 we found that of the 24 *GOLGA* repeats in the 15q25 region, 21 are found in the human *de novo* assembly (CHM1) which is twice the number of copies compared to other primate species (9 in chimpanzee, 10 in gorilla and 8 in orangutan) (S4 Table). The high recovery rate of *GOLGA* repeats in CHM1 as compared to GRCh38 (21/24) suggests that the large majority of these sequences are resolved in *de novo* PacBio assemblies and that the reduced copy number in Clint\_PTRv2/panTro6, Susie3, and Susie\_PABv2/ponAbe3 is not due to gaps in their respective assemblies.

### Pathogenic rearrangements at 15q25

Three different classes of 15q25 microdeletions associated with developmental delay and intellectual disability have been described [19–24]. The microdeletions can be classified based on recurrent breakpoints, with breakpoints between duplication blocks A and B (A-B deletions), B and C (B-C deletions) and A and C (A-C deletions). The three blocks of segmental duplications that mediate the rearrangements are 350 kbp, 560 kbp and 115 kbp in size. Each block contains at least one copy of the *GOLGA* core duplcon (Fig 4; S1 Table).

Using single-nucleotide polymorphism (SNP) microarrays, we analyzed a patient with global developmental delay harboring a 15q25 deletion and mapped the disease-critical region to a 1.6 Mbp region spanned by segmental duplication blocks A and B (Fig 4). To refine the breakpoints with greater precision, we performed whole-genome sequencing (WGS) of the 15q25 deletion sample using Illumina HiSeq X Ten (150 bp PE reads; 26.2X coverage for whole chromosome 15) and aligned the sequences to the human reference. Using singly unique nucleotide (SUN) variants that allowed us to discriminate between the paralogous copies [39], we narrowed the deletion breakpoints to a 20 kbp (chr15:82478935–82498934) segment within duplication block A and a 101 kbp (chr15:84404774–84506312) segment within block B. Blast2seq analysis of the sequence mapping within the breakpoints intervals shows that the longest alignments with 99% similarity correspond to two sequences of 9.4 kbp (blast2SeqA) and 9 kbp (blast2SeqB), mapping at *GOLGA2P10* sequences, in inverted orientation (Fig 4; S1 File).

### Erosion of recombination suppression at 15q25 in great apes

Centromeres and their neighboring pericentromeric chromatin are well-established cold spots of meiotic crossover activity [3–5]. We hypothesized that inactivation of the ancestral centromere at 15q25 reduced the strength of recombination suppression at this locus, leading to higher rates of rearrangement and genome instability. Three lines of evidence support this interpretation. First, there are active meiotic recombination hotspots within the 15q25 region of the human genome [40]. Second, *GOLGA* repeats within the 15q25 region engage in frequent bouts of interlocus gene conversion [41]. Both of these observations point to homology-driven repair activity within the 15q25 region. Third, broad-scale recombination rates over the

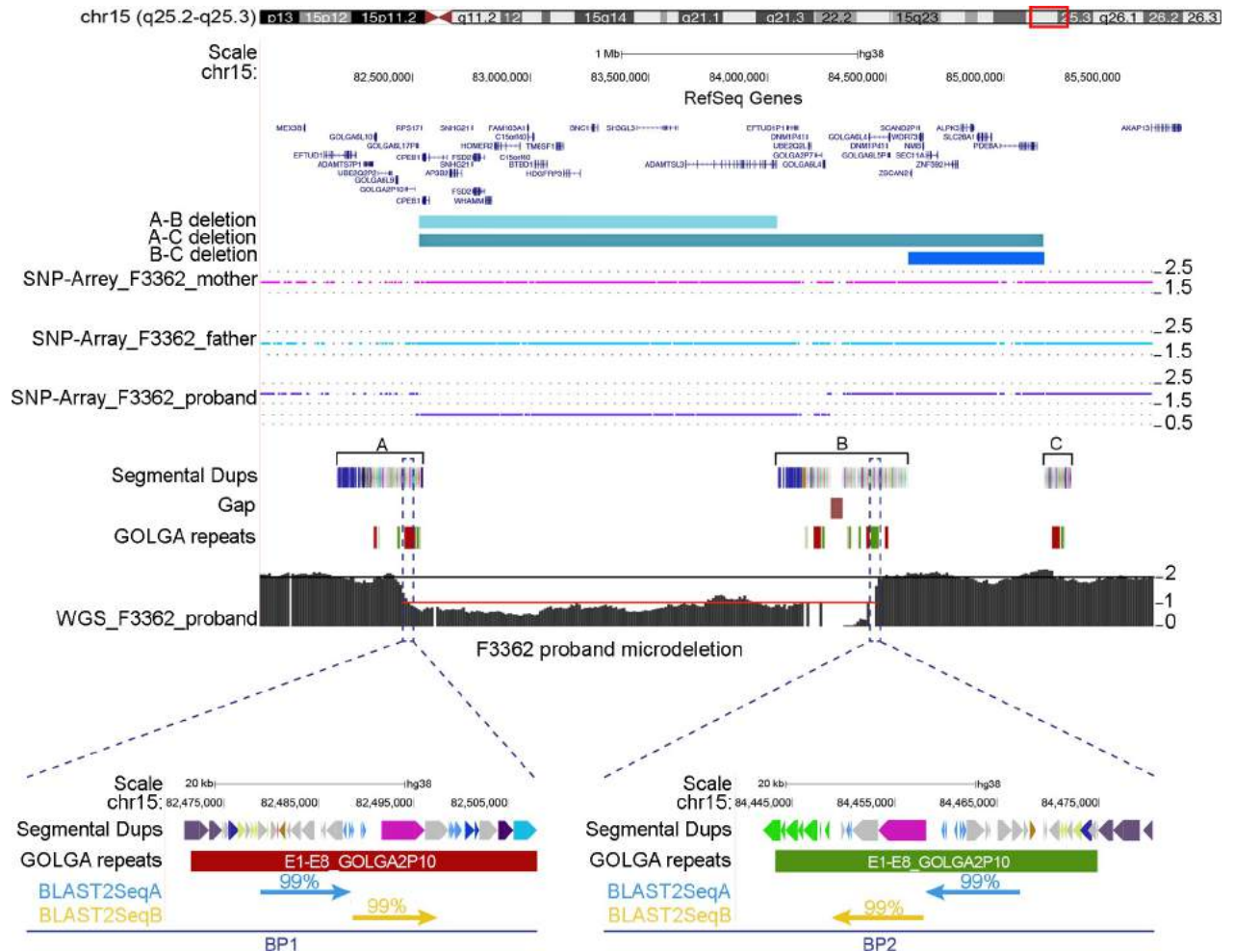


**Fig 4. Deletions at the 15q25 region.** Three different classes of microdeletions with breakpoints between segmental duplication blocks A-B, A-C and B-C are shown as colored boxes. Segmental duplications are shown with colored boxes. *GOLGA* repeat locations from the blat analysis of *GOLGA2P10* and *GOLGA6L5P* are depicted with green and red boxes mapping on plus or minus strand, respectively. SNP array and whole-genome sequencing (WGS) data of a patient with a 15q25 A-B deletion are shown. The SNP array highlights a copy number (CN) of 2 for the parents while the proband shows a CN of 1 for the deleted region. WGS shows a CN of 2 for the regions flanking the microdeletion (black line) and a CN of 1 (red line) for the deleted region. At the bottom of the figure are shown the results of a blast2Seq alignment between the two microdeletion breakpoint intervals. The two largest alignments of 9.4 kbp (blast2SeqA) and 9 kbp (blast2SeqB) with 99% similarity are shown with light blue and yellow arrows, respectively. *GOLGA2P10* repeats, which encompass the regions of high similarity at the breakpoints, are also shown in the zoom inset.

<https://doi.org/10.1371/journal.pgen.1008075.g004>

15q25 region are elevated relative to the recombination levels of active centromeres and pericentromeric regions in the human genome. We observe a similar relaxation of recombination rate suppression in the inactivated 15q25 ancestral centromere region in bonobo, chimpanzee, and gorilla. We caution that recombination map quality is likely reduced across the structurally complex 15q25 locus, and the absence of informative centromeric markers precludes estimates of recombination rate within these gapped regions on the assembly. However, these qualitative findings suggest that the repositioning of the chromosome 15 centromere in the common ancestor of great apes weakened the recombination-suppressive environment that defines centromeres and set the stage for recurrent homology-driven rearrangements at the human 15q25 locus.



## Discussion

In this study, we sought to better understand the mechanisms leading to the genomic instability of the 15q25 locus by characterizing evolutionary and contemporary rearrangements by FISH, single-cell Strand-seq, PacBio SMRT sequencing, and Bionano optical mapping analyses. Chromosome 15q25 harbors a complex genomic region with three large blocks of segmental duplications containing several copies of the *GOLGA* core duplicon, previously shown to be involved in several recurrent pathogenic and evolutionary rearrangements on chromosome 15 [2, 12–14]. The middle block of segmental duplications contains a gap in the current release of the human reference assembly. Using SMRT technology, we sequenced and *de novo* assembled a tiling path of four BAC clones (657 kbp region) across this medically relevant region from the library of a hydatidiform mole and showed that the gap was flanked by two identical copies of *GOLGA* core duplicons that might have confounded mapping and assembly of the region. Alternatively, this might be a biological difference in structural haplotypes and/or copy number of *GOLGA* between human individuals.

Microarray analysis of 15q25 microdeletions in previous [19–24] and current studies refined breakpoint locations to segmental duplication blocks A, B and C; however, probe cross-hybridization prevented further narrowing of breakpoint locations within the duplications. All three segmental duplication clusters have multiple regions of high sequence identity—the most significant in direct orientation has 99% identity across 59 kbp. Here we performed WGS of a 15q25 microdeletion between duplication blocks A and B. SUN variant mapping allowed us to differentiate the segmental duplication paralogous copies [39] and revealed that the breakpoints map precisely to the *GOLGA* core duplicon sequences, which are organized in a palindromic configuration. Previous studies of many different chromosome 15 rearrangements, including several recurrent microdeletion/duplication syndromes and more complex rearrangements such as inverted duplications and triplications of chromosome 15 [13, 34], have shown that the breakpoints of all of these appear to coincide precisely with the location of the duplication family containing the *GOLGA* gene. An example is the 2 Mbp microdeletion encompassing the 15q13.3 region associated with intellectual disability, schizophrenia, autism and epilepsy [13]. WGS of two idiopathic autism patients carrying *de novo* 15q13.3 microdeletions showed that the two probands have different breakpoints but in both cases they map to *GOLGA* sequences [13].

Taken together these results suggest that despite the presence of large segmental duplications in direct orientation, known to be a predisposing factor for non-allelic homologous recombination (NAHR) leading to deletion/duplication events, palindromic *GOLGA* repeats seem to be preferential sites for NAHR promoting disease-related instability of chromosome 15. The presence of *GOLGA* core duplicons at multiple disease-associated rearrangements [13, 15–18] and evolutionary breakpoints [12–14] indicate the high level of genomic instability driven by these sequences.

The chromosome 15q25 locus approximates the position of the ancestral centromere, which became inactivated about 25 million years ago [2]. This inactivation followed a noncentromeric chromosomal fission of an ancestral chromosome that gave rise to human and great apes chromosomes 14 and 15 [2]. The duplications flanking the ancestral centromere were formed within a pericentromeric context where recombination was almost absent [3–5]. Our recombination and evolutionary analyses support the hypothesis that following inactivation of the ancestral centromere, the constraint against recombination in this area was relaxed, rendering the locus permissive to NAHR-mediated rearrangements. We speculate that such events ultimately led to two local inversions specific to humans and African great apes. These inversions may have ultimately helped to disperse the *GOLGA* core elements that are now

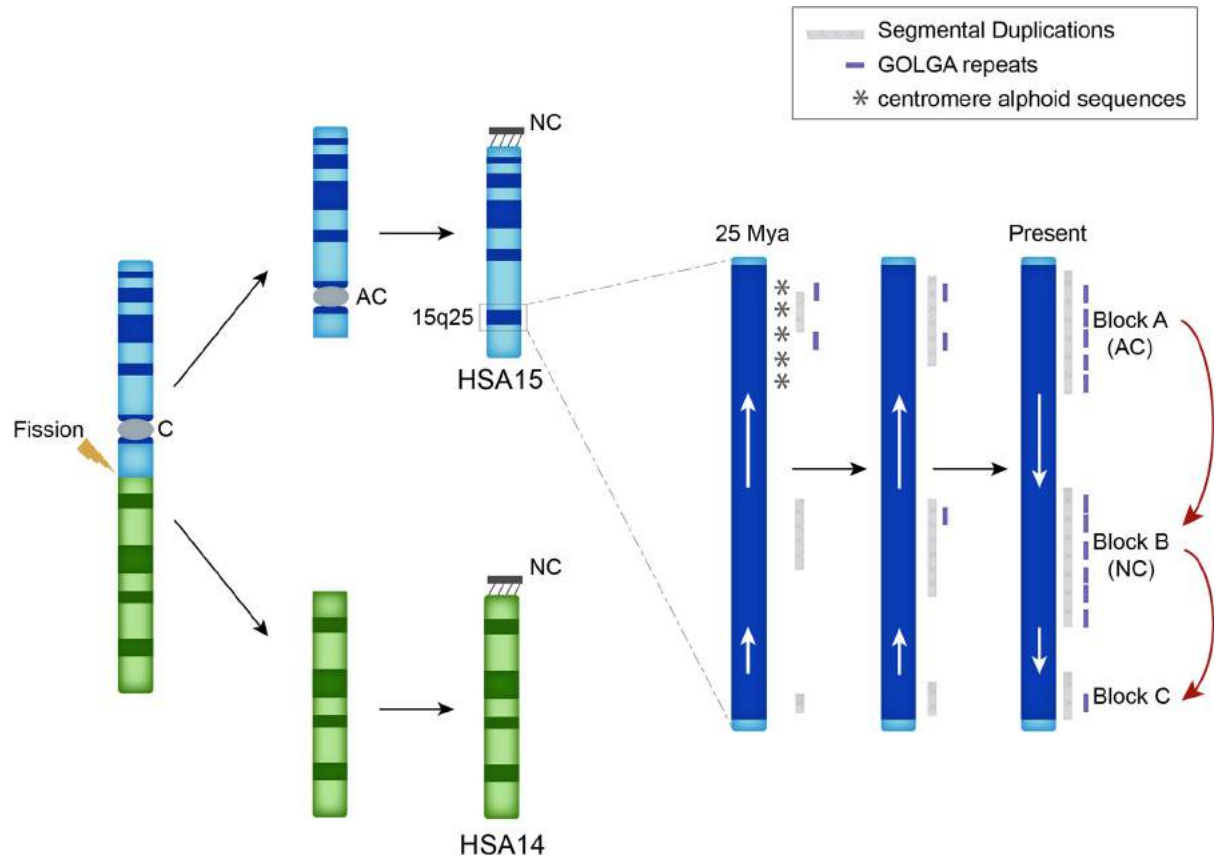


**Fig 5. Human chromosome 15 evolution and *GOLGA* core elements dispersion.** A fission event of an ancestral chromosome led to human and great ape chromosomes 14 (green ideogram) and 15 (blue ideogram). The zoomed-in view shows how the inactivation of the ancestral centromere after the fission event released the recombination constraints typical of pericentromeric regions leading to two inversions, shown with the white arrows, which resulted in a dispersal of *GOLGA* repeats (purple blocks) and segmental duplications (gray bars). AC, ancestral centromere. NC, neocentromere.

<https://doi.org/10.1371/journal.pgen.1008075.g005>

mediating pathogenic microdeletions (Fig 5). To test this hypothesis, we performed a BLAT analysis on the latest releases of the chimpanzee, gorilla, orangutan and macaque genome assemblies and found that human has nine copies of the core duplicon in excess compared to macaque.

The distal inversion is polymorphic within the chimpanzee population (39% allele frequency), while all the other species are configured in the opposite orientation compared to human suggesting that the inversion occurred in the human–chimpanzee ancestor and is highly polymorphic in chimpanzee. These findings are strikingly reminiscent of the 17q21.31 chromosome inversion [42], which is flanked by *LRRC37* core duplications on either side of the inversion region and is highly polymorphic in multiple species, especially in chimpanzee (56% allele frequency).

The proximal inversion is 1.5 Mbp in size and likely occurred in the human–African great ape ancestor. The orthologous region in chimpanzee, however, is in the opposite orientation as that of human, suggesting that the region either flipped back to the ancestral orientation in the chimpanzee lineage or the chimpanzee configuration may represent incomplete lineage sorting of an ancestral state. FISH and Strand-seq analyses of 44 human samples show that this inversion is still polymorphic in humans, with a minor allele frequency of 1.14%. The inversion corresponds to the exact same region that is deleted in patients with intellectual disability,

suggesting that the inversion may represent a premutation state to pathogenic rearrangements, as previously observed for other regions of the genome, such as the 17q21.31, 7q11.23 and 8p23.1 loci [42–44]. The inversion could change the orientation and composition of *GOLGA* repeats (depending on breakpoints), and this could impact the likelihood of a recombination event generating a deletion.

Interestingly, chromosome 15q25 is also one of the hotspots of neocentromere appearance in clinical cases [45]. The majority of neocentromeres reported in clinical samples rescue acentric chromosome fragments associated with duplications or chromosomal rearrangements found in patients with developmental disabilities [46]. From a literature review we identified several recurrent rearrangements, consisting of tetrasomies from 15q25→qter due to anaphoid chromosomal markers with a neocentromere at 15q25 (S5A Fig) [2, 25–29, 46–63]. Ventura and colleagues performed detailed mapping of the ancestral centromere as well as a neocentromere mapping to chromosome 15q25 and established that the ancestral centromere and the neocentromere map to two different clusters of segmental duplications separated by a 1.5 Mbp single-copy region [2]. Notably, we show that this region corresponds exactly to the 1.5 Mbp proximal inversion that occurred in the human–African great ape ancestor after inactivation of the ancestral centromere. Following inactivation, an increased frequency of ectopic rearrangements at 15q25 might have resulted in evolutionary inversions that led to a duplicative transposition of *GOLGA* core elements from one breakpoint to the other (from segmental duplication block A to B).

The existence of human individuals heterozygous for the proximal inversion led us to hypothesize that inversions may be a driving force in the formation of 15q25 neocentric invdup marker chromosomes. FISH mapping of the breakpoints of invdup markers from both 8p and 15q suggests that between the two duplicated symmetrical arms is found an unduplicated region containing proximal sequences contiguous with one of the arms (S5B Fig) [2, 44]. Such an arrangement is consistent with meiotic recombination between chromosomes that are heterozygous for a polymorphic inversion flanked by inverted segmental duplications. During cell division, asynapsis at the inverted region may promote the refolding of one chromosome onto itself, allowing intrachromatid synapsis and NAHR between two *GOLGA* repeats (S5C Fig). This would favor the formation of the 15q25→qter inverted-duplicated chromosomal markers, similar to what has been previously shown for the 8p23.1 inversion polymorphism [44]. In conclusion, our findings highlight the intimate relationship between inversions and core duplcons and reinforce the hypothesis that *GOLGA* repeats played a fundamental role in shaping the architecture of chromosome 15 in humans and great apes and continue to predispose it to disease-causing rearrangements.

In conclusion, we propose the following model. Core duplcons in 15q25 were formed within a pericentromeric context, and sequences in the same region have continued to undergo sequence exchange/duplication within the human lineage long after the centromere became inactivated about 25 million years ago. This had significant implications for genomic stability in the region. It is highly likely that following inactivation of the ancestral centromere, the constraint against recombination in this area was relaxed. This would have increased the frequency of ectopic rearrangements, accelerating the dispersal of the linked *GOLGA* duplcons and leading to two local inversions specific to humans and African great apes. Our findings highlight the intimate relationship between inversions and core duplcons and reinforce the hypothesis that *GOLGA* repeats played a fundamental role in shaping the architecture of chromosome 15 in humans and great apes and continue to predispose it to disease-causing rearrangements.

## Material and methods

### Ethics statement

The study was approved (Prot. 117CE;6/11/2017) by the local Ethics committee of the IRCCS "Casa Sollievo della Sofferenza" Hospital, San Giovanni Rotondo (FG). Written, informed consent was received.

### FISH analysis

Interphase nuclei were obtained from lymphoblast and fibroblast cell lines from 22 human HapMap individuals (Coriell Cell Repository, Camden, NJ, USA), eight chimpanzees (*Pan troglodytes*), four orangutans (*Pongo pygmaeus*), four gorillas (*Gorilla gorilla*) and one macaque (*Macaca mulatta*) (S2 Table). FISH experiments were performed using human fosmid (n = 6) clones (S6 Table) directly labeled by nick-translation with Cy3-dUTP (Perkin-Elmer), Cy5-dUTP (Perkin-Elmer) and fluorescein-dUTP (Enzo) as described by Lichter et al. [64], with minor modifications. Briefly, 300 ng of labeled probe were used for the FISH experiments; hybridization was performed at 37°C in 2xSSC, 50% (v/v) formamide, 10% (w/v) dextran sulphate and 3 mg sonicated salmon sperm DNA, in a volume of 10 mL. Posthybridization washing was at 60°C in 0.1xSSC (three times, high stringency, for hybridizations on human, chimpanzee, gorilla and orangutan) or at 37°C in 2xSSC and 42°C in 2xSSC, 50% formamide (three times each, low stringency, for hybridizations on macaque). Nuclei were simultaneously DAPI stained. Digital images were obtained using a Leica DMRXA2 epifluorescence microscope equipped with a cooled CCD camera (Princeton Instruments). DAPI, Cy3, Cy5 and fluorescein fluorescence signals, detected with specific filters, were recorded separately as grayscale images. Pseudocoloring and merging of images were performed using Adobe Photoshop software. Proximal and distal inversions were interrogated using two probes within the putative inversion region and a reference probe outside, as previously described [37].

### SNP array assay

SNP array-based copy number variant (CNV) analysis was performed on genomic DNA extracted from peripheral blood lymphocytes of the patient and parents, after obtaining written informed consent, using the CytoScan HD Array (Affymetrix, Santa Clara, CA, USA) as previously described [65]. Data analysis was performed using the Chromosome Analysis Suite software version 3.1 (Affymetrix, Santa Clara, CA, USA). A CNV was validated if at least 25 contiguous probes showed an abnormal log<sub>2</sub> ratio. The clinical significance of each CNV detected was assessed by comparison with public databases such as the Database of Genomic Variants (DGV; available online at: <http://dgv.tcag.ca/>), DECIPHER (<https://decipher.sanger.ac.uk/>), and ClinVar (<https://www.ncbi.nlm.nih.gov/clinvar/>). We also checked an internal database of 3,500 patients studied by SNP array in our laboratory since 2010 with a diagnosis of syndromic/non-syndromic neurodevelopmental disorders. Finally, to predict the pathogenic role of the identified microdeletions/microduplications, we followed the American College of Medical Genetics guidelines [66].

### Whole-genome sequencing of a 15q25 microdeletion sample

Read-depth profiles were generated by extracting the first 36 bp of each read from a BWA-MEM aligned BAM file and aligning these reads to the hg38 genome at all possible positions using mrsFAST-Ultra [67]. Read-depth profiles were converted to copy number estimates at edit distances of 2 and 0 to define total and locus-specific (SUN) copy number estimates at ~93% of confidence, as described in Sudmant et al. 2010 [39]. Coverage for chromosome 15 is



26.2X for the full reads and ~6.3X for the first 36mer. Sequence read-depth corresponding to SUN variants was then used to refine the microdeletion breakpoints as previously described [39].

### Strand-seq data analysis

The inversion status of Strand-seq libraries generated from a pooled cord blood sample comprising 47 unrelated donors (described in detail in: [30]) was assessed at the 15q25 locus. Briefly, Strand-seq sequence data were aligned to GRCh37/hg19, BED-formatted for upload to the UCSC Genome Browser, and analyzed using the open-source 'Invert.R' software (<https://sourceforge.net/projects/strandseq-invertr/>). Only cells that inherited chromosome 15 in the WW (W, Watson; reverse or minus strand) or CC (C, Crick; forward or plus strand) were analyzed ( $n = 22$ ) to ensure homozygous inversions were fully captured. Libraries were tested for a segmental change in strand orientation at the putative inversion loci (coordinates lifted to GRCh37/hg19; proximal inversion at chr15:83202890–84714735 and distal inversion at chr15:85139055–85713003), and genotypes were confirmed from the Invert.R results [30].

### GOLGA copy number analysis

To estimate the copy number of *GOLGA* repeats in all the tested species we performed a blat analysis. We downloaded *GOLGA2P10* and *GOLGA6L5P* exon sequences from the UCSC Genome Browser and used the blat tool to compare them with the human reference (GRCh38/hg38). We also performed the same analysis for chimpanzee (Clint\_PTRv2/panTro6), gorilla (gorGor4.1/gorGor4), orangutan (Susie\_PABv2/ponAbe3), and macaque (BCM Mmul\_8.0.1/rheMac8).

We then analyzed the copy number of *GOLGA* in 15q25 locus using PacBio-based assemblies of human CHM1 ([https://www.ncbi.nlm.nih.gov/assembly/GCA\\_001297185.1](https://www.ncbi.nlm.nih.gov/assembly/GCA_001297185.1)), chimpanzee ([https://www.ncbi.nlm.nih.gov/assembly/GCF\\_002880755.1](https://www.ncbi.nlm.nih.gov/assembly/GCF_002880755.1)), gorilla ([https://www.ncbi.nlm.nih.gov/assembly/GCA\\_900006655.3](https://www.ncbi.nlm.nih.gov/assembly/GCA_900006655.3)), and orangutan ([https://www.ncbi.nlm.nih.gov/assembly/GCF\\_002880775.1](https://www.ncbi.nlm.nih.gov/assembly/GCF_002880775.1)). Contigs from PacBio assemblies were aligned to the human reference using Mashmap 2.05 with default parameters. Three filtering steps were then applied to the alignments. First, alignments were filtered such that contigs were only mapped to one location in GRCh38. Second, remaining alignments were intersected with the 24 regions found in the BLAT analysis using BEDTools6. Finally, these intersections were filtered to only those with at least 90% overlap with one of the 24 defined *GOLGA* regions. After these steps, the *GOLGA* copy number was estimated by counting the number of *GOLGA* regions that were intersected by each primate assembly.

### PacBio SMRT clone sequencing and assembly

DNA was isolated from CH17, CH251 and CH276 BAC clones (S3 Table) as previously described [68]. PacBio (Pacific Biosciences, Inc., Menlo Park, CA, USA) SMRTbell libraries were prepared and sequenced using RS II P6-C4 chemistry. We performed *de novo* assembly of pooled BAC inserts (5–6 BACs per pool) using the Canu assembler [69] followed by consensus calling using Quiver [68]. PacBio assemblies were reviewed for misassembly by sequencing to a minimum coverage depth of 200X and visualizing read depth of PacBio reads in Parasight (<http://eichlerlab.gs.washington.edu/jeff/parasight/index.html>) using coverage summaries generated during the resequencing protocol [68]. As a final validation, we mapped publically available BAC end sequences to high-quality finished clone inserts to confirm order and orientation. Human, chimpanzee, orangutan and macaque assemblies, including PacBio sequenced clones from CH17, CH251, CH276 and CH250 BAC libraries, were assembled with

Sequencher and compared to the human reference genome using Miropeats [70] and BLAST [71]. Duplication analysis using whole-genome shotgun sequence detection (WSSD) was performed as previously described [72].

### Bionano Genomics optical mapping

High molecular weight DNA from one chimpanzee (Clint), one gorilla (Kamilah), and one orangutan (Susie) were used to construct Bionano optical maps (S2 Table). The chimpanzee and orangutan maps were constructed as previously described by Kronenberg et al. [73]. To label the chimpanzee and orangutan genomes, two different enzymes were used to ensure contiguous coverage. The two labelling enzymes used (Nt.BspQI and Nb.BssSI) are nickases, and each enzyme makes single-stranded nicks at specific recognition motifs along the genomes. However, whenever two nick sites in opposite strands are in close proximity, double-stranded breaks would be created in the DNA. Such double-stranded breaks—also known as fragile sites—would create permanent disruptions in the DNA molecules and the assembled contigs. Therefore, to bridge these fragile sites, in a separate labelling experiment, a second enzyme that recognizes a different motif site was used. The gorilla maps were constructed using DLE-1 non-nicking enzyme, which is a newer enzyme that directly labels its recognition sites without creating any nicks. Thus, for that experiment, no fragile sites were created, and we achieved continuous coverage across the genome. Briefly, labelling and staining of the DNA were performed according to a protocol developed by Bionano Genomics. Labelling was performed by incubating 750 ng genomic DNA with 1X DLE-1 Enzyme (Bionano Genomics) for 2 hours at 37°C, followed by 20 minutes at 70°C, in the presence of 1X DL-Green and 1X Direct Labelling Enzyme (DLE-1) Buffer. Following proteinase K digestion and DL-Green cleanup, the labelled DNA was mixed with 1X Flow Buffer, in the presence of 1X DTT, and left to incubate overnight at 4°C. Staining was performed by adding 3.2 µl of a DNA stain solution for every 300 ng of pre-stained DNA and incubating at room temperature for at least two hours before loading onto the Bionano Chip. Loading of the chip and running of the Bionano Genomics Saphyr System were all performed according to the Saphyr System User Guide (<https://bionanogenomics.com/support-page/saphyr-system/>).

### Recombination rate data and analysis

Fine-scale recombination rates for human, chimpanzee, bonobo, and gorilla were obtained from previously published sources [74, 75]. Recombination rates were averaged over 500 kbp windows and plotted as a function of distance to active, annotated centromeres on hg38 and the ancestral centromere at 15q25. Recombination data were smoothed using locally weighted smoothing with  $\alpha = 0.05$  for ease of visualization. The coordinates of the ancestral 15q25 centromere were delineated by clones RP11-152F13 and RP11-635O8 [2]. The positions of known recombination hotspots [40] and documented sites of interlocus gene conversion [41] were used to substantiate evidence for homology-driven repair activity at 15q25.

### Data access

Sequencing data from Illumina HiSeq X Ten can be found at the Sequence Read Archive (SRA) under BioProject ID PRJNA493749, as BAM file (GRCh38/hg38). PacBio SMRT sequences of CH17 clones can be found under BioProject ID PRJNA514724. Complete sequences of primate BAC clones (S3 Table) can be found as NC\_036894.1, NC\_036918.1, AC275844.1, AC212984.3, AC210775.3 and AC211297.2.

## Supporting information

**S1 Fig. PacBio SMRT sequencing of CH17 BAC clones across the gap region.** Shown is a Miropeats comparison of a contig obtained from PacBio SMRT sequencing of four CH17 BAC clones and the hg38 human reference. Results due to segmental duplications are shown with gray lines. Black lines connect matching segments between the CH17 contig (bottom) and the reference genome (top), gray lines connect segmental duplications, and red lines connect the region spanning the gap, present once in the CH17 contig and twice in the reference genome. Segmental duplication colors show the ancestral origins of duplications based on comparison with mammalian groups assigned by DupMasker [76]. *GOLGA* repeats mapping on the plus and minus strands are depicted with green and red boxes, respectively. (TIF)

**S2 Fig. PacBio SMRT sequencing of primate BAC clones.** (A) Comparison between human and orangutan duplication blocks. Duplication blocks B and C in human are shown within orange and green boxes, respectively. The purple box indicates the B/C duplication block hybrid in orangutan. Miropeats comparison of sequenced clones mapping at the duplication blocks in human and orangutan genomes are shown. Black lines connect matching segments between human and orangutan. Green and purple lines represent sequence in inverted orientation between the two species, with the green lines showing the proximal breakpoint of the 600 kbp distal inversion. Differences in *GOLGA* repeat content between human and orangutan are also shown. Segmental duplication colors show the ancestral origins of duplications based on comparison with mammalian groups assigned by DupMasker [76]. (B) Miropeats comparison of the B/C hybrid block region in orangutan and macaque. Black lines connect matching segments between human and macaque while red lines indicate sequences in inverted orientation within the B/C hybrid block in macaque relative to orangutan. *GOLGA* repeats in orangutan and macaque are shown. (C) Miropeats comparison of a chimpanzee sequenced clone mapping at the C duplication block in human and chimpanzee genomes. Black lines connect matching segments between human and chimpanzee. *GOLGA* repeats in chimpanzee and human are also shown. (TIF)

**S3 Fig. *GOLGA2P10* and *GOLGA6L5P* BLAT results.** Results of BLAT analysis against the three segmental duplication blocks at the 15q25 locus are shown. Gray and light blue bars represent, respectively, *GOLGA2P10* and *GOLGA6L5P* exon BLAT results with white arrowheads inside the bars showing the orientation of the repeats. Segmental duplications and RefSeq genes (curated subset) are also shown. (TIF)

**S4 Fig. Recombination rates across human, chimpanzee, bonobo, and gorilla.** Broad-scale recombination rates for human, chimpanzee, bonobo, and gorilla autosomes (grey lines) plotted as a function of distance from active, annotated centromeres (red dashed line) on hg38. For chromosome 15 (black line), recombination rates are also plotted as a function of distance from the ancestral 15q25 centromere (red dashed line). Recombination rates were averaged over 500kbp windows. For each figure panel, lines are zero-centered on the autosomal centromere midpoints or the ancestral 15q25 centromere locus (red dashed line). Although recombination rates are reduced in the vicinity of the ancestral 15q25 centromere, suppression is not as strong as observed for active centromeres. (TIF)

**S5 Fig. Mechanism of marker chromosomes formation.** (A) Colored bars show microdeletions and inverted-duplicated supernumerary marker chromosomes (SMCs) involving the 15q25 region, previously characterized either by array CGH or FISH analyses. Two sets of marker chromosomes have been described up to now, consisting of an inverted-duplicated segment either between duplication block B and 15qter (Set 1) or between duplication block C and 15qter (Set 2). (B) On the left is depicted the marker chromosome characterized by Ventura and colleagues. Two duplicated segments (external blue arrowheads) are separated by a stretch of single-copy sequence. NC, neocentromere. On the right, two chromosome 15 homologs are shown with and without the proximal inversion. The orientation of the distal and proximal regions are shown by colored arrowheads, in red for inverted orientation and in green for direct orientation. (C) Mechanisms leading to the formation of marker chromosomes at 15q25. During cell division, asynapsis at the inverted region promotes the refolding of either the direct or inverted chromosome onto itself, allowing intrachromatid synapsis and NAHR between *GOLGA* repeats mapping at segmental duplication blocks A, B and C. Unequal recombination between different blocks leads to the formation of SMCs of different sizes, with the unique region corresponding to the proximal and/or distal 15q25 regions, and a duplication (blue arrowheads) of the terminal part of the q arm. The SMC on the right side of the panel corresponds to the one described by Ventura and colleagues. (TIF)

**S1 File. Blast2Seq alignment results.**

(PDF)

**S1 Table. BLAT results of *GOLGA2P10* and *GOLGA6L5P* in human and nonhuman primate reference genomes.**

(XLSX)

**S2 Table. Inversion analyses in human and nonhuman primate individuals.**

(XLSX)

**S3 Table. PacBio or Sanger sequenced clones.**

(XLSX)

**S4 Table. BLAT results of *GOLGA2P10* and *GOLGA6L5P* in human and nonhuman primate PacBio assemblies.**

(XLSX)

**S5 Table. Multiple regions of high sequence identity between three segmental duplication blocks.**

(XLSX)

**S6 Table. Fosmid clones used for FISH assays.**

(XLSX)

## Acknowledgments

We thank O. Zuffardi, C. R. Catacchio, and T. Brown for critical review of the manuscript. We also thank Cristina Cecere for the graphic work.

## Author Contributions

**Conceptualization:** Flavia A. M. Maggiolini, Francesca Antonacci.

**Data curation:** Flavia A. M. Maggiolini, Francesca Antonacci.

**Funding acquisition:** Evan E. Eichler, Francesca Antonacci.

**Investigation:** Flavia A. M. Maggiolini, Beth L. Dumont, Ashley D. Sanders, Andy Wing Chun Pang, Mitchell R. Vollger, Evan E. Eichler, Francesca Antonacci.

**Project administration:** Francesca Antonacci.

**Resources:** Orazio Palumbo, Pietro Palumbo, Maria Accadia, Massimo Carella, Evan E. Eichler.

**Supervision:** Francesca Antonacci.

**Validation:** Flavia A. M. Maggiolini, Stuart Cantsilieris, Pietro D'Addabbo, Michele Manganeli, Bradley P. Coe, Francesca Antonacci.

**Visualization:** Flavia A. M. Maggiolini, Stuart Cantsilieris, Pietro D'Addabbo, Bradley P. Coe, Ashley D. Sanders, Andy Wing Chun Pang, Mitchell R. Vollger, Francesca Antonacci.

**Writing – original draft:** Flavia A. M. Maggiolini, Francesca Antonacci.

**Writing – review & editing:** Flavia A. M. Maggiolini, Francesca Antonacci.

## References

1. Murphy WJ, Stanyon R, O'Brien SJ. Evolution of mammalian genome organization inferred from comparative gene mapping. *Genome Biol.* 2001; 2(6):REVIEWS0005. PMID: [11423011](#); PubMed Central PMCID: [PMCPMC138942](#).
2. Ventura M, Mudge JM, Palumbo V, Burn S, Blennow E, Pierluigi M, et al. Neocentromeres in 15q24-26 map to duplicons which flanked an ancestral centromere in 15q25. *Genome Res.* 2003; 13(9):2059–68. <https://doi.org/10.1101/gr.1155103> PMID: [12915487](#); PubMed Central PMCID: [PMCPMC403685](#).
3. Choo KH. Why is the centromere so cold? *Genome Res.* 1998; 8(2):81–2. PMID: [9477334](#).
4. Round EK, Flowers SK, Richards EJ. Arabidopsis thaliana centromere regions: genetic map positions and repetitive DNA structure. *Genome Res.* 1997; 7(11):1045–53. PMID: [9371740](#).
5. Mahtani MM, Willard HF. A primary genetic map of the pericentromeric region of the human X chromosome. *Genomics.* 1988; 2(4):294–301. PMID: [2906040](#).
6. Zody MC, Garber M, Sharpe T, Young SK, Rowen L, O'Neill K, et al. Analysis of the DNA sequence and duplication history of human chromosome 15. *Nature.* 2006; 440(7084):671–5. <https://doi.org/10.1038/nature04601> PMID: [16572171](#).
7. Marques-Bonet T, Eichler EE. The evolution of human segmental duplications and the core duplication hypothesis. *Cold Spring Harb Symp Quant Biol.* 2009; 74:355–62. <https://doi.org/10.1101/sqb.2009.74.011> PMID: [19717539](#); PubMed Central PMCID: [PMCPMC4114149](#).
8. Jiang Z, Tang H, Ventura M, Cardone MF, Marques-Bonet T, She X, et al. Ancestral reconstruction of segmental duplications reveals punctuated cores of human genome evolution. *Nat Genet.* 2007; 39(11):1361–8. <https://doi.org/10.1038/ng.2007.9> PMID: [17922013](#).
9. Pujana MA, Nadal M, Gratacos M, Peral B, Csiszar K, Gonzalez-Sarmiento R, et al. Additional complexity on human chromosome 15q: identification of a set of newly recognized duplicons (LCR15) on 15q11-q13, 15q24, and 15q26. *Genome Res.* 2001; 11(1):98–111. PMID: [11156619](#); PubMed Central PMCID: [PMCPMC311040](#).
10. Marques-Bonet T, Kidd JM, Ventura M, Graves TA, Cheng Z, Hillier LW, et al. A burst of segmental duplications in the genome of the African great ape ancestor. *Nature.* 2009; 457(7231):877–81. <https://doi.org/10.1038/nature07744> PMID: [19212409](#); PubMed Central PMCID: [PMCPMC2751663](#).
11. Sudmant PH, Huddleston J, Catacchio CR, Malig M, Hillier LW, Baker C, et al. Evolution and diversity of copy number variation in the great ape lineage. *Genome research.* 2013; 23(9):1373–82. Epub 2013/07/05. <https://doi.org/10.1101/gr.158543.113> PMID: [23825009](#); PubMed Central PMCID: [PMC3759715](#).
12. Giannuzzi G, Paziienza M, Huddleston J, Antonacci F, Malig M, Vives L, et al. Hominoid fission of chromosome 14/15 and the role of segmental duplications. *Genome Res.* 2013; 23(11):1763–73. <https://doi.org/10.1101/gr.156240.113> PMID: [24077392](#); PubMed Central PMCID: [PMCPMC3814877](#).



13. Antonacci F, Dennis MY, Huddleston J, Sudmant PH, Steinberg KM, Rosenfeld JA, et al. Palindromic GOLGA8 core duplicons promote chromosome 15q13.3 microdeletion and evolutionary instability. *Nat Genet.* 2014; 46(12):1293–302. <https://doi.org/10.1038/ng.3120> PMID: 25326701; PubMed Central PMCID: PMC4244265.
14. Pujana MA, Nadal M, Guitart M, Armengol L, Gratacos M, Estivill X. Human chromosome 15q11-q14 regions of rearrangements contain clusters of LCR15 duplicons. *Eur J Hum Genet.* 2002; 10(1):26–35. <https://doi.org/10.1038/sj.ejhg.5200760> PMID: 11896453.
15. Mefford HC, Rosenfeld JA, Shur N, Slavotinek AM, Cox VA, Hennekam RC, et al. Further clinical and molecular delineation of the 15q24 microdeletion syndrome. *Journal of medical genetics.* 2012; 49(2):110–8. Epub 2011/12/20. <https://doi.org/10.1136/jmedgenet-2011-100499> PMID: 22180641; PubMed Central PMCID: PMC3261729.
16. Wat MJ, Enciso VB, Wiszniewski W, Resnick T, Bader P, Roeder ER, et al. Recurrent microdeletions of 15q25.2 are associated with increased risk of congenital diaphragmatic hernia, cognitive deficits and possibly Diamond—Blackfan anaemia. *Journal of medical genetics.* 2010; 47(11):777–81. Epub 2010/10/06. <https://doi.org/10.1136/jmg.2009.075903> PMID: 20921022; PubMed Central PMCID: PMC3225959.
17. Amos-Landgraf JM, Ji Y, Gottlieb W, Depinet T, Wandstrat AE, Cassidy SB, et al. Chromosome breakage in the Prader-Willi and Angelman syndromes involves recombination between large, transcribed repeats at proximal and distal breakpoints. *American journal of human genetics.* 1999; 65(2):370–86. Epub 1999/07/27. <https://doi.org/10.1086/302510> PMID: 10417280; PubMed Central PMCID: PMC1377936.
18. El-Hattab AW, Smolarek TA, Walker ME, Schorry EK, Immken LL, Patel G, et al. Redefined genomic architecture in 15q24 directed by patient deletion/duplication breakpoint mapping. *Human genetics.* 2009; 126(4):589–602. Epub 2009/06/27. <https://doi.org/10.1007/s00439-009-0706-x> PMID: 19557438; PubMed Central PMCID: PMC3669685.
19. Doelken SC, Seeger K, Hundsdoerfer P, Weber-Ferro W, Klopocki E, Graul-Neumann L. Proximal and distal 15q25.2 microdeletions—genotype-phenotype delineation of two neurodevelopmental susceptibility loci. *Am J Med Genet A.* 2013; 161A(1):218–24. <https://doi.org/10.1002/ajmg.a.35695> PMID: 23239641.
20. Burgess T, Brown NJ, Stark Z, Bruno DL, Oertel R, Chong B, et al. Characterization of core clinical phenotypes associated with recurrent proximal 15q25.2 microdeletions. *Am J Med Genet A.* 2014; 164A(1):77–86. <https://doi.org/10.1002/ajmg.a.36203> PMID: 24352913.
21. Wat MJ, Enciso VB, Wiszniewski W, Resnick T, Bader P, Roeder ER, et al. Recurrent microdeletions of 15q25.2 are associated with increased risk of congenital diaphragmatic hernia, cognitive deficits and possibly Diamond—Blackfan anaemia. *J Med Genet.* 2010; 47(11):777–81. <https://doi.org/10.1136/jmg.2009.075903> PMID: 20921022; PubMed Central PMCID: PMC3225959.
22. Cooper GM, Coe BP, Girirajan S, Rosenfeld JA, Vu TH, Baker C, et al. A copy number variation morbidity map of developmental delay. *Nat Genet.* 2011; 43(9):838–46. <https://doi.org/10.1038/ng.909> PMID: 21841781; PubMed Central PMCID: PMC3171215.
23. Mefford HC, Clauin S, Sharp AJ, Moller RS, Ullmann R, Kapur R, et al. Recurrent reciprocal genomic rearrangements of 17q12 are associated with renal disease, diabetes, and epilepsy. *Am J Hum Genet.* 2007; 81(5):1057–69. <https://doi.org/10.1086/522591> PMID: 17924346; PubMed Central PMCID: PMC3226563.
24. Palumbo O, Palumbo P, Palladino T, Stallone R, Miroballo M, Piemontese MR, et al. An emerging phenotype of interstitial 15q25.2 microdeletions: clinical report and review. *Am J Med Genet A.* 2012; 158A(12):3182–9. <https://doi.org/10.1002/ajmg.a.35631> PMID: 23166063.
25. Liehr T, Claussen U, Starke H. Small supernumerary marker chromosomes (sSMC) in humans. *Cytogenet Genome Res.* 2004; 107(1–2):55–67. <https://doi.org/10.1159/000079572> PMID: 15305057.
26. Liehr T, Utine GE, Trautmann U, Rauch A, Kuechler A, Pietrzak J, et al. Neocentric small supernumerary marker chromosomes (sSMC)—three more cases and review of the literature. *Cytogenet Genome Res.* 2007; 118(1):31–7. <https://doi.org/10.1159/000106438> PMID: 17901697.
27. Tatton-Brown K, Pilz DT, Orstavik KH, Patton M, Barber JC, Collinson MN, et al. 15q overgrowth syndrome: a newly recognized phenotype associated with overgrowth, learning difficulties, characteristic facial appearance, renal anomalies and increased dosage of distal chromosome 15q. *Am J Med Genet A.* 2009; 149A(2):147–54. <https://doi.org/10.1002/ajmg.a.32534> PMID: 19133692.
28. George-Abraham JK, Zimmerman SL, Hinton RB, Marino BS, Witte DP, Hopkin RJ. Tetrasomy 15q25.2—>qter identified with SNP microarray in a patient with multiple anomalies including complex cardiovascular malformation. *Am J Med Genet A.* 2012; 158A(8):1971–6. <https://doi.org/10.1002/ajmg.a.35428> PMID: 22711292.

29. Xu H, Xiao B, Ji X, Hu Q, Chen Y, Qiu W. Nonmosaic tetrasomy 15q25.2 → qter identified with SNP microarray in a patient with characteristic facial appearance and review of the literature. *Eur J Med Genet.* 2014; 57(7):329–33. <https://doi.org/10.1016/j.ejmg.2014.04.011> PMID: 24793337.
30. Sanders AD, Hills M, Porubsky D, Guryev V, Falconer E, Lansdorp PM. Characterizing polymorphic inversions in human genomes by single-cell sequencing. *Genome Res.* 2016; 26(11):1575–87. <https://doi.org/10.1101/gr.201160.115> PMID: 27472961; PubMed Central PMCID: PMC5088599.
31. Fan JB, Surti U, Taillon-Miller P, Hsie L, Kennedy GC, Hoffner L, et al. Paternal origins of complete hydatidiform moles proven by whole genome single-nucleotide polymorphism haplotyping. *Genomics.* 2002; 79(1):58–62. <https://doi.org/10.1006/geno.2001.6676> PMID: 11827458.
32. Bailey JA, Eichler EE. Primate segmental duplications: crucibles of evolution, diversity and disease. *Nat Rev Genet.* 2006; 7(7):552–64. <https://doi.org/10.1038/nrg1895> PMID: 16770338.
33. Marques-Bonet T, Girirajan S, Eichler EE. The origins and impact of primate segmental duplications. *Trends Genet.* 2009; 25(10):443–54. <https://doi.org/10.1016/j.tig.2009.08.002> PMID: 19796838; PubMed Central PMCID: PMC2847396.
34. Watson CT, Marques-Bonet T, Sharp AJ, Mefford HC. The genetics of microdeletion and microduplication syndromes: an update. *Annu Rev Genomics Hum Genet.* 2014; 15:215–44. <https://doi.org/10.1146/annurev-genom-091212-153408> PMID: 24773319; PubMed Central PMCID: PMC4476258.
35. Antonacci F, Kidd JM, Marques-Bonet T, Teague B, Ventura M, Girirajan S, et al. A large and complex structural polymorphism at 16p12.1 underlies microdeletion disease risk. *Nat Genet.* 2010; 42(9):745–50. <https://doi.org/10.1038/ng.643> PMID: 20729854; PubMed Central PMCID: PMC2930074.
36. Antonacci F, Kidd JM, Marques-Bonet T, Ventura M, Siswara P, Jiang Z, et al. Characterization of six human disease-associated inversion polymorphisms. *Hum Mol Genet.* 2009; 18(14):2555–66. <https://doi.org/10.1093/hmg/ddp187> PMID: 19383631; PubMed Central PMCID: PMC2701327.
37. Catacchio CR, Maggolini FAM, D'Addabbo P, Bitonto M, Capozzi O, Lepore Signorile M, et al. Inversion variants in human and primate genomes. *Genome Res.* 2018; 28(6):910–20. <https://doi.org/10.1101/gr.234831.118> PMID: 29776991; PubMed Central PMCID: PMC5991517.
38. Steinberg KM, Antonacci F, Sudmant PH, Kidd JM, Campbell CD, Vives L, et al. Structural diversity and African origin of the 17q21.31 inversion polymorphism. *Nat Genet.* 2012; 44(8):872–80. <https://doi.org/10.1038/ng.2335> PMID: 22751100; PubMed Central PMCID: PMC3408829.
39. Sudmant PH, Kitzman JO, Antonacci F, Alkan C, Malig M, Tsalenko A, et al. Diversity of human copy number variation and multicopy genes. *Science.* 2010; 330(6004):641–6. <https://doi.org/10.1126/science.1197005> PMID: 21030649; PubMed Central PMCID: PMC3020103.
40. Pratto F, Brick K, Khil P, Smagulova F, Petukhova GV, Camerini-Otero RD. DNA recombination. Recombination initiation maps of individual human genomes. *Science.* 2014; 346(6211):1256442. <https://doi.org/10.1126/science.1256442> PMID: 25395542; PubMed Central PMCID: PMC5588152.
41. Dumont BL. Interlocus gene conversion explains at least 2.7% of single nucleotide variants in human segmental duplications. *BMC Genomics.* 2015; 16:456. <https://doi.org/10.1186/s12864-015-1681-3> PMID: 26077037; PubMed Central PMCID: PMC4467073.
42. Zody MC, Jiang Z, Fung HC, Antonacci F, Hillier LW, Cardone MF, et al. Evolutionary toggling of the MAPT 17q21.31 inversion region. *Nat Genet.* 2008; 40(9):1076–83. <https://doi.org/10.1038/ng.193> PMID: 19165922; PubMed Central PMCID: PMC2684794.
43. Osborne LR, Li M, Pober B, Chitayat D, Bodurtha J, Mandel A, et al. A 1.5 million-base pair inversion polymorphism in families with Williams-Beuren syndrome. *Nat Genet.* 2001; 29(3):321–5. <https://doi.org/10.1038/ng753> PMID: 11685205; PubMed Central PMCID: PMC2889916.
44. Giglio S, Broman KW, Matsumoto N, Calvari V, Gimelli G, Neumann T, et al. Olfactory receptor-gene clusters, genomic-inversion polymorphisms, and common chromosome rearrangements. *Am J Hum Genet.* 2001; 68(4):874–83. <https://doi.org/10.1086/319506> PMID: 11231899; PubMed Central PMCID: PMC1275641.
45. Amor DJ, Choo KH. Neocentromeres: role in human disease, evolution, and centromere study. *Am J Hum Genet.* 2002; 71(4):695–714. <https://doi.org/10.1086/342730> PMID: 12196915; PubMed Central PMCID: PMC378529.
46. Marshall OJ, Chueh AC, Wong LH, Choo KH. Neocentromeres: new insights into centromere structure, disease development, and karyotype evolution. *Am J Hum Genet.* 2008; 82(2):261–82. <https://doi.org/10.1016/j.ajhg.2007.11.009> PMID: 18252209; PubMed Central PMCID: PMC2427194.
47. Blennow E, Bui TH, Kristoffersson U, Vujic M, Anneren G, Holmberg E, et al. Swedish survey on extra structurally abnormal chromosomes in 39 105 consecutive prenatal diagnoses: prevalence and characterization by fluorescence in situ hybridization. *Prenat Diagn.* 1994; 14(11):1019–28. PMID: 7877949.

48. Blennow E, Telenius H, de Vos D, Larsson C, Henriksson P, Johansson O, et al. Tetrasomy 15q: two marker chromosomes with no detectable alpha-satellite DNA. *Am J Hum Genet.* 1994; 54(5):877–83. PMID: [8178828](#); PubMed Central PMCID: [PMCPMC1918253](#).
49. Van den Enden A, Verschraegen-Spae MR, Van Roy N, Decaluwe W, De Praeter C, Speleman F. Mosaic tetrasomy 15q25→qter in a newborn infant with multiple anomalies. *Am J Med Genet.* 1996; 63(3):482–5. [https://doi.org/10.1002/\(SICI\)1096-8628\(19960614\)63:3<482::AID-AJMG13>3.0.CO;2-I](https://doi.org/10.1002/(SICI)1096-8628(19960614)63:3<482::AID-AJMG13>3.0.CO;2-I) PMID: [8737657](#).
50. Depinet TW, Zackowski JL, Earnshaw WC, Kaffe S, Sekhon GS, Stallard R, et al. Characterization of neo-centromeres in marker chromosomes lacking detectable alpha-satellite DNA. *Hum Mol Genet.* 1997; 6(8):1195–204. PMID: [9259264](#).
51. Huang B, Ning Y, Lamb AN, Sandlin CJ, Jamehdor M, Ried T, et al. Identification of an unusual marker chromosome by spectral karyotyping. *Am J Med Genet.* 1998; 80(4):368–72. PMID: [9856565](#).
52. Wandstrat AE, Leana-Cox J, Jenkins L, Schwartz S. Molecular cytogenetic evidence for a common breakpoint in the largest inverted duplications of chromosome 15. *Am J Hum Genet.* 1998; 62(4):925–36. <https://doi.org/10.1086/301777> PMID: [9529335](#); PubMed Central PMCID: [PMCPMC1377019](#).
53. Rowe AG, Abrams L, Qu Y, Chen E, Cotter PD. Tetrasomy 15q25→qter: cytogenetic and molecular characterization of an analphoid supernumerary marker chromosome. *Am J Med Genet.* 2000; 93(5):393–8. PMID: [10951463](#).
54. Hu J, McPherson E, Surti U, Hasegawa SL, Gunawardena S, Gollin SM. Tetrasomy 15q25.3→qter resulting from an analphoid supernumerary marker chromosome in a patient with multiple anomalies and bilateral Wilms tumors. *Am J Med Genet.* 2002; 113(1):82–8. <https://doi.org/10.1002/ajmg.10708> PMID: [12400070](#).
55. Spiegel M, Hickmann G, Senger G, Kozlowski P, Bartsch O. Two new cases of analphoid marker chromosomes. *Am J Med Genet A.* 2003; 116A(3):284–9. <https://doi.org/10.1002/ajmg.a.10916> PMID: [12503108](#).
56. Chen CP, Lin CC, Li YC, Chern SR, Lee CC, Chen WL, et al. Clinical, cytogenetic, and molecular analyses of prenatally diagnosed mosaic tetrasomy for distal chromosome 15q and review of the literature. *Prenat Diagn.* 2004; 24(10):767–73. <https://doi.org/10.1002/pd.977> PMID: [15503270](#).
57. Huang XL, de Michelena MI, Mark H, Harston R, Benke PJ, Price SJ, et al. Characterization of an analphoid supernumerary marker chromosome derived from 15q25→qter using high-resolution CGH and multiplex FISH analyses. *Clin Genet.* 2005; 68(6):513–9. <https://doi.org/10.1111/j.1399-0004.2005.00523.x> PMID: [16283881](#).
58. Tonnie H, Pietrzak J, Bocian E, MacDermont K, Kuechler A, Belitz B, et al. New immortalized cell lines of patients with small supernumerary marker chromosome: towards the establishment of a cell bank. *J Histochem Cytochem.* 2007; 55(6):651–60. <https://doi.org/10.1369/jhc.6A7161.2007> PMID: [17341473](#).
59. Levy B, Tegay D, Papenhausen P, Tepperberg J, Nahum O, Tsuchida T, et al. Tetrasomy 15q26: a distinct syndrome or Shprintzen-Goldberg syndrome phenocopy? *Genet Med.* 2012; 14(9):811–8. <https://doi.org/10.1038/gim.2012.54> PMID: [22653535](#).
60. Liehr T, Cirkovic S, Lalic T, Guc-Scekic M, de Almeida C, Weimer J, et al. Complex small supernumerary marker chromosomes—an update. *Mol Cytogenet.* 2013; 6:46. <https://doi.org/10.1186/1755-8166-6-46> PMID: [24171835](#); PubMed Central PMCID: [PMCPMC4129180](#).
61. Jafari-Ghahfarokhi H, Moradi-Chaleshtori M, Liehr T, Hashemzadeh-Chaleshtori M, Teimori H, Ghasemi-Dehkordi P. Small supernumerary marker chromosomes and their correlation with specific syndromes. *Adv Biomed Res.* 2015; 4:140. <https://doi.org/10.4103/2277-9175.161542> PMID: [26322288](#); PubMed Central PMCID: [PMCPMC4544121](#).
62. Cox DM, Butler MG. Distal Partial Trisomy 15q26 and Partial Monosomy 16p13.3 in a 36-Year-Old Male with Clinical Features of Both Chromosomal Abnormalities. *Cytogenet Genome Res.* 2015; 145(1):29–34. <https://doi.org/10.1159/000381293> PMID: [25871641](#); PubMed Central PMCID: [PMCPMC5463451](#).
63. Cannarella R, Mattina T, Condorelli RA, Mongioi LM, Pandini G, La Vignera S, et al. Chromosome 15 structural abnormalities: effect on IGF1R gene expression and function. *Endocr Connect.* 2017; 6(7):528–39. <https://doi.org/10.1530/EC-17-0158> PMID: [28899882](#); PubMed Central PMCID: [PMCPMC5597972](#).
64. Lichter P, Tang CJ, Call K, Hermanson G, Evans GA, Housman D, et al. High-resolution mapping of human chromosome 11 by in situ hybridization with cosmid clones. *Science.* 1990; 247(4938):64–9. PMID: [2294592](#).
65. Palumbo O, Accadia M, Palumbo P, Leone MP, Scorrano A, Palladino T, et al. Refinement of the critical 7p22.1 deletion region: Haploinsufficiency of ACTB is the cause of the 7p22.1 microdeletion-related developmental disorders. *Eur J Med Genet.* 2018; 61(5):248–52. <https://doi.org/10.1016/j.ejmg.2017.12.008> PMID: [29274487](#).



66. Kearney HM, Thorland EC, Brown KK, Quintero-Rivera F, South ST, Working Group of the American College of Medical Genetics Laboratory Quality Assurance C. American College of Medical Genetics standards and guidelines for interpretation and reporting of postnatal constitutional copy number variants. *Genet Med.* 2011; 13(7):680–5. <https://doi.org/10.1097/GIM.0b013e3182217a3a> PMID: 21681106.
67. Hach F, Hormozdiari F, Alkan C, Hormozdiari F, Birol I, Eichler EE, et al. mrsFAST: a cache-oblivious algorithm for short-read mapping. *Nat Methods.* 2010; 7(8):576–7. <https://doi.org/10.1038/nmeth0810-576> PMID: 20676076; PubMed Central PMCID: PMC3115707.
68. Huddleston J, Ranade S, Malig M, Antonacci F, Chaisson M, Hon L, et al. Reconstructing complex regions of genomes using long-read sequencing technology. *Genome Res.* 2014; 24(4):688–96. <https://doi.org/10.1101/gr.168450.113> PMID: 24418700; PubMed Central PMCID: PMC3975067.
69. Koren S, Walenz BP, Berlin K, Miller JR, Bergman NH, Phillippy AM. Canu: scalable and accurate long-read assembly via adaptive k-mer weighting and repeat separation. *Genome Res.* 2017; 27(5):722–36. <https://doi.org/10.1101/gr.215087.116> PMID: 28298431; PubMed Central PMCID: PMC5411767.
70. Parsons JD. Miropeats: graphical DNA sequence comparisons. *Comput Appl Biosci.* 1995; 11(6):615–9. Epub 1995/12/01. PMID: 8808577.
71. Altschul SF, Gish W, Miller W, Myers EW, Lipman DJ. Basic local alignment search tool. *J Mol Biol.* 1990; 215(3):403–10. [https://doi.org/10.1016/S0022-2836\(05\)80360-2](https://doi.org/10.1016/S0022-2836(05)80360-2) PMID: 2231712.
72. Bailey JA, Gu Z, Clark RA, Reinert K, Samonte RV, Schwartz S, et al. Recent segmental duplications in the human genome. *Science.* 2002; 297(5583):1003–7. <https://doi.org/10.1126/science.1072047> PMID: 12169732.
73. Kronenberg ZN, Fiddes IT, Gordon D, Murali S, Cantsilieris S, Meyerson OS, et al. High-resolution comparative analysis of great ape genomes. *Science.* 2018; 360(6393). <https://doi.org/10.1126/science.aar6343> PMID: 29880660.
74. Stevison LS, Woerner AE, Kidd JM, Kelley JL, Veeramah KR, McManus KF, et al. The Time Scale of Recombination Rate Evolution in Great Apes. *Mol Biol Evol.* 2016; 33(4):928–45. <https://doi.org/10.1093/molbev/msv331> PMID: 26671457; PubMed Central PMCID: PMC5870646.
75. International HapMap C, Frazer KA, Ballinger DG, Cox DR, Hinds DA, Stuve LL, et al. A second generation human haplotype map of over 3.1 million SNPs. *Nature.* 2007; 449(7164):851–61. <https://doi.org/10.1038/nature06258> PMID: 17943122; PubMed Central PMCID: PMC2689609.
76. Jiang Z, Hubley R, Smit A, Eichler EE. DupMasker: a tool for annotating primate segmental duplications. *Genome Res.* 2008; 18(8):1362–8. <https://doi.org/10.1101/gr.078477.108> PMID: 18502942; PubMed Central PMCID: PMC2493431.

There were two patients reported to suffer from mild sleep disturbance and another two patients experiencing gastrointestinal symptoms, such as mild constipation. The average duration of treatment was 28.9 weeks.

In conclusion, our preliminary results showed that atenolol might be as effective as propranolol for the treatment of IH. The adverse effects observed were negligible. Atenolol administered only once daily certainly improved patients' compliance. Therefore, if confirmed in additional randomized controlled studies, atenolol may become a reasonable alternative to propranolol.

A. Alexopoulos,\* I. Thanopoulou, M. Dakoutrou,  
E. Georgiadou, G.P. Chrousos, T. Kakourou

First Department of Pediatrics, "Aghia Sofia" Children's Hospital,  
University of Athens, Athens, Greece

\*Correspondence: A. Alexopoulos. E-mail: atosmedicals@yahoo.co.uk

## References

- Leaute-Labreze C, Prey S, Ezzedine K. Infantile haemangioma: part II. Risks, complications and treatment. *J Eur Acad Dermatol Venereol* 2011; **25**: 1254–1260.
- Haggstrom AN, Drolet BA, Baselga E *et al*. Prospective study of infantile hemangiomas: demographic, prenatal, and perinatal characteristics. *J Pediatr* 2007; **150**: 291–294.
- Enjolras O, Gelbert F. Superficial hemangiomas: associations and management. *Pediatr Dermatol* 1997; **14**: 173–179.
- Shayan YR, Prendiville JS, Goldman RD. Use of propranolol in treating hemangiomas. *Can Fam Physician* 2011; **57**: 302–303.
- Ji Y, Wang Q, Chen S *et al*. Oral atenolol therapy for proliferating infantile hemangioma: a prospective study. *Medicine (Baltimore)* 2016; **95**: e3908.
- de Graaf M, Raphael MF, Breugem CC *et al*. Treatment of infantile haemangiomas with atenolol: comparison with a historical propranolol group. *J Plast Reconstr Aesthet Surg* 2013; **66**: 1732–1740.
- Tasani M, Glover M, Martinez AE, Shaw L. Atenolol treatment for infantile haemangioma. *Br J Dermatol* 2017; **176**: 1400–1402.

DOI: 10.1111/jdv.14590

## MC1R genotype and psoriasis: is there a link revealing a phenotypic difference?

Editor

Psychological stress is known to trigger inflammatory skin diseases such as psoriasis. Recently, levels of hormones derived from pre-opiomelanocortin (POMC) were related to different types of psoriasis.<sup>1</sup> In particular,  $\alpha$ -MSH, a POMC derivative, is known for its role in pigmentation and for its anti-inflammatory activity. Accordingly, it has been recently suggested for the treatment of imiquimod-induced psoriasis.<sup>2,3</sup>

For this reason, we decided to investigate the status of  $\alpha$ -MSH receptor, the melanocortin 1 receptor (MC1R). The MC1R gene is a highly polymorphic gene codifying for a transmembrane

G-protein-coupled receptor. Some MC1R alleles have been associated with fair skin, increased sensitivity to ultraviolet (UV) radiation (the 'so-called RHC phenotype associated with RHC variants), psoralen-UVA photochemotherapy erythema sensitivity, a worse outcome of melanoma patients treated with anti-BRAF and increased skin cancer risk.<sup>4–9</sup> Nevertheless, its role in skin inflammatory diseases, as compared to non-psoriatic controls, has not been previously described.

We report herein a preliminary analysis of MC1R genotype in psoriatic patients, as compared to non-psoriatic controls. Participants were recruited from a single Dermatology Unit (Bari). We included 24 consecutive patients affected by stable plaque psoriasis lasting at least 6 months (three of which affected by psoriatic arthritis) and 53 controls.

Clinical skin examination, detailed questionnaire and MC1R sequencing, after signing a written informed consent, were performed for all subjects enrolled and are reported in Table 1. MC1R genotype and sequence analysis were performed as previously described.<sup>5</sup> Table 2 shows MC1R genotype in both cases and controls. Procedures followed were in accordance with the ethical standards of the responsible committee on human experimentation and with the Helsinki Declaration.

Statistical analysis was performed using SPSS statistical package (IBM, Armonk, NY, U.S.A.).

**Table 1** Results of the univariate analysis

		Psoriasis (%)	Control (%)	P*
<b>Sex</b>	Female	8 (33.3)	27 (50.9)	0.151†
	Male	16 (66.7)	26 (49.1)	
<b>Age</b>	≤50	16 (66.7)	24 (45.3)	0.082†
	>50	8 (33.3)	29 (54.7)	
<b>Smoking habits</b>		8 (33.3)	14 (56)	0.534‡
<b>Alcohol addiction</b>		4 (16.7)	14 (56)	0.4‡
<b>Hair colour</b>	Light (red and blond)	0	10 (18.9)	0.026‡
	Dark (brown and black)	24 (100)	43 (81.1)	
<b>Eye colour</b>	Light (blue or grey, green or hazel)	4 (16.7)	22 (41.5)	0.039‡
	Dark (light brown and dark brown)	20 (83.3)	31 (58.5)	
<b>Skin colour</b>	Light	9 (37.5)	37 (69.8)	0.007†
	Dark	15 (62.5)	16 (30.2)	
<b>Number of nevi</b>	≤50	20 (83.3)	46 (86.8)	0.732‡
	>50	4 (16.7)	7 (13.2)	
<b>Multiple MC1R variants</b>		0	11 (20.7)	0.014‡

\*A P-value < 0.05 was considered significant.

†Pearson chi-square test.

‡Fisher's exact test.

**Table 2** MC1R genotype

MC1R status	Psoriasis	%	Control	%
WT or silent polymorphism	9	37.5	17	32
Single polymorphism				
V60L	10	41.7	10	19
RHC variants	4	16.7	11	21
Others	1	4.1	4	8
Multiple polymorphisms	0		11	21

The univariate analysis highlighted a significant association between psoriasis and dark skin ( $P = 0.007$ ; OR 3.854, 95% CI 1.399–10.617), hair ( $P = 0.039$ ) and eye colour ( $P = 0.026$ ; OR 3.548, 95% CI 1.064–11.835). Furthermore, psoriasis is associated with absence of multiple MC1R variants ( $P = 0.014$ ) (Table 1).

We show that dark skin, hair and eye colour are related to psoriasis while the presence of MC1R multiple variants is a protective factor in psoriatics, as compared to controls.

MC1R polymorphisms are related to different degrees of receptor functional impairment, depending on the specific polymorphism and number of variants.<sup>5,6</sup> As a matter of fact, our results show that psoriatic patients are more likely to be wt or carriers of a single MC1R polymorphism. These data suggest that the preserved functionality of MC1R in psoriatics can be related to peculiar phenotypic features (dark skin, eye and hair colour), as compared to controls. Interestingly, the functional integrity of MC1R in psoriatic patients would be essential to exert the anti-inflammatory effects due to the binding of  $\alpha$ -MSH and related analogues.<sup>10</sup> This is the first paper focusing on the role and the possible impact of MC1R genotype in psoriasis. A limitation of our study is the number of patients enrolled. Further investigation is necessary to confirm these results.

S. Guida,<sup>1,\*</sup> C. Foti,<sup>2</sup> M. Manganeli,<sup>3</sup> N. Bartolomeo,<sup>4</sup> G. Pellacani,<sup>1</sup> D. Bonamonte,<sup>2</sup> R. Filotico,<sup>5</sup> G. Guida<sup>3,\*</sup>

<sup>1</sup>Dermatology Unit, University of Modena and Reggio Emilia, Modena, Italy, <sup>2</sup>Dermatological Clinic, Department of Biomedical Science and Human Oncology, University of Bari, Bari, Italy, <sup>3</sup>Molecular Biology Section, Department of Basic Medical Sciences, Neurosciences and Sense Organs, University of Bari, Bari, Italy, <sup>4</sup>Hygiene Section, Department of Biomedical Sciences and Human Oncology, University of Bari, Bari, Italy, <sup>5</sup>Dermatology Unit, Hospital "A. Perrino", Brindisi, Italy  
\*Correspondence: S. Guida. E-mail: drstefaniaguida@gmail.com and G. Guida. E-mail: gabriella.guida@uniba.it

## References

- Kim JE, Cho DH, Kim HS *et al.* Expression of the corticotropin-releasing hormone-proopiomelanocortin axis in the various clinical types of psoriasis. *Exp Dermatol* 2007; **16**: 104–109.
- Shah PP, Desai PR, Boakye CH *et al.* Percutaneous delivery of  $\alpha$ -melanocyte-stimulating hormone for the treatment of imiquimod-induced psoriasis. *J Drug Target* 2016; **24**: 537–547.
- Getting SJ. Targeting melanocortin receptors as potential novel therapeutics. *Pharmacol Ther* 2006; **111**: 1–15.
- Tagliabue E, Gandini S, García-Borrón JC *et al.* Association of melanocortin-1 receptor variants with pigimentary traits in humans: A pooled analysis from the M-Skip project. *J Invest Dermatol* 2016; **136**: 1914–1917.
- Guida S, Bartolomeo N, Zanna PT *et al.* Sporadic melanoma in South-Eastern Italy: the impact of melanocortin 1 receptor (MC1R) polymorphism analysis in low-risk people and report of three novel variants. *Arch Dermatol Res* 2015; **307**: 495–503.
- Sánchez-Laorden BL, Herraiz C, Valencia JC, Hearing VJ, Jiménez-Cervantes C, García-Borrón JC. Aberrant trafficking of human melanocortin 1 receptor variants associated with red hair and skin cancer: Steady-state retention of mutant forms in the proximal golgi. *J Cell Physiol* 2009; **220**: 640–654.
- Zanna P, Maida I, Grieco C *et al.* Three novel human sporadic melanoma cell lines: signaling pathways controlled by MC1R, BRAF and  $\beta$ -catenins. *J Biol Regul Homeost Agents* 2013; **27**: 131–141.
- Smith G, Wilkie MJ, Deeni YY *et al.* Melanocortin 1 receptor (MC1R) genotype influences erythral sensitivity to psoralen-ultraviolet A photochemotherapy. *Br J Dermatol* 2007; **157**: 1230–1234.
- Guida M, Strippoli S, Ferretta A *et al.* Detrimental effects of melanocortin-1 receptor (MC1R) variants on the clinical outcomes of BRAF V600 metastatic melanoma patients treated with BRAF inhibitors. *Pigment Cell Melanoma Res* 2016; **29**: 679–687.
- Nasti TH, Timares L. MC1R, eumelanin and pheomelanin: their role in determining the susceptibility to skin cancer. *Photochem Photobiol* 2015; **91**: 188–200.

DOI: 10.1111/jdv.14607

## Safety of secukinumab in hepatitis B virus

### Editor

The usage of TNF antagonists in patients with hepatitis B virus (HBV) can result in viral reactivation and potential liver failure. However, little is known about the risk of viral reactivation with the newer IL-17 antagonists. We report a patient with seropositive hepatitis B, ankylosing spondylitis and disabling palmar-plantar psoriasis treated successfully with secukinumab without liver complications.

A 47-year-old woman presented with an 11-year history of plantar psoriasis, HBV, fatty liver disease and ankylosing spondylitis. Her treatment was delayed due to concern for safety issues on biologic therapies. Secukinumab (150 mg every 4 weeks) was initiated after laboratories indicated adequate liver function (AST 44, ALT 50). Symptomatic improvement of ankylosing spondylitis without improvement in her dermatologic condition was noted 2 months later, so secukinumab was subsequently increased to 300 mg every 4 weeks. This resulted in improvement in joint pain and clearance of psoriasis. Our patient has been stable on secukinumab (300 mg monthly) for 14 months with no elevation of liver enzymes or reactivation of HBV.

There are scant reports of secukinumab treatment utilized in the setting of HBV infection (five patients), HCV infection